Reactivity of (bi)metallic catalysts for reforming of biomass derived alcohols

PROEFSCHRIFT

ter verkrijging van de graad van doctor aan de Technische Universiteit Eindhoven, op gezag van de rector magnificus prof.dr.ir. C.J. van Duijn, voor een commissie aangewezen door het College voor Promoties, in het openbaar te verdedigen op woensdag 26 februari 2014 om 16:00 uur

door

Ayşegül Çiftçi

geboren te Ankara, Turkije

Dit proefschrift is goedgekeurd door de promotoren en de samenstelling van de promotiecommissie is als volgt:

voorzitter: prof.dr.ir. J.C. Schouten
1^e promotor: prof.dr.ir. E.J.M. Hensen
2^e promotor: prof.dr. R.A. van Santen
leden: prof.dr. K. Seshan (University of Twente)
prof.dr. D.Y. Murzin (Åbo Akademi University)
prof.dr. J.W. Niemantsverdriet
dr.ir. T.A. Nijhuis

Dedicated to my husband Selçuk, my parents and my sister

"It is good to have an end to journey toward; but it is the journey that matters, in the end."

(Ernest Hemingway)

Table of Contents

Chapter 1

General Introduction

1.1 The energy challenge

Due to rapid global changes in energy demand, energy markets continuously evolve. In order to fulfill the growing needs, the diversity of energy supply is increasing. Currently, more than three quarters of the world's energy demand is supplied from fossil resources such as oil, natural gas and coal [1]. Oil is the primary energy source, accounting for about a third of the global energy consumption in 2012 (Figure 1.1a) [2]. Natural gas is known as the cleanest fossil fuel as it releases less carbon dioxide when compared to other fossil fuels. The use of natural gas increased its share in global primary energy consumption to above 25 % in 2012. As a consequence of rising crude oil prices, new technology has been developed to extract oil and gas from shale rock. In particular, shale gas production has risen substantially in the US leading to very low pricing. It is predicted that exploration and production from shale rock will be a game changer in the coming decade. Coal is the most environmentally stressing of all fossil resources. In the areas where it is extensively exploited, coal is a major source of air pollution. Nevertheless, in terms of annual global consumption it is still the world's fastest-growing fossil fuel, in large because China's need for energy. Nuclear energy is an alternative energy source but subject of ongoing debates due to safety issues. Due to the Fukushima Daiichi incident nuclear energy experienced a significant decline with nuclear power plants being postponed and new projects being put on hold. Hydroelectric power, which is the most widely used form of renewable energy, accounted for 6.7 % of global energy generation in 2012. Utilization of other renewables like wind, solar, geothermal energy and biomass increased by 15 % such that 4.7 % of global power supply was met by these renewables in 2012 [2].

The excessive use of fossil fuels by modern society leads to substantial environmental problems. Global warming associated with the increased rates of greenhouse gas emissions is an environmental issue with potentially disastrous impact on our planet [3]. Besides, the resource scarcity of finite fossil fuel reserves and the fact that they are mainly located at politically unstable regions around the world contribute to the issue of energy security. By 2012, world's proved reserves for oil, natural gas and coal are reported to be sufficient to meet 53, 56 and 110 years of global energy production, respectively [2]. Despite the increasing depletion rates of cheap crude oil, the use of fossil resources still grows [4]. In addition, the rapid increase in oil prices as illustrated in Figure 1.1b necessitates the use of cheaper energy sources [2,5]. For reducing our dependence on fossil resources and meeting

strict environmental legislation, the energy share from renewable resources must be increased.
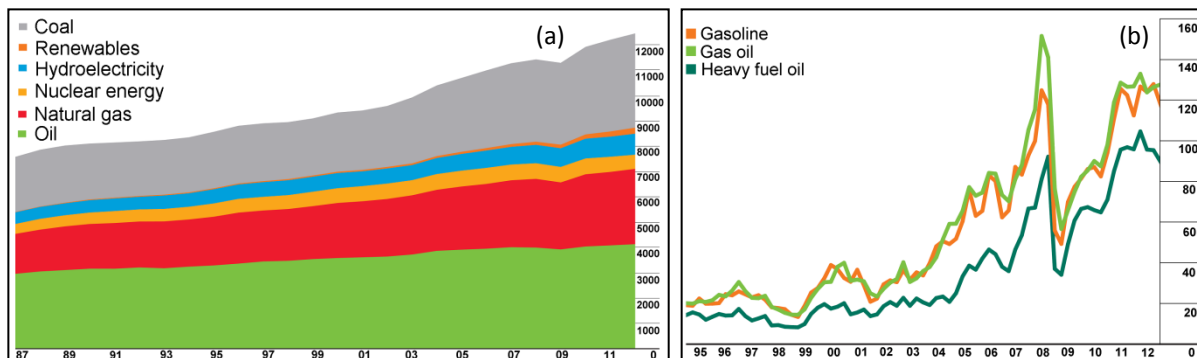
Figure 1.1: (a) The evolution of different sources in the world's primary energy consumption (in million tones oil equivalent) between years 1987 and 2012: Energy based on traded fuels. (b) The trend in the Rotterdam product prices (US dollars per barrel) of gasoline, gas oil and heavy fuel oil between years 1995 and 2012 (reprinted from [2]).

The transportation sector is the major consumer of fuels derived from fossil resources such as diesel, gasoline and liquefied petroleum gas [6]. It is projected that the number of cars will triple by 2050. Biofuels form a viable alternative for fulfilling the transportation needs. They comprise liquid and gaseous fuels predominantly produced from biomass [7]. Much alike practice in current oil refineries, it is projected that the oxygenated hydrocarbons typically present in biomass can be used in the manufacture of a limited number of platform chemicals. These platform chemicals will be processed further to yield important end-products such as liquid fuels as well as plastics, drugs, food, etc. Considering the conflicts that arise between biofuels production and food supply, the use of lignocellulosic biomass is preferred, because such feed materials are obtained from non-edible portions of biomass and agricultural wastes and residues. Typically, lignocellulosic materials are less expensive than conventional agricultural products.

A switch from fuels obtained from fossil to biobased, preferably lignocellulosic, resources brings numerous advantages. First of all, biofuels would considerably reduce the environmental stress such as climate change. Secondly, unlike petroleum, natural gas and coal, biofuel resources are geographically more evenly distributed. Sustained supply from abundant biomass resources would ensure a domestic secure energy supply. Also, the increased use of biofuels contributes to the regional development since the processes involved might also provide employment for the local people in rural areas [8].

1.2 Basic concepts of catalysis

Catalysis lies at the heart of many chemical transformations with nearly 85-90 % of the products of chemical industry being obtained via catalytic processes. If catalysts were not applied in chemical reactions, the current advanced technological state of our society could not have been achieved. Also, catalysis is crucial to manufacture the fertilizers to sustain the large global population. A catalyst is a substance that is used to convert reactants to products

with increased reaction rate without itself being consumed during the reaction. The term "catalysis" was first employed by the Swedish chemist Jöns Jacob Berzelius in 1836. The origins of the name is based on the Greek words κατά (kata, "down") and λύω (luō, "loose"), meaning break up or destroy wholly. Materials and compounds which are essential to our daily lives, such as fuel oil, medicines, plastics, polymers, etc. are generated through catalytic processes. Figure 1.2 schematically shows the difference of non-catalytic and catalytic reaction energy paths. The use of a catalyst significantly lowers the energy barrier of a reaction by enabling an alternative pathway with lower activation energy. Catalysts increase the rates of reactions by several orders of magnitude and enable them to be performed at milder temperature and pressure [9].

The working principle of a catalyst can be explained as a cyclic event which starts with the formation of bonds between reactant molecules and the catalyst. As this step is exothermic, the free energy decreases. Then the reaction of the adsorbates takes place by formation and breaking of bonds. The cycle closes with the separation of the product from the catalyst in an endothermic step [9].
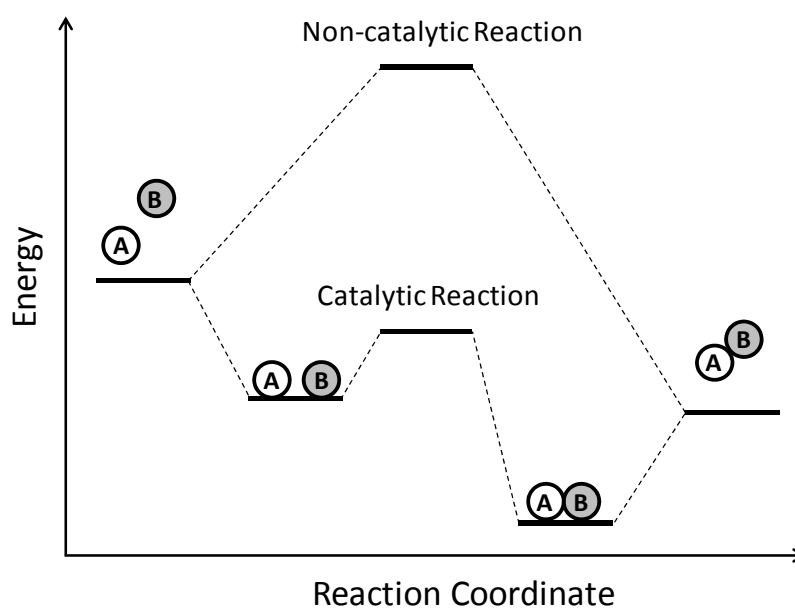
Figure 1.2: Potential energy diagram for catalyzed and uncatalyzed reaction (A+B→AB) (modified from [9]).

The chemical nature of catalysts is diverse in terms of form, size and composition. Catalysts can be employed in liquid or gas phases or at the surface of solids. When the catalyst and the reactants are in the same phase the reaction is called homogeneous. A simple example to a homogeneously catalyzed reaction is the decomposition of ozone into oxygen with chlorine atoms. Cl atoms leave the reaction cycle without any change and both the reactant and the catalyst are in gas phase. Enzymes, namely the proteins which accelerate chemical reactions in biological systems, are the so-called natural catalysts. Some examples of biocatalytic reactions are the build-up of proteins and DNA, the decomposition of hydrogen peroxide to water and oxygen by the catalase enzyme in the human body and the

storage of solar energy in the chemical bonds of sugars [9,10]. Heterogeneous catalysis usually refers to the use of solids for converting reactants in the liquid or gas phase. Typically, a solid catalyst consists of metal particles on a support material. The total surface area of the support can have an impact on the performance of the catalyst. Therefore, precious metal particles (such as Pt or Rh) are typically dispersed on high surface area support materials in order to enhance efficiency and reduce cost [9].

1.2.1 Major industrial applications of catalysis

First industrial applications of heterogeneous catalysis date back to the beginning of the 20th century. The low cost route for producing ammonia by flowing nitrogen and hydrogen through a reactor tube loaded with an inorganic solid (Born-Haber process) was a breakthrough in the chemical industry. Other early applications are the catalytic coal liquefaction process for production of basic organic chemicals and the conversion of coal-derived synthesis gas (syngas, a mixture of hydrogen and carbon monoxide) into motor fuels and chemicals via the Fischer-Tropsch process. Oil became the major source of transportation fuels and chemicals after the Second World War. Oil refining is carried out via many different reactions in the presence of various types of heterogeneous catalysts. Catalytic reforming, hydrotreatment, fluid catalytic cracking, alkylation are some important examples of catalytic processes in the oil refinery. Zeolites are the workhorses for catalytic cracking of crude oil, which is a crucial step for decreasing the molecular size and producing more valuable fuel fractions such as gasoline and diesel. Zeolite materials are highly porous crystals which consist of a silica-alumina matrix. Another application is the hydrotreating of crude oil which aims at removal of heteroatoms (such as S and N) by using $CoS-MoS_2/Al_2O_3$ and $NiS-MoS_2/Al_2O_3$ based catalysts. An illustrative example of heterogeneous catalysis which is integrated in our daily lives is the automotive exhaust catalysts. Platinum and rhodium metal particles supported on a ceramic monolith form a three-way catalyst that limits CO, NO and hydrocarbons emissions [9,11]. Currently, the main areas where catalysis is applied on a large scale are in refining, chemicals, polymers and emission control.

1.2.2 Structure sensitivity

Understanding of heterogeneous catalysis at the molecular level is essential for designing novel catalysts for sustainable processes. Due to the advances in in-situ spectroscopy, theoretical modeling and computational methods, there has been a significant progress in understanding of the mechanistic aspects controlling the complex heterogeneous catalytic systems over the past century [12,13]. Catalytic reactions are classified into two groups as structure-sensitive and structure-insensitive reactions. Electronic effects due to the coordination environment of a catalyst or geometric factors related to the formation of ensembles of surface sites with different topologies stem from the changes in the catalytic structure. Structure sensitivity refers to the change in the reactivity of metal nanoparticles with particle size. Change in the size of a metal cluster can have a strong influence on the binding energy of reactants, intermediates and products. As the size of the metal clusters decreases to nanometer dimensions, unique electronic properties and distinct surface

reactivity are observed. As the cluster grows, the coordination number, i.e. the number of nearest metal neighbors, increases steadily. Typically, the reactivity of a coordinatively unsaturated surface atom increases with decreasing coordination number. Besides, as the cluster size decreases to molecular scales the percentage of step, kink, edge and corner atoms increases at the expense of regular terrace sites. Such catalytic sites which are abudant in coordinatively unsaturated surfaces, promote dissociation reactions [12,14]. An example of a structure sensitive reaction is the low temperature CO oxidation on supported Au nanoparticles. For decades, gold was perceived as a non-reactive metal. The pioneering work of Haruta showed that by careful preparation of highly dispersed Au nanoparticles smaller than 5 nm in size, a remarkable increase in their CO oxidation activity could be achieved [15]. This example is an illustration of how the catalytic nature of gold can be tuned via controlling the particle size. Selectivity, which refers to the formation of a specific product following a particular reaction sequence, is also influenced by such electronic and geometric factors. Another important aspect in heterogeneous catalysis is the effect of the support material on the size, shape and morphology of the metal nanoparticles. The acid/based properties, the presence of hydroxyl groups or defects influence the properties of the nanoparticles [12]. As an example, ceria supported precious metal catalysts exhibit interesting activity in low-temperature water-gas shift reaction. This promotional effect stems from the easy water activation due to the redox properties of the ceria supported catalysts [16].

In heterogeneous catalysis, addition of a second metal is an effective way for tailoring the electronic and geometric structures of the nanoparticles to enhance their catalytic activity and selectivity. Bimetallic catalysts obtained by mixing two metal precursor solutions generally show enhanced physical and chemical properties due to a synergetic effect. Bimetallic catalysts can be divided into three main types based on their mixing patterns. Core-shell structures are formed when the second metal grows around the reduced inner core metal. Heterostructured nanoparticles are formed when two metals grow individually by sharing a mixed interface. Alloy nanoparticles are homogeneous mixtures of two metals with metal-metal bonds. An example which illustrates the promotional effect of bimetallic particles is the enhanced adsorption strength of reactants as a result of a reduced ensemble size or an increased metal-adsorbate bond energy. Some bimetallic catalysts show a higher catalytic stability by hindering agglomeration or catalytic poisoning [12,17]. A well-known example of a commercial bimetallic catalyst is $PtRe/Al_2O_3$, which is used in the catalytic reforming of petroleum naphtha fractions. The addition of Re to the Pt-based catalyst significantly improved its lifetime and the selectivity towards aromatic hydrocarbons. Characterization studies indicated the formation of a PtRe alloy with Re being reduced to metallic state. There are also observations that indicated the presence of some Re species with a higher oxidation state which are in contact with the support. The increased stability of $PtRe/Al_2O_3$ in comparison to the monometallic Pt/Al_2O_3 system is explained by the ensemble effect. Large ensembles of Pt atoms, which are the active surfaces for coke deposition, are

divided into smaller ones upon addition of Re. When exposed to sulfur, the inactive Re-S groups prevent the formation of irreversible coke species on the catalyst surface [18-20].

1.3 Catalytic biomass valorization

Carbohydrates produced by plants are C5 and C6 sugar molecules. Starch, a glucose polysaccharide with α-linkages, is one of the major components of biomass. As it is basically a food constituent, its utilization for chemical transformations is not favorable. Lignocelluloses, which are the wood-derived portions of biomass, consist of cellulose (a crystalline glucose polymer, 40-50 %), hemicellulose (a complex amorphous polymer with xylose as the major monomer unit, 25-30 %), lignin (a large polyaromatic compound, 25-30 %) and some minerals and organic compounds such as wax, proteins, fatty acids, etc. As it is non-edible and has a high energy content, lignocellulosic biomass is the most attractive feedstock for the large scale production of biofuels and chemicals [21,22].

The transition to a carbohydrate based economy necessitates the efficient development of novel catalytic processes. Due to the differences in the structures of petroleum and biomass feedstock, development of new catalytic materials which are tailored for selective conversion of carbohydrates is necessary. Petroleum contains a low concentration of functional groups such as –OH, –C=O, –COOH. Therefore, such feeds are suitable for use as fuel after processes like cracking, isomerization, etc. The main challenge for petroleum processing is the selective functionalization of the feed molecules. Biomass feed is very different from petroleum because it contains a very high degree of functionalities. This complicates its transformation into similar high value products and makes it essential to develop efficient methods to selectively deoxygenate carbohydrate molecules [1].

A big advantage of the functionalities in carbohydrates is that it makes them much less volatile and more reactive than petroleum-derived feed molecules. Therefore, their catalytic processes are usually carried out in liquid-phase. The high hydrophilicity of carbohydrates enables their catalytic reactions to occur in aqueous phase or in a biphasic medium of an aqueous and an organic phase. The typical reaction conditions in petroleum and biomass conversion processes are displayed in Figure 1.3. It clearly shows that the conversion of petroleum is carried out at high temperatures in vapor phase, while carbohydrates are processed at mild temperatures in liquid phase [1].
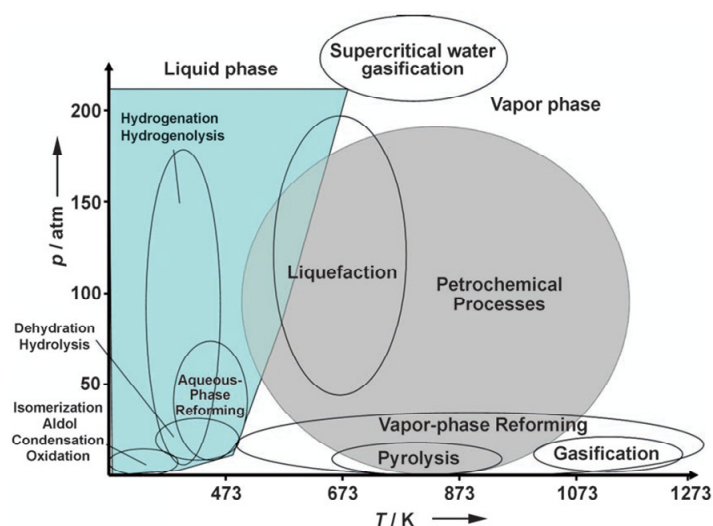
Figure 1.3: Approximate reaction conditions for the catalytic processing of petroleum versus biomass-derived carbohydrates (reprinted from [1]).

1.3.1 General approaches

Lignocellulosic biomass can be processed via thermochemical transformation or breaking down into sugar molecules. Figure 1.4 summarizes the potential strategies for making use of this type of biomass. Gasification is a CO_2-netural alternative for meeting heat and electricity demands. Heating in a limited amount of oxygen above 700 °C decomposes biomass into syngas. Further processing of syngas via Fischer-Tropsch generates gasoline and diesel fuel [23]. Converting to methanol and by further processing to olefins or to high purity hydrogen via water-gas shift reaction are other ways of making use of syngas. Another method is pyrolysis which is basically the heating of the feed in the absence of oxygen and it produces a mixture of gases, oil, char and tar. To generate transportation fuels from lignocellulosic biomass, it is necessary to upgrade the bio-oil through catalytic processes such as hydrodeoxygenation or zeolite upgrading. Currently the oil derived from pyrolysis is used in boilers for stationary power and heat generation. Due to the difficulties in tuning the selectivity and high operation costs due to high temperatures, thermochemical processes are not favorable for the production of value-added chemicals from biomass on a large scale. Hydrolysis of biomass to form sugar monomers in the presence of acid catalysts or enzymes is the first step in the selective conversion of biomass into useful monomer units at low temperatures. From these aqueous sugar fractions, alcohols, liquid alkanes, aromatic hydrocarbons and hydrogen can be produced. Lignin can be upgraded to transportation fuels via hydrodeoxygenation or zeolite processing [22,24-26].
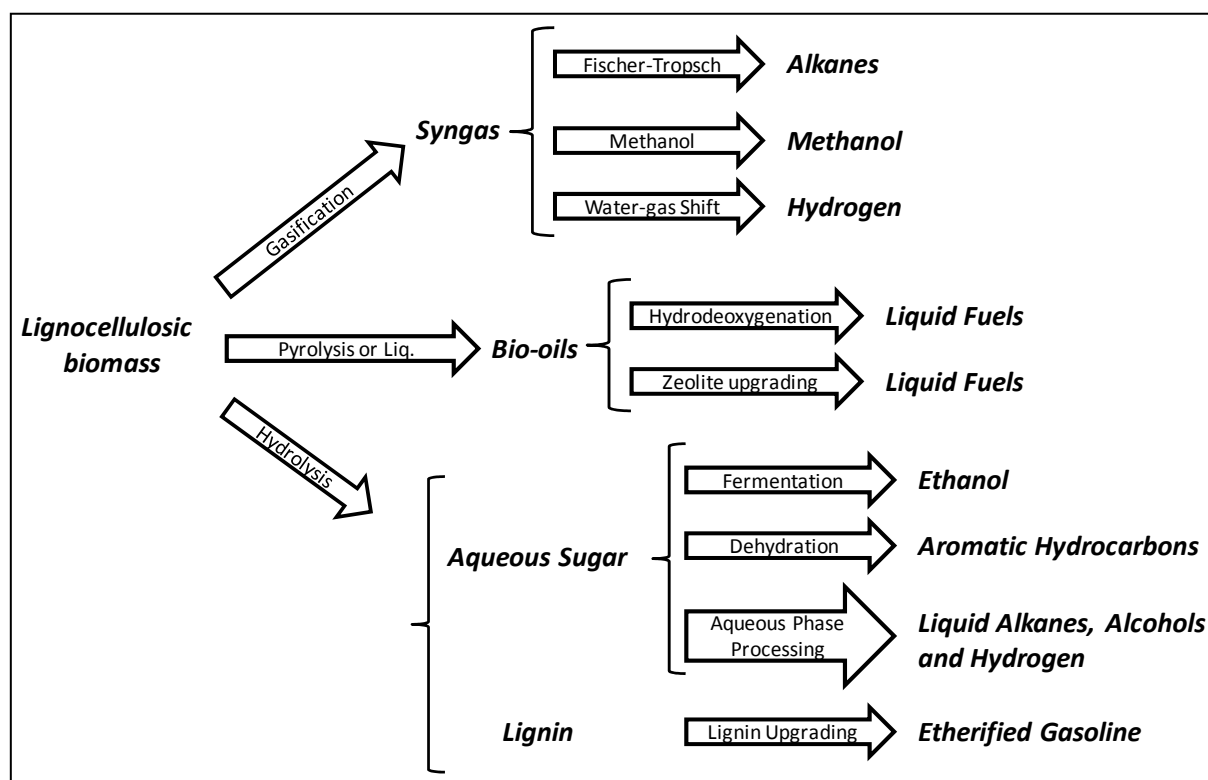
Figure 1.4: Strategies for production of fuels from lignocellulosic biomass (modified from [24,25]).

1.3.2 Production of renewable hydrogen

An important product derived from biomass is hydrogen. Hydrogen is considered as a new energy vector for a sustainable future with many social, economical and environmental benefits. Major opportunities for the utilization of renewable hydrogen are: as a chemical feedstock for the manufacture of ammonia and fertilizers, as a chemical reagent utilized to produce liquid fuels via the Fischer-Tropsch process and as a future fuel source for PEM fuel cells to generate electricity [27,28]. Hydrogen is a clean energy carrier with no CO_2 emissions and a high energy capacity (122 kJ/g). The use of hydrogen as an energy source in transportation sector will significantly reduce the environmental pollution created by the current gasoline or diesel powered engines. Major challenges for a hydrogen-based economy are related to safety and storage issues. These could be addressed by developing new transportation infrastructures and new chemical systems for hydrogen storage, such as metal hydrides. [29]

In addition to its potential as an energy carrier, an important key role of hydrogen is as a key reactant in future biorefineries. Hydrogen is considered as an integral part of a biorefinery as it is utilized as a chemical reactant for hydrogenation reactions of carbohydrates to glycols [25]. The predominant process to make hydrogen is by steam reforming of natural gas and light hydrocarbons [30]. The contributions of coal gasification and water electrolysis are in comparison small but useful additional routes. The amount of hydrogen produced from biomass-derived feed molecules is very minor at only 1 % of the total hydrogen production. It is therefore not surprising that this research area is of great interest because its potential is very high [27-29,31-38]. Alcohols are known to be more

reactive and their catalytic decomposition is much faster when compared to the hydrocarbons used in conventional steam reforming processes. An example of recent research efforts is the reforming of aqueous bio-ethanol to generate renewable hydrogen [39-44]. Noble metal catalysts containing Rh or Pt and non-noble metals catalysts with Ni or Co are widely being explored for this purpose [43,44]. Studies are also focused on the development of bimetallic catalysts that are more efficient in the activation of steam and more stable during reaction. For example, Tomishige and co-workers found that the addition of Nb, V, Mo to Pt/SiO$_2$ catalysts significantly increased the hydrogen formation rates in ethanol steam reforming [45]. Ethanol is conventionally derived from the fermentation of sugars, which are obtained by hydrolysis of carbohydrate constituents of lignocellulosic biomass (see Figure 1.4). Ethanol is also considered as a platform chemical for the production of useful chemicals such as acetaldehyde, acetic acid, ethyl acetate, diethyl ether, and ethylene oxide [46]. Recently, a selectivity of 95 % towards acetic acid and >90 % conversion is achieved in ethanol oxidation over nanoscale Au particles on TiO$_2$ or MgAl$_2$O$_4$ [47].

Another sustainable approach to produce clean hydrogen is from water via water splitting through electrolysis, thermolysis or photoelectrolysis [38,48]. As a solar fuel, formic acid has a great potential for generating hydrogen too. Formic acid is generated as a by-product of levulinic acid production in acid-catalyzed conversion of carbohydrates. Its catalytic decomposition at ambient temperatures yields high purity hydrogen and it is considered as an environmentally benign hydrogen storage material [49]. Besides, it has gained importance as a hydrogen donor in transfer hydrogenation reactions [50,51].

1.3.3 Aqueous phase reforming

Aqueous phase reforming (APR) of polyols derived from the carbohydrate constituents of biomass is an energy efficient sustainable process for obtaining clean hydrogen and useful chemicals. APR takes place at low temperatures (200-250 °C) and mild pressures (10-50 bar). A major advantage of aqueous phase processing of polyols is the absence for a need to vaporize the feedstock. Since polyols are highly soluble in water, reactants for the APR process are typically the mixtures of sugar alcohols and water at various concentrations [1,28,52-57]. In the course of the development of the APR process, there have been many studies by several research groups which focus on the use of several different oxygenated hydrocarbons derived from biomass. Sugars such as glucose or polyols such as methanol, ethanol, ethylene glycol, glycerol, sorbitol are some examples of carbohydrate feed molecules used in APR.

The APR of glycerol has been studied by many research groups because of its similar but simpler chemical structure in comparison to complex carbohydrates and its abundance [57-67]. Glycerol has a strong potential to become a primary feedstock for the biorefinery [47]. It is generated as a by-product (10 % in weight) during biodiesel production from renewable resources [68]. Regarding the economical viability of this green process, the surplus of glycerol generated along with biodiesel should be utilized for producing higher value products. Pyrolysis, steam reforming, partial oxidation, autothermal reforming and

aqueous phase reforming are the main processes for converting glycerol to hydrogen or syngas [69,70]. Hydrogenolysis of glycerol to 1,2-propanediol or 1,3-propanediol, oxidation of glycerol to fine chemicals such as 1,3-dihydroxyacetone, glyceric acid, tartronic acid, glycolic acid, dehyhdration of glycerol to acrolein or acetol, carboxylation of glycerol to glycerol carbonate are some examples of environmentally benign catalytic methods for producing valuable chemicals which are conventionally derived from petroleum [71]. The overall equation for complete reforming of glycerol is given in equation (1).

$$C_3H_8O_3 + 3H_2O \rightarrow 3CO_2 + 7H_2 \hspace{4cm} (1)$$

The catalytic pathway for aqueous phase reforming of oxygenated hydrocarbons consists of two major routes. First one starts with the dehydrogenation of the feedstock to form the corresponding aldehyde, followed by the cleavage of C-C bonds (decarbonylation). CO formed as a result of decarbonylation is converted to H_2 and CO_2 via the water-gas shift (WGS) reaction. A second route consists of the cleavage of C-O bonds (dehydration) of the oxygenated feedstock. Hydrogen produced in the first route is consumed to hydrogenate the dehydrated reaction intermediates to diols. Further dehydration and hydrogenation reactions lead to the formation of monofunctional alcohols and alkanes [28,66].

The most widely used APR catalysts are based on transition metals dispersed on high surface area support materials. Typically Pt, Pd, Rh, Ru, Ni, Cu nanoparticles are dispersed on silica, alumina or activated carbon following the pore volume impregnation method. Solutions of metal precursor added on the porous supports followed by drying and reduction of the material under hydrogen flow at mild temperatures generate highly dispersed metal catalysts. Early efforts of Dumesic and his co-workers were mainly focused on identifying the factors controlling the selectivity of APR process by studying the nature of the catalyst. The catalytic performance of a series of precious metals was tested in APR. Selectivity trends were found to be significantly influenced by the nature of the transition metal. Pt and Pd, for instance, were reported to be highly selective towards hydrogen formation. Metals such as Ni, Ru and Rh, on the other hand, were reported to be active in alkane formation. Pt is the most studied metal and it is preferred for obtaining hydrogen via APR due to its optimum activity in decarbonylation and water-gas shift. Support materials which possess some degree of acidity enhance the balance between the rates of dehydration and hydrogenation reactions and hence promote the rate of glycerol hydrogenolysis [28].

Bimetalllic catalysts have been explored in aqueous phase conversion of glycerol and higher oxygenates. Dumesic and his co-workers prepared NiSn catalysts supported on Al_2O_3 from their Raney-Ni catalysts. Recently, the addition of metals such as Re, Mo, W to supported noble metals such as Pt or Rh has been studied by several research groups [58,72-74]. King and his wo-workers compared the activity of carbon supported PtRe with equal moles of Pt and Re to a monometallic carbon supported Pt catalyst. They observed an increase in overall activity as well as an increase in the formation of products formed via dehydration reactions [74]. Tomishige and his co-workers focused their efforts on hydrogenolysis of glycerol to diols in liquid phase under externally supplied hydrogen. IrRe

and RhRe supported on silica were found to be selective towards 1,3-propanediol whereas Ir and Rh alone basically produced 1,2-propanediol during aqueous phase hydrogenolysis of glycerol [75-79]. Murzin and his co-workers recently investigated the promotional effect of Re in aqueous phase reforming of xylitol, which is an abundant polyol produced via hydrogenation of xylose [80]. In general, an increase in overall APR activity and selectivity towards deoxygenated products were observed upon addition of Re to conventional Pt catalysts [72]. Significant efforts have been devoted to understanding the structure of Re-promoted Pt and Rh catalysts. The acidity brought by Re was discussed to be at the origin of increased dehydration rates. The addition of Re was argued to influence the rate of CO removal from the catalyst surface. Therefore, the conversion of CO via the WGS reaction was proposed to have an influence on the activity of liquid phase conversion reactions of glycerol [72,73].

WGS reaction, as described in equation (2), enables the rapid conversion of CO to H_2 and CO_2 under aqueous phase reforming reaction conditions.

$$CO + H_2O \leftrightarrows CO_2 + H_2 \qquad\qquad\qquad (2)$$

WGS is employed in many technical operations where hydrogen enrichment is essential. For instance, it is used to increase the hydrogen concentration of the effluent gas obtained from the conventional steam reforming process. Typically, the reformate contains 1-10 % of CO, which is undesired for fuel cell applications. As the reaction is moderately exothermic ($\Delta H_R = -41.2$ kJ mol^{-1}), high conversions are reached when WGS is applied at low temperatures. In industry, low temperature WGS (~200 °C) is generally performed over $CuO/ZnO/Al_2O_3$ catalysts and high temperature WGS (~450 °C) catalysts are based on iron and chromium oxides (Fe_2O_3/Cr_2O_3) [81-89].

1.4 Scope of the thesis

Reforming of glycerol in aqueous phase is a method of obtaining sustainable hydrogen, alkanes and alcohols. Although several studies have been conducted to identify the effect of the nature of the support or the active metal phase, several issues remain to be addressed concerning the overall performance and selectivity trends in aqueous phase reforming of polyols. Chapter 2 focuses on the influence of the support on the catalytic performance of Pt based catalysts in the APR of glycerol. A set of alumina, silica and amorphous silica alumina based supports were extensively characterized before and after glycerol APR and the results are discussed in terms of the influence of the support composition. PtRe make much better APR catalysts than Pt, yet the exact reason for this improved performance has not been unequivocally clarified yet. Besides overall performance, it is also interesting to study how the catalyst composition affects the selectivity trends. Chapter 3 therefore deals with the Pt-Re synergy in activated carbon supported bimetallic catalysts. The influence of Re on a conventional Pt/C catalyst was studied by preparing a set of PtRe catalysts with varying Re content as well as monometallic Pt and Re catalysts for reasons of comparison. Separate gas-phase model reaction experiments such as water-gas shift, acetaldehyde decomposition and ethanol steam reforming were employed to understand

better the influence of the PtRe synergy on the various reaction pathways involved in APR. Chapter 4 investigates the effect of using different reducible oxide supports (such as ceria, ceria-zirconia and titania) for dispersing Pt and Re. The discussion is extended by comparing the activity of PtRe supported on titania with that of PtRe/C. Chapter 5 examines the effect of Pt and PtRe particle size in the aqueous phase conversion of glycerol. Re was loaded on Pt/C catalysts with different particle sizes via the catalytic reduction method. These catalysts were extensively characterized and their activities were compared. In Chapter 6 APR activities of Re-promoted Pt and Rh are compared. Characterization studies focusing on the particle size, electronic structure and reducibility enabled us to get an insight on the synergetic effect in PtRe and RhRe catalytic systems.

Decomposition of bio-ethanol yields several commodity chemicals as well as renewable hydrogen. Similarly, formic acid decomposes to produce CO-free hydrogen. Chapter 7 focuses on the reactivity of a series of ceria-supported Pt and Au catalysts for the decomposition of ethanol and formic acid. The influence of different planes of the ceria support on active metal phase was investigated by detailed characterization and the effect of the feed composition was studied. Finally, the main results of this thesis are briefly discussed in the summary.

References

[1] J.N. Chheda, G.W. Huber, J.A. Dumesic, Angew. Chem. Int. Edit. 46 (2007) 7164-7183.
[2] "BP Statistical Review of Energy 2013", BP, can be found under http://www.bp.com/content/dam/bp/pdf/statistical-review/statistical_review_of_world_energy_2013.pdf.
[3] "Intergovernmental Panel on Climate Change (IPCC). Climate change 2013: the physical science basis." (2013).
[4] R.J. Brecha, Sustainability 5 (2013) 664-694.
[5] S. Shafiee, E. Topal, Energy Policy 37 (2009) 181-189.
[6] A. Demirbas, Prog. Energ. Combust. 33 (2007) 1-18.
[7] I.J. Loppacher, W.A. Kerr, Energy Politics 5 (2005) 7-27.
[8] B. Hahn-Hagerdal, M. Galbe, M.F. Gorwa-Grauslund, G. Liden, G. Zacchi, Trends Biotechnol. 24 (2006) 549-556.
[9] I. Chorkendorff and J.W. Niemantsverdriet, Concepts of Modern Catalysis and Kinetics, Wiley, 2007.
[10] P. Chelikani, I. Fita, P.C. Loewen, CMLS, Cell. Mol. Life Sci. 61 (2004) 192-208.
[11] R.A. van Santen, P.W.N.M. van Leeuwen, J.A. Moulijn, and B.A. Averill, Catalysis: An Integrated Approach, Elsevier, 1999.
[12] R.A.van Santen and M.Neurock, Molecular Heterogeneous Catalysis: A Conceptual and Computational Approach, Wiley-VCH, Weinheim, 2007.
[13] G.A. Somorjai, Chem. Rev. 96 (1996) 1223-1235.
[14] M. Boudart, J. Mol. Catal. 30 (1985) 27-38.
[15] M. Haruta, Catal. Today 36 (1997) 153-166.
[16] R.J. Gorte, S. Zhao, Catal. Today 104 (2005) 18-24.
[17] A.K. Singh, Q. Xu, ChemCatChem 5 (2013) 652-676.
[18] H.E.Kluksdahl, US Patent 3 415 737 (1968) , to Chevron Research Company.
[19] J.L. Xiao, R.J. Puddephatt, Coord. Chem. Rev. 143 (1995) 457-500.
[20] J.L. Carter, G.B. McVinker, W. Weissman, M.S. Kmak, J.H. Sinfelt, Appl. Catal. 3 (1982) 327-346.
[21] A. Corma, S. Iborra, A. Velty, Chem. Rev. 107 (2007) 2411-2502.
[22] P.L. Dhepe, A. Fukuoka, ChemSusChem 1 (2008) 969-975.
[23] M.E. Dry, Catal. Today 71 (2002) 227-241.
[24] G.W. Huber, J.A. Dumesic, Catal. Today 111 (2006) 119-132.
[25] G.W. Huber, S. Iborra, A. Corma, Chem. Rev. 106 (2006) 4044-4098.
[26] D. Sutton, B. Kelleher, J.R.H. Ross, Fuel Process. Technol. 73 (2001) 155-173.

[27] J.R. Rostrup-Nielsen, Phys. Chem. Chem. Phys. 3 (2001) 283-288.
[28] R.R. Davda, J.W. Shabaker, G.W. Huber, R.D. Cortright, J.A. Dumesic, Appl. Catal. B 56 (2005) 171-186.
[29] R.S. Cherry, Int. J. Hydrogen Energ. 29 (2004) 125-129.
[30] J.R. Rostrup-Nielsen, Catal. Today 18 (1993) 305-324.
[31] Y. Suzuki, Int. J. Hydrogen Energ. 7 (1982) 227-230.
[32] K. Nath, D. Das, Veziroglu N.T., Curr. Sci. 85 (2003) 265-271.
[33] D. Das, N. Khanna, N.T. Veziroglu, Chem. Ind. Chem. Eng. Q. 14 (2008) 57-67.
[34] H. Balat, E. Kirtay, Int. J. of Hydrogen Energ. 35 (2010) 7416-7426.
[35] M. Balat, Int. J. Hydrogen Energ. 33 (2008) 4013-4029.
[36] G. Nahar, V. Dupont, Biofuels 3 (2012) 167-191.
[37] R.M. Navarro, M.A. Pena, J.L.G. Fierro, Chem. Rev. 107 (2007) 3952-3991.
[38] J.D. Holladay, J. Hu, D.L. King, Y. Wang, Catal. Today 139 (2009) 244-260.
[39] A. Bshish, Z. Yaakob, B. Narayanan, R. Ramakrishnan, A. Ebshish, Chem. Pap. 65 (2011) 251-266.
[40] J.L. Silveira, L.B. Braga, A.C.C. de Souza, J.S. Antunes, R. Zanzi, Renew. Sust. Energ. Rev. 13 (2009) 2525-2534.
[41] N. Bion, D. Duprez, F. Epron, ChemSusChem 5 (2012) 76-84.
[42] A. Haryanto, S. Fernando, N. Murali, S. Adhikari, Energ. Fuel. 19 (2005) 2098-2106.
[43] M. Ni, D.Y.C. Leung, M.K.H. Leung, Int. J. Hydrogen Energ. 32 (2007) 3238-3247.
[44] N. Bion, F. Epron, and D. Duprez, Catalysis: 22 (2010) 1-55.
[45] S. Ito, K. Tomishige, Catal. Comm. 12 (2010) 157-160.
[46] T. Takei, N. Iguchi, M. Haruta, Catal. Surv. Asia 15 (2011) 80-88.
[47] J.J. Bozell, G.R. Petersen, Green Chem. 12 (2010) 539-554.
[48] K.S. Joya, Y.F. Joya, K. Ocakoglu, R. van de Krol, Angew. Chem. Int. Ed. 52 (2013) 10426-10437.
[49] B.R. Loges, A. Boddien, F. Gartner, H. Junge, M. Beller, Top Catal. 53 (2010) 902-914.
[50] R.A.W. Johnstone, A.H. Wilby, I.D. Entwistle, Chem. Rev. 85 (1985) 129-170.
[51] D.A. Bulushev, J.R.H. Ross, Catal. Today 163 (2011) 42-46.
[52] R.D. Cortright, R.R. Davda, J.A. Dumesic, Nature 418 (2002) 964-967.
[53] G.W. Huber, J.W. Shabaker, S.T. Evans, J.A. Dumesic, Appl. Catal. B 62 (2006) 226-235.
[54] E.L. Kunkes, D.A. Simonetti, R.M. West, J.C. Serrano-Ruiz, C.A. Gartner, J.A. Dumesic, Science 322 (2008) 417-421.
[55] J.W. Shabaker, G.W. Huber, R.R. Davda, R.D. Cortright, J.A. Dumesic, Catal. Lett. 88 (2003) 1-8.
[56] J.W. Shabaker, R.R. Davda, G.W. Huber, R.D. Cortright, J.A. Dumesic, J. Catal. 215 (2003) 344-352.
[57] H.J. Park, H.D. Kim, T.W. Kim, K.E. Jeong, H.J. Chae, S.Y. Jeong, Y.M. Chung, Y.K. Park, C.U. Kim, ChemSusChem 5 (2012) 629-633.
[58] P.J. Dietrich, R.J. Lobo-Lapidus, T.P. Wu, A. Sumer, M.C. Akatay, B.R. Fingland, N. Guo, J.A. Dumesic, C.L. Marshall, E. Stach, J. Jellinek, W.N. Delgass, F.H. Ribeiro, J.T. Miller, Top. Catal. 55 (2012) 53-69.
[59] M. El Doukkali, A. Iriondo, P.L. Arias, J. Requies, I. Gandarias, L. Jalowiecki-Duhamel, F. Dumeignil, Appl. Catal. B 125 (2012) 516-529.
[60] Y. Guo, M.U. Azmat, X.H. Liu, Y.Q. Wang, G.Z. Lu, Appl. Energ. 92 (2012) 218-223.
[61] D.L. King, L.A. Zhang, G. Xia, A.M. Karim, D.J. Heldebrant, X.Q. Wang, T. Peterson, Y. Wang, Appl. Catal. B 99 (2010) 206-213.
[62] K. Lehnert, P. Claus, Catal. Comm. 9 (2008) 2543-2546.
[63] N. Luo, X. Fu, F. Cao, T. Xiao, P.P. Edwards, Fuel 87 (2008) 3483-3489.
[64] R.L. Manfro, A.F. da Costa, N.F.P. Ribeiro, M.M.V.M. Souza, Fuel Process. Technol. 92 (2011) 330-335.
[65] A.O. Menezes, M.T. Rodrigues, A. Zimmaro, L.E.P. Borges, M.A. Fraga, Renew. Energ. 36 (2011) 595-599.
[66] A. Wawrzetz, B. Peng, A. Hrabar, A. Jentys, A.A. Lemonidou, J.A. Lercher, J. Catal. 269 (2010) 411-420.
[67] G. Wen, Y. Xu, H. Ma, Z. Xu, Z. Tian, Int. J. Hydrogen Energ. 33 (2008) 6657-6666.
[68] E. Santacesaria, G.M. Vicente, M. Di Serio, R. Tesser, Catal. Today 195 (2012) 2-13.
[69] Y.C. Lin, Int. J. Hydrogen Energ. 38 (2013) 2678-2700.
[70] P.D. Vaidya, A.E. Rodrigues, Chem. Eng. Technol. 32 (2009) 1463-1469.
[71] C.H. Zhou, H. Zhao, D.S. Tong, L.M. Wu, W.H. Yu, Catal. Rev. 55 (2013) 369-453.
[72] D.M. Alonso, S.G. Wettstein, J.A. Dumesic, Chem. Soc. Rev. 41 (2012).
[73] E.L. Kunkes, D.A. Simonetti, J.A. Dumesic, W.D. Pyrz, L.E. Murillo, J.G.G. Chen, D.J. Buttrey, J. Catal. 260 (2008) 164-177.
[74] L. Zhang, A.M. Karim, M.H. Engelhard, Z.H. Wei, D.L. King, Y. Wang, J. Catal. 287 (2012) 37-43.

[75]   Y. Amada, Y. Shinmi, S. Koso, T. Kubota, Y. Nakagawa, K. Tomishige, Appl. Catal. B 105 (2011) 117-127.

[76]   S. Koso, H. Watanabe, K. Okumura, Y. Nakagawa, K. Tomishige, Appl. Catal. B 111 (2012) 27-37.

[77]   Y. Nakagawa, Y. Shinmi, S. Koso, K. Tomishige, J. Catal. 272 (2010) 191-194.

[78]   A. Shimao, S. Koso, N. Ueda, Y. Shinmi, I. Furikado, K. Tomishige, Chem. Lett. 38 (2009) 540-541.

[79]   Y. Shinmi, S. Koso, T. Kubota, Y. Nakagawa, K. Tomishige, Appl. Catal. B 94 (2010) 318-326.

[80]   A.V. Kirilin, A.V. Tokarev, H. Manyar, C. Hardacre, T. Salmi, J.P. Mikkola, D.Y. Murzin, Catal. Today (in press) DOI: 10.1016/j.cattod.2013.09.020.

[81]   S. Werner, PhD Thesis "Ultra-Low Temperature Water-Gas Shift Reaction with Supported Ionic Liquid Phase (SILP) Catalysts." 2011 Universität Erlangen-Nürnberg.

[82]   D.C. Grenoble, M.M. Estadt, D.F. Ollis, J. Catal. 67 (1981) 90-102.

[83]   C.V. Ovesen, P. Stoltze, J.K. Norskov, C.T. Campbell, J. Catal. 134 (1992) 445-468.

[84]   C. Ratnasamy, J.P. Wagner, Catal. Rev. 51 (2009) 325-440.

[85]   G. Jacobs and B.H. Davis, Catalysis 20, (2007) 122-285.

[86]   R.M. Laine, E.J. Crawford, J. Mol. Catal. 44 (1988) 357-387.

[87]   D.S. Newsome, Catal. Rev. 21 (1980) 275-318.

[88]   C. Rhodes, G.J. Hutchings, A.M. Ward, Catal. Today 23 (1995) 43-58.

[89]   O. Thinon, F. Diehl, P. Avenier, Y. Schuurman, Catal. Today 137 (2008) 29-35.

Support effects in the aqueous phase reforming of glycerol over supported platinum catalysts

Summary

Aqueous phase glycerol reforming was studied for a set of Pt catalysts supported on γ-Al_2O_3, SiO_2 and amorphous silica-alumina (ASA) with varying alumina concentrations. The main products in the gas phase at 225 °C under 29 bar N_2 pressure for a feed of 20 wt% glycerol are H_2, CO_2 and C_1-C_3 alkanes, and 1,2-propanediol, hydroxyacetone and C_1-C_3 monoalcohols are the products in the liquid phase. Boehmite formation is observed for the γ-Al_2O_3 and ASA supported catalysts. The higher the Al concentration of ASA, the more pronounced boehmite formation is. Especially at low Al concentrations, boehmite formation is limited and silica leaches from the ASA support under reaction conditions. The increased surface acidity as a result of boehmite formation leads to increased hydroxyacetone (glycerol dehydration) and 1,2-propanediol formation (hydroxyacetone hydrogenation). The activity of boehmite supported Pt for hydrodeoxygenation and reforming reactions is higher than that of γ-Al_2O_3 and SiO_2 supported Pt.
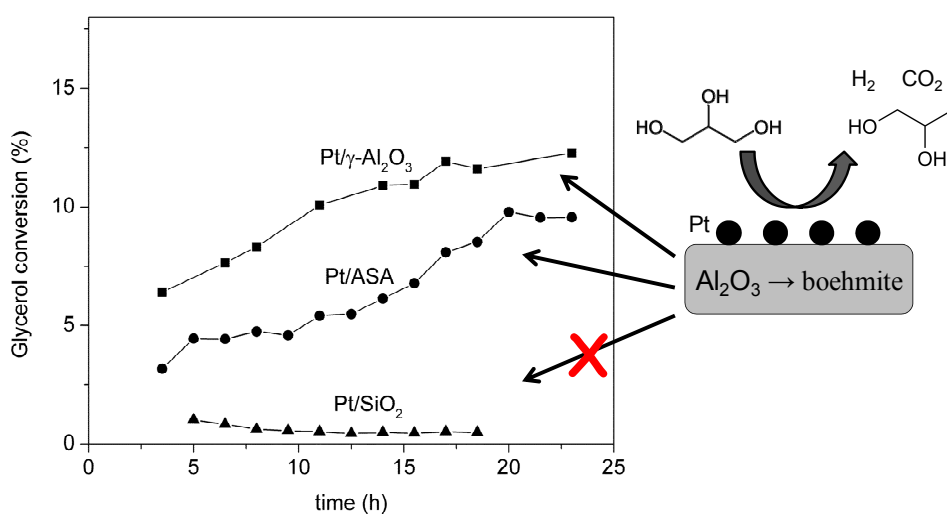
2.1 Introduction

Biomass is considered as a sustainable replacement of finite petroleum reserves for the production of fuels and chemicals. In general, there is a mismatch between the composition of the biomass derived feedstocks and the desired fuel components and chemicals, especially in terms of the O/C ratio. Therefore, active and selective catalysts to upgrade such products streams need to be developed. Glycerol is a by-product of bio-diesel production and considered to play a central role in future biorefineries [1,2]. Next to ethylene glycol, it is also often used as a model compound for the conversion of polyols derived from lignocellulose. Aqueous phase reforming (APR) converts such feedstocks to H_2, whereas hydrodeoxygenation reactions produce oxygenated chemicals, in case of glycerol propanediols. Processing of glycerol and related feedstocks in the aqueous phase is attractive because of the limited volatility of the reactants and higher energy efficiency [3]. Another advantage of this approach is that product H_2 only contains very small concentrations of CO, which is useful when producing fuels for electrochemical devices.

Liquid phase processing of polyols has been the subject of a large number of recent studies [3-18]. The selectivity will depend on the rates of C-C bond and C-O bond hydrogenolysis reactions [4,5,12-17]. From glycerol, diols are either obtained by consecutive dehydration and hydrogenation reactions or by dehydrogenation and direct bond cleavage of intermediates, whilst preserving the carbon-carbon bonds. The former reaction sequence requires two types of active sites, namely acid ones for the dehydration and metal sites for hydrogenation. The latter reaction is preferred in the presence of H_2. Carbon-carbon bond cleavage, which eventually will lead to H_2 and CO_2, takes place over metallic sites. Recently, the group of Lercher has shown that diols and triols are mainly converted due to dehydration, whereas mono-alcohols convert via dehydrogenation followed by decarbonylation (C-C bond cleavage) [18].

In general, supported Pt catalysts have been most frequently used for APR. Besides carbon, also Al_2O_3 and SiO_2 have been employed as carrier material for Pt nanoparticles. For instance, Pt/Al_2O_3 was found to give the highest H_2 selectivity in APR of ethylene glycol [9]. However, Luo et al. found evidence that γ-Al_2O_3 undergoes a phase transformation under APR reaction conditions [7]. In line with this, Ravenelle et al. [19] showed that under aqueous phase reforming conditions γ-Al_2O_3 is transformed into a hydrated boehmite phase with significant changes in surface area and acidity. The authors also noted that the supported metal particles decreased the rate of the transformation of γ-Al_2O_3 to boehmite. The use of silica as support has been associated with lower H_2 selectivity compared to Pt/Al_2O_3 in APR of ethylene glycol [11]. Also, the use of amorphous silica-alumina (ASA) supports has been described for catalysts for the APR process. Gandarias et al. investigated the role of acid sites of Pt/ASA in glycerol hydrogenolysis to obtain 1,2-propanediol [20]. Dehydration of glycerol to hydroxyacetone was thought to be catalyzed by the acid sites of the ASA and hydrogenation to 1,2-propanediol by Pt.

Despite the clearly important role of the support on the selectivity of the aqueous phase processing of glycerol, a detailed comparison of silica, alumina and silica-alumina has not been reported. Another important issue, which has been addressed only to a limited extent, is the support stability in aqueous phase conversion of glycerol. It is, therefore, the objective of the present study is to explore the effect of the nature of the support as well as its stability on the activity and product selectivity in aqueous phase reforming and hydrodeoxygenation of glycerol over a series of γ-Al_2O_3, SiO_2 and amorphous silica-alumina supported Pt catalysts.

In order to have a set of well-defined Pt/ASA catalysts, we used the homogeneous deposition precipitation method to prepare a number of ASA supports of equal Brønsted acid strength (at least as judged from their activity in the gas-phase hydroisomerization of n-heptane), but different chemical composition [21]. Earlier, the gas phase toluene hydrogenation activities of the present set of Pt catalysts were discussed [22]. Pt/ASA exhibited a much higher hydrogenation activity than Pt/γ-Al_2O_3 and Pt/SiO_2 in accordance with work of the group of Lercher [23]. These differences are argued to be caused by changes in the electronegativity of the support, thereby influencing the quality of the Pt hydrogenation sites. Pt/γ-Al_2O_3 has a much lower hydrogenation activity because of the lower electronegativity of this support compared to the mixed oxides. The low activity of Pt/SiO_2 is explained by the absence of Lewis acid surface sites that communicate the support electronegativity to the Pt phase. In the present work, similar catalysts will be tested in the aqueous phase processing of glycerol with special attention being paid to the support in fresh and spent catalysts.

2.2 Experimental

Amorphous silica-alumina (ASA) was synthesized by homogeneous deposition-precipitation of Al^{3+} on silica followed by calcination [21]. A set of ASA materials was prepared with nominal Al_2O_3 concentrations of 5, 15 and 20 wt%. The final calcination temperature of these ASA supports was 800 °C. A commercial ASA support with a nominal Al_2O_3 concentration of 55 wt% was calcined at 450 °C. γ-Al_2O_3 (Ketjen CK-300) and SiO_2 (Degussa) were used as received. Pt-containing catalysts were prepared by incipient wetness impregnation of the dried supports with an appropriate amount of an aqueous $Pt(NH_3)_4(NO_3)_2$ solution to obtain a final Pt loading around 1.0 wt%. Following impregnation, the catalysts were first dried at 110 °C and subsequently calcined in static air at 450 °C. The catalysts are denoted by Pt/S with S being the γ-Al_2O_3, SiO_2 or ASA(y) with y representing the Al_2O_3 concentration as determined by ICP.

The metal dispersion and particle size were measured by H_2 chemisorption in a Micromeritics ASAP 2020 system. Prior to measurement, an amount of catalyst sample was treated in air at 450 °C for 1 h, then cooled to 100 °C and evacuated for 1 h. Under flowing hydrogen, the sample was then heated to 260 °C at a ramp rate of 10 °C/min and reduced at this temperature for 165 min. After evacuating at 435 °C for 5 h, the sample was further

evacuated at 35 °C and hydrogen chemisorption measurements were carried out via the double isotherm method.

Kinetic measurements were done in an upflow reactor at a WHSV of 4.2 h^{-1} using 150 mg catalyst at a temperature of 225 °C. The total pressure was maintained at 29 bar pressure by a nitrogen flow (0.6 ml/min), while an aqueous solution of glycerol (20 wt%) was fed to the reactor (flow rate of glycerol in the feed was 0.11 mmol/min). Prior to experiments, the catalysts were reduced at 300 °C for 2 h (ramp rate of 2 °C/min) under H$_2$ flow (100 ml/min). The liquid samples were analyzed by a gas chromatograph equipped with FID/MS detector and a CP-Wax 57 CB column. Gaseous products were analyzed online by a gas chromatograph equipped with a TCD and two capillary columns (MS-5S and Para-Plot Q).

X-ray diffraction (XRD) analysis was carried out by a Bruker D4 Endavour diffractometer using a Cu Kα radiation source with a 2θ scanning range between 10 ° to 70 °. TGA of the spent catalysts was carried out in a Mettler Toledo TGA/DSC System in flowing air by heating to 800 °C at a rate of 10 °C/min. Magic-angle spinning (MAS) ^{27}Al NMR spectra of the fresh and spent catalysts were recorded on a Bruker DMX500 spectrometer operating at a ^{27}Al NMR frequency of 130 MHz. The ^{27}Al chemical shifts are referenced to a saturated Al(NO$_3$)$_3$ solution. An accurately weighed amount of sample was packed in a 4 mm (2.5 mm for a few samples) zirconia rotor. Typically, the samples were exposed to saturated water vapor at room temperature for one day prior to measurements. The sample rotation speed was 9 kHz (25 kHz for the 2.5 mm zirconia rotor).

2.3 Results and Discussion

The physicochemical properties of the supports and the metal dispersion of the reduced Pt-containing catalysts are collected in Table 2.1. As outlined before [21], the surface of these amorphous silica-aluminas is made up from (i) a mixed silica-alumina phase, which presumably also contains the strong and weak Brønsted acid sites and (ii) alumina domains. Part of these alumina domains (Al^{VI}O$_x$) contain only six-coordinated Al, are highly dispersed and remain in close interaction with the ASA phase. Another part of these domains is more segregated from the ASA phase and has similar properties as γ-Al$_2$O$_3$. While the former is due to grafting processes of Al species on the silica surface, the latter mainly originates from precipitation. Whereas the ASAs with a nominal alumina content lower than 20 wt% predominantly contain Al^{VI}O$_x$ domains, only ASA(55) contains a free γ-Al$_2$O$_3$ phase. The average Pt particle size of the γ-Al$_2$O$_3$ and SiO$_2$ supported catalysts were 1.5 and 1.8 nm, respectively. With ASA as the support, the average particle size was found to be in the range 3.4 - 5.6 nm depending on the composition of the support. The dispersion of Pt decreased with decreasing Al concentration of the ASA support.

The catalysts were evaluated for their performance in the aqueous phase glycerol conversion at a WHSV of 4.2 h^{-1}. Reaction results collected after 3.5, 11 and 23 h are presented in Tables 2.2, 2.3 and 2.4, respectively. For all catalysts, the glycerol conversion was lower than 12%. Pt/SiO$_2$ exhibited a much lower activity than the catalysts based on the aluminum-containing supports. The glycerol conversion increased with Al content of the

support, in parallel to the increase in the rate of hydrogen formation. The highest rate of hydrogen formation was observed for Pt/γ-Al$_2$O$_3$. The selectivity to liquid phase products after 23 h was higher than 70 % in all cases.

Table 2.1: Physicochemical properties of the supports, metal dispersions and particle sizes of the catalysts as determined by H$_2$ chemisorption.

Catalyst	Surface Areas of the Supports (m^2/g)	Distribution of Al[1]			D (%)	d_{Pt} (nm)
		ASA phase (wt%)	Al$_2$O$_3$ domains			
			Al^{VI}O$_x$ (wt%)	Free γ-Al$_2$O$_3$ (wt%)		
Pt/SiO$_2$	260	-	-	-	64	1.8
Pt/ASA(4.3)	419	3.7	0.6	-	20	5.6
Pt/ASA(12.1)	373	9.1	3.0	-	27	4.1
Pt/ASA(20)	354	15.6	4.4	-	33	3.4
Pt/ASA(55)	350	9	13	33	26	4.4
Pt/γ-Al$_2$O$_3$	250	-	-	100	75	1.5

[1]The Al content (in wt% Al$_2$O$_3$) of the mixed silica-alumina (ASA) and alumina phases. The flexibility of the coordination of Al^{VI} before and after exposure to ammonia was used to distinguish between Al in alumina domains and Al in a mixed silica-alumina phase.

It is well documented that the space velocity has a significant effect on product selectivity. For instance, Li et al. [24] observed an increase in the selectivity to liquid phase products from 18 to 98 % for sorbitol conversion upon an increase of WHSV from 0.7 to 11.6 h^{-1}. This should relate to the reforming of the intermediate in the liquid phase. In agreement with this, it was observed that the increasing conversion of the catalysts led to a decrease of the selectivity of liquid phase products with increasing Al concentration of the support. The dominant products observed in the gas phase were H$_2$, CO$_2$, CH$_4$, C$_2$H$_6$ with trace amounts of C$_3$H$_8$. CO formation was not observed, which is desirable when the goal is to produce H$_2$ for PEMFC applications [25].

Table 2.2: Reaction data after 3.5 h for the aqueous phase conversion of glycerol (at 225 °C, 29 bar, WHSV of 4.2 h^{-1}) over the Pt loaded catalysts.

	Pt/γ-Al$_2$O$_3$	Pt/ASA(55)	Pt/ASA(20)	Pt/ASA(12.1)	Pt/ASA(4.3)	Pt/SiO$_2$
X glycerol (%)[1]	6.4	3.2	2.9	2.8	3.0	1.0
$S_{C, G}$ (%)[2]	46	29	24	20	19	6
$S_{C, L}$ (%)[3]	54	71	76	80	81	94
Rate (H$_2$)[4]	94	60	33	37	27	1.5
Y (CO$_2$)	2.49	0.85	0.68	0.54	0.53	0.06
Y (methane)	0.42	0.10	0.05	0.04	0.04	-
Y (ethane)	-	0.06	0.05	0.07	0.08	-
Y (propanal)	0.02	0.04	0.04	0.04	0.06	0.01
Y (propanols)	0.05	0.15	0.17	0.19	0.33	0.02
Y (methanol)	0.14	0.06	0.04	0.04	0.03	0.01
Y (ethanol)	0.87	0.44	0.44	0.41	0.43	0.03
Y (ethylene glycol)	0.24	0.22	0.19	0.24	0.20	0.06
Y (1,2-PDO)	1.39	0.82	0.78	0.70	0.63	0.15
Y (hydroxyacetone)	0.73	0.39	0.44	0.50	0.64	0.66

[1]Glycerol conversion, [2]Carbon-based products selectivity in gas phase (C in gaseous products/total converted C), [3]Carbon-based products selectivity in liquid phase (C in liquid products/ total converted C), [4]Rate of H$_2$ production (μmol g$_{cat}$$^{-1}$ min^{-1}), Y represents the yield (%) of carbon containing products based on carbon atoms.

Table 2.3: Reaction data after 11 h for the aqueous phase conversion of glycerol (at 225 °C, 29 bar, WHSV of 4.2 h^{-1}) over the Pt loaded catalysts.

	Pt/γ-Al$_2$O$_3$	Pt/ASA(55)	Pt/ASA(20)	Pt/ASA(12.1)	Pt/ASA(4.3)	Pt/SiO$_2$
X glycerol (%)[1]	10.1	5.4	3.8	3.0	2.9	0.5
$S_{C, G}$ (%)[2]	26	22	22	20	18	5
$S_{C, L}$ (%)[3]	74	78	78	80	82	95
Rate (H$_2$)[4]	147	61	17	28	28	2.2
Y (CO$_2$)	2.52	1.11	0.79	0.55	0.51	0.02
Y (methane)	0.25	0.12	0.07	0.04	0.02	-
Y (ethane)	-	0.08	0.09	0.07	0.08	-
Y (propanal)	0.04	0.06	0.07	0.06	0.05	-
Y (propanols)	0.13	0.21	0.34	0.27	0.25	-
Y (methanol)	0.28	0.07	0.03	0.04	0.03	-
Y (ethanol)	1.65	0.84	0.48	0.44	0.35	-
Y (ethylene glycol)	0.67	0.29	0.12	0.20	0.24	-
Y (1,2-PDO)	3.54	1.91	1.02	0.66	0.70	0.03
Y (hydroxyacetone)	0.88	0.64	0.71	0.59	0.64	0.45

[1]Glycerol conversion, [2]Carbon-based products selectivity in gas phase (C in gaseous products/total converted C), [3]Carbon-based products selectivity in liquid phase (C in liquid products/ total converted C), [4]Rate of H$_2$ production (μmol g$_{cat}^{-1}$ min^{-1}), Y represents the yield (%) of carbon-containing products based on carbon atoms.

Table 2.4: Reaction data after 23 h for the aqueous phase conversion of glycerol (at 225 °C, 29 bar, WHSV of 4.2 h^{-1}) over the Pt loaded catalysts.

	Pt/γ-Al$_2$O$_3$	Pt/ASA(55)	Pt/ASA(20)	Pt/ASA(12.1)	Pt/ASA(4.3)	Pt/SiO$_2$
X glycerol (%)[1]	11.9	9.6	6.5	3.7	3.5	0.5
$S_{C, G}$ (%)[2]	27	16	14	19	14	-
$S_{C, L}$ (%)[3]	73	84	86	81	86	100
Rate (H$_2$)[4]	160	66	14	20	21	-
Y (CO$_2$)	2.96	1.33	0.72	0.58	0.44	-
Y (methane)	0.21	0.10	0.07	0.04	0.02	-
Y (ethane)	0.04	0.07	0.10	0.06	0.04	-
Y (propanal)	0.05	0.07	0.08	0.06	0.04	-
Y (propanols)	0.17	0.23	0.36	0.22	0.19	-
Y (methanol)	0.33	0.09	0.03	0.03	0.03	-
Y (ethanol)	1.92	1.54	0.72	0.47	0.31	-
Y (ethylene glycol)	0.84	0.52	0.22	0.19	0.32	-
Y (1,2-PDO)	4.43	4.54	3.04	1.28	1.38	0.03
Y (hydroxyacetone)	0.87	0.90	1.09	0.70	0.70	0.46
Coke (wt%)	7.56	8.81	6.44	5.98	2.14	0.93

[1]Glycerol conversion, [2]Carbon-based products selectivity in gas phase (C in gaseous products/total converted C), [3]Carbon-based products selectivity in liquid phase (C in liquid products/ total converted C), [4]Rate of H$_2$ production (μmol g$_{cat}^{-1}$ min^{-1}), Y represents the yield (%) of carbon containing products based on carbon atoms.

The main products in the liquid phase are hydroxyacetone, 1,2-propanediol, ethylene glycol, ethanol and propanols, mainly 1-propanol. Small amounts of methanol, propanal, propanoic acid, acetaldehyde and 1,3-propanediol were also observed. 1,2-propanediol and hydroxyacetone were the dominant products. 1,2-propanediol is the product of the hydrogenation of hydroxyacetone, which is formed by initial glycerol dehydration. This reaction sequence is consistent with the high hydroxyacetone selectivity for Pt/SiO_2 (93 % after 23 h), which exhibits the lowest glycerol conversion, and also with the decreasing selectivities for increasingly more active catalysts (20, 19, 17, 10 and 7 % after 23 h for Pt/ASA(4.3), Pt/ASA(12.1), Pt/ASA(20) and Pt/ASA(55) and $Pt/\gamma-Al_2O_3$, respectively). The dehydration of glycerol to hydroxyacetone is acid catalyzed. The very low activity for Pt/SiO_2 should, therefore, be due to the low acidity of the silica support, which is likely due to the residual Al content of silica (0.5 wt%). The alternative that it is due to protons generated from dissolution of CO_2 as suggested by D'Hondt et al. in their study of glycerol conversion over Pt/NaY [26] is less likely. In comparison with the other catalysts, the Pt phase in Pt/SiO_2 is not very active for reforming.

It is more challenging to understand the support effect for the other catalysts. If strong Brønsted acid sites would be required for glycerol dehydration and assuming that this step is rate limiting, one expects similar activities for the Pt/ASA catalysts and a lower activity for $Pt/\gamma-Al_2O_3$. In contrast, we observe that $Pt/\gamma-Al_2O_3$ is the most active and shows the highest hydroxyacetone yield. For longer reaction times Pt/ASA(55) becomes the catalyst with the highest hydroxyacetone yield. Since for this set of catalysts the main products are hydroxyacetone and 1,2-propanediol and, likely, some of the other hydrodeoxygenation products such as propanal, 1-propanol, 2-propanol also derive from these intermediates, it can be inferred that the few strong Brønsted acid sites of the amorphous silica-alumina are not the dominant active sites for glycerol dehydration.

It is instructive to compare the time on stream behaviour of the catalysts (Fig. 2.1). As discussed above, the conversion for Pt/SiO_2 is low and decreases further with time on stream. Shabaker et al. found evidence for the dissolution and degradation of silica in aqueous phase conversion of ethylene glycol [9]. Hence, support degradation may lead to coalescence and sintering of metal particles as observed by Maris et al. [15]. Douidah et al. reported that the Pt dispersion loss was much less for Pt/Al_2O_3 than for Pt/SiO_2 [27]. Contrasting the behavior of Pt/SiO_2, the aluminum-containing catalysts increase in activity with time on stream. The initial activity of $Pt/\gamma-Al_2O_3$ is already higher than that of Pt/ASA after a reaction time of 5 h. For Pt/ASA, the activation is most pronounced for Pt/ASA(55) and the activity increases becomes smaller with decreasing Al concentrations of the support. Thus, we conclude that the supports undergo changes under hydrothermal reaction conditions.
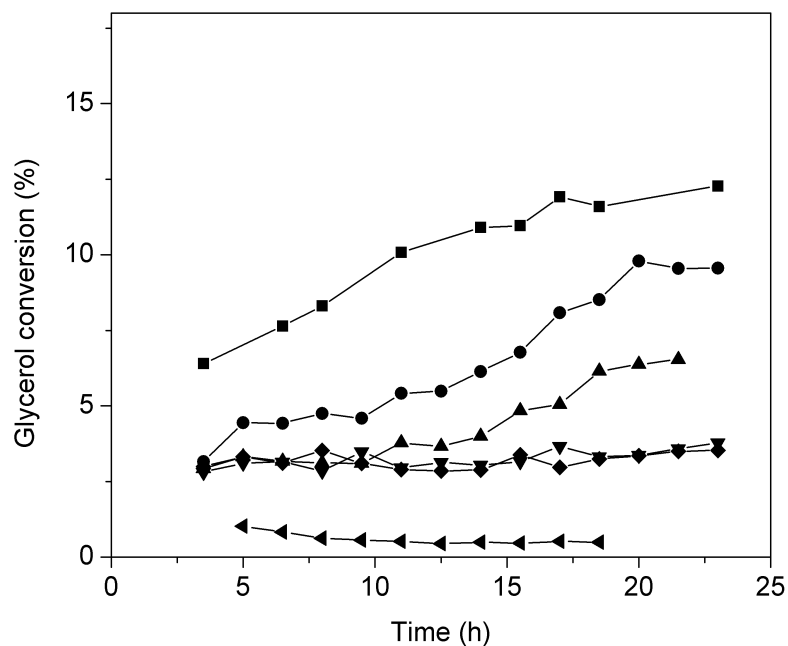
Figure 2.1: Overall conversion of glycerol (at 225 °C, 29 bar, WHSV of 4.2 h^{-1}) as a function of time on stream for (*square*) Pt/γ-Al$_2$O$_3$, (*circle*) Pt/ASA(55), (*up triangle*) Pt/ASA(20), (*down triangle*) Pt/ASA(12.1), (*diamond*) Pt/ASA(4.3) and (*left triangle*) Pt/SiO$_2$.
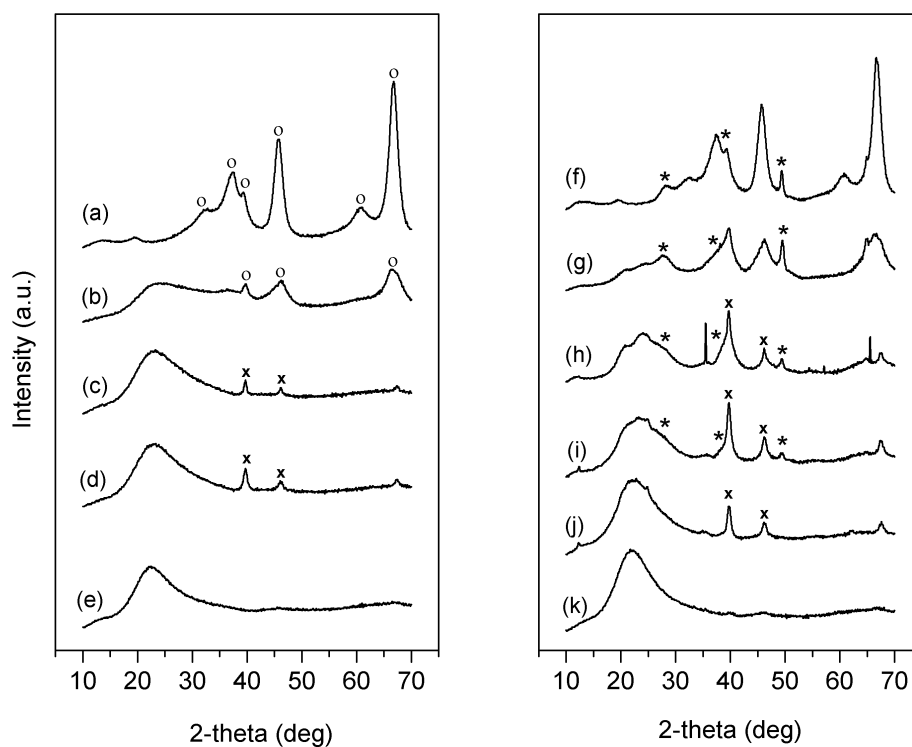
Figure 2.2: X-ray diffraction patterns of fresh (left) and spent (right) catalysts. (a,f) Pt/γ-Al$_2$O$_3$; (b,g) Pt/ASA(55); (c,h) Pt/ASA(20); (d,i) Pt/ASA(12.1); (j) Pt/ASA(4.3); (e,k) Pt/SiO$_2$ (peak assignment: (o) γ-Al$_2$O$_3$ phase, (*) boehmite phase, (x) Pt phase).

Therefore, XRD patterns and ^{27}Al NMR spectra of the catalysts were measured before and after the reaction. XRD results and hence the evidence for boehmite formation during

catalyst operation are complied in Fig. 2.2. The formation of γ-AlO(OH) has been reported before for γ-Al$_2$O$_3$ supports operating under hydrothermal conditions [4,7,10,19,28] and is related to the hydroxylation of alumina domains [29]. The boehmite concentration in the spent catalysts is highest for Pt/ASA(55) and Pt/γ-Al$_2$O$_3$ followed by Pt/ASA(20) and Pt/ASA(12.1). The XRD pattern of spent Pt/ASA(4.3) does not give evidence for boehmite formation. In accordance with the high Al concentration of Pt/ASA(55), this ASA already contains free γ-Al$_2$O$_3$ (Table 2.1), although part of the intensity might also derive from the relatively large Pt particles in this catalyst. The other supports with a lower content do not contain this transition alumina, also not after use as catalyst in glycerol conversion. XRD also provides indications for the growth of the Pt particles during reaction. The Pt particles should remain fairly small for Pt/γ-Al$_2$O$_3$ and Pt/SiO$_2$, because the characteristic diffraction peaks of large Pt particles are not observed in the spent catalysts. The XRD patterns of Pt/ASA(4.3), Pt/ASA(12.1) and Pt/ASA(20), however, point to a considerable growth of the Pt particles. Note that the peaks in Fig. 2.2 assigned to Pt were not present in the XRD patterns of the parent support materials (not shown).

Table 2.5: Distribution of Al of fresh and spent samples as determined by ^{27}Al NMR spectroscopy.[1]

Catalyst		Al^{IV}	Al^V	Al^{VI}	Si/Al
Pt/ASA (4.3)	fresh	58 (56)	-	42 (2)	22
	spent	40 (54)	-	60 (3)	12
Pt/ASA(12.1)	fresh	50 (57)	8 (31)	42 (7)	7.3
	spent	25 (57)	4 (31)	71 (7)	2.4
Pt/ASA(20)	fresh	43 (57)	10 (30)	47 (3)	4.0
	spent	15 (60)	3 (31)	82 (5)	0.9
Pt/ASA(55)	fresh	32 (62)	7 (31)	61 (7)	0.8
	spent	21 (62)	-	79 (7)	0.6
Pt/γ-Al$_2$O$_3$	fresh	32 (66)	-	68 (9)	-
	spent	30 (66)	-	70 (9)	-

[1]Contribution in % and chemical shift in ppm between brackets.

Table 2.5 collects the results of the deconvolution of ^{27}Al NMR spectra of fresh and spent catalysts. The corresponding spectra are given in the Fig. 2.3. It is generally observed that the Al^{VI} content is higher for the spent than for the fresh samples. This tendency is less pronounced for the more aluminum-rich supports. Obviously, this relates to the preferential location of Al at the silica surface in the silica-aluminas. Reiterating from a previous related work that ASA(4.3) mainly contains isolated grafted Al atoms on SiO$_2$ [21], hydrothermal treatment results in partial hydrolysis of the bonds with the surface and a strong increase of the Al^{VI} content. Although more elaborate experiments would be required to establish whether these Al^{VI} are still isolated, it can at least be inferred with reasonable certainty from the XRD pattern of spent Pt/ASA(4.3) that they have not agglomerated into a boehmite phase. Another salient finding is the decrease of the Si/Al ratio during catalyst operation, which points to dissolution of silicon from the support. The changes to the Al phase are qualitatively similar for Pt/ASA(12.1) with substantial amounts of Al^{VI} formed during reaction and a significant decrease of the Si/Al content. In this case, however, boehmite

formation is clearly observed by XRD. We suggest that the reason for this difference is related to the fact that in ASA(12.1) already a higher concentration of alumina domains is present, because the Al loading exceeds the monolayer coverage of silica. Earlier, it has been shown that these alumina domains only contain Al^{VI} with Al^{V} at their periphery [21]. ASA(20) contains a large fraction of alumina domains and, accordingly, a larger amount of boehmite is observed by XRD. Finally, ASA(55) already contains a free γ-Al_2O_3 phase due to the calcination of the boehmite that is precipitated during its preparation. This phase is, similarly to γ-Al_2O_3, a suitable precursor to boehmite as shown by XRD. It has been reported before that the acid and basic sites of boehmite catalyze the dehydration of glycerol to hydroxyacetone [4]. This is confirmed by the present results showing that supports, which facilitate boehmite formation, *i.e.* γ-Al_2O_3 and ASA(55), exhibit much higher activity than the supports that predominantly contain isolated Al. The activity of Pt/ASA(20) has an intermediate activity, because it has some alumina domains.

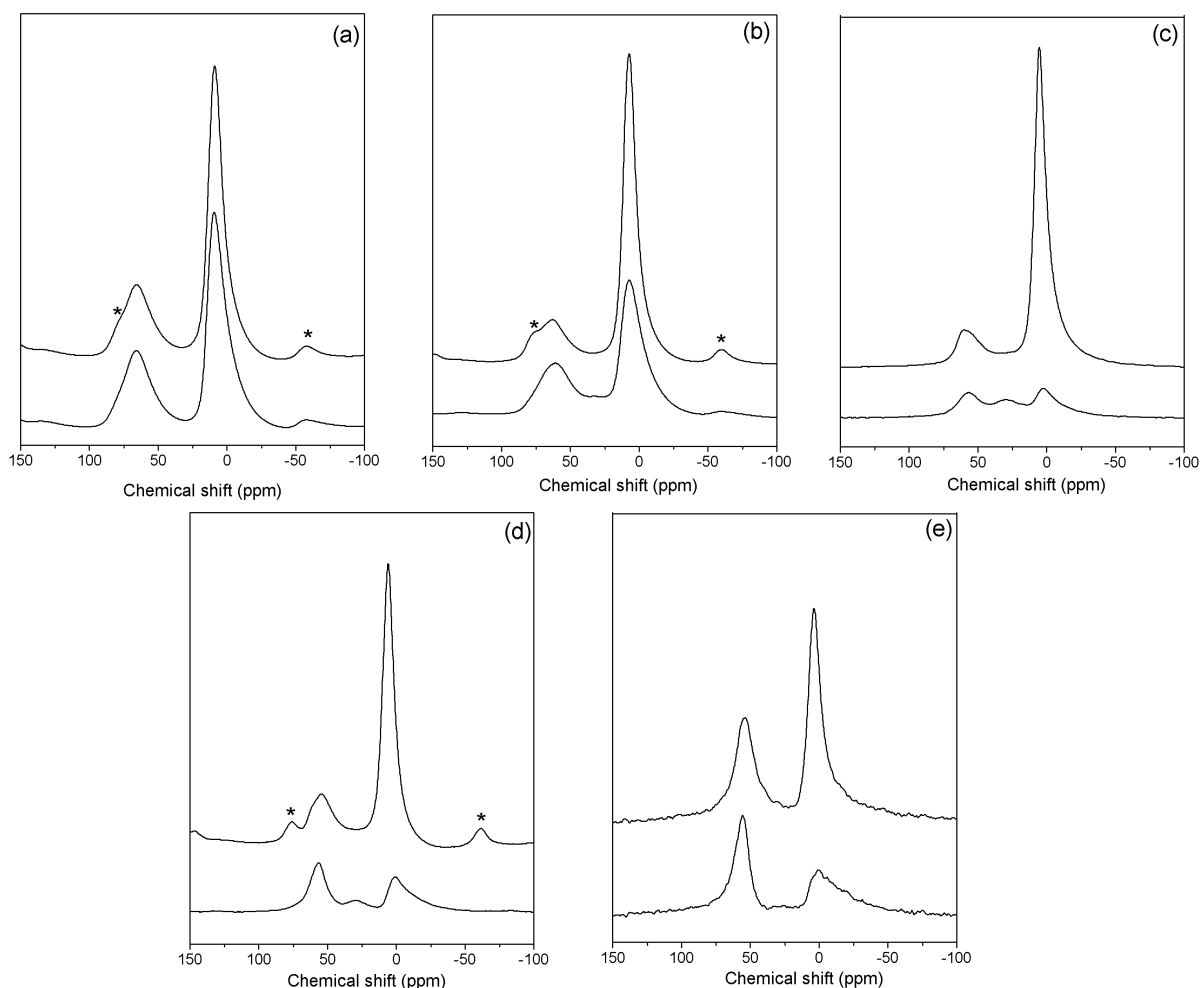**Figure 2.3:** ^{27}Al NMR spectra of fresh (bottom spectra) and spent (top spectra) catalysts. (a) Pt/γ-Al_2O_3; (b) Pt/ASA(55); (c) Pt/ASA(20); (d) Pt/ASA(12.1); (e) Pt/ASA(4.3). For each pair, data is normalized by the loaded sample weight. The asterisk represents the spinning side bands observed for the samples measured at lower spinning speed.

As proposed earlier [4], the aqueous phase reforming of glycerol over a bi-functional acid-metal catalyst proceeds through a limited number of main reaction routes distinguished by initial dehydrogenation or dehydration of glycerol. The dehydrogenation reaction of glycerol to glyceraldehyde, followed by decarbonylation and the water-gas shift reaction is predominantly catalyzed by the metal function of the catalyst (route I). Note that glyceraldehyde is typically not observed because it is rapidly converted by Pt catalysts [4]. The second dehydration route depends on the support acidity and starts with the formation of hydroxyacetone and is followed by its hydrogenation to 1,2-propanediol over the metal sites (route II). Over the $Pt/\gamma-Al_2O_3$ catalyst the yield of products formed through the support-catalyzed route II increased 2.5 folds with time on stream by comparison of the data after 3.5 and 23 h. This increase in the activity of the support catalyzed route can be related to the formation of boehmite during the reaction. The metal-catalyzed route I became 1.5 times more active. The fact that the activity of Pt increases with reaction time suggests that Pt on boehmite is more active in reforming than Pt on $\gamma-Al_2O_3$. An alternative explanation might be a substantial change in the Pt particle size. In the case of the Pt/ASA more dramatic effects are observed. The phase transition of ASA(55) led to a nearly 5-fold increase of route II. Also, the activity of route I doubled, which suggests that the phase transition in ASA(55) has similar effects on the activity of Pt as for the $\gamma-Al_2O_3$ supported catalyst. For the Pt/ASA(20), the increase of route II was 3-to-4-fold. For Pt/ASA(12.1) and Pt/ASA(4.3), on the other hand, this increase was only about 1.5-fold. Notably, the increase in the yield of the products formed through the metal-catalyzed route I became smaller as the Al content of the ASA support decreased. For Pt/ASA(4.3), even a slight decrease in the yield of these products was observed. We speculate that these trends are caused by the different surface coverage of silica with Al species. For relatively high Al content, the surface has a boehmite character and the Pt phase remains in interaction with boehmite. This seems to be predominantly the case for $Pt/\gamma-Al_2O_3$, Pt/ASA(55) and Pt/ASA(20). For catalysts with lower Al concentrations, the most extreme case being Pt/ASA(4.3), the slight agglomeration of Al into boehmite will cause some Pt particles to end up on a silica-rich surfaces, with a relatively lower activity.

Based on the much higher activity of Pt/ASA in gas-phase toluene hydrogenation as compared to Pt/SiO_2 and $Pt/\gamma-Al_2O_3$ [22], larger differences would have been expected within the present set of catalysts, at least concerning the 1,2-propanediol yield. The weak hydrogenation performance of Pt/SiO_2 is evident from this study by observation that only little hydroxyacetone is hydrogenated to 1,2-propanediol. However, the differences between $Pt/\gamma-Al_2O_3$ and Pt/ASA seem to be mainly caused by the differences in conversion. This is perhaps not so surprising, as the support surface of both $\gamma-Al_2O_3$ and amorphous silica-alumina transformed into a boehmite phase during catalyst operation and, accordingly, the Pt phase will not have the exceptional properties it would have on a real Pt/ASA surface. From Tables 2.2-2.4 no clear correlation can be derived between the rate of H_2 production and the Pt particle size. As suggested above, besides the support effect also a change in particle size might contribute to the considerable activity changes with time on stream. However, determination of the average Pt particle size of spent Pt/Al_2O_3 and Pt/ASA(55) by high-

resolution TEM gave values of 2.0 ± 0.4 nm and 3.9 ± 1.4 nm, respectively, close to the values of the fresh catalysts. Therefore, it follows that the influence of the support composition on the intrinsic activity of Pt is dominant over other effects. By TEM we determined the average particle sizes for spent Pt/ASA(4.3), Pt/ASA(12.1) and Pt/ASA(20) to be 11.1, 6.2 and 5.2 nm, respectively. These results clearly show that the Pt particles are stabilized on the alumina/boehmite phases but not on the silica/silica-alumina surfaces of the more siliceous ASA supports, consistent with the observations by XRD. As argued above, the hydrogenation activity of Pt/SiO_2 is significantly lower than that of Pt on Al-containing supports. Therefore, one predicts that the dehydrogenation activity of Pt/SiO_2 is low, which explains its poor reforming activity as the important initial step is the dehydrogenation of glycerol to glyceraldehyde [4].

Finally, we also determined the amount of coke on the catalysts after 23 h reaction by TGA analysis (bottom row Table 2.4). Expectedly, Pt/SiO_2 has the least amount of coke deposited on its surface. The amount of coke formed on ASA supported samples are comparable to those reported by Gandarias et al. [20]. The amount of coke for Pt/ASA catalysts increases with the Al content in line with the increasing activity trend. However, Pt/ASA(55) had a higher coke content than $Pt/\gamma-Al_2O_3$, which may perhaps be related to the higher density of strong acid sites.

2.4 Conclusions

A set of Pt nanoparticles catalysts supported on $\gamma-Al_2O_3$, SiO_2 and amorphous silica-aluminas with varying alumina content was tested for their activity in aqueous phase glycerol reforming reaction at 225 °C and 29 bar N_2 pressure. The main products in the gas phase were H_2, CO_2 and C_1-C_3 alkanes. In the liquid phase the main products were 1,2-propanediol, hydroxyacetone and C_1-C_3 monofunctional alcohols. The evolution of conversion and selectivities with reaction time suggested that the Al-containing supports underwent considerable changes. XRD and ^{27}Al NMR measurements evidenced the formation of boehmite from alumina phases. Its formation is most pronounced for samples that contain free $\gamma-Al_2O_3$, but boehmite also forms in amorphous silica-aluminas with lower Al content that predominantly contain very small alumina domains. At the same time, silica leaches from the catalyst support, the leaching degree being more pronounced for silica-rich ASA compositions. Boehmite catalyzes the dehydration of glycerol to hydroxyacetone, which is further hydrogenated to 1,2-propanediol by Pt. The reaction data indicate that Pt in interaction with boehmite is more active in hydroxyacetone hydrogenation (1,2-propanediol) and glycerol dehydrogenation (glyceraldehyde) reactions than Pt in interaction with $\gamma-Al_2O_3$ and silica. Higher surface acidity due to boehmite formation leads to higher selectivity to 1,2-propanediol over reforming products. For ASA with low Al content, part of the Pt ends up on more silica-rich parts after Al agglomeration and the metal function deactivates. The few strong Brønsted acid sites of ASA do not play a significant role in liquid phase processing of glycerol.

References

[1]   B. Sels, E. D'Hondt, P. Jacobs, in: G. Centi, R.A. van Santen (Eds.), Catalysis for Renewables: From Feedstock to Energy Production, Wiley-VCH Verlag GmbH & Co. KGaA, Weinheim, Germany, 2007, pp. 223-255.

[2]   T. Werpy, G. Petersen, Top Value Added Chemicals From Biomass, US DOE Report, 2004.

[3]   R.R. Davda, J.W. Shabaker, G.W. Huber, R.D. Cortright, J.A. Dumesic, Appl. Catal. B 56 (2005) 171-186.

[4]   A. Wawrzetz, B. Peng, A. Hrabar, A. Jentys, A.A. Lemonidou, J.A. Lercher, J. Catal. 269 (2010) 411-420.

[5]   R.D. Cortright, R.R. Davda, J.A. Dumesic, Nature 418 (2002) 964-967.

[6]   P.D. Vaidya, A.E. Rodrigues, Chem. Eng. Technol. 32 (2009) 1463-1469.

[7]   N. Luo, X. Fu, F. Cao, T. Xiao, P.P. Edwards, Fuel 87 (2008) 3483-3489.

[8]   K. Lehnert, P. Claus, Catal. Commun. 9 (2008) 2543-2546.

[9]   J.W. Shabaker, G.W. Huber, R.R. Davda, R.D. Cortright, J.A. Dumesic, Catal. Lett. 88 (2003) 1-8.

[10]   G. Wen, Y. Xu, H. Ma, Z. Xu, Z. Tian, Int. J. Hydrogen Energy 33 (2008) 6657-6666.

[11]   R.R. Davda, J.W. Shabaker, G.W. Huber, R.D. Cortright, J.A. Dumesic, Appl. Catal. B 43 (2003) 13-26.

[12]   G.W. Huber, J.W. Shabaker, J.A. Dumesic, Science 300 (2003) 2075-2077.

[13]   G.W. Huber, J.A. Dumesic, Catal. Today 111 (2006) 119-132.

[14]   T. Miyazawa, S. Koso, K. Kunimori, K. Tomishige, Appl. Catal. A 329 (2007) 30-35.

[15]   E.P. Maris, R.J. Davis, J. Catal. 249 (2007) 328-337.

[16]   E.P. Maris, W.C. Ketchie, M. Murayama, R.J. Davis, J. Catal. 251 (2007) 281-294.

[17]   T. Miyazawa, Y. Kusunoki, K. Kunimori, K. Tomishige, J. Catal. 240 (2006) 213-221.

[18]   B. Peng, C. Zhao, I. Mejia-Centeno, G.A. Fuentes, A. Jentys, J.A. Lercher, Catal. Today 183 (2012) 3-9.

[19]   R.M. Ravenelle, J.R. Copeland, W.G. Kim, J.C. Crittenden, C. Sievers, ACS Catal. 1 (2011) 552-561.

[20]   I. Gandarias, P.L. Arias, J. Requies, M.B. Güemez, J.L.G. Fierro, Appl. Catal. B 97 (2010) 248-256.

[21]   E.J.M. Hensen, D.G. Poduval, P.C.M.M. Magusin, A.E. Coumans, J.A.R. van Veen, J. Catal. 269 (2010) 201-218.

[22]   A.E. Coumans, D.G. Poduval, J.A.R. van Veen, E.J.M. Hensen, Appl. Catal. A 411–412 (2012) 51-59.

[23]   M.F. Williams, B. Fonfé, C. Woltz, A. Jentys, J.A.R. van Veen, J.A. Lercher, J. Catal. 251 (2007) 497-506.

[24]   N. Li and G.W. Huber, J. Catal. 270 (2010) 48-59.

[25]   T.V. Choudhary, D.W. Goodman, Catal. Today 77 (2002) 65-78.

[26]   E. D`Hondt, S. Vyver, B.F. Sels, P.A. Jacobs, Chem. Commun. (2008) 6011-6012.

[27]   A. Douidah, P. Marecot, J. Barbier, Appl. Catal. A 225 (2002) 11-19.

[28]   W.C. Ketchie, E.P. Maris, R.J. Davis, Chem. Mater. 19 (2007) 3406-3411.

[29]   S.C. Shen, Q. Chen, P.S. Chow, G.H. Tan, X.T. Zeng, Z. Wang, R.B.H. Tan, J. Phys. Chem. C 111 (2007) 700-707.

Chapter 3

Pt-Re synergy in aqueous phase reforming of glycerol and the water-gas shift reaction

Summary

The synergy between Pt and Re in aqueous phase reforming (APR) of glycerol and the water-gas shift reaction (WGS) was investigated for a series of carbon-supported Pt, Re and PtRe catalysts. The overall activity of the bimetallic catalysts in APR of glycerol increases with Re content. The ratio of products obtained via C-O bond cleavage to those obtained by C-C bond cleavage also increases with Re content. H_2-TPR studies and EXAFS show that Pt and PtRe catalysts are well reduced and remain so during gas and aqueous phase reactions. PtRe catalysts are substantially more active in C-C bond cleavage (acetaldehyde decomposition) than their monometallic counterparts, although there is no strong dependence on the Pt/Re ratio. Higher dehydration rates for PtRe alloys correlate to the increasing concentration of steam-treating induced Brønsted acid sites. The higher glycerol conversion rate of PtRe catalysts compared to Pt mainly stems from the higher rate of CO removal from the surface by the WGS reaction. Pt and Re exhibit a very strong synergy in the gas-phase WGS reaction. Consistent with this, CO stripping voltammetry points to lower onset of CO electro-oxidation for PtRe than for Pt. It is argued that the main influence of Re is its stronger binding of oxygen species facilitating water activation, producing OH species which are involved in the WGS reaction and in C-O bond cleavage reactions.
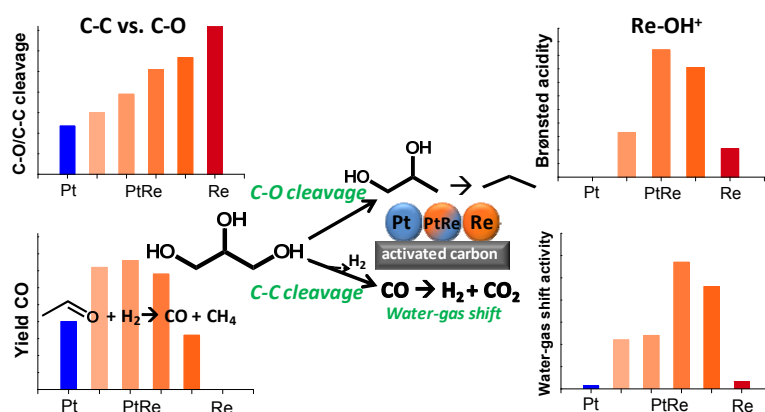
3.1 Introduction

The feedstock of the chemical industry will be shifting from petroleum to renewable feedstock such as biomass due to depletion of finite fossil oil reserves and environmental problems caused by their excessive use. As a clean and sustainable source of carbon, biomass is an attractive alternative for obtaining useful chemicals and fuels. Different from petroleum, biomass has a high concentration of oxygenated groups. Thus, transition to a carbohydrate based economy necessitates the development of new catalytic systems that can selectively defunctionalize such feedstock. Various concepts for valorizing the carbohydrate constituents of biomass have been proposed in literature [1-8]. Aqueous phase reforming (APR) of carbohydrate constituents of biomass forms an attractive approach for producing fuels and/or hydrogen at low temperature and mild pressure [9]. Glycerol is a model compound for complex carbohydrates and its aqueous phase reforming has accordingly already been the subject of a significant number of studies [2,9-15]. In addition, glycerol is a potential platform chemical in future biorefineries, because it is the by-product of the transesterification of vegetable oils and fats into biodiesel. Creating alternative routes for utilizing glycerol by-product is essential in order to render biodiesel production process economically feasible [16-20]. In this respect, generation of hydrogen and value-added chemicals through reforming of glycerol in the aqueous phase is considered promising [17,18,21,22].

APR of glycerol involves the cleavage of C-C, C-H, C-O and O-H bonds. Dehydrogenation of glycerol followed by C-C cleavage and subsequent water-gas shift reaction lead to formation of H_2 and CO_2. An advantage of the low temperature APR process is the very low concentration of CO in the product stream due to the position of the water-gas shift equilibrium. Production of CO-free H_2 from glycerol requires catalysts with high activity in C-C bond breaking and water-gas shift reactions. Catalysts with a high methanation activity are undesirable. In general, supported Pt catalysts have been most frequently used in APR reactions [2,23,24]. In order to investigate the intrinsic catalytic properties of the metal phase, one preferably uses an inert support stable under APR conditions. For this purpose, carbon is the most suitable carrier, because it is stable under hydrothermal conditions due to its hydrophobic nature [24], unlike alumina or silica.

Recently, alloying precious metals with other transition metals (e.g. Re, Mo, W) has been shown to render more active catalysts for APR of glycerol [11,12,14,25,26] as well as in the hydrogenolysis of glycerol [27-32]. The conversion of heavier alcohols and cyclic ethers has also been studied [33-35]. In general, PtRe catalysts exhibit higher overall activity in glycerol conversion and catalyze preferentially C-O bond cleavage reactions compared to Pt catalysts. In literature, different hypotheses have been put forward to explain the promotional effect of Re on Pt based catalysts in the aqueous phase processing of glycerol. For instance, the binding energy of CO to Pt is argued to be lower in the presence of Re, which leads to less severe poisoning of the catalytically active surface sites [26,36]. Related to this, the water-gas shift (WGS) reaction is thought to remove CO as CO_2 during APR. The increase of WGS reaction rates by addition of Re to Pt catalysts supported on TiO_2 [37-44], ZrO_2

[39,40,45] and CeO$_2$-ZrO$_2$ [46,47] has been reported. The relation between the WGS and APR reactions was investigated in the recent work of Guo et al. for a set of catalysts consisting of Pt on basic oxide supports [48]. The basicity of the support was found to strongly influence the WGS and, thus, the APR activity. Another hypothesis for the promotional effect of Re is related to the acidity brought about by hydroxylated rhenium surface species present under hydrothermal conditions [12,25,33,49]. The active sites of the PtRe alloy catalyst are generally thought to consist of metallic Pt surface sites with neighbouring Re atoms, which can strongly bind oxygen species such as hydroxyl groups [25,26]. Some researchers related the promotional effect of Re mainly to acidic Re-OH sites in close proximity to Pt [12,25,33].

The mechanism underlying the promotional effect of Re on Pt catalysts in APR of polyols has not been fully resolved yet. For oxide-supported metal catalysts, we may expect synergy between the metallic Pt phase, which adsorbs CO, and the oxide support facilitating water activation [50,51]. Clearly, a systematic analysis of the synergy between Pt and Re in nanoparticles supported on a hydrothermally stable inert carrier such as carbon is welcome. To the best of our knowledge, till to date there is no study discussing the catalytic performance in glycerol APR of a set of well-characterized carbon-supported PtRe catalysts with varying Pt/Re ratios. The present work also includes model activity studies of the WGS reaction, acetaldehyde decarbonylation and ethanol steam reforming. To this end, a set of carbon-supported PtRe catalysts at constant Pt and increasing Re content were prepared. The catalysts were extensively characterized using various techniques such as TEM, EXAFS and XANES at Pt and Re edges, NH$_3$-TPD, XPS and TPR. IR spectroscopy of adsorbed pyridine was used to probe for Brønsted acidity in a similar set of silica-supported catalysts. The WGS activity of these catalysts was determined in the gas phase and additional CO stripping voltammetry measurements were performed to follow trends in the aqueous phase. The APR activity of the carbon-supported catalysts was evaluated using glycerol as reactant in order to establish correlations between the catalytic activities, selectivity trends and the modifications introduced in the catalytically active sites upon alloying Pt with Re.

3.2 Experimental

3.2.1 Catalyst preparation

The catalysts were prepared by incipient wetness impregnation of an activated carbon with solutions of appropriate concentrations of hexachloroplatinic acid (H$_2$PtCl$_6$.6H$_2$O) and/or perrhenic acid (HReO$_4$) (Aldrich, 65-70 wt% in H$_2$O, 99.99%). After drying the activated carbon support (Norit RX3-EXTRA, surface area: 1190 m^2/g, water pore volume: 1 ml/g) at 110 °C overnight, an appropriate amount of H$_2$PtCl$_6$.6H$_2$O precursor was dissolved in deionized water. After impregnation of the Pt precursor, the sample was dried at 110 °C overnight. PtRe/C samples were prepared by subsequent impregnation of the dried Pt/C samples with a perrhenic acid solution followed by a drying step at 110 °C overnight. The Pt:Re molar ratio was adjusted to 2:1, 1:1, 1:2 and 1:5. A Re/C sample was prepared using perrhenic acid using the same method. These samples are denoted by Pt/C, PtRe/C and Re/C.

For electrochemical measurements, a second set of carbon-supported catalysts was prepared. For this set, Vulcan XC-72 was used as the support. The catalysts were prepared by the same incipient wetness impregnation method used for the activated carbon supported catalysts. These samples are denoted as Pt/C-V and PtRe/C-V. The Pt loading was 5 wt% and, for bimetallic catalysts, the Pt:Re molar ratios were adjusted to 1:1, 1:2 and 1:5.

For FTIR measurements of adsorbed pyridine and ethanol steam reforming activity measurements, a third set of silica-supported catalysts was prepared. For this set, silica (Shell, surface area: 210 m^2/g, water pore volume: 1.05 ml/g, sieve fraction 125-250 μm) was used as support. The catalysts were prepared by incipient wetness impregnation method using $Pt(NH_3)_4(NO_3)_2$ (Alfa Aesar) and perrhenic acid ($HReO_4$) (Aldrich, 65-70 wt% in H_2O, 99.99%) as the Pt and Re precursors, respectively. These samples are denoted as Pt/SiO_2, Re/SiO_2 and $PtRe/SiO_2$. The Pt:Re molar ratios were adjusted to 1:1, 1:2 and 1:5. The bimetallic samples were prepared by sequential impregnation with Pt being introduced first. After impregnation of the metal precursors the samples were dried at 110 °C overnight. Subsequently, Pt/SiO_2 was calcined in static air at 500 °C, whereas Re/SiO_2 was calcined at 250 °C to avoid the loss of Re due to the formation of volatile oxides. Similarly, after each impregnation step, the bimetallic catalysts were calcined at 250 °C.

3.2.2 Catalyst characterization

Elemental analysis – The metal loading was determined by inductively coupled plasma atomic emission spectrometry (ICP-AES) analysis performed on a Goffin Meyvis Spectro Cirus[ccd] apparatus. The carbon-supported samples were dissolved in a 3:1 HCl/HNO$_3$ solution. The metals in the silica-supported samples were dissolved in a mixture of H_2SO_4 and HCl with a droplet of H_2O_2 addition. In order to dissolve silica, an appropriate amount of HF:H_2O (1:15) solution was added.

X-ray photoelectron spectroscopy (XPS) – XPS measurements were performed using a Kratos AXIS Ultra spectrometer, equipped with a monochromatic X-ray source and a delay-line detector (DLD). Spectra were obtained by using the aluminium anode (Al Kα = 1486.6 eV) operating at 150 W. Survey scans were measured at constant pass energy of 160 eV and region scans at 40 eV. The background pressure was kept at 2×10^{-9} mbar. Quasi-in situ XPS measurements for some of the catalysts were performed after reduction of the samples in a tubular quartz reactor with 10 °C/min heating rate from room temperature to 400 °C in a flow of 10 vol% H_2 in He (total flow 100 ml/min). After cooling to room temperature, the lids at the inlet and outlet of the reactor were closed to prevent any interaction with air and the samples were prepared for XPS measurement in an Ar-flushed glove box.

Electron microscopy – High-angle annular dark-field scanning transmission electron microscopy (HAADF-STEM) images were acquired at room temperature on the TU/e CryoTitan (FEI company). The microscope is equipped with a field emission gun (FEG), a Cryo-TWIN objective lens and was operated at an acceleration voltage of 300 kV in nanoprobe STEM mode. Representative STEM images of the samples of 2048 pixel by 2048 pixel in size, were acquired with a Fishione HAADF detector using a probe convergence

angle of 10 mrad, a dwell time of 32 µs and a camera length of 89 mm. For particle size measurements images at a nominal magnification of 320 kx, corresponding to a pixel size of 0.17 nm, were used, which allows reliable detection of particles as small as ~ 0.8 nm. Bright-field transmission electron micrographs (BF-TEM) were acquired on a FEI Tecnai 20 transmission electron microscope at an acceleration voltage of 200 kV with a LaB_6 filament. Typically, a small amount of sample was ground and suspended in pure ethanol, sonicated and dispersed over a Cu grid with a holey carbon film. Pt/C and PtRe/C samples were reduced in 10 vol% H_2 in He (total flow 100 ml/min) at 300 °C for 2 hours. Re/C was reduced at 500 °C.

X-ray absorption spectroscopy (XAS) – XAS was carried out at the Dutch-Belgian Beamline (Dubble) at the European Synchrotron Radiation Facility (ESRF), Grenoble, France (storage ring 6.0 GeV, ring current 200 mA). Data were collected at the Pt L_{III} and Re L_{III} edges in transmission mode. Energy selection was done by a double crystal Si(111) monochromator solid-state detector. Background removal was carried out by standard procedures. EXAFS analysis was then performed with EXCURVE931 on k^3-weighted unfiltered raw data using the curved wave theory. Phase shifts were derived from ab initio calculations using Hedin-Lundqvist exchange potentials and Von Barth ground states. Energy calibration was carried out with Pt foil. The amplitude reduction factor S_0^2 associated with central atom shake-up and shake-off effects was set at 0.99 by calibration of the first- and second shell Pt–Pt coordination numbers to 12 and 4, respectively, for the k^3-weighted Extended X-ray Absorption Fine Structure (EXAFS) fits of the Pt foil. For the spectra recorded at the Re L_{III} edge, Re powder and NH_4ReO_4 were fitted as the reference spectra and S_o^2 for the Re-Re and Re-O shells were set as 0.99 and 0.677, respectively. Spectra were recorded in a stainless-steel controlled atmosphere cell. The cell was heated with two firerods controlled by a temperature controller. A thermocouple was placed close to the catalyst sample. Typically, a predetermined amount of finely grinded sample was pressed in a stainless steel holder and placed in the cell. Carbon foils were held between two high-purity carbon spacers. Gases (He and H_2) were delivered by thermal mass flow controllers (Bronkhorst). The catalyst sample was heated at a rate of 10 °C/min up to a final temperature of 550 °C, whilst recording X-ray Absorption Near-edge Structure (XANES) spectra. After reduction at 300 °C and 550 °C for 1 h, the sample was cooled and two EXAFS spectra were recorded. A second set of XAS measurements were performed under in situ WGS reaction conditions. After recording the room temperature EXAFS of the catalysts reduced at 300 °C, the sample was heated to 150 °C under Helium flow. At 150 °C, CO was mixed with He and fed through a Controlled Evaporator Mixer unit where steam was generated to obtain a $H_2O:CO$ ratio of 3. The sample was heated at a ramp rate of 10 °C/min and XANES spectra were recorded during in situ WGS reaction at 200 and 250 °C. Finally, EXAFS spectra for each sample were recorded during WGS reaction at 300 °C. A third set of XAS measurements were performed under aqueous phase reforming conditions. The catalyst sample was first reduced following the procedure described above. The reduced sample was then exposed to water or 10 wt% aqueous ethylene glycol feed through an HPLC pump at a

flow rate of 0.05 ml/min. The pressure of the transmission cell was controlled by a back pressure regulator and during the experiments the pressure was kept at 30 bar. The cell was sealed with glassy carbon windows (Sigradur, 1 mm thick). XANES spectra were recorded under aqueous conditions by feeding water at 50, 100 and 225 °C and by feeding aqueous ethylene glycol at 225 °C.

Temperature programmed reduction (TPR) – TPR experiments were performed in a flow apparatus equipped with a fixed-bed reactor, a computer-controlled oven and a thermal conductivity detector. Typically, 28 mg catalyst was loaded in a tubular quartz reactor. The sample was reduced in 4 vol% H_2 in N_2 at a flow rate of 8 ml/min, whilst heating from room temperature up to 800 °C at a ramp rate of 10 °C/min. The H_2 signal was calibrated using a CuO/SiO_2 reference catalyst.

Temperature programmed desorption of NH_3 – Temperature programmed desorption (TPD) of pre-adsorbed NH_3 was carried out by loading 120 mg catalyst in a tubular quartz reactor. Pt/C and PtRe/C catalysts were reduced at 300 °C (Re/C reduced at 550 °C) in flowing H_2/He mixture. After cooling, the catalyst was exposed to pure NH_3 at room temperature. Prior to NH_3 exposure, some of the reduced samples were steamed for 1 h at 225 °C by bubbling 50 ml/min He through a saturator containing water kept at room temperature (water partial pressure was about 2.7 kPa). After the catalyst was swept with 100 ml/min He for 6 h at room tempeature, the temperature was increased linearly with a rate of 10 °C/min in 50 ml/min He and the signals of He, NH_3 and H_2O (m/z = 4, 17, 18) were recorded by online mass spectrometry (quadrupole mass spectrometer, Balzers TPG-300), simultaneously. The contribution of H_2O to the m/z = 17 signal of NH_3 was corrected for all samples.

Fourier transform infrared spectroscopy (FTIR) of adsorbed pyridine – Silica was used as the support as carbon is not suitable for infrared measurements. FTIR spectra of the samples were recorded in the range of 4000-400 cm^{-1} by a Bruker Vertex V70v instrument. The spectra were acquired at a 2 cm^{-1} resolution and averaged over 32 scans. The samples were prepared as thin self-supporting wafers of 5-10 mg/cm^2 and placed inside a controlled environment infrared transmission cell, capable of heating and cooling, gas dosing and evacuation. Prior to measurements, all catalysts were reduced at 300 °C (Re/SiO_2 reduced at 500 °C) by flowing 20 vol% H_2 in N_2 for 1 h. Some of the samples were exposed to steam at 225 °C by bubbling N_2 through a saturator containing water kept at room temperature (water partial pressure ~2.7 kPa), followed by flushing with pure N_2 and subsequent evacuation at 225 °C. After saturating the samples with pyridine at 150 °C, the cell was evacuated at 150 °C. All spectra presented were normalized to the weight of the pellet sample.

Electrochemical measurements – Online electrochemical mass spectroscopy (OLEMS) was used to evaluate the performance of the carbon-supported Pt and PtRe catalysts in CO stripping voltammetry. For these measurements, Vulcan XC-72 was used as the support because of its excellent electric conductivity. To increase data quality, a Pt loading of 5 wt% was used. OLEMS is a technique to measure the gaseous products evolving from an electrocatalyst placed as a working electrode in a standard electrochemical cell. The

details of the OLEMS setup was described elsewhere [52]. Essentially, the setup consists of a capillary tube with a small gas inlet tip made of PEEK (polyether ether ketone) inside of which a porous Teflon plug is pressed. The capillary tube is connected to the mass spectrometer (MS) and the tip can be brought in close proximity (10-20 μm) to the electrode in the hanging meniscus configuration by means of a micrometer positioning system and a camera. For the preparation of the working electrode, the catalyst was first reduced at 400 °C. 5 mg of this pre-reduced catalyst was mixed with a 5 wt% Nafion solution and ground for 5 min. 5 mg of this Nafion/electrocatalyst composite was mixed with a 24 % isopropanol solution and then stirred for 10 min and sonicated for 30 min to obtain a well-dipersed electrocatalyst ink. A 2.5 μl droplet of ink was pipetted onto the clean gold electrode surface and dried in ambient conditions. The as-prepared electrodes were tested in the OLEMS setup in 0.5 M H_2SO_4 solution at 80 °C. For the CO stripping voltammetry experiments, the electrode was first exposed to CO for 10 min followed by blowing Ar through the solution with continuous mixing for another 10 min in order to remove the CO from the solution. The potential was then changed from negative to positive to oxidize CO to CO_2 by scanning at a rate of 5 mV/s. The currents and signals of CO_2 were collected simultaneously. Red rod (0.19 V *vs.* SHE) and Pt plate electrodes were used as reference and counter electrodes, respectively. The corresponding signal for CO_2 (m/z = 44) was recorded by the mass spectrometer.

3.2.3 Catalytic activity measurements

3.2.3.1 Aqueous phase reforming of glycerol

APR reactions were carried out at 225 °C under 25 bar initial N_2 pressure using 60 g of 10 wt% aqueous glycerol solution in a 120 ml autoclave. An amount of 75 mg of reduced catalyst was loaded in the autoclave together with an appropriate amount of deaerated water in a N_2-flushed glovebag. The autoclave was purged five times with 10 bar of N_2 in order to remove air from the autoclave. A 50/50 w/w mixture of glycerol and water was charged into the reactor from an external holding vessel after the autoclave containing water and the catalyst reached the desired reaction temperature. The stirring speed was 600 rpm. Liquid samples were withdrawn by a ROLSI injector and analyzed by a Trace GC equipped using a Stabilwax column and a FID detector. Gas samples were collected online and analyzed by a Focus GC equipped with a TCD detector and CP-Porabond Q and RT-MolSieve-5A columns. The carbon product selectivities were calculated by:

$$S_i(\%) = \frac{mol\ of\ product_i\ formed\ \times number\ of\ C\ atoms}{mol\ of\ glycerol\ in\ the\ feed \times conversion\ \times 3} \times 100$$

3.2.3.2 Acetaldehyde decomposition

Acetaldehyde decomposition experiments were performed in a continuous flow reactor setup. Hydrogen and acetaldehyde were fed as reactants. Acetaldehyde was introduced by bubbling helium through a saturator kept at such a temperature to obtain a gas-phase acetaldehyde concentration of 3 vol%. Samples were first reduced at 300 °C (samples

containing only Re reduced at 500 $^\circ$C). The reaction was carried out at 225 °C at a GHSV of 7200 $ml_{acetaldehyde}/g_{cat}$.h. The reactor effluent was analyzed by online gas chromatography (Interscience GC-8000 Top). Permanent gases were analyzed on Shincarbon ST80/100 packed column connected to a TCD (thermal conductivity detector) and hydrocarbons were analyzed on a RT-Q bond column connected to a FID (flame ionization detector).

3.2.3.3 Ethanol steam reforming

Ethanol steam reforming experiments were carried out in a continuous flow reactor setup. Typically, 50 mg of catalyst (sieve fraction 125–250 μm) diluted with 500 mg of α-Al_2O_3 was loaded into a stainless steel reactor. Prior to reaction, the catalyst was reduced in a mixture of 20 vol% H_2 in N_2 at 400 °C. The reactant feed mixture was obtained by evaporating ethanol and water in a He stream in two controlled evaporator mixers (Bronkhorst). The ratio $C_2H_5OH:H_2O$ was adjusted as 1:6. All tubings were kept above 120 °C to avoid condensation of the reactants and products. The total gas flow rate was 250 ml/min and the GHSV was 8400 ml_{EtOH}/g_{cat}.h. The reactor effluent was analyzed by online gas chromatography (Interscience GC-8000 Top, permanent gases on Shincarbon ST80/100 packed column connected to a TCD and hydrocarbons on a RT-Q bond column connected to a FID).

3.2.3.4 Water-gas shift reaction (WGS)

WGS reaction experiments were performed in a parallel ten-flow microreactor system [53]. Steam was supplied by evaporation of deionized water in a Controlled Evaporator Mixer unit (Bronkhorst) in combination with a liquid flow controller. Gas flows were controlled by thermal mass flow controllers (Brooks and Bronkhorst). All tubings were kept above 100 °C after the point of steam introduction to avoid condensation. The dry product gas mixture was analyzed by an online gas chromatograph (Interscience CompactGC) equipped with Porapak Q (TCD) and Molecular sieve 5A (TCD) columns. Experiments were carried out in a mixture of 2.5 vol% CO and 7.5 vol% H_2O balanced by He at a dry GHSV (gas hourly space velocity) of ~1.1×10^5 h^{-1} in the temperature range 135-400 °C. Typically, the catalyst was diluted with an appropriate amount of SiC of the same sieve fraction. The material was contained between two quartz wool plugs in a quartz reactor. Prior to catalytic activity measurements, the catalyst was reduced in a flow of 20 vol% H_2 in He at a ramp rate of 5 °C/min to 300 or 500 °C followed by an isothermal period of 0.5 h. The reactor was cooled in He to the reaction temperature. The catalyst was exposed to the reaction mixture for 10 min prior to the start of recording product gas mixture. At each reaction temperature, the CO conversion was followed for 1.5 h.

3.3 Results

3.3.1 Catalyst characterization

Table 3.1 lists the metal loadings of the catalysts. The Pt content of all activated carbon-supported mono- and bimetallic catalysts is close to 2.5 wt%. The Re loading of Re/C is very close to that in PtRe(1:1)/C. For the reduction behaviour of these catalysts, we first report general trends determined by TPR (Fig. 3.1). Re reduction in Re/C starts around 300 °C, proceeds with a broad shoulder from 432 to 558 °C, and ends with a broad peak centered around 642 °C. Reduction of PtRe/C catalysts occurs at lower temperatures. All of the TPR profiles of PtRe/C catalysts contain a single reduction feature at around 240 °C, with a broad high-temperature shoulder reaching up to about 750 °C. The contribution of the latter increases with increasing Re content. The reduction profile of Pt/C shows two broad peaks below 400 °C. Clearly, the total amount of H_2 consumed for Pt/C is much lower than for the bimetallic catalysts. The lower reduction temperature for PtRe bimetallic catalysts compared to Re/C (downward shift of ~ 100 °C) shows that Pt facilitates the reduction of Re, which is due to spillover of dissociated H atoms from metallic Pt to Re-oxide [36,54]. The TPR profile of the bare carbon support contains a high temperature peak between 600-800 °C, which is also visible in the profiles of the metal-containing catalysts. We speculate that these features have to do with reduction of functional groups at the surface of the carbon support [36]. For PtRe samples with higher Re content (Pt:Re ratios of 1:1, 1:2 and 1:5), the broad shoulder starting after 300 °C suggests the presence of some residual isolated ReO_x species attached to the carbon surface. The amount of such ReO_x sites increases with Re content and, possibly, the reduction of surface functional groups of the carbon support occurs together with the reduction of such Re oxide species. The H_2/Pt ratio is higher than the expected value of 2 for Pt/C, which points to reduction of some of the surface oxygen groups of the carbon support. The H_2/M value (amount of hydrogen consumed divided by the total moles of Pt and Re) for PtRe(2:1)/C is higher as a result of the presence of Re and it decreases with increasing Re/Pt ratio. Although further research might be necessary to prove this, these data suggest that the reduction of support oxygen groups is more dominant in Pt/C than in the PtRe/C catalysts.

A more detailed analysis of the reduction behavior of the catalysts is provided by in situ XANES measurements. The Pt L_{III} edge near-edge spectra of mono- and bimetallic catalysts are presented in Fig. 3.2. For the PtRe catalysts (Fig. 3.2b-e) the intensity of the Pt L_{III} white line, which depends on the density of unoccupied d-states, decreases with increasing reduction temperature. The changes in the near-edge spectra demonstrate the reduction of PtO_x to metallic Pt. XANES spectra recorded at temperatures higher than 100 °C differ substantially from those at 100 °C. However, the changes in the spectra at temperatures of 200 °C up until 550 °C are rather small. This indicates that the reduction of Pt in the PtRe/C catalysts mainly occurs between 100 and 200 °C. For the PtRe catalyst with the highest Re content (PtRe(1:5)/C), the position of the edge shifts to higher energy compared to the Pt foil and reduced Pt/C. This further points to influence of Re on the electronic structure of Pt species in the bimetallic catalysts [55]. For the monometallic Pt catalyst (Fig. 3.2a), the whiteline feature as well as the near-edge spectra recorded after reduction at 250 °C and 550

°C are similar to the whiteline of the Pt foil, which shows that Pt/C is in reduced state after reduction at 250 °C.

Table 3.1: Metal loading as determined by ICP analysis.

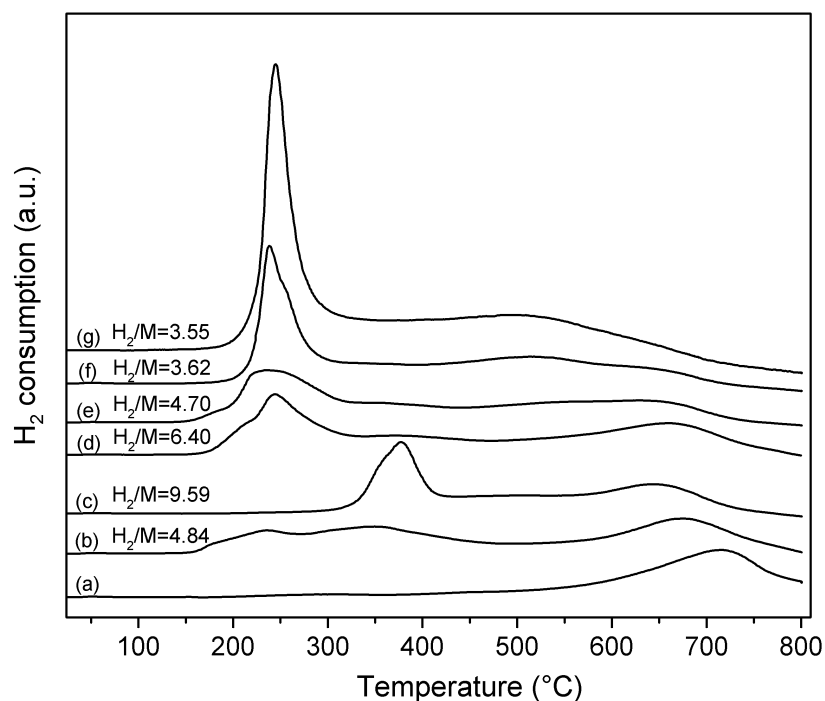| Catalyst	Metal Loading (wt%)		Pt/Re ratio
	Pt	Re	
Pt/C	2.44±0.07	-	-
Re/C	-	2.78±0.02	-
PtRe(2:1)/C	2.48±0.06	1.53±0.02	1.55
PtRe(1:1)/C	2.53±0.04	2.86±0.02	0.84
PtRe(1:2)/C	2.51±0.04	5.58±0.04	0.43
PtRe(1:5)/C	2.28±0.02	13.41±0.02	0.16
Pt/C-V	4.13±0.04	-	-
PtRe(1:2)/C-V	3.64±0.03	9.55±0.03	0.36
Pt/SiO$_2$	2.92±0.03	-	-
PtRe(1:1)/SiO$_2$	2.46±0.04	1.35±0.03	1.74
PtRe(1:2)/SiO$_2$	2.81±0.02	5.75±0.04	0.47
PtRe(1:5)/SiO$_2$	2.80±0.03	9.42±0.05	0.28

Figure 3.1: TPR profiles of (a) the bare carbon (Norit RX-3 extra) support, (b) Pt/C, (c) Re/C, (d) PtRe(2:1)/C, (e) PtRe(1:1)/C, (f) PtRe(1:2)/C and (g) PtRe(1:5)/C. The H$_2$/Metal ratios calculated from the amounts of hydrogen consumed (between 20-300 °C for Pt/C and PtRe/C and between 20-500 °C for Re/C) are indicated on the TPR traces.
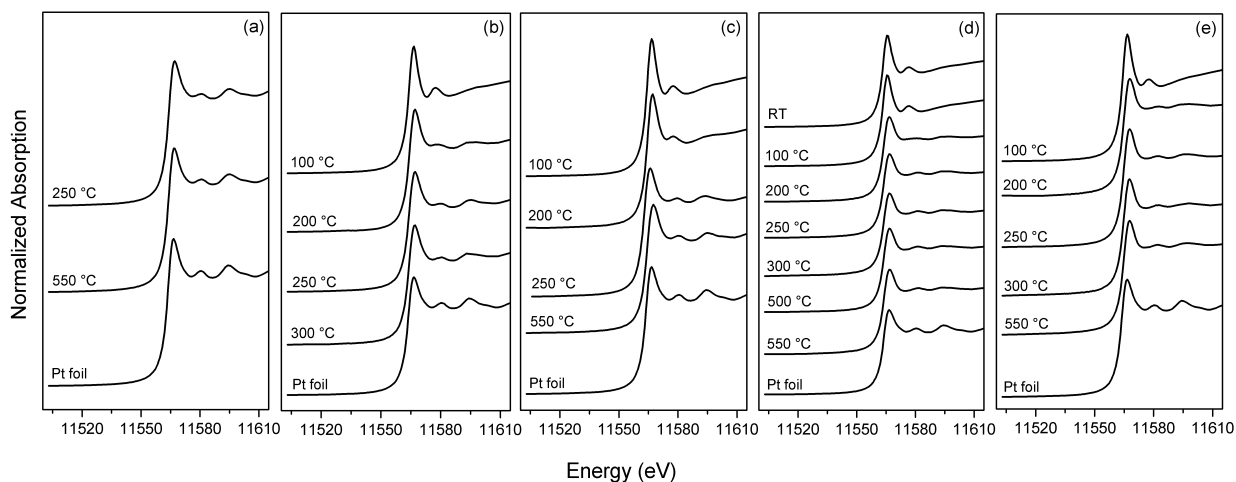
Figure 3.2: Pt L_{III}-edge XANES spectra recorded of (a) Pt/C, (b) PtRe(2:1)/C, (c) PtRe(1:1)/C, (d) PtRe(1:2)/C, and (e) PtRe(1:5)/C after reduction at different temperatures. RT: room temperature.

Fig. 3.3 shows Re L_{III} near-edge XANES spectra of PtRe(1:2)/C and PtRe(1:5)/C catalysts after reduction at different temperatures. For both samples, a clear shift to lower energies and a decrease in the whiteline intensity is observed with increasing reduction temperature. Comparison of the spectra obtained after reduction at 100, 250 and 550 °C evidences that the reduction of Re in the PtRe/C catalysts takes predominantly place between 100 and 250 °C. There is almost no change in the Re L_{III} edge near-edge spectra of PtRe(1:2)/C and PtRe(1:5)/C, when the reduction temperature is increased from 250 to 550 °C. We determined the shift in the edge energies for each spectrum and plotted them as a function of the reduction temperature (Fig. 3.4). From near-edge spectra of NH_4ReO_4, ReO_3, ReO_2 and Re reference compounds, the edge shift values for Re^{+7}, Re^{+6}, Re^{+4} and Re^0 were determined. Clearly, the edge shift for the fresh catalysts and those reduced at 100 °C are similar to that of Re^{+7} in NH_4ReO_4. With increasing reduction temperature up to 250 °C, the edge shift value decreases for the PtRe catalysts, which points to reduction of Re. On the contrary, the Re in Re/C does not reduce as follows from the absence of a shift for Re/C. A further increase in the reduction temperature does not result in significant changes for PtRe catalysts. The most likely interpretation is that the Re is nearly completely reduced, a small part remaining oxidic. This observation is in line with findings in earlier studies [56,57]. In concord with the TPR results, Re in Re/C is reduced when the reduction temperature is increased to 550 °C. It is noteworthy that Re in the PtRe catalysts with higher Re content has a higher oxidation state than in the samples with less Re. This is in agreement with the results of XPS. XP spectra of the as-prepared catalysts and those reduced at 400 °C (not shown) show a shift to higher binding energies of the Pt and Re 4f states with increasing Re content in the bimetallic catalysts. This indicates that the addition of Re results in a decrease in the electron density of both Pt and Re. However, a change in particle size may also affect the binding energy. These data are consistent with the results of Zhang et al. [25] and evidence that Pt and Re is in the reduced state with the amount of oxidic Re species being below the detection limit in XPS.
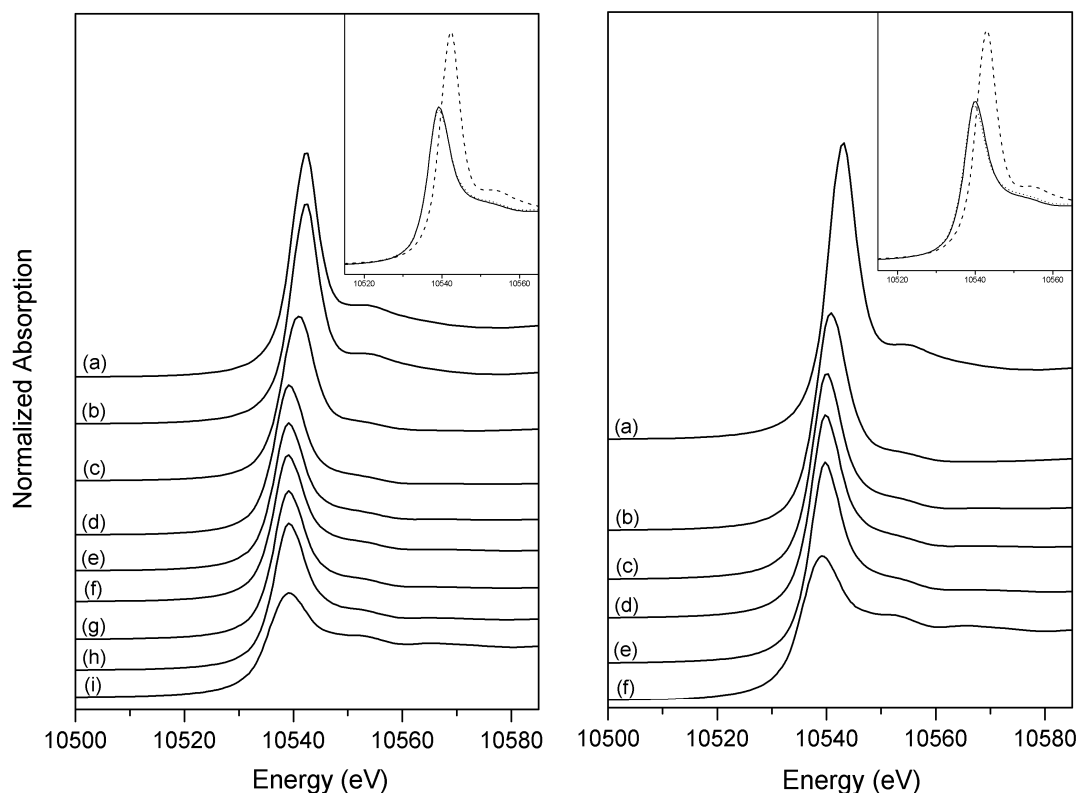
Figure 3.3: Re L_{III}-edge XANES spectra recorded of (left) PtRe(1:2)/C at room temperature (a), after reduction at 100 °C (b), 200 °C (c), 250 °C (d), 300 °C (e), 400 °C (f), 500 °C (g), 550 °C (h) and Re powder (i), and (right) PtRe(1:5)/C after reduction at 100 °C (a), 200 °C (b), 250 °C (c), 300 °C (d), 550 °C (e) and Re powder (f). Comparison of XANES spectra of both samples (upper right corner) reduced at 100 °C (dashed line), 250 °C (straight line) and 550 °C (dotted line).
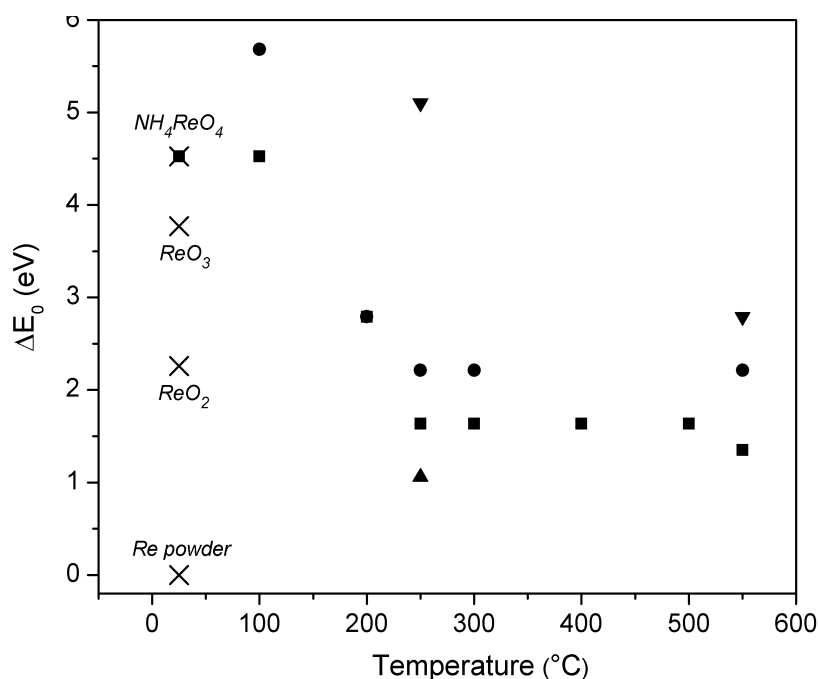

Figure 3.4: Shift in the Re L_{III}-edge energy of PtRe(1:1)/C (*up triangle*), PtRe(1:2)/C (*square*), PtRe(1:5)/C (*circle*) and Re/C (*down triangle*) from the Re L_{III}-edge energy (E_0) of Re powder (10535.2 eV) at different reduction temperatures. The shift in the edge energies of the XANES spectra of reference materials (x) are indicated.

Fig. 3.5a-e shows the Fourier Transform (FT) EXAFS functions of k^3-weighted $\chi(k)$ for the carbon-supported Pt and PtRe catalysts recorded at the Pt L_{III} edge after reduction at 300 °C. The fit parameters are summarized in Table 3.2. The FT spectra of the Pt/C catalyst after reduction at 300 °C were fitted by a single Pt-Pt shell. The coordination number (CN) for the Pt-Pt shell was determined to be 8.3. For the PtRe catalysts reduced at 300 °C, the FT spectra were fitted with a single Pt-M shell, where M represents the backscattering atom being either Pt or Re. Since the backscattering functions of Pt and Re are very similar, it is not straightforward to distinguish by EXAFS between Pt bound to Re or Pt and *vice-versa* [27]. The absence of a Pt-O shell shows that Pt in the bimetallic catalysts is also well reduced after reduction at 300 °C. For all the PtRe catalysts, the CN of the Pt-M shell increases with increasing reduction temperature. This is due to an increase of the size and/or ordering of the nanoparticles. With the increase of the Pt:Re ratio from 2:1 to 1:5, the Pt-M shell CN decreases. This is a strong indication that the size of the alloy particles decreases with increasing Re content. In line with this, the Pt-M coordination distance becomes smaller with increasing Re content.
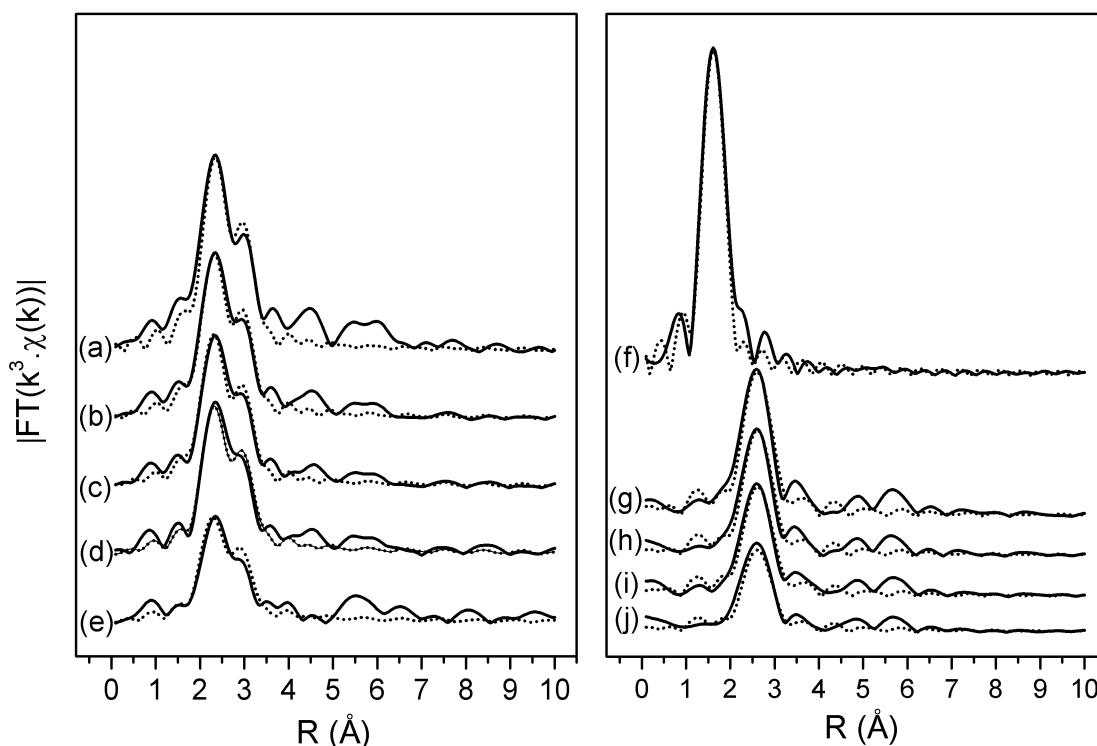

Figure 3.5: FT EXAFS functions obtained from the k^3 –weighted Pt L_{III} edge EXAFS oscillations of (left) Pt/C (a), PtRe(2:1)/C (b), PtRe(1:1)/C (c), PtRe(1:2)/C (d), PtRe(1:5)/C (e) after reduction at 300 °C and (right) the FT EXAFS functions obtained from the k^3 –weighted Re L_{III} edge EXAFS oscillations of Re/C after reduction at 250 °C (f), PtRe(2:1)/C (g), PtRe(1:1)/C (h), PtRe(1:2)/C (i) and PtRe(1:5)/C (j) after reduction at 300 °C. Dotted lines represent the fitted spectra.

Table 3.2: Fit parameters of k^3-weighted EXAFS spectra at the Pt L_{III}-edge of supported Pt and PtRe catalysts. M represents the backscatterer atom (Pt or Re) which was fitted by setting Pt as the atom type.

Catalyst	Treatment	EXAFS analysis				
		Shell	R (Å)	CN	$\Delta\sigma^2$ (Å^2)	E_0 (eV)
Pt/C	H_2, 300 °C	Pt-Pt	2.745	8.3	0.009	-9.8
	H_2, 550 °C	Pt-Pt	2.758	9.8	0.007	-10.5
PtRe(2:1)/C	H_2, 300 °C	Pt-M_{Pt}	2.728	7.5	0.010	8.9
PtRe(1:1)/C	H_2, 300 °C	Pt-M_{Pt}	2.720	6.8	0.010	-9.5
	H_2, 550 °C	Pt-M_{Pt}	2.751	9.1	0.010	-9.5
PtRe(1:2)/C	H_2, 300 °C	Pt-M_{Pt}	2.719	5.6	0.008	-10.3
	H_2, 550 °C	Pt-M_{Pt}	2.722	5.7	0.008	-11.3
PtRe(1:5)/C	H_2, 300 °C	Pt-M_{Pt}	2.687	3.8	0.008	-9.5
	H_2, 550 °C	Pt-M_{Pt}	2.715	4.3	0.009	-10.3

Table 3.3: Fit parameters of k^3-weighted EXAFS spectra at the Re L_{III}-edge of supported catalysts. M represents the backscatterer atom (Pt or Re) which was fitted by setting Re as the atom type.

Catalyst	Treatment	EXAFS analysis				
		Shell	R (Å)	CN	$\Delta\sigma^2$ (Å^2)	E_0 (eV)
Re/C	H_2, 250 °C	Re-O	1.730	4.3	0.002	-10.4
	H_2, 550 °C	Re-O	1.665	0.8	0.002	0.4
		Re-Re	2.665	6.7	0.016	
PtRe(2:1)/C	H_2, 300 °C	Re-M_{Re}	2.658	7.2	0.007	-3.6
PtRe(1:1)/C	H_2, 300 °C	Re-M_{Re}	2.662	6.2	0.007	-3.9
PtRe(1:2)/C	H_2, 300 °C	Re-M_{Re}	2.671	5.2	0.007	-5.6
	H_2, 550 °C	Re-M_{Re}	2.684	8.1	0.009	-5.7
PtRe(1:5)/C	H_2, 300 °C	Re-M_{Re}	2.658	4.1	0.008	-4.2
	H_2, 550 °C	Re-M_{Re}	2.672	5.2	0.009	-4.5

The FT functions at the Re L_{III} edge of PtRe/C and Re/C after reduction at 300 °C (250 °C for Re/C) are shown in Fig. 3.5f-j. Table 3.3 lists the fit parameters for the Re L_{III} edge spectra. The FT spectrum of Re/C after reduction at 250 °C was fitted by a single Re-O shell with a CN of 4.3 and at a R of 1.73 Å. This shows that the monometallic Re/C catalyst mainly contains Re-oxide after reduction at 250 °C. After reduction at 550 °C, the FT spectrum contains a Re-Re shell in addition to a Re-O shell. From the finding that the CN of the Re-Re shell is much higher (6.7) than that of the Re-O shell (0.8), we conclude that Re/C mainly contains metallic Re with a small portion of oxidic Re species after reduction at 550 °C. For the FT spectra of the bimetallic samples, Re was used as the sole backscatterer metal atom. The Re L_{III} edge FT spectra of the PtRe catalysts after reduction at 300 °C could be fitted with a single Re-M shell. When the reduction temperature is increased to 550 °C, the CN of the Re-M shell is found to increase for PtRe(1:2)/C and PtRe(1:5)/C, which is in line with the trend in Pt-M coordination numbers. It is also seen that the CN of the Re-M shell decreases with increasing Re content. This supports the conclusion from the Pt EXAFS data that the size of the PtRe particles decreases with increasing Re content. Although in principle the decreasing overall Pt-M coordination number can also point to increased disorder in the

nanoparticles, the observation that the bond distance of the Pt-M shell becomes smaller with increasing Re content supports the claim of smaller particles. This contraction is usually observed when the size of nanoparticles decreases below a few nm.

Bright-field TEM pictures of the carbon-supported Pt and PtRe catalysts are shown in Fig. 3.6. The average particle size of Pt/C was found to be approximately 1 nm (Fig. 3.6a). The average metal particle sizes of PtRe(2:1) and PtRe(1:1) were very similar to that of Pt/C. For PtRe(1:2) and PtRe(1:5), it was much more difficult to discern the nanoparticles. HAADF-STEM pictures of the catalysts are shown in Fig. 3.7. The number-weighted average particle size of Pt/C was found to be approximately 2 nm (Fig. 3.7a). The average metal particle sizes of PtRe(2:1) and PtRe(1:1) were determined as 1.8 and 1.5 nm, respectively. For PtRe(1:5), it was much more difficult to discern the nanoparticles, likely because they are even smaller than the nanoparticles in the other catalysts in line with findings in literature [58]. For PtRe(1:5), some larger nanoparticles were also observed, indicating that the high Re loading may lead to some inhomogeneous distribution of the metal phase on the support surface. HAADF-STEM also shows that reduced Re/C (500 °C) contains a very heterogeneous distribution of particles ranging from small to very large. Next to particles of 1-2 nm in size, we observe large agglomerates, which may represent a fraction of particles not fully reduced. The larger particles observed for PtRe(1:5)/C could therefore also be related to similar not fully reduced Re particles.
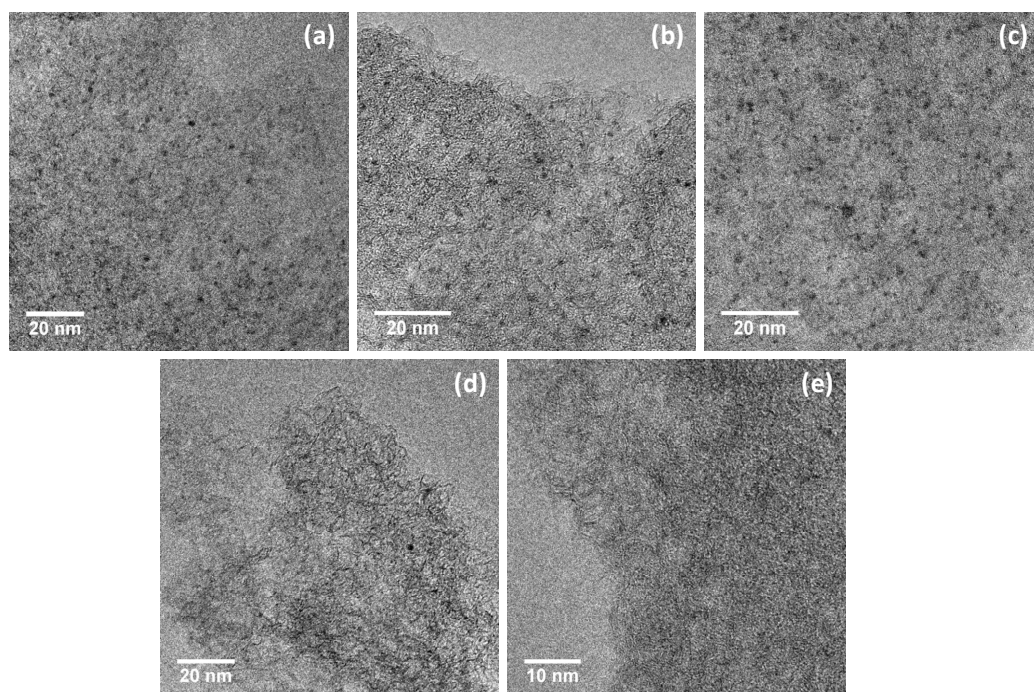

Figure 3.6: Bright-field TEM pictures of (a) Pt/C, (b) PtRe(2:1)/C, (c) PtRe(1:1)/C, (d) PtRe(1:2)/C and (e) PtRe(1:5)/C after reduction at 300 °C.
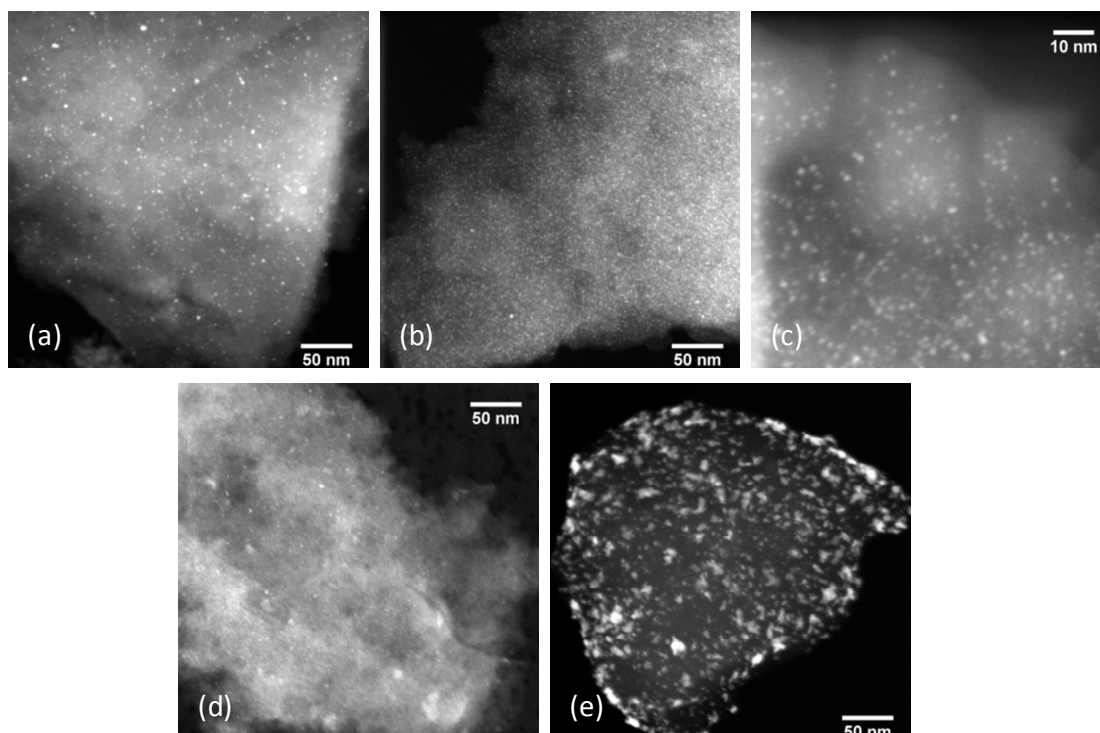
Figure 3.7: High-angle annular dark-field STEM images of (a) Pt/C, (b) PtRe(2:1)/C, (c) PtRe(1:1)/C, (d) PtRe(1:5)/C after reduction at 300 °C and (e) Re/C after reduction at 500 °C.

NH$_3$-TPD experiments were carried out after reduction of Pt/C and PtRe/C at 300 °C and of Re/C at 550 °C. A first set of experiments was performed by exposing the reduced samples to NH$_3$ at room temperature. The NH$_3$-TPD profiles are presented in Figs. 3.8a-c. The much higher desorption peak of PtRe(1:2)/C compared to the monometallic catalysts is consistent with the higher dispersion of the metal phase in the former catalyst, in accordance with the EXAFS and TEM results. Desorption of NH$_3$ starts at 100 °C for Re/C and Pt/C. The onset of NH$_3$ desorption occurs at slightly lower temperature than for PtRe/C. For all of the samples, broad desorption peaks are observed. These features relate to removal of ammonia chemisorbed to the metallic sites [59-61]. A second set of experiments was done by exposing the reduced sample to steam at 225 °C prior to NH$_3$ exposure. Figure 3.8d-f shows the NH$_3$ TPD profiles of the steam-treated catalysts. A prominent feature in the desorption profiles of the steam-exposed Re and PtRe samples is the appearance of a second peak at 208 °C for Re/C and at 244 °C for PtRe(1:2)/C. We attribute this feature to the acidity induced by Re-OH species formed upon exposure of Re-containing samples to steam at 225 °C. Acidity brought about by Re-OH species in alloyed transition metal catalysts has been mentioned before [12,25,33]. Based on assignments in earlier studies, these peaks represent acid sites with weak-to-medium strength [62,63]. This feature does not show up for the Pt-only catalyst. The NH$_3$ desorption feature of Pt/C shows two broad peaks, which are preserved after steaming. This is most likely related to two different surface facets with different NH$_3$ binding energies.
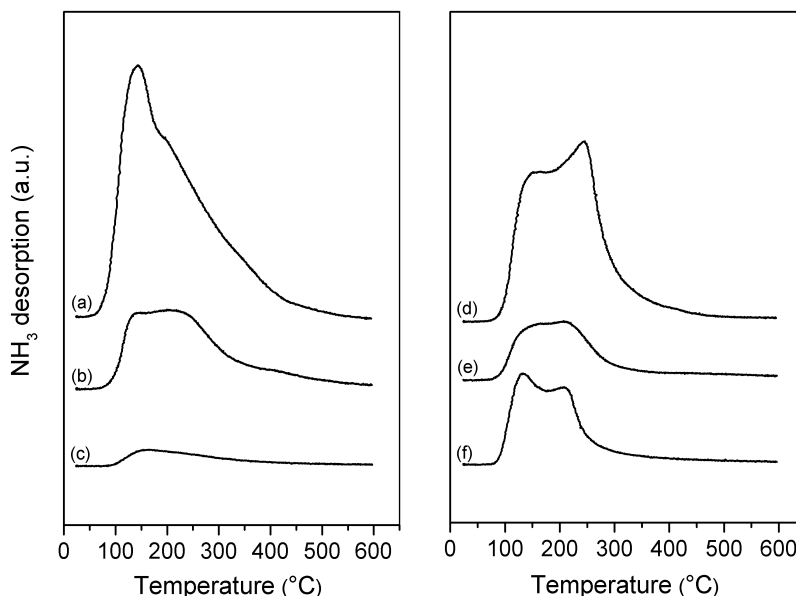
Figure 3.8: NH$_3$ TPD profiles of (a,d) PtRe(1:2)/C, (b,e) Pt/C and (c,f) Re/C (left) before and (right) after steam treatment at 225 °C.

The weight-normalized IR spectra after exposure to pyridine and subsequent removal of physisorbed pyridine at 150 °C for silica-supported equivalents of the Pt(Re)/C catalysts are shown in Fig. 3.9. It was verified that steamed Pt/SiO$_2$ and PtRe(1:2)/SiO$_2$ catalysts had NH$_3$-TPD desorption profiles similar to the carbon-supported catalysts (not shown). IR spectroscopy of adsorbed pyridine was performed on reduced samples before and after exposure to steam at 225 °C. IR bands at 1620 and 1455 cm^{-1} are generally assigned to pyridine adsorbed to Lewis acid sites, whereas bands at 1638 and 1543 cm^{-1} emerge from pyridine interacting with Brønsted acid sites. The band at 1490 cm^{-1} is usually attributed to Brønsted and Lewis acid sites [64,65]. The spectra of PtRe/SiO$_2$ and Re/SiO$_2$ clearly evidence the generation of Brønsted acid sites upon steaming. Based on extinction coefficients in literature [66], the concentration of Brønsted acid sites were calculated and found to decrease in the order PtRe(1:2)/SiO$_2$ (94 μmol/g) > PtRe(1:5)/SiO$_2$ (81 μmol/g) > PtRe(1:1)/SiO$_2$ (33 μmol/g) > Re/SiO$_2$ (21 μmol/g). The ratio of Brønsted acid sites per mol of Re in the PtRe catalysts were determined as 0.46, 0.30 and 0.16 for Pt:Re ratios of 1:1, 1:2 and 1:5, respectively. We conclude that the fraction of Re-OH species associated with Brønsted acid sites decreases with increasing Re content. Steam-treated PtRe(1:2) contains the highest concentration of Brønsted acid sites per catalyst weight and thus should be most acidic under reaction conditions. Non-steamed PtRe(1:2)/SiO$_2$ and PtRe(1:5)/SiO$_2$ also contain a small amount of Brønsted acid sites (Fig. 3.9e,g), which may point to the interaction of the catalyst with some residual water in the IR cell. Steamed Pt/SiO$_2$ hardly contains Brønsted acid sites (Fig. 3.9j). Zhang et al. showed before that PtRe catalysts contain Brønsted acid sites in contrast to Pt catalysts [25].
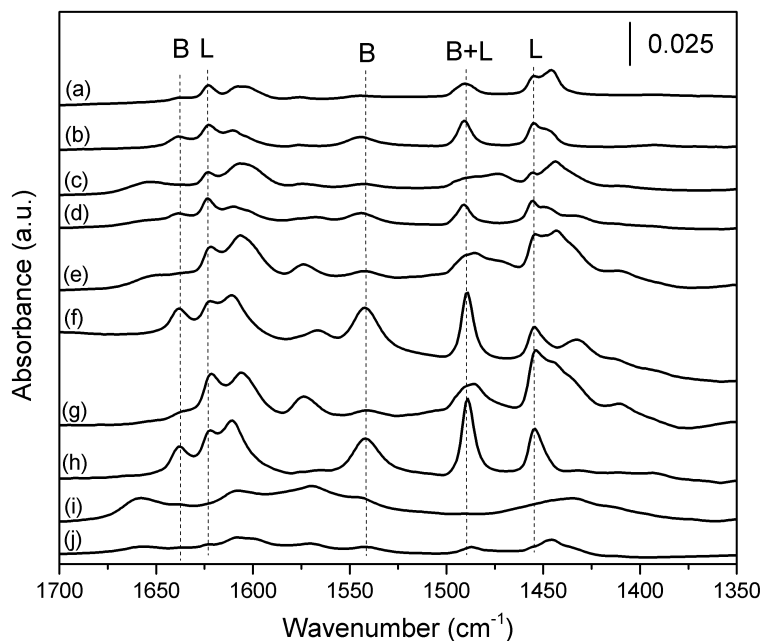
Figure 3.9: FTIR spectra of adsorbed pyridine on Re/SiO$_2$ (a), steamed Re/SiO$_2$ (b), PtRe(1:1)/SiO$_2$ (c), steamed PtRe(1:1)/SiO$_2$ (d), PtRe(1:2)/SiO$_2$ (e), steamed PtRe(1:2)/SiO$_2$ (f), PtRe(1:5)/SiO$_2$ (g), steamed PtRe(1:5)/SiO$_2$ (h), Pt/SiO$_2$ (i), steamed Pt/SiO$_2$ (j) after after evacuation of the physisorbed pyridine at 150 °C. B, L and B+L indicate the peaks associated with Brønsted, Lewis and the combination of Brønsted and Lewis acid sites, respectively.

3.3.2 Catalytic activity measurements

3.3.2.1 Aqueous phase reforming of glycerol

Carbon-supported Pt, Re and PtRe catalysts were tested in APR of glycerol. Fig. 3.10 shows glycerol conversion by batch time. The bimetallic PtRe/C catalysts show significantly higher activity compared to Pt/C. Re/C is nearly inactive. The highest activity was observed for PtRe/C catalysts with Pt:Re ratios of 1:2 and 1:5. Their conversions were quite similar. Tables 3.4-3.7 collects the product selectivities for Pt/C, PtRe(2:1)/C, PtRe(1:2)/C and PtRe(1:5)/C. For Pt/C, the main gas-phase products are H$_2$, CO$_2$ and alkanes (CH$_4$, C$_2$H$_6$ and trace amounts of C$_3$H$_8$). The selectivity to alkanes for a Pt/Al$_2$O$_3$ catalyst in a continuous flow reactor at similar conversion was lower (Chapter 2 of this thesis). The difference could be due to the faster degradation of the reaction intermediates in a batch reactor. In line with this, it was reported that the formation of alkanes was favored at lower space velocity in a continuous flow fixed bed reactor system [67]. The main products in the liquid phase are hydroxyacetone, 1,2-propanediol (1,2-PDO), ethylene glycol, alcohols (methanol, ethanol and propanols), acetic acid and propanoic acid. Analysis of the product selectivities as a function of time shows that glycerol dehydration to hydroxyacetone is the first step in 1,2-PDO formation (Tables 3.4-3.7), which is in agreement with previous works discussing the reaction mechanism of glycerol APR on Pt catalysts [2]. Hydrogenation of hydroxyacetone results in 1,2-PDO. With the activity of Re/C being very low, its main reaction product is hydroxyacetone, the primary product of the reaction of glycerol. This suggests that the

majority of the other liquid products such as diols and alcohols as well as alkanes are produced by further reaction of the intermediates formed by glycerol dehydration.
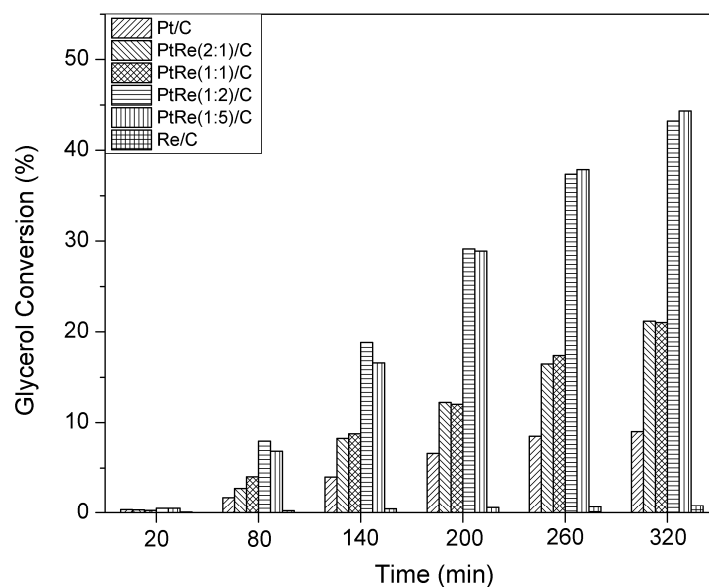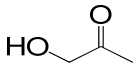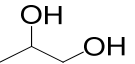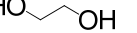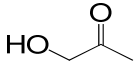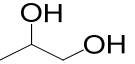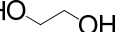

Figure 3.10: Glycerol conversion values by time for the Pt/C, Re/C and PtRe/C catalysts at 225 °C. Re/C was reduced at 500 °C, the rest of the catalysts were reduced at 300 °C. (Feed: 60 g of 10 wt% aqueous glycerol solution, catalyst amount: 75 mg).

Table 3.4: Conversion (X) of glycerol (%) and product selectivities (%) in APR of glycerol for Pt/C as a function of time at 225 °C. (Feed: 60 g of 10 wt% aqueous glycerol solution, catalyst amount: 75 mg).
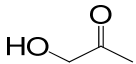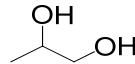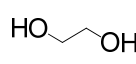
Time (min)	Xglycerol	CO_2	CH_4	C_2H_6	C_3H_8	hydroxyacetone	1,2-propanediol	ethylene glycol	alcohols[1]	acids[2]	others[3]	H_2[4]
20	0.3	7.9	0	0	0	92.1	0	0	0	0	0	0
80	1.7	33.6	3.8	2.0	0.4	42.1	14.1	3.9	0	0	0.1	35.1
140	4.0	44.8	7.1	3.4	0.5	16.4	24.6	3.0	0	0	0.2	36.4
200	6.6	46.7	8.3	4.2	0.7	14.0	23.1	1.7	1.4	0	0	32.9
260	8.5	47.2	9.2	5.4	0.8	11.1	23.1	1.8	1.4	0	0	30.6
320	9.0	47.7	9.3	6.2	0.9	8.9	23.5	1.7	1.4	0	0.4	27.3

[1]alcohols: methanol, ethanol, 1-propanol, 2-propanol
[2]acids: acetic acid, propanoic acid
[3]others: CO, propionaldehyde, 1,3-propanediol
[4]selectivity to hydrogen was calculated with the formula: (moles of H_2)/(moles of glycerol converted)/7x100.

Table 3.5: Conversion (X) of glycerol (%) and product selectivities (%) in APR of glycerol for PtRe(2:1)/C as a function of time at 225 °C. (Feed: 60 g of 10 wt% aqueous glycerol solution, catalyst amount: 75 mg).

Time (min)	Xglycerol	CO_2	CH_4	C_2H_6	C_3H_8	hydroxyacetone	1,2-propanediol	ethylene glycol	alcohols[1]	acids[2]	others[3]	H_2[4]
20	0.3	19.4	0	3.1	0	55.8	11.3	0	5.9	4.6	0	0
80	2.7	39.9	3.9	5.7	3.4	16.8	24.2	3.5	2.0	0.8	0	33.8
140	8.3	47.1	5.5	10.1	3.2	5.7	22.2	2.8	2.3	0.7	0.4	32.3
200	12.2	47.8	6.1	11.7	4.1	4.1	18.1	2.3	4.3	0.9	0.6	27.3
260	16.4	49.3	6.8	14.1	5.3	2.7	14.7	1.9	4.0	0.8	0.4	25.9
320	21.1	46.8	6.5	14.9	6.1	1.9	18.0	2.9	1.4	0.5	1.0	22.7

[1]alcohols: methanol, ethanol, 1-propanol, 2-propanol
[2]acids: acetic acid, propanoic acid
[3]others: CO, propionaldehyde, 1,3-propanediol
[4]selectivity to hydrogen was calculated with the formula: (moles of H_2)/(moles of glycerol converted)/7x100.

Table 3.6: Conversion (X) of glycerol (%) and product selectivities (%) in APR of glycerol for PtRe(1:2)/C as a function of time at 225 °C. (Feed: 60 g of 10 wt% aqueous glycerol solution, catalyst amount: 75 mg).
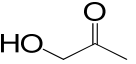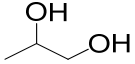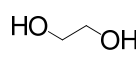
Time (min)	Xglycerol	CO_2	CH_4	C_2H_6	C_3H_8	HO–CO–CH$_3$	HO–CH(OH)–CH$_2$OH	HO–CH$_2$CH$_2$–OH	alcohols[1]	acids[2]	others[3]	H_2[4]
20	0.5	12.2	0.5	2.1	0	85.3	0	0	0	0	0	0
80	8.0	23.5	2.3	6.8	4.6	15.1	33.6	4.2	5.6	3.1	1.2	11.9
140	18.8	32.8	4.0	12.2	8.2	6.0	24.6	2.9	4.3	4.3	0.7	10.2
200	29.1	33.2	4.5	14.3	9.7	3.8	21.2	2.5	4.2	4.9	1.7	8.4
260	37.4	34.1	4.8	16.2	11.4	2.8	17.9	2.3	4.5	4.9	1.1	7.8
320	43.2	34.4	5.0	17.7	13.0	2.1	16.2	2.2	3.2	5.1	1.1	7.2

[1]alcohols: methanol, ethanol, 1-propanol, 2-propanol
[2]acids: acetic acid, propanoic acid
[3]others: CO, propionaldehyde, 1,3-propanediol
[4]selectivity to hydrogen was calculated with the formula: (moles of H_2)/(moles of glycerol converted)/7x100.

Table 3.7: Conversion (X) of glycerol (%) and product selectivities (%) in APR of glycerol for PtRe(1:5)/C as a function of time at 225 °C. (Feed: 60 g of 10 wt% aqueous glycerol solution, catalyst amount: 75 mg).

Time (min)	Xglycerol	CO_2	CH_4	C_2H_6	C_3H_8	HO–CO–CH$_3$	HO–CH(OH)–CH$_2$OH	HO–CH$_2$CH$_2$–OH	alcohols[1]	acids[2]	others[3]	H_2[4]
20	0.5	16.2	0	3.5	0	49.5	16.5	0	12.0	2.4	0	0
80	6.8	27.1	2.7	9.3	10.2	11.0	27.1	3.8	4.1	3.6	1.1	11.1
140	16.6	35.7	4.4	15.0	15.3	4.6	14.4	1.6	2.8	5.6	0.6	8.2
200	28.9	36.7	4.9	17.7	17.1	2.5	10.9	1.3	2.9	4.9	1.1	6.0
260	37.8	36.4	5.2	19.6	19.0	1.7	8.9	1.1	2.6	4.5	1.0	6.0
320	44.3	36.3	5.4	21.2	20.9	1.3	7.3	0.9	1.9	4.2	0.6	4.8

[1]alcohols: methanol, ethanol, 1-propanol, 2-propanol
[2]acids: acetic acid, propanoic acid
[3]others: CO, propionaldehyde, 1,3-propanediol
[4]selectivity to hydrogen was calculated with the formula: (moles of H_2)/(moles of glycerol converted)/7x100.

Fig. 3.11a shows the H_2/CO_2 ratios in the gas phase during glycerol APR. The H_2/CO_2 ratio for Pt/C after 80 min of reaction is 2.4, which is close to the stoichiometric ratio of 2.33 expected from the classic combination of glycerol reforming and the WGS reaction. As the reaction is carried out in a batch reactor, the H_2/CO_2 ratio decreased in time as product H_2 is used for hydrogenation of reaction intermediates. The H_2/CO_2 ratio decreases with increasing Re content. Fig. 3.11b shows the ratio of the amount of products obtained by C-O bond cleavage reactions to the amount of products obtained by C-C bond cleavage reactions based on the description of Zhang et al. [25]. With increasing Re content, the C-O/C-C bond cleavage ratio increases. The salient correlation between the decreasing trends in H_2/CO_2 ratios and the increasing trends in the C-O/C-C cleavage rates with increasing Re content is consistent with the supposition that the decrease in H_2 selectivity for PtRe/C when compared to Pt/C (Tables 3.4-3.7) is mainly due to hydrogenation of dehydrated reaction intermediates. The concentration of these intermediate compounds is accordingly expected to increase with increasing Re content. Indeed, the yield of propane increases considerably concomitant with the decrease in hydrogen selectivity. This is in agreement with our assertion that the alkanes, in particular propane, are mainly derived from the further reactions of the dehydrated reaction intermediates such as 1,2-PDO and propanols.
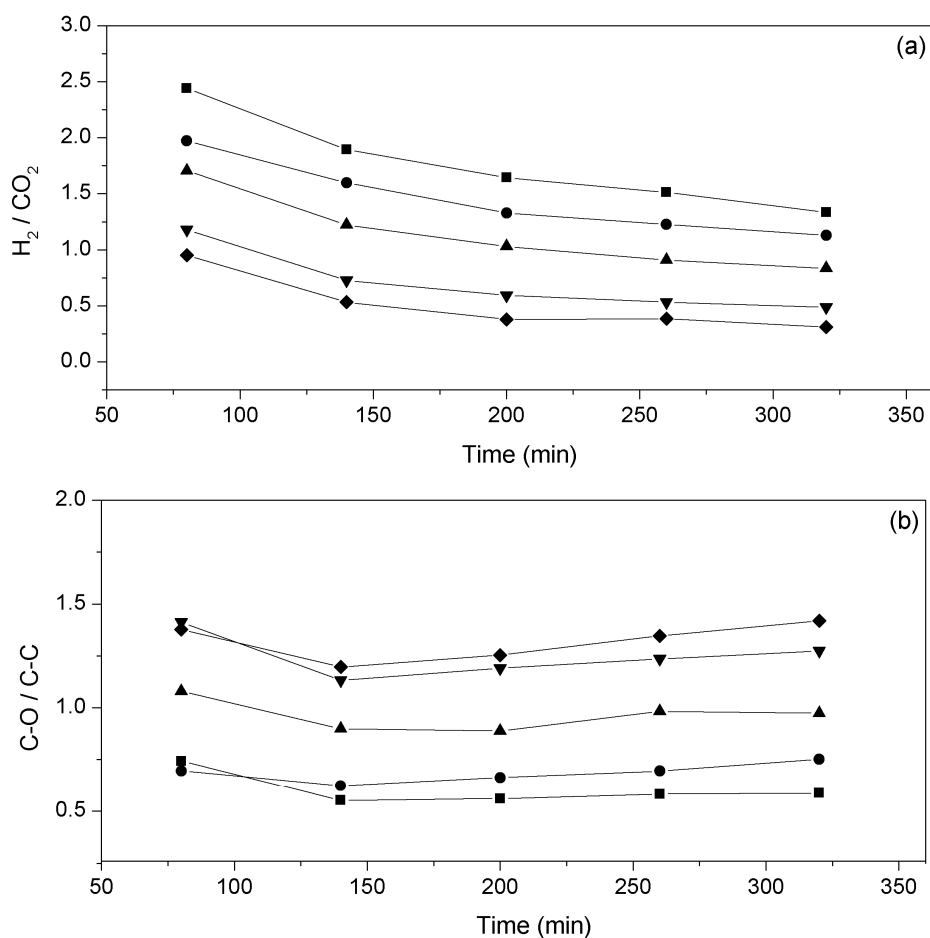

Figure 3.11: H_2/CO_2 ratios (top) and C-O/C-C ratios (bottom) obtained in APR of glycerol for Pt/C (*square*), PtRe(2:1)/C (*circle*), PtRe(1:1)/C (*up triangle*), PtRe(1:2)/C (*down triangle*) and PtRe(1:5)/C (*diamond*) at 225 °C. (Feed: 60 g of 10 wt% aqueous glycerol solution, catalyst amount: 75 mg).

To ascertain that the metal phase in the Pt and PtRe catalysts retained its metallic state during aqueous phase reforming reactions, we carried out in situ XANES in water or in a 10 wt% aqueous ethylene glycol for Pt/C, PtRe(1:1)/C and PtRe(1:2)/C. The spectra in Fig. 3.12 do not contain indications for oxidation of Pt under aqueous phase conditions. Although XANES spectra recorded at the Re L_{III}-edge for PtRe(1:1)/C and PtRe(1:2)/C during water exposure at 50 °C point to some oxidation of Re (Fig. 3.13), spectra recorded at higher temperatures in the presence of water or aqueous ethylene glycol show a decrease in the shift in the edge energies close to the value of the initially reduced catalyst. These results are in agreement with the recent work of Chia et al., who found that Re does not oxidize under aqueous phase hydrogenolysis reactions performed over RhRe/C [68].
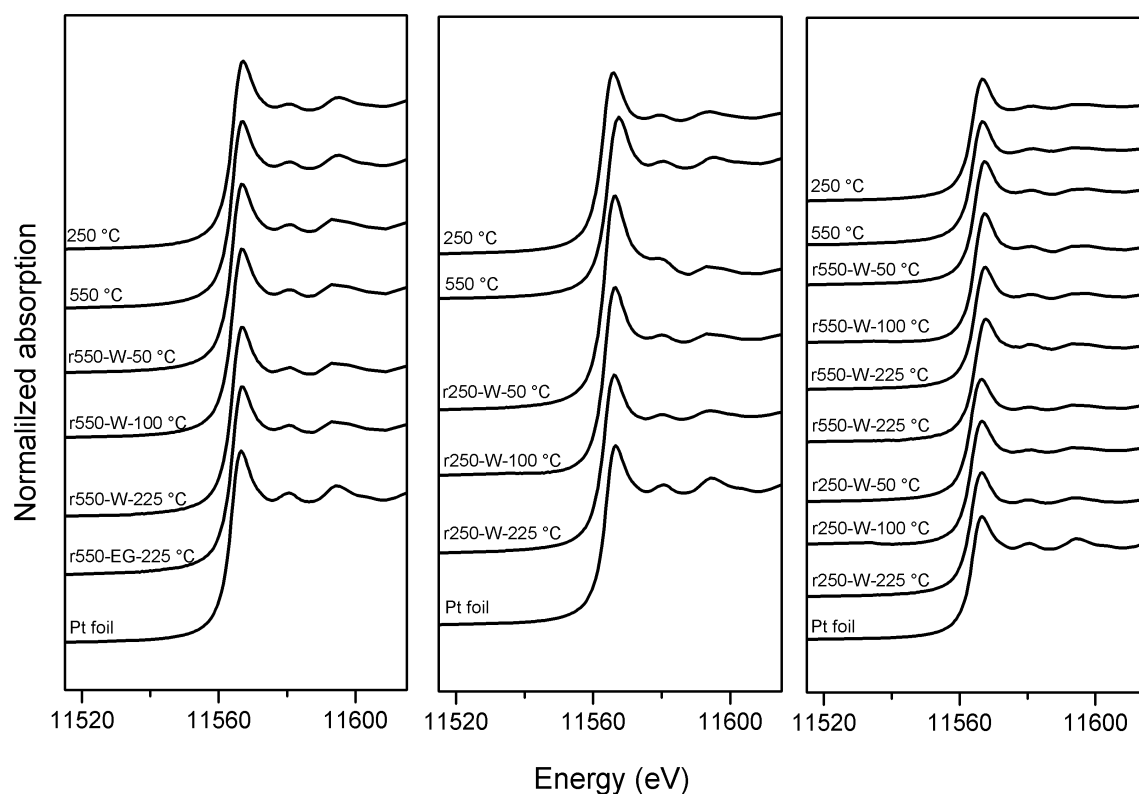

Figure 3.12: XANES spectra recorded at the Pt-L_{III} edge during water (W) or 10 wt% aqueous ethylene glycol (EG) exposure to Pt/C (left), PtRe(1:1)/C (middle), PtRe(1:2)/C (right) at 30 bar at different temperatures. The XANES spectra of reduced catalysts (250 and 550 °C) are included. r250 and r550 represent the reduction temperature of the catalysts prior to water exposure.

Figure 3.13: XANES spectra recorded at the Re-L$_{III}$ edge during water (W) or 10 wt% aqueous ethylene glycol (EG) exposure to PtRe(1:1)/C (left), PtRe(1:2)/C (right) at 30 bar at different temperatures. The XANES spectra of reduced catalysts (250 and 550 °C) are included. r250 and r550 represent the reduction te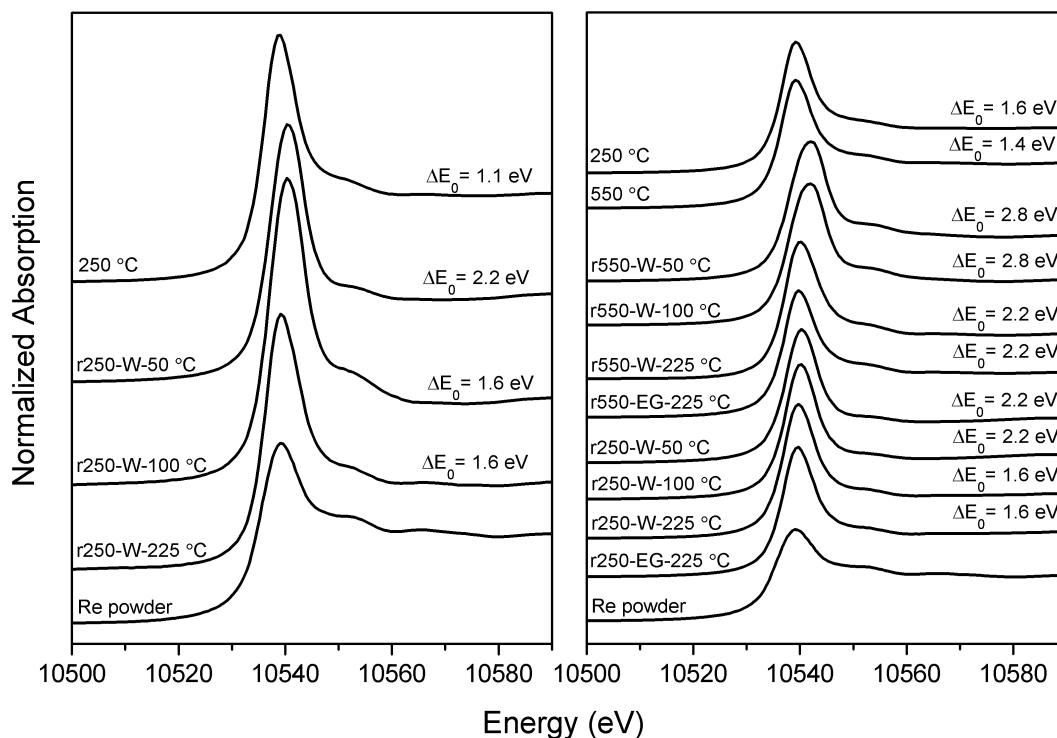mperature of the catalysts prior to water exposure. ΔE_0 is the shift in the edge energy when compared to metallic Re.

3.3.2.2 Acetaldehyde decomposition

Acetaldehyde decomposition was used to probe the decarbonylation activity of the various catalysts. The feed mixture contained hydrogen to avoid excessive carbon lay-down on the metal nanoparticles. The results are collected in Table 3.8. The main decomposition products CO and CH$_4$ were found in equimolar ratios during all experiments. No catalyst deactivation was observed during the course of the catalytic activity measurements. For Pt/C, only CO and CH$_4$ were observed as reaction products. For PtRe/C catalysts, a small amount of ethanol was formed indicative of the higher hydrogenation activity of the bimetallic catalysts. Except for PtRe(1:5)/C, the activity of the PtRe/C catalysts was nearly twice that of the Pt/C catalyst. PtRe(1:5)/C displayed almost similar activity as Pt/C. We also determined that there is no effect of steam co-feeding on the activity for PtRe(1:2)/C, even when steam is added in large excess to acetaldehyde (Fig. 3.14). Finally, we confirmed that in the absence of hydrogen PtRe(1:2)/C also converted acetaldehyde, but quickly deactivated.

Table 3.8: Acetaldehyde conversion, TOF, CO (CH$_4$) yields and selectivities for acetaldehyde decarbonylation experiments (T= 225 °C, GHSV= 7200 ml$_{acetaldehyde}$/g$_{cat}$.h; gas-phase composition H$_2$:C$_2$H$_4$O=1:1 by volume with balance He).

Catalyst	Conversion C$_2$H$_4$O (%)[1]	TOF (mol$_{C2H4O}$/mmol$_{Pt}$.h)	Yield CO (CH$_4$) (%)[1]	Selectivity CO (CH$_4$) (%)
Pt/C	20	0.6	10	50
PtRe(2:1)/C	40	1.1	18	45
PtRe(1:1)/C	45	1.2	19	42
PtRe(1:2)/C	41	1.1	17	41
PtRe(1:5)/C	20	0.6	8	42
Re/C	0	0	0	0

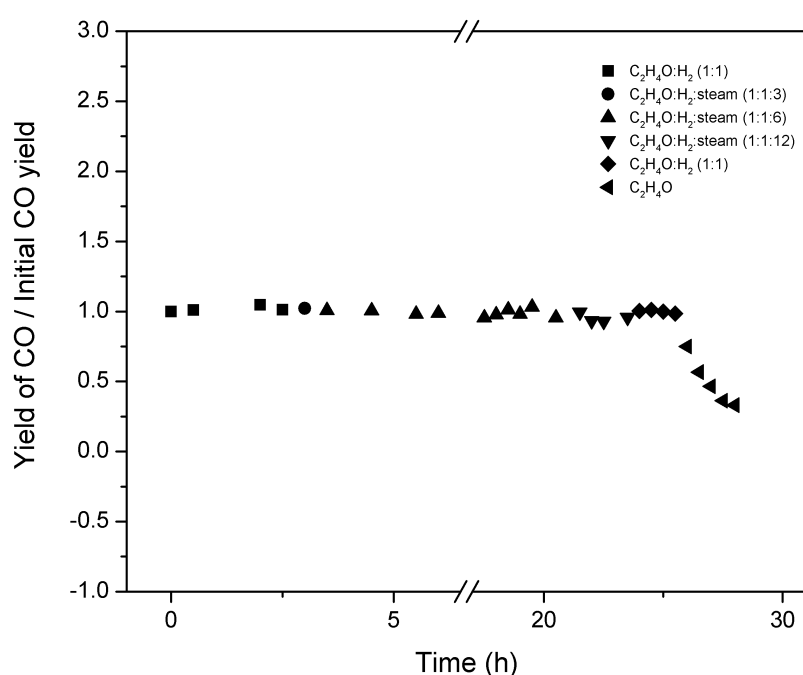[1] Average of at least 4 h time on stream

Figure 3.14: Change in the CO (CH$_4$) yield with changing feed concentrations with respect to the initial CO yield obtained at the original feed concentrations (C$_2$H$_4$O:H$_2$ =1:1, no steam addition) over the PtRe(1:2)/C catalyst at 225 °C. GHSV is kept constant at 7200 ml$_{acetaldehyde}$/g$_{cat}$.h.

3.3.2.3 Water-gas shift reaction

As the water-gas shift reaction is an important step in the APR reaction mechanism, we evaluated the performance of the carbon-supported catalysts in the WGS reaction in two separate sets of experiments. The first set was performed in the gas phase. The CO conversion as a function of temperature for all of the catalysts is shown in Fig. 3.15. The activities of the samples were determined by increasing the reaction temperature from 130 °C to 400 °C and, thereafter, decreasing the temperature to 275 °C. The activity of Pt/C is below 5 %, even at the highest temperature. The most important findings derived from these measurements are (i) Re/C is more active in the WGS reaction than Pt/C and (ii) PtRe/C catalysts are much more active than the monometallic ones. To facilitate a comparison, Fig.

3.16 compares the WGS rates at 250 °C. The WGS activity shows a maximum for a Pt:Re ratio of 1:2 in the carbon-supported bimetallic catalysts.
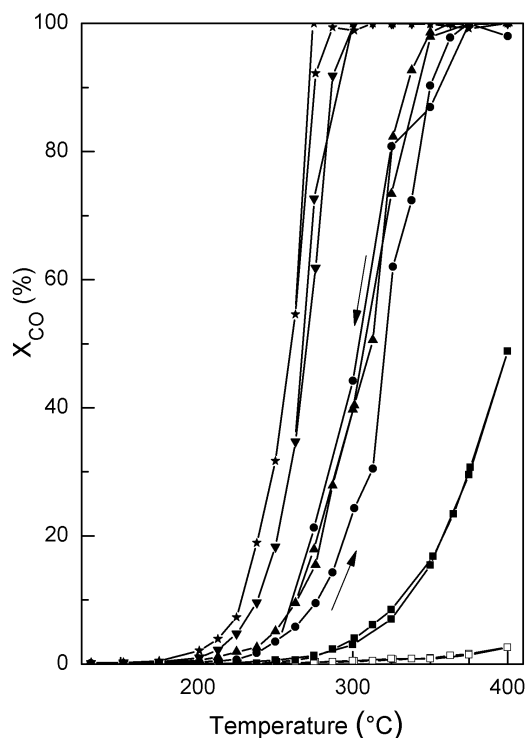

Figure 3.15: Conversion of CO in WGS over Pt/C (*open square*), PtRe(2:1)/C (*circle*), PtRe(1:1)/C (*up triangle*), PtRe(1:2)/C (*down triangle*), PtRe(1:5)/C (*star*) and Re/C (*closed square*). Re/C was reduced at 500 °C, the rest of the catalysts were reduced at 300 °C. The arrows indicate the increasing and decreasing temperatures during the experiments performed in a cycle. (2.5 vol% CO and 7.5 vol% H_2O balanced by He at a dry GHSV of ~1.1×10^5 h^{-1}).
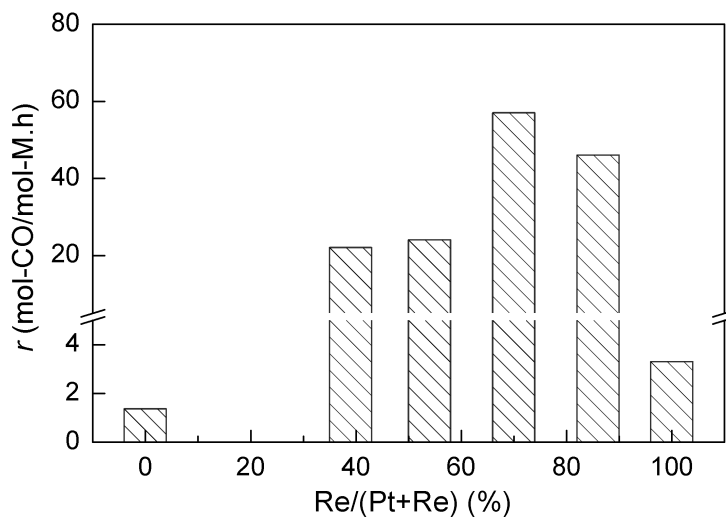

Figure 3.16: Rates of WGS reaction on carbon-supported Pt, Re and PtRe catalysts as a function of varying Re content. Re/C was reduced at 500 °C, the rest of the catalysts were reduced at 300 °C. Reactions carried out at 250 °C. (2.5 vol% CO and 7.5 vol% H_2O balanced by He at a dry GHSV of ~1.1×10^5 h^{-1}).

XANES spectra recorded during WGS at 200, 250 and 300 °C at the Pt L_{III} and Re L_{III} (Fig.s 3.17-3.18) edges did not evidence oxidation of the Pt and/or Re. Table 3.9 lists the fit parameters for the k^3-weighted EXAFS spectra at the Pt and Re L_{III} edges recorded during WGS reaction. These data show that the nanoparticles in the Pt/C and PtRe/C catalysts remain metallic. The metal coordination numbers for Pt/C and PtRe/C with the lowest Re content (PtRe(2:1)/C and PtRe(1:1)/C) remain almost the same or increase slightly. However, significant increases in the CN's of the Pt-M and Re-M shells are observed for PtRe(1:5)/C. Similarly, the CN of the Re-M shell increases from 5.2 to 8.8 for the PtRe(1:2)/C catalyst. These data suggest the growth of the initially very small bimetallic PtRe nanoparticles during the WGS reaction. However, the WGS activity of PtRe/C catalysts during cooling from 400 °C was typically similar as it was during the initial forward heating trend, so that the changes probed by XAS probably reflect changes in the ordering of the PtRe nanoparticles rather than substantial sintering effects.
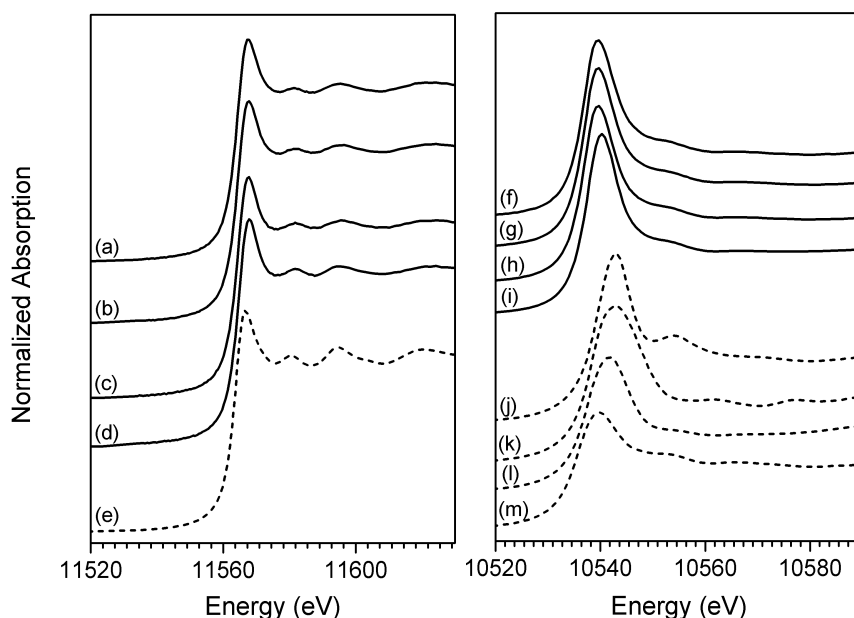

Figure 3.17: Pt L_{III} (left) and Re L_{III} edge (right) edge XANES spectra recorded at 300 °C during WGS over PtRe(2:1)/C (a,f), PtRe(1:1)/C (b,g), PtRe(1:2)/C (c,h), PtRe(1:5)/C (d,i). Reference XANES spectra for Pt foil (e), NH_4ReO_7 (j), ReO_3 (k), ReO_2 (l) and Re powder (m) are included for comparison.
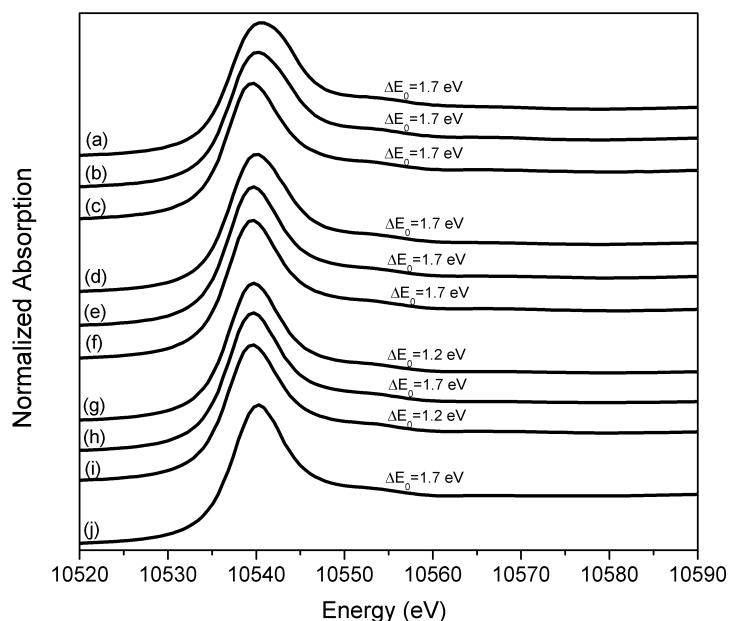
Figure 3.18: Re L_{III}-edge XANES spectra recorded during WGS over PtRe(2:1)/C at 200 °C (a), 250 °C (b) and 300 °C (c); PtRe(1:1)/C at 200 °C (d), 250 °C (e) and 300 °C (f); PtRe(1:2)/C at 200 °C (g), 250 °C (h) and 300 °C (i); PtRe(1:5)/C at 300 °C (j). ΔE_0 is the shift in the edge energy when compared to metallic Re.

Table 3.9: Fit parameters of k^3-weighted EXAFS spectra at the Pt L_{III} and Re L_{III}-edges of supported catalysts recorded during the WGS reaction at 300 °C.

Catalyst	EXAFS analysis				
	Shell	R (Å)	CN	$\Delta\sigma^2$ (Å^2)	E_0 (eV)
Pt/C	Pt-Pt	2.744	9.8	0.014	-9.5
PtRe(2:1)/C	Pt-M$_{Pt}$	2.734	7.8	0.013	-9.6
	Re-M$_{Re}$	2.675	8.3	0.010	-4.6
PtRe(1:1)/C	Pt-M$_{Pt}$	2.726	5.9	0.011	-10.1
	Re-M$_{Re}$	2.673	8.0	0.011	-5.1
PtRe(1:2)/C	Pt-M$_{Pt}$	2.707	5.8	0.012	-8.9
	Re-M$_{Re}$	2.678	8.8	0.012	-5.7
PtRe(1:5)/C	Pt-M$_{Pt}$	2.731	6.5	0.011	-9.4
	Re-M$_{Re}$	2.658	10.1	0.012	-0.7

In order to have a link between the gas-phase WGS measurements and the aqueous-phase reforming experiments in which WGS may play a key role, we also carried out CO stripping voltammetry of carbon-supported Pt and PtRe. The corresponding cyclic voltammograms (CV) of CO stripping measurements are shown in Fig. 3.19a. For these measurements, we used Vulcan XC72 carbon as the support because of its better electric conductivity than activated carbon. The trend in catalytic performance for glycerol APR of these catalysts is very similar to that of the activated carbon-supported catalysts (Fig. 3.20). The higher conversions obtained for the Vulcan supported catalysts is due to their higher metal loading. The CV of Pt/C-V shows a CO oxidation peak centered around 0.4 V. The

formation of CO_2 by mass spectrometry is observed at a slightly higher voltage of 0.45 V. This small delay is typically observed in OLEMS measurements and caused by the transport of gases through the mass spectrometric detection system [52,69]. The onset of CO oxidation is at about 0.23 V for Pt/C-V and 0.13 V for PtRe/C-V. The mass spectrometry data confirm that the evolution of CO_2 starts ~0.1 V earlier for PtRe catalysts than for Pt/C-V (Fig. 3.19b). As the intensities of the mass spectrometer signal depend on many factors, such as the tip-electrode distance, the porosity of the Teflon plug, the quality of the vacuum inside the system [52], which will vary from one experiment to another, the present results will be treated in a qualitative manner only. The widely accepted mechanism for CO electro-oxidation involves the reaction of adsorbed CO with OH species formed on the Pt surface by dissociation of H_2O [70-73]. The strong adsorption of CO on the Pt surface significantly decreases the activity of the electrode. Pt-based alloys such as Pt-Ru and Pt-Sn have been found to show enhanced activity in electro-oxidation of CO. In the Pt-Ru alloy electrodes, Ru provides nucleation sites for oxygen-containing species at low potentials and oxidation takes place by migration of CO to these sites [70]. The increased activity of Pt-Sn electrodes was related to the reduced state of Sn atoms, which influences the surface properties of the Pt atoms so that oxygen is adsorbed more strongly [74]. The lower onset potential of CO oxidation in the case of our PtRe catalysts suggests an increased abundance of OH species when compared to the monometallic Pt, effectively increasing the rate of CO oxidation. Summarizing, alloying Pt with Re increases its activity in WGS as well as in electro-oxidation of CO.
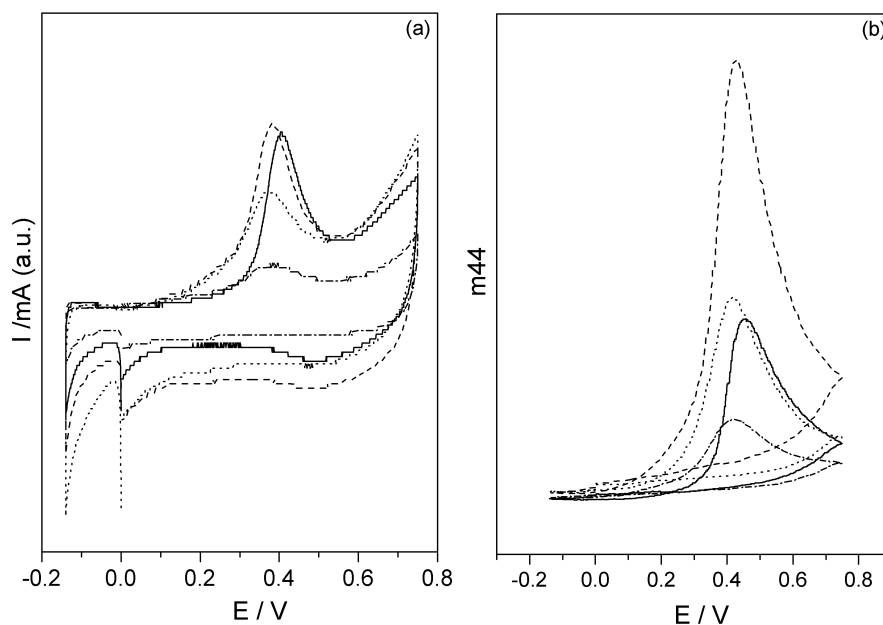

Figure 3.19: Cyclic voltammograms (CV) (a) and mass spectrometry cyclic voltammograms (MSCV) for mass signal of 44 (b) for Pt/C-V (—), PtRe(1:1)/C-V (- - -) , PtRe(1:2)/C-V (·······), PtRe(1:5)/C-V (-··-) catalysts in CO stripping.
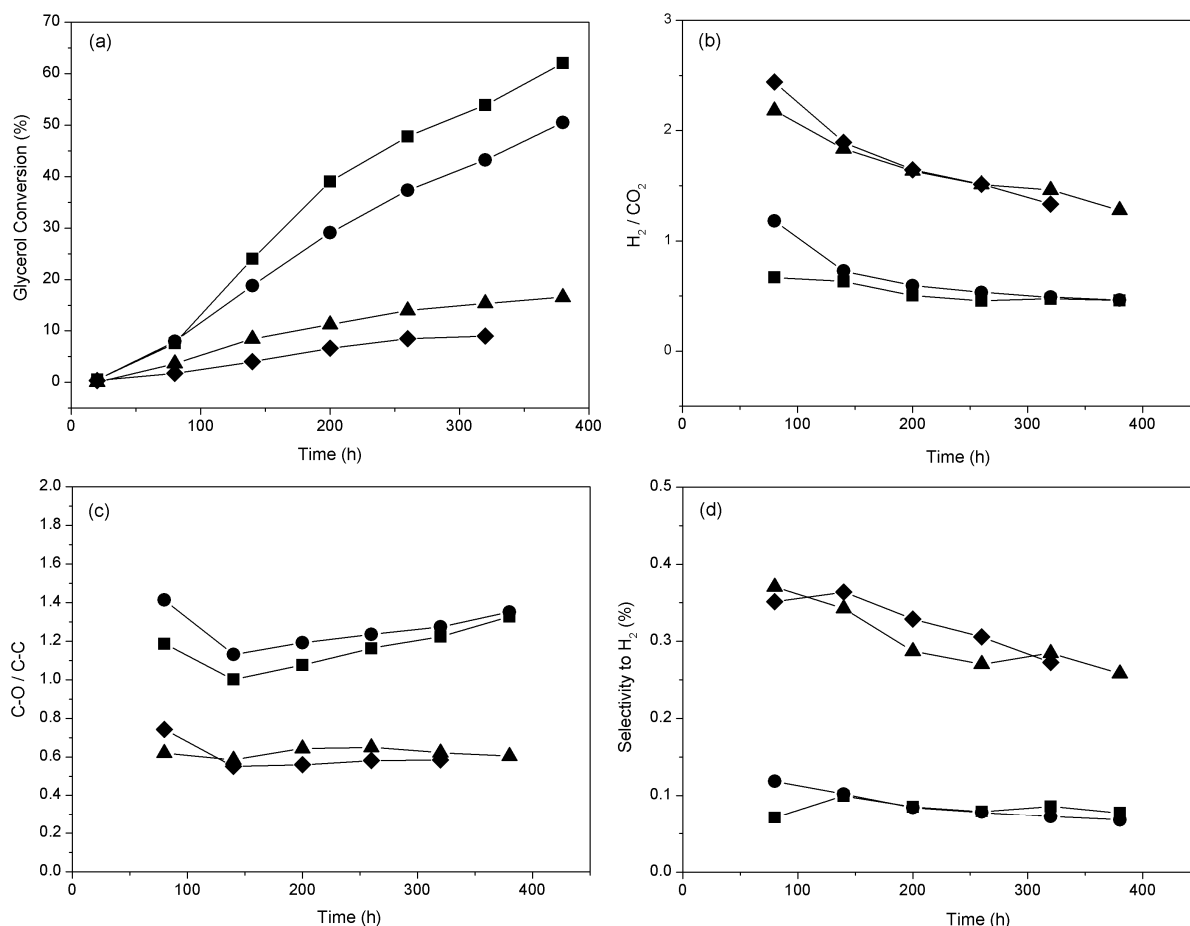
Figure 3.20: Comparison of overall glycerol conversion (a), H_2/CO_2 ratio (b), C-O/C-C ratio (c) and H_2 selectivity (d) values obtained in APR of glycerol over Pt/C-V (*up triangle*), PtRe(1:2)/C-V (*square*), Pt/C (*diamond*) and PtRe(1:2)/C (*circle*) catalysts at 225 °C. (Feed: 60 g of 10 wt% aqueous glycerol solution, catalyst amount: 75 mg).

3.4 Discussion

In the present work, we aimed to provide further insights into the influence of Re on Pt for the APR of glycerol and model reactions relevant to glycerol conversion. The glycerol conversion rates of the bimetallic PtRe catalysts are substantially higher than of their monometallic counterparts. The catalytic activity of Re/C is negligible. The maximum activity is obtained for catalysts with nominal Pt:Re ratios of 1:2 and 1:5. The synergetic effect between Pt and Re in the aqueous phase reforming activity of polyols has been reported before [12,14,25,26].

The characterization data clearly show that Pt aids in the reduction of the oxidic Re precursor [27,36,75]. This is well known for bimetallic PtRe catalysts, which are extensively employed for the reforming of naphtha feedstock and, accordingly, have been the subject of many detailed investigations [57,58,76,77]. Whereas Re itself needs to be reduced at temperatures in excess of 500 °C, in its alloy with Pt reduction of Re is already finished at around 200 °C as follows from TPR and XANES measurements. Although direct evidence for alloy formation is lacking, there are very clear indications in the XANES data for electronic interactions between Pt and Re. Part of these changes may be due to the effect of

particle size. Indeed, alloying Re with Pt results in smaller bimetallic nanoparticles as follows from EXAFS as well as TEM analysis. We observe that increasing Re content results in higher dispersion of PtRe nanoparticles for our carbon support, whereas Dumesic's group found an increase of the particle size upon alloying Pt with Re [26]. As pointed out before [78,79], the metal precursor-support interactions are notably affected by surface modification of carbon by oxidation treatments. The activated carbon support used in this study has been repeatedly treated with HNO_3, so that the high dispersions in our work are most likely due to the presence of a large number of functional groups acting as anchoring sites for metal precursors.

The synergy between Pt and Re not only enhances the overall conversion rate of glycerol during APR but also leads to significant changes in the product selectivities. The APR reaction mechanism involves two main types of reactions that convert the feedstock (Scheme 3.1). The first one involves dehydrogenation of alcohol functionalities to the corresponding aldehyde followed by decarbonylation (C-C bond cleavage). In case of glycerol, glyceraldehyde is converted to CO and ethylene glycol. The CO product is converted to CO_2 in the WGS reaction, whose equilibrium under APR conditions allows for its nearly complete conversion to CO_2. The second pathway involves cleavage of C-O bonds by dehydration. These reaction intermediates are hydrogenated by the in situ produced hydrogen from the first reaction pathway. The main product from glycerol via this route is 1,2-propanediol. The other products of its further conversion are propanols and propane. Combining these two pathways leads to a mixture of monofunctional alcohols, alkanes and CO_2.
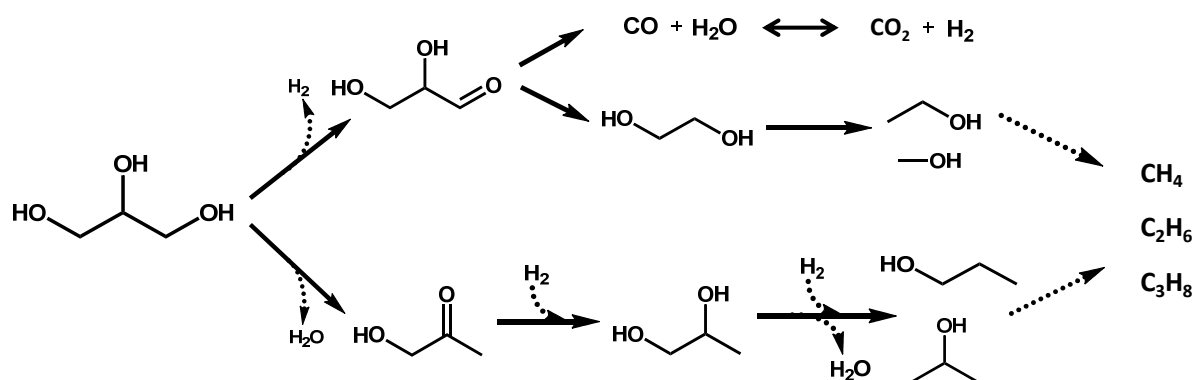
Scheme 3.1: The proposed reaction scheme for APR of glycerol.

Fig. 3.11 clearly shows that addition of Re to Pt and also increasing the Re content results in increasing rates of C-O over C-C bond cleavage reactions and, at the same time, a decreasing H_2/CO_2 ratio in the product mixture. For the C-O over C-C bond cleavage ratio, we follow the method outlined by Zhang et al. [25], who showed that this ratio was higher for a PtRe/C with a Pt:Re ratio of unity than for Pt/C. The present data show that the ratio of the rates of dehydration over decarbonylation steps gradually increases with Re content. The decrease in the H_2/CO_2 ratio with Re content is consistent with this, as H_2 is consumed in the hydrogenation of the double bonds formed during dehydration.

In order to study the effect of Re on the decarbonylation activity, we evaluated the mono- and bimetallic catalysts in the decomposition of acetaldehyde to CH_4 and CO in separate gas-phase experiments. Except for PtRe(1:5)/C, these measurements evidence much higher decarbonylation activity of the bimetallic catalysts. However, the decarbonylation activity of the other PtRe catalysts does not depend on the Pt:Re ratio. Well-reduced Re/C is not active in this reaction. The low hydrogenation activity of Re, which causes too slow removal of the CH_x surface intermediates and extensive carbon lay-down, is related to the strong Re-carbon bond (Re-C and Pt-C bond energies were calculated as 713 and 657 kJ/mol, respectively [80]). Tentatively, we attribute the lower activity of PtRe(1:5)/C also to a predominance of Re sites on the surface of the bimetallic nanoparticles, possibly partially deactivating the catalytic surface. This is consistent with the lower yield of ethanol observed for the catalysts with the lowest Pt:Re ratio. The finding that the decarbonylation activity of the other PtRe catalysts does not depend on the Pt:Re ratio and also that the two most active catalysts in glycerol APR, PtRe(1:2)/C and PtRe(1:5)/C, exhibit very different activity in decarbonylation provides strong indications that differences in decarbonylation activity are not at the origin of the synergetic effect between Pt and Re in the the APR of glycerol. The addition of steam to the acetaldehyde/H_2 feed mixture did not affect noticeably the CO yield (Fig. 3.14). This result shows that adsorbed oxygen or hydroxyl species do not affect the C-C bond cleavage rate of PtRe alloys. This is to be contrasted to the well-known effect of sulfur species on PtRe catalysts exploited in commercial naphtha reforming: only by addition of H_2S does the undesired C-C bond cleavage activity of PtRe catalysts become depressed [81]. The strong adsorption of sulfur on Re centers effectively breaks up larger PtRe ensembles active in C-C bond cleavage reactions.

To further investigate the relation with reforming, we evaluated the catalytic performance of a set of silica-supported Pt and PtRe catalysts for steam reforming of ethanol (Table 3.10, Fig.s 3.21-3.22). Tomishige and co-workers found that V-, Nb- and Mo-oxide modified Pt catalysts showed higher activity in ethanol steam reforming than the unpromoted Pt catalyst [82]. Silica was employed as the support because of the suspected instability of the carbon support during reforming at higher temperatures. At the lowest temperature of 200 °C, the PtRe catalysts are much more active than Pt/SiO_2. The activity increases with Re content. The product selectivities between the various catalysts are not very different. The main product at these temperatures is the dehydrogenation product acetaldehyde. Therefore, the reason for the much higher activity of PtRe as compared to Pt should be its increased activity in hydrogenation/dehydrogenation. Apparently, the rate of decarbonylation of acetaldehyde is very small. At 300 °C, the product selectivities evidence that the rate of acetaldehyde decarbonylation is significant. Importantly, it is seen that the yield of CH_4 displays a maximum for PtRe(1:2)/SiO_2. The decarbonylation activities of these silica-supported Pt and PtRe catalysts closely tracks the trend observed for their carbon-supported counterparts. Summarizing, there is strong synergy between Pt and Re for the dehydrogenation of ethanol and decarbonylation of acetaldehyde. The optimum ratio appears to occur for a Pt:Re ratio of

1:2, the poor performance at higher Re content being due to the predominance of Re on the surface of the bimetallic nanoparticles.

Table 3.10: Catalytic activity (ethanol conversion and selectivity to CO, CH$_4$, CO$_2$, C$_2$H$_4$O) obtained over Pt/SiO$_2$, PtRe(1:1)/SiO$_2$, PtRe(1:2)/SiO$_2$, PtRe(1:5)/SiO$_2$ in steam reforming of ethanol at 200 and 300 °C (GHSV= 8400 ml$_{EtOH}$/g$_{cat}$.h, EtOH:steam = 1:6).

Catalyst	T (°C)	X$_{EtOH}$ (%)	S$_{CO}$ (%)	S$_{CH4}$ (%)	S$_{CO2}$ (%)	S$_{C2H4O}$ (%)
Pt/SiO$_2$	200	1.0	5.7	19	-	76
	300	14	26	44	15	15
PtRe(1:1)/SiO$_2$	200	13	13	13	0.7	74
	300	42	34	36	3.3	27
PtRe(1:2)/SiO$_2$	200	29	11	13	0.6	76
	300	51	29	33	1.5	37
PtRe(1:5)/SiO$_2$	200	41	12	13	0.4	76
	300	37	18	20	0.5	61
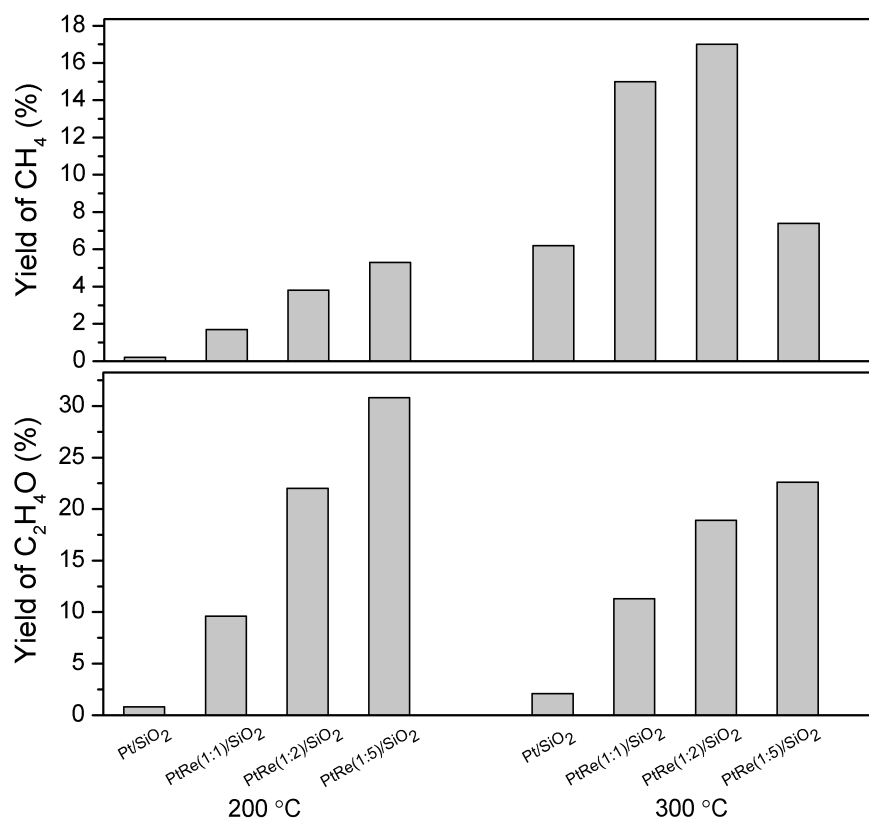
Figure 3.21: Yield of CH$_4$ and C$_2$H$_4$O obtained over Pt/SiO$_2$, PtRe(1:1)/SiO$_2$, PtRe(1:2)/SiO$_2$ and PtRe(1:5)/SiO$_2$ in steam reforming of ethanol at 200 and 300 °C (GHSV= 8400 ml$_{EtOH}$/g$_{cat}$.h, EtOH:steam = 1:6).
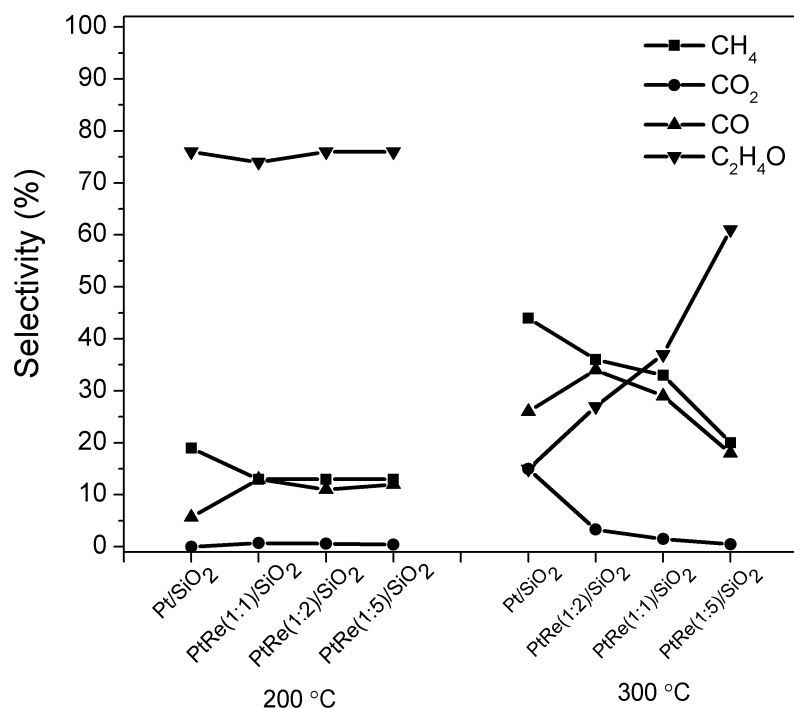
Figure 3.22: Selectivity to CO, CO_2, CH_4 and C_2H_4O obtained in steam reforming of ethanol over Pt/SiO$_2$, PtRe(1:1)/SiO$_2$, PtRe(1:2)/SiO$_2$ and PtRe(1:5)/SiO$_2$ at 200 and 300 °C (GHSV= 8400 ml$_{EtOH}$/g$_{cat}$.h, EtOH:steam = 1:6).

From the finding that PtRe catalysts display higher C-O *vs.* C-C bond cleavage activity compared to Pt and the observation that C-C bond cleavage rates are also higher for PtRe, it follows that there must also be a strong synergy between Pt and Re for C-O bond cleavage via dehydration during the APR of glycerol. It has indeed earlier been established that dehydration of alcohol functionalities is catalyzed by transient Re-OH species in the PtRe and RhRe nanoparticles [25,33,68]. Chia et al. evidenced that the acidity of RhRe for hydrogenolysis of C-O bonds originates from the activation of water molecules over Re atoms on the surface of Rh-Re particles [68]. Similary, Zhang et al. showed that in APR of glycerol Re-OH acts as Brønsted acid sites, while neighbouring Pt could provide Lewis acid sites [25]. Consistent with these earlier studies, we find that steaming of well-reduced PtRe/C and Re/C catalysts produces such acidic sites, which can be tracked by NH$_3$-TPD. The NH$_3$-TPD of Pt/C only shows the presence of metallic sites, which chemisorb NH$_3$ more weakly than on protons. Here, we also followed acidity generation due to water exposure by means of IR spectroscopy of adsorbed pyridine. This required the use of the set of silica-supported catalysts. These IR data provide further evidence for the generation of strong Brønsted acid sites on the surface of the Re sites as a result of steaming the reduced catalysts at 225 °C. The number of acid sites strongly increases with the Re content and is almost similar for PtRe(1:2)/SiO$_2$ and PtRe(1:5)/SiO$_2$. This trends well with the ratio of C-O/C-C bond cleavage products obtained for the carbon-supported counterparts containing the same Pt and Re contents. The lowest C-C cleavage activity of PtRe(1:5)/C leads to an increase in the ratio of C-O/C-C bond cleavage products in APR. Although the C-C bond cleavage activity of

PtRe(1:2)/C is almost twice of that obtained over PtRe(1:5)/C, the ratio of C-O/C-C bond cleavage products obtained over PtRe(1:2)/C in APR is only slightly lower than that obtained over PtRe(1:5)/C. This implies that PtRe(1:2)/C has the highest C-O bond cleavage activity and thus the highest density of acid sites, which is in line with results from IR spectroscopy of adsorbed pyridine. The use of physical mixtures of metal and acid catalysts has been explored amongst others by Chia et al., who found that the hydrogenolysis of cyclic ethers to the corresponding alcohols over monometallic Rh/C in the presence of H_2SO_4 or HCl proceeds at rates and selectivities that are significantly lower than those over carbon-supported RhRe. It is important to note that these authors concluded from DFT calculations that the synergy in RhRe/C and PtRe/C catalysts is similar [33].

Another important reaction involved during glycerol APR is the WGS reaction. Although it is not directly involved in the conversion of glycerol, it has been argued that strong adsorption of product CO lowers the reactivity of Pt [26,36]. Thus, a high WGS activity will decrease the steady-state CO coverage and improve the catalytic performance towards conversion of glycerol and reaction intermediates. The WGS rates expressed per mol of Pt increase with Re content. For example PtRe(2:1)/C is 6 times more active than Pt/C at 225 °C; the corresponding increase for PtRe(1:5)/C is nearly 60-fold. The promotional effect of Re addition to Pt/C follows the trend in APR of glycerol. The rate of APR over the PtRe catalysts with lower Re contents (PtRe(2:1)/C and PtRe(1:1)/C) is more than two times higher (270 $mmol_{glycerol}/mmol_{Pt}.h$) than that of Pt/C (117 $mmol_{glycerol}/mmol_{Pt}.h$). PtRe(1:2)/C and PtRe(1:5)/C catalysts are about five times (546 and 616 $mmol_{glycerol}/mmol_{Pt}.h$) more active than the monometallic Pt catalyst. The gas-phase WGS activity results are consistent with results from CO stripping voltammetry. The electro-current onset for CO removal from carbon-supported Pt nanoparticles is substantially lowered upon alloying with Re. The potential at which CO oxidation occurs suggests that OH species are involved in the CO oxidation reaction leading to a COOH surface intermediate. The importance of this intermediate in CO conversion to CO_2 is consistent with results of an earlier computational study on the WGS reaction on Pt(111) [83]. Accordingly, we conclude that increased performance of Pt/C in glycerol APR upon alloying with Re stems from enhanced WGS activity, which removes strongly adsorbed CO from the Pt surface.

Finally, it is worthwhile to briefly discuss the origin of the increased WGS activity of PtRe alloys compared to Pt. As pointed out by the Mavrikakis group WGS on Pt(111) proceeds via a COOH surface intermediate and is limited by water activation [83]. Water dissociation to OH and O intermediates is endothermic on Pt surfaces, resulting in their low surface coverages. The use of more reactive metals such as Rh increases the rate of water dissociation and O and OH surface coverage, resulting in increased reforming activity [84]. Preliminary DFT calculations show that OH* (adsorbed OH) formation reaction ($H_2O \rightarrow$ OH* + ½ H_2) is endothermic at +3 kJ/mol for Pt(111) and much more favorable at -61 kJ/mol for Re(0001) [85]. Accordingly, we predict higher steady-state OH surface coverage. A very important role of Pt in PtRe bimetallic catalysts is to facilitate the reduction of Re. During reforming, the higher hydrogenation activity of PtRe alloys compared to Re will prevent

excessive carbon lay-down consistent with the higher acetaldehyde hydrogenation activity of PtRe compared to Re. The higher hydrogenation activity is related to the lower binding energy of carbon on Pt. The presence of Pt in the alloyed surface will provide sites with lower metal-oxygen and metal-carbon bond energies, allowing for adsorption of reactants, *i.e.* CO for WGS and glycerol for dehydrogenation and decarboxylation, next to Re sites which will be covered by oxygen-containing species.

3.5 Conclusions

Alloying carbon-supported Pt with Re increases the overall conversion in glycerol APR. The higher the Re content, the higher the APR activity is. The ratio of products obtained via dehydration (C-O cleavage) reactions to those obtained via decarbonylation (C-C cleavage) reactions increases with increasing Re content. The effect of alloying is investigated in more detail using model reactions and surface characterization. All Pt and bimetallic catalysts are well reduced during pretreatment and remain so during gas and aqueous phase reactions as evidenced by XAS measurements. As follows from acetaldehyde decomposition activity measurements, PtRe catalysts are substantially more active in C-C bond cleavage than Pt. The activity does not depend on the Pt/Re ratio. The higher C-O bond cleavage rates correlate to the presence of acidic sites generated in the steam treated PtRe alloys as follows from NH_3-TPD and pyridine IR measurements. The high overall conversion rate of PtRe catalysts compared to Pt mainly relates to the higher rate of CO removal from the surface, which is due to the much increased WGS activity of the alloys. The strong synergy observed during gas-phase WGS measurements is also evident during CO stripping voltammetry measurements showing a lower onset of CO electro-oxidation for PtRe compared to Pt.

References

[1]   D.M. Alonso, J.Q. Bond, J.A. Dumesic, Green Chem. 12 (2010) 1493-1513.
[2]   A. Wawrzetz, B. Peng, A. Hrabar, A. Jentys, A.A. Lemonidou, J.A. Lercher, J. Catal. 269 (2010) 411-420.
[3]   G. Centi and R.A.van Santen, Catalysis for Renewables: From Feedstock to Energy Production, Wiley-VCH, Weinheim, 2007.
[4]   A. Corma, S. Iborra, A. Velty, Chem. Rev. 107 (2007) 2411-2502.
[5]   C. Zhao, J.Y. He, A.A. Lemonidou, X.B. Li, J.A. Lercher, J. Catal. 280 (2011) 8-16.
[6]   S. Dutta, S. De, M.I. Alam, M.M. Abu-Omar, B. Saha, J. Catal. 288 (2012) 8-15.
[7]   R. Weingarten, G.A. Tompsett, W.C. Conner, G.W. Huber, J. Catal. 279 (2011) 174-182.
[8]   N. Li, G.W. Huber, J. Catal. 270 (2010) 48-59.
[9]   R.R. Davda, J.W. Shabaker, G.W. Huber, R.D. Cortright, J.A. Dumesic, Appl. Catal. B 56 (2005) 171-186.
[10] S. Adhikari, S.D. Fernando, A. Haryanto, Energ. Convers. Manage. 50 (2009) 2600-2604.
[11] P.J. Dietrich, R.J. Lobo-Lapidus, T.P. Wu, A. Sumer, M.C. Akatay, B.R. Fingland, N. Guo, J.A. Dumesic, C.L. Marshall, E. Stach, J. Jellinek, W.N. Delgass, F.H. Ribeiro, J.T. Miller, Top. Catal. 55 (2012) 53-69.
[12] D.L. King, L.A. Zhang, G. Xia, A.M. Karim, D.J. Heldebrant, X.Q. Wang, T. Peterson, Y. Wang, Appl. Catal. B 99 (2010) 206-213.
[13] R.L. Manfro, A.F. da Costa, N.F.P. Ribeiro, M.M.V.M. Souza, Fuel Process. Technol. 92 (2011) 330-335.
[14] D.M. Alonso, S.G. Wettstein, J.A. Dumesic, Chem. Soc. Rev. 41 (2012).
[15] A. Martin, U. Armbruster, I. Gandarias, P.L. Arias, Eur. J. Lipid Sci. Tech. 115 (2013) 9-27.

[16] E. Santacesaria, G.M. Vicente, M. Di Serio, R. Tesser, Catal. Today 195 (2012) 2-13.
[17] C.H.C. Zhou, J.N. Beltramini, Y.X. Fan, G.Q.M. Lu, Chem. Soc. Rev. 37 (2008) 527-549.
[18] A. Behr, J. Eilting, K. Irawadi, J. Leschinski, F. Lindner, Green Chem. 10 (2008) 13-30.
[19] J.J. Bozell, G.R. Petersen, Green Chem. 12 (2010) 539-554.
[20] Y.L. Gu, F. Jerome, Green Chem. 12 (2010) 1127-1138.
[21] P.R. de la Piscina, N. Homs, Chem. Soc. Rev. 37 (2008) 2459-2467.
[22] G.W. Huber, S. Iborra, A. Corma, Chem. Rev. 106 (2006) 4044-4098.
[23] R.R. Davda, J.W. Shabaker, G.W. Huber, R.D. Cortright, J.A. Dumesic, Appl. Catal. B 43 (2003) 13-26.
[24] J.W. Shabaker, G.W. Huber, R.R. Davda, R.D. Cortright, J.A. Dumesic, Catal. Lett. 88 (2003) 1-8.
[25] L. Zhang, A.M. Karim, M.H. Engelhard, Z.H. Wei, D.L. King, Y. Wang, J. Catal. 287 (2012) 37-43.
[26] E.L. Kunkes, D.A. Simonetti, J.A. Dumesic, W.D. Pyrz, L.E. Murillo, J.G.G. Chen, D.J. Buttrey, J. Catal. 260 (2008) 164-177.
[27] O.M. Daniel, A. DeLaRiva, E.L. Kunkes, A.K. Datye, J.A. Dumesic, R.J. Davis, ChemCatChem 2 (2010) 1107-1114.
[28] L. Ma, D.H. He, Z.P. Li, Catal. Comm. 9 (2008) 2489-2495.
[29] A. Shimao, S. Koso, N. Ueda, Y. Shinmi, I. Furikado, K. Tomishige, Chem. Lett. 38 (2009) 540-541.
[30] Y. Shinmi, S. Koso, T. Kubota, Y. Nakagawa, K. Tomishige, Appl. Catal. B 94 (2010) 318-326.
[31] Y. Nakagawa, Y. Shinmi, S. Koso, K. Tomishige, J. Catal. 272 (2010) 191-194.
[32] Y. Nakagawa, K. Tomishige, Catal. Surv. Asia 15 (2011) 111-116.
[33] M. Chia, Y.J. Pagan-Torres, D. Hibbitts, Q.H. Tan, H.N. Pham, A.K. Datye, M. Neurock, R.J. Davis, J.A. Dumesic, J. Am. Chem. Soc. 133 (2011) 12675-12689.
[34] K.Y. Chen, S. Koso, T. Kubota, Y. Nakagawa, K. Tomishige, ChemCatChem 2 (2010) 547-555.
[35] S. Koso, N. Ueda, Y. Shinmi, K. Okumura, T. Kizuka, K. Tomishige, J. Catal. 267 (2009) 89-92.
[36] D.A. Simonetti, E.L. Kunkes, J.A. Dumesic, J. Catal. 247 (2007) 298-306.
[37] K.G. Azzam, I.V. Babich, K. Seshan, L. Lefferts, J. Catal. 251 (2007) 163-171.
[38] K.G. Azzam, I.V. Babich, K. Seshan, L. Lefferts, Appl. Catal. B 80 (2008) 129-140.
[39] H. Iida, A. Igarashi, Appl. Catal. A 303 (2006) 192-198.
[40] H. Iida, A. Igarashi, Appl. Catal. A 303 (2006) 48-55.
[41] H. Iida, K. Yonezawa, M. Kosaka, A. Igarashi, Catal. Comm. 10 (2009) 627-630.
[42] Y. Sato, K. Terada, S. Hasegawa, T. Miyao, S. Naito, Appl. Catal. A 296 (2005) 80-89.
[43] Y. Sato, K. Terada, Y. Soma, T. Miyao, S. Naito, Catal. Comm. 7 (2006) 91-95.
[44] X.L. Zhu, T. Hoang, L.L. Lobban, R.G. Mallinson, Appl. Catal. B 94 (2010) 311-317.
[45] W. Ruettinger, X.S. Liu, X.M. Xu, R.J. Farrauto, Top. Catal. 51 (2008) 60-67.
[46] S.Y. Choung, M. Ferrandon, T. Krause, Catal. Today 99 (2005) 257-262.
[47] R. Radhakrishnan, R.R. Willigan, Z. Dardas, T.H. Vanderspurt, Appl. Catal. B 66 (2006) 23-28.
[48] Y. Guo, M.U. Azmat, X.H. Liu, Y.Q. Wang, G.Z. Lu, Appl. Energ. 92 (2012) 218-223.
[49] L. Ma, Y.M. Li, D.H. He, Chinese J. Catal. 32 (2011) 872-876.
[50] R.J. Gorte, S. Zhao, Catal. Today 104 (2005) 18-24.
[51] D.C. Grenoble, M.M. Estadt, D.F. Ollis, J. Catal. 67 (1981) 90-102.
[52] A.H. Wonders, T.H.M. Housmans, V. Rosca, M.T.M. Koper, J. Appl. Electrochem. 36 (2006) 1215-1221.
[53] D.A.J.M. Ligthart, R.A. van Santen, E.J.M. Hensen, Angew. Chem. Int. Edit. 50 (2011) 5306-5310.
[54] T. Ebashi, Y. Ishida, Y. Nakagawa, S. Ito, T. Kubota, K. Tomishige, J. Phys. Chem. C 114 (2010) 6518-6526.
[55] F. Hilbrig, C. Michel, G.L. Haller, J. Phys. Chem. 96 (1992) 9893-9899.
[56] J. Sa, C. Kartusch, M. Makosch, C. Paun, J.A. van Bokhoven, E. Kleymenov, J. Szlachetko, M. Nachtegaal, H.G. Manyar, C. Hardacre, Chem. Commun. 47 (2011) 6590-6592.
[57] J.L. Xiao, R.J. Puddephatt, Coord. Chem. Rev. 143 (1995) 457-500.
[58] H. Dexpert, P. Lagarde, J.P. Bournonville, J. Mol. Catal. 25 (1984) 347-355.
[59] C. Fierro, J. Phys. Chem. 92 (1988) 4401-4405.
[60] R.C. Baetzold, G. Apai, E. Shustorovich, Appl. Surf. Sci. 19 (1984) 135-144.
[61] G. Apai, R.C. Baetzold, P.J. Jupiter, A.J. Viescas, I. Lindau, Surf. Sci. 134 (1983) 122-134.
[62] P. Berteau, B. Delmon, Catal. Today 5 (1989) 121-137.
[63] S. Narayanan, A. Sultana, Q. Thinh Le, A. Auroux, Appl. Catal. A 168 (1998) 373-384.
[64] O.M. Busch, W. Brijoux, S. Thomson, F. Schuth, J. Catal. 222 (2004) 174-179.
[65] J. Ryczkowski, Catal. Today 68 (2001) 263-381.
[66] J. Datka, A.M. Turek, J.M. Jehng, I.E. Wachs, J. Catal. 135 (1992) 186-199.
[67] E.L. Kunkes, D.A. Simonetti, R.M. West, J.C. Serrano-Ruiz, C.A. Gartner, J.A. Dumesic, Science 322 (2008) 417-421.

[68] M. Chia, B.J. O'Neill, R. Alamillo, P.J. Dietrich, F.H. Ribeiro, J.T. Miller, J.A. Dumesic, J. Catal. 308 (2013) 226-236.
[69] T.H.M. Housmans, A.H. Wonders, M.T.M. Koper, J. Phys. Chem. B 110 (2006) 10021-10031.
[70] H.A. Gasteiger, N. Markovic, P.N. Ross, E.J. Cairns, J. Phys. Chem. 98 (1994) 617-625.
[71] S. Gilman, J. Phys. Chem. 68 (1964) 70-80.
[72] A.B. Anderson, E. Grantscharova, J. Phys. Chem. 99 (1995) 9143-9148.
[73] C. Saravanan, M.T.M. Koper, N.M. Markovic, M. Head-Gordon, P.N. Ross, Phys. Chem. Chem. Phys. 4 (2002) 2660-2666.
[74] M.M.P. Janssen, J. Moolhuysen, J. Catal. 46 (1977) 289-296.
[75] J.K.A. Clarke, A.C.M. Creaner, Ind. Eng. Chem. Prod. R. D. 20 (1981) 574-593.
[76] H.E.Kluksdahl, US Patent 3 415 737 (1968) , to Chevron Research Company.
[77] M.F.L. Johnson, V.M. Leroy, J. Catal. 35 (1974) 434-440.
[78] G.C. Torres, E.L. Jablonski, G.T. Baronetti, A.A. Castro, S.R. de Miguel, O.A. Scelza, M.D. Blanco, M.A.P. Jimenez, J.L.G. Fierro, Appl. Catal. A 161 (1997) 213-226.
[79] M.C. Roman-Martinez, D. Cazorla-Amoros, A. Linares-Solano, C.S.M. De Lecea, H. Yamashita, M. Anpo, Carbon 33 (1995) 3-13.
[80] R.A.van Santen and M.Neurock, Molecular Heterogeneous Catalysis: A Conceptual and Computational Approach, Wiley-VCH, Weinheim, 2007.
[81] P. Biloen, J.N. Helle, H. Verbeek, F.M. Dautzenberg, W.M.H. Sachtler, J. Catal. 63 (1980) 112-118.
[82] S. Ito, K. Tomishige, Catal. Comm. 12 (2010) 157-160.
[83] L.C. Grabow, A.A. Gokhale, S.T. Evans, J.A. Dumesic, M. Mavrikakis, J. Phys. Chem. C 112 (2008) 4608-4617.
[84] T. Zhu, P.W. van Grootel, I.A.W. Filot, S.G. Sun, R.A. van Santen, E.J.M. Hensen, J. Catal. 297 (2013) 227-235.
[85] Adsorption energies determined by DFT calculations on Pt(111) and Re(0001) surfaces using the VASP code with the PW91 exchange-correlation functional (energy cutoff 500 eV; p(3x3) unit cell; 3x3x1 k-point sampling of the Brillouin zone).

Chapter 4

Pt-Re synergy on reducible oxide supports in aqueous phase reforming of glycerol

Summary

A significant support effect is observed for the aqueous phase reforming (APR) of glycerol over a series of Pt and PtRe loaded ceria, ceria-zirconia, zirconia and titania supported catalysts. Glycerol conversion rates decreased in the order Pt/TiO_2 > Pt/ZrO_2 > $Pt/CeZrO_2$ > Pt/CeO_2. Upon addition of Re, APR activities of all the Pt catalysts increased. Re promotion for glycerol APR is strongest for $PtRe/CeO_2$. Pt/CeO_2 is least active because of incomplete reduction of Pt. Pt is more easily reduced in $PtRe/CeO_2$ because of the strong Pt-Re interaction. When compared to previous data about carbon-supported Pt and PtRe, the oxide supported catalysts were more active in the WGS reaction, with titania giving the most active catalysts. The reason is the activation of water on the titania support. The acidity of these groups also results in increased C-O cleavage rates of Pt/TiO_2 as compared to Pt/C in APR. A more detailed comparison of Pt(Re)/C and Pt(Re)/TiO_2 is made. The use of acetaldehyde decomposition to determine the rate of C-C bond cleavage also evidenced a strong promoting effect of Re on the supported Pt catalysts. Whilst all catalysts produce carbon monoxide, methane and ethanol during acetaldehyde decomposition, Pt(Re)/TiO_2 stand out by their formation of products such as ethylene, ethane, propylene and propane, indicative of a mechanism also involving ethanol dehydration and olefin coupling to CH_x surface intermediates derived from acetaldehyde. The activity in overall glycerol conversion in APR decreased in the order $PtRe/C$ > $PtRe/TiO_2$ > Pt/TiO_2 > Pt/C.
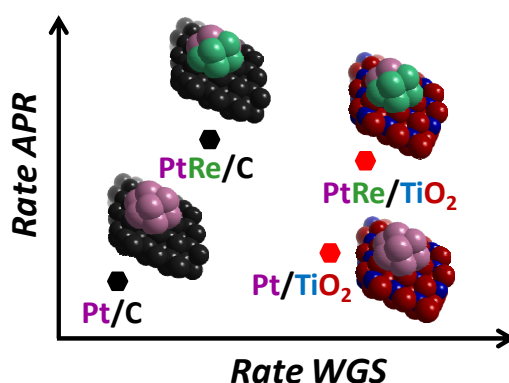
4.1 Introduction

Aqueous phase reforming of biomass-derived carbohydrates is an attractive process for obtaining chemicals, transportation fuels and hydrogen from renewable carbon feedstocks [1,2]. Glycerol is a viable feedstock for APR, because it may become available in significant quantities as by-product of biodiesel production [3,4]. Besides, it serves as a common model compound for the reforming of polyols, among which sugars derived from the (hemi-) cellulosic part of second-generation biomass are most relevant. The APR reaction mechanism involves the cleavage of C-C and C-O bonds, resulting respectively in decarbonylation and dehydration of the polyol feedstock and the reaction intermediates, and the water-gas shift (WGS) reaction [1,2,5]. It has been argued that the WGS reaction is important to maintain high overall APR activity by removing strongly bound CO from the catalyst surface. Indeed, it has been found that overall APR performance correlates to WGS activity [6], as discussed in Chapter 3. In general, Pt has been identified as the most active transition metal for the WGS reaction [7-9]. This would seem to be in concord with the preference for Pt in APR studies [1]. Pt has also a reasonable activity in C-C bond cleavage and hydrogenation reactions because of its intermediate metal-carbon bond strength. For the APR reaction, the most employed supports for Pt nanoparticles are carbon [10-13] and Al_2O_3 [2,14].

It has been typically found that the support has a significant influence the overall activity and product selectivity in APR reactions [1,15], as discussed in Chapter 2. Metal oxide carriers play a key role in many catalytic processes including clean energy generation, abatement of environmental pollution and CO removal from hydrogen-rich streams (PROX) [16,17]. For the WGS reaction, it is well established that reducible oxide supports such as ceria and titania in combination with noble metals such as Pt and Au make very active WGS catalysts, presumably due to the involvement of the metal/metal oxide-support interface in water activation [7,9,18-20]. In Chapter 7, we studied the activity of Au and Pt nanoparticles dispersed on ceria for ethanol steam reforming. Aqueous phase reforming of model reactants over catalysts prepared by dispersing metal nanoparticles on oxidic supports has been the topic of many investigations [6,15,21-23].

In recent years, the subject of bimetallic catalysts has been receiving growing attention. In APR, PtRe bimetallic catalysts show better performance than Pt catalysts [10-12]. Addition of Re promotes C-C and C-O bond cleavage reactions. The latter is thought to occur by dehydration of alcoholic functions catalyzed by Brønsted acid sites formed on the catalytic surface, as discussed in Chapter 3. The presence of such sites effectively increases the formation of alkanes over total reforming to CO_2 and H_2. Separate gas-phase model experiments indicate that addition of Re to carbon-supported Pt catalysts results in a substantial increase of the WGS activity. It has also been suggested that the increased WGS activity results in faster removal of CO from the catalytic surface, thereby increasing the overall conversion rate in APR (Chapter 3). The WGS activity of Re-promoted Pt catalysts supported on reducible oxides has also been studied [24-33].

In the present study we explored the effect of the support on the performance of Pt and PtRe catalysts in APR of glycerol. To this end, a set of Pt and PtRe catalysts with a Pt:Re molar ratio of 1:2 was prepared using ceria, ceria-zirconia, zirconia and titania supports. The catalysts were extensively characterized using TPR, EXAFS and XANES at the Pt and Re edges, FTIR of adsorbed pyridine, XPS and TEM. Their catalytic activities were determined for the APR of glycerol as well as for model gas-phase acetaldehyde decomposition and WGS reactions. We will discuss the support effect for Pt and PtRe on the APR reaction, the role of Brønsted acidity on the metal and the support phase and the synergetic effect of the support *vs.* Re on the WGS activity of Pt catalysts. For the latter purpose, we will compare the results for Pt/TiO_2 and $PtRe/TiO_2$ to their carbon-supported counterparts.

4.2 Experimental

4.2.1 Catalyst preparation

Pt and PtRe catalysts were prepared by incipient wetness impregnation of four different types of oxide supports with solutions of appropriate concentrations of platinum-tetraamine nitrate ($Pt(NH_3)_4(NO_3)_2$, Alfa Aesar) and/or perrhenic acid ($HReO_4$, Aldrich, 65-70 wt% in H_2O, 99.99%). Prior to impregnation, the support material was dried overnight at 110 °C. After impregnation, the sample was dried again overnight at 110 °C. Supported PtRe samples were prepared by subsequent impregnation of the dried Pt catalyst with a perrhenic acid solution followed by another drying step at 110 °C. The Pt:Re molar ratio was adjusted to 1:2. As supports ceria, zirconia, cera-zirconia and titania were used. Nanorod-shaped ceria (CeO_2) was prepared by a homogeneous deposition precipitation method as reported in Chapter 7. Before use, CeO_2 was calcined at 500 °C. Zirconia (RC-100 with 99.74 % ZrO_2 and 0.13 % TiO_2) was obtained from Gimex. A high porosity cerium-doped zirconium hydroxide with a nominal composition of $Ce_{0.25}Zr_{0.75}O_2$ was supplied by MEL Chemicals [34]. The $CeZrO_2$ and ZrO_2 supports were calcined at 600 °C prior to impregnation. Titania (Degussa P25) was calcined at 350 °C prior to use.

4.2.2 Catalyst characterization

The metal loading was determined by inductively coupled plasma atomic emission spectrometry (ICP-AES) analysis performed on a Goffin Meyvis Spectro Cirus^{ccd} apparatus. The CeO_2 supported samples were dissolved in an equivolume mixture of H_2O and H_2SO_4. ZrO_2 and $CeZrO_2$ supported samples were dissolved in a solution of 5 M $(NH_4)_2SO_4$ in H_2SO_4. TiO_2 supported samples were dissolved in solutions of 3:1 HCl/HNO_3 and 1:1 H_2O/H_2SO_4.

X-ray photoelectron spectroscopy (XPS) measurements of the as-prepared catalysts were performed using a Thermo Scientific K-Alpha, equipped with a monochromatic small-spot X-ray source and a 180° double focusing hemispherical analyzer with a 128-channel detector. Spectra were obtained using an aluminium anode (Al Kα = 1486.6 eV) operating at 72 W and a spot size of 400 μm. Survey scans were measured at a constant pass energy of 200 eV and region scans at 50 eV. The background pressure was 2×10^{-9} mbar. During

measurements the background pressure was kept at 3×10^{-7} mbar Ar because of the charge compensation dual beam source.

Transmission electron micrographs were acquired on a FEI Tecnai 20 transmission electron microscope (TEM) at an acceleration voltage of 200 kV with a LaB_6 filament. Typically, a small amount of sample was ground and suspended in pure ethanol, sonicated and dispersed over a Cu grid with a holey carbon film. Prior to deposition on the TEM grid, a small amount of catalyst was reduced in 10 vol% H_2 in He (total flow 100 ml/min) at 300 °C for 2 h.

X-ray absorption spectroscopy (XAS) was carried out at the Dutch-Belgian Beamline (Dubble) at the European Synchrotron Radiation Facility (ESRF), Grenoble, France (storage ring 6.0 GeV, ring current 200 mA). Data were collected at the Pt L_{III} and Re L_{III} edges in transmission mode. Energy selection was done by a double crystal Si(111) monochromator solid-state detector. Background removal was carried out by standard procedures. EXAFS analysis was then performed with EXCURVE931 on k^3-weighted unfiltered raw data using the curved wave theory. Phase shifts were derived from ab initio calculations using Hedin-Lundqvist exchange potentials and Von Barth ground states. Energy calibration was carried out with Pt foil. The amplitude reduction factor S_0^2 associated with central atom shake-up and shake-off effects was set at 0.99 by calibration of the first- and second shell Pt–Pt coordination numbers to 12 and 4, respectively, for the k^3-weighted EXAFS fits of the Pt foil. For the spectra recorded at the Re L_{III} edge, Re powder was fitted as the reference spectra and S_0^2 for the Re-Re shell was set as 0.75. Spectra were recorded in a stainless-steel controlled atmosphere cell. The cell was heated with two firerods controlled by a temperature controller. A thermocouple was placed close to the catalyst sample. Typically, a predetermined amount of finely grinded sample was pressed in a stainless steel holder and placed in the cell. Carbon foils were held between two high-purity carbon spacers. Gases (He and H_2) were delivered by thermal mass flow controllers (Bronkhorst). The catalyst sample was heated at a rate of 10 °C/min up to 300 °C. After recording the room temperature EXAFS of the reduced catalysts, the sample was heated to 150 °C under He flow. At 150 °C, CO was mixed with He and fed through a Controlled Evaporator Mixer unit where steam was generated to obtain a $H_2O:CO$ ratio of 3. The sample was heated at a rate of 10 °C/min and XANES spectra were recorded during in situ WGS reaction at 200 and 250 °C. Finally, EXAFS spectra were recorded during WGS reaction at 300 °C.

Temperature-programmed reduction (TPR) experiments were performed in a flow apparatus equipped with a fixed-bed reactor, a computer-controlled oven and a thermal conductivity detector. A small amount of catalyst (typically 10 mg) was loaded in a tubular quartz reactor. The sample was reduced in a flow of 8 ml/min of a mixture of 4 vol% H_2 in N_2, whilst heating from room temperature to 800 °C at a rate of 10 °C/min. The TCD signal was calibrated using a CuO/SiO_2 reference catalyst.

FTIR spectroscopy of adsorbed pyridine was performed on a Bruker Vertex V70v instrument. FTIR spectra were recorded in the 4000-400 cm^{-1} range at a resolution of 2 cm^{-1}

and by averaging 32 scans. The samples were prepared as thin self-supporting wafers of 5-10 mg/cm^2 and placed inside a controlled environment infrared transmission cell, capable of heating and cooling, gas dosing and evacuation. Prior to measurement, the catalyst was reduced at 300 °C by flowing 20 vol% H_2 in N_2 for 1 h. Some of the samples were exposed to steam at 225 °C by bubbling N_2 through a saturator containing water kept at room temperature (water partial pressure ~2.7 kPa), followed by flushing with pure N_2 and subsequent evacuation at 225 °C. After saturating the evacuated sample with pyridine at 150 °C, the cell was evacuated at 150 °C. All spectra presented were normalized to the weight of the pellet.

4.2.3 Catalytic activity measurements

4.2.3.1 Aqueous phase reforming of glycerol

APR reactions were carried out at 225 °C under 25 bar initial N_2 pressure using 60 g of 10 wt% aqueous glycerol solution in a 120 ml autoclave. An amount of 75 mg of reduced catalyst (300 °C) was loaded in the autoclave together with an appropriate amount of deaerated water in a N_2-flushed glovebag. The autoclave was purged five times with 10 bar N_2 in order to remove air from the autoclave. A 50/50 w/w mixture of glycerol and water was charged into the reactor from an external holding vessel after the autoclave containing water and the catalyst reached the desired reaction temperature. The stirring speed was 600 rpm. Liquid samples were withdrawn by a ROLSI injector and analyzed by a Trace GC equipped using a Stabilwax column and a FID detector. Gas samples were collected online and analyzed by a Focus GC equipped with a TCD detector and CP-Porabond Q and RT-MolSieve-5A columns. The carbon product selectivities were calculated by:

$$S_i(\%) = \frac{mol\ of\ product_i\ formed\ \times\ number\ of\ C\ atoms}{mol\ of\ glycerol\ in\ the\ feed \times conversion \times 3} \times 100$$

4.2.3.2 Water-gas shift reaction (WGS)

WGS reaction experiments were performed in a parallel ten-flow microreactor system [35]. Steam was supplied by evaporation of deionized water in a CEM unit with a liquid flow controller (Bronkhorst). Gas flows were controlled by thermal MFCs (Brooks and Bronkhorst) and tubings were kept >100 °C. The dry product gas mixture was analyzed by an online GC (Interscience CompactGC) equipped with appropriate TCD columns. Experiments were carried out in a mixture of 2.5 vol% CO and 7.5 vol% H_2O balanced by He at a dry GHSV of ~1.3×10^5 h^{-1} in the temperature range 130-400 °C. Typically, the catalyst was diluted with SiC of the same sieve fraction. The material was contained between two quartz wool plugs in a quartz reactor. Prior to catalytic activity measurements, the catalyst was reduced in a flow of 20 vol% H_2 in He at a ramp rate of 5 °C/min to 300 °C followed by an isothermal period of 0.5 h. The reactor was cooled in He to the reaction temperature. The catalyst was exposed to the reaction mixture for 10 min prior to the start of recording product gas mixture. At each reaction temperature, the CO conversion was followed for 1.5 h.

4.2.3.3 Acetaldehyde decomposition

Acetaldehyde decomposition experiments were performed in a continuous flow reactor setup. Hydrogen and acetaldehyde were fed as the feed components. Acetaldehyde was fed by bubbling helium through a saturator kept at such a temperature to obtain a gas-phase acetaldehyde concentration of 3 vol%. Samples were first reduced at 300 °C. The reaction was carried out at 225 °C at a GHSV of 7200 $ml_{acetaldehyde}/g_{cat}$.h. The reactor effluent was analyzed by online gas chromatography (Interscience GC-8000 Top, permanent gases on Shincarbon ST80/100 packed column connected to a TCD and hydrocarbons on a RT-Q bond column connected to a FID).

4.3 Results and discussion

4.3.1 Characterization of the catalysts

The metal loadings of the Pt and PtRe catalysts are collected in Table 4.1. The Pt content of all of the catalysts was found to be in the range 2.5-3 wt%. The Pt/Re molar ratio is about 0.5 for all bimetallic catalysts. TPR profiles of the catalysts show that the bimetallic catalysts are reduced at slightly higher temperatures when compared to their monometallic counterparts (Fig. 4.1). It is well known that the reduction of Re by itself starts around 300 °C and is completed close to 500 °C [36]. The TPR profiles of Pt/CeO_2 and $Pt/CeZrO_2$ show single reduction peaks centered at around 230 and 235 °C, respectively. These sharp features are due to the reduction of the metal precursor and, almost concomitantly, the ceria support surface. The reduction of the surface of the support is facilitated by spillover hydrogen from the reduced metal. As a result of support reduction, the H_2/Pt ratio is much higher than expected on the basis of Pt reduction. Upon addition of Re, the reduction features for Pt/CeO_2 and $Pt/CeZrO_2$ become broader and at least two reduction features are observed (Fig. 4.1e-f). The H_2/metal ratio is less than half of the values found for the monometallic catalysts, which suggests that the spillover process is much weaker. This may point to a decreased metal-support interaction of bimetallic PtRe nanoparticles. The reduction of Pt/ZrO_2 and Pt/TiO_2 takes place at slightly lower temperatures compared to Pt/CeO_2 and $Pt/CeZrO_2$. This points to weaker interaction of the Pt precursor phase with ZrO_2 and TiO_2. The TPR profile of $PtRe/TiO_2$ starts with a sharp feature centered around 220 °C followed by a broad shoulder at 235 °C, which ends at 300 °C. Typically, the onset of reduction of the PtRe catalysts is higher than that of Pt-only catalysts, suggesting that the Pt and Re precursor phases are in intimate contact in the catalyst precursor. The TPR profiles show that reduction of all catalysts is nearly completed at 300 °C.

Table 4.1: Metal loadings and average particle sizes for the supported catalysts.

Catalyst	Metal loading[1] (wt%)		Pt/Re ratio	Average particle size[2] (nm)
	Pt	Re		
Pt/CeO$_2$	2.72	-	-	0.7±0.2
PtRe/CeO$_2$	2.74	5.29	0.49	0.7±0.2
Pt/CeZrO$_2$	2.76	-	-	0.8±0.3
PtRe/CeZrO$_2$	2.50	5.07	0.47	0.6±0.2
Pt/ZrO$_2$	2.85	-	-	1.3±0.5
PtRe/ZrO$_2$	2.57	4.81	0.51	1.0±0.4
Pt/TiO$_2$	2.99	-	-	1.5±0.3
PtRe/TiO$_2$	2.70	4.53	0.57	0.8±0.2

[1] determined by ICP analysis. [2] determined by TEM analysis of the reduced catalysts
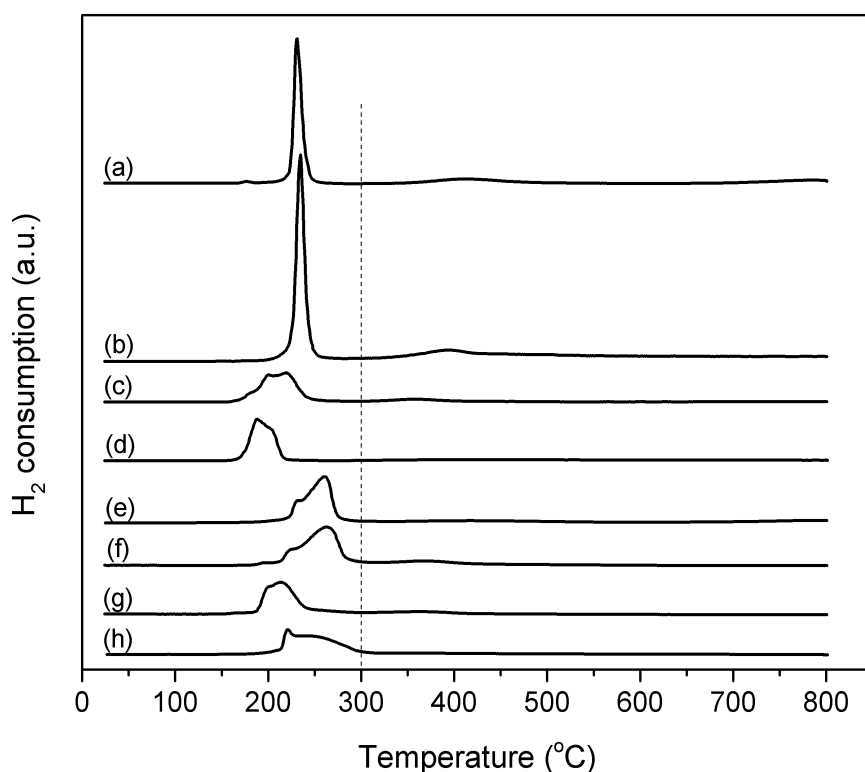
Figure 4.1: TPR profiles of (a) Pt/CeO$_2$, (b) Pt/CeZrO$_2$, (c) Pt/ZrO$_2$, (d) Pt/TiO$_2$, (e) PtRe/CeO$_2$, (f) PtRe/CeZrO$_2$, (g) PtRe/ZrO$_2$ and (h) PtRe/TiO$_2$.

Near-edge spectra recorded at the Pt L$_{III}$ edge for reduced catalysts exhibit qualitatively similar features in terms of the white line intensity and edge energy as the reference Pt foil (Fig. 4.2). This implies that Pt is completely reduced. Near-edge spectra at the Re L$_{III}$ edge of the same catalysts (Fig. 4.2d-f) show that Re is also nearly completely reduced. However, comparison of the Re L$_{III}$ edge energies of reduced catalysts and metallic Re powder (Fig. 4.2h) suggests that a small amount of Re is not completely reduced. The difficult-to-reduce portion may relate to Re-oxide species that do not directly interact with Pt.

The edge shift (ΔE_0) for reduced PtRe/TiO$_2$ (0.6 eV) is smaller than respective values for PtRe/CeZrO$_2$ and PtRe/CeO$_2$ (1.7 eV). This difference may be taken as an indication that the amount of isolated Re-oxide species is lower in PtRe/TiO$_2$. An alternative explanation could be the strong interaction between the metal precursors and the ceria and ceria-zirconia supports, which results in less complete Re reduction.
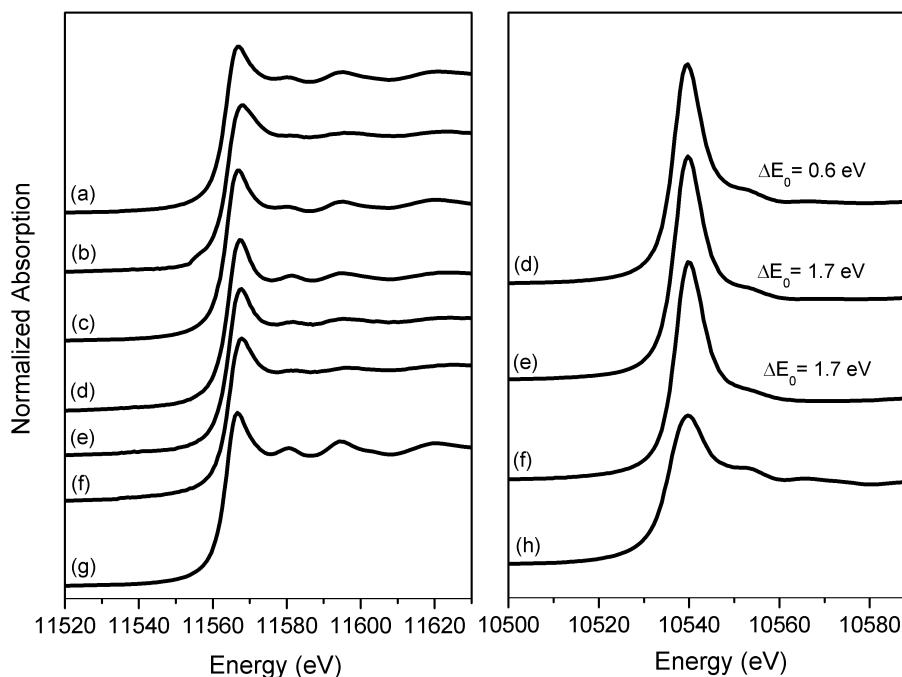

Figure 4.2: Pt L$_{III}$-edge (left) and Re L$_{III}$-edge (right) near-edge spectra recorded of Pt/TiO$_2$ (a), Pt/CeZrO$_2$ (b), Pt/CeO$_2$ (c), PtRe/TiO$_2$ (d), PtRe/CeZrO$_2$ (e), PtRe/CeO$_2$ (f) catalysts reduced at 300 °C. The near-edge spectra of Pt foil (g) and Re powder (h) are plotted as reference. ΔE_0 is the shift in the edge energy when compared to metallic Re.

To further investigate the metal-support interactions, XP spectra of the as-prepared catalysts were analyzed (Figure 4.3). The binding energy of the Pt 4f$_{7/2}$ feature was observed to increase in the order Pt/TiO$_2$ < Pt/ZrO$_2$ < Pt/CeO$_2$ < Pt/CeZrO$_2$. This trend is in agreement with the conclusions drawn from the TPR data that the metal-support interactions for the ceria- and ceria-zirconia-supported catalysts are strongest. Upon alloying the monometallic catalysts with Re, a slight shift of the Pt features to higher binding energies is observed for all the samples. The shift is smallest for CeO$_2$ and CeZrO$_2$ supported and greatest for TiO$_2$- and ZrO$_2$-supported catalysts. This would also seem to imply that the contact between Pt and Re is most intimate when these metals are supported on TiO$_2$ and ZrO$_2$. The XP spectra in the Re 4f region show that the binding energy of the Re 4f$_{7/2}$ peaks for the PtRe/CeO$_2$ is slightly lower than for the other bimetallic catalysts, implying that the effect of alloying Pt and Re is least pronounced on the CeO$_2$ support.
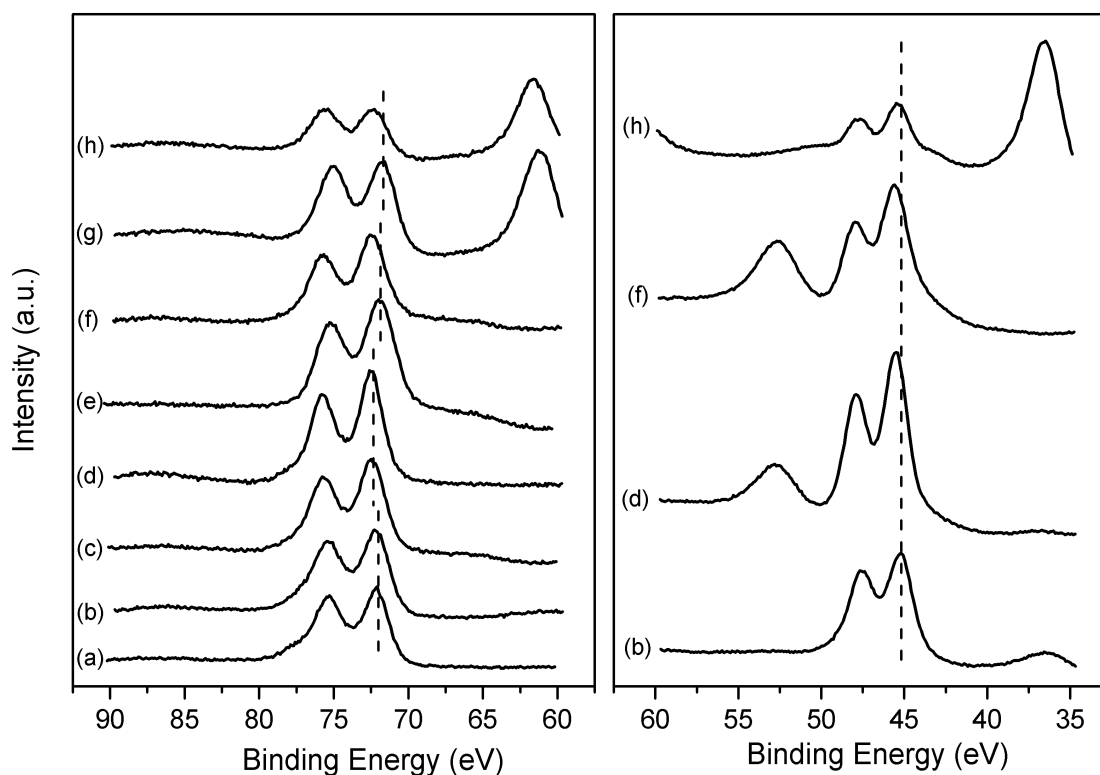
Figure 4.3: XP spectra at the Pt 4f (left) and Re 4f (right) regions of the as-prepared samples (a) Pt/CeO$_2$, (b) PtRe/CeO$_2$, (c) Pt/CeZrO$_2$, (d) PtRe/CeZrO$_2$, (e) Pt/ZrO$_2$, (f) PtRe/ZrO$_2$, (g) Pt/TiO$_2$ and (h) PtRe/TiO$_2$.

Fig. 4.4 shows representative TEM images of supported Pt and PtRe catalysts. The average metal particle size for the various catalysts determined by TEM analysis are collected in Table 4.1. The average sizes for the nanoparticles in Pt/CeO$_2$ and Pt/CeZrO$_2$ are smaller than 1 nm and there is hardly any influence of addition of Re. The subnanometer particle size of Pt on ceria-containing supports is most likely related to the strong metal-support interaction. The average metal particle sizes of Pt/ZrO$_2$ and Pt/TiO$_2$ are 1.5 and 1.3 nm, respectively. The effect of Re addition to these two catalysts is much more substantial and results in average particle sizes of 0.8 and 1.0 nm for the bimetallic catalysts, respectively.
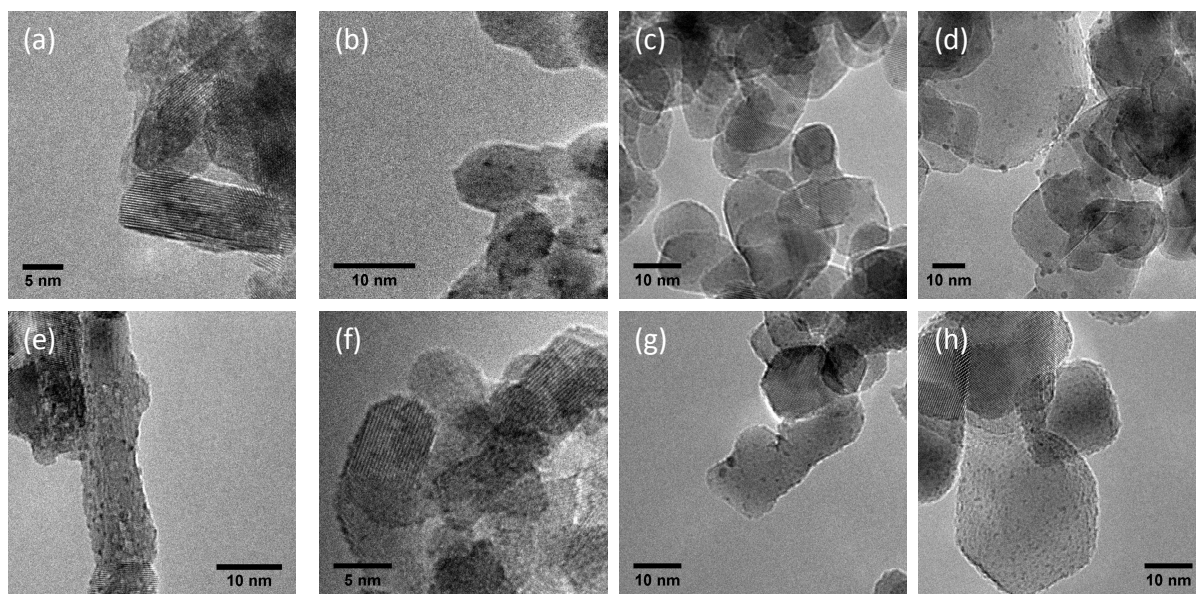
Figure 4.4: TEM pictures of (a) Pt/CeO$_2$, (b) Pt/CeZrO$_2$, (c) Pt/ZrO$_2$, (d) Pt/TiO$_2$, (e) PtRe/CeO$_2$, (f) PtRe/CeZrO$_2$, (g) PtRe/ZrO$_2$ and (h) PtRe/TiO$_2$ catalysts.

Table 4.2: Fit parameters of k^3-weighted EXAFS spectra at the Pt L$_{III}$-edge of supported Pt and PtRe catalysts reduced at 300 °C. M represents the backscatterer atom (Pt or Re).

Catalyst	EXAFS analysis				
	Shell	R (Å)	CN	$\Delta\sigma^2$ (Å^2)	E$_0$ (eV)
Pt/CeO$_2$	Pt-Pt	2.619	4.1	0.003	-3.8
	Pt-O	1.981	0.8	0.006	
PtRe/CeO$_2$	Pt-M$_{Pt}$	2.687	4.1	0.011	-6.8
	Pt-O	1.808	0.1	0.009	
	Re-M$_{Re}$	2.487	6.5	0.011	10.9
	Re-O	1.927	0.8	0.008	
Pt/TiO$_2$	Pt-Pt	2.754	8.3	0.009	-10.3
PtRe/TiO$_2$	Pt-M$_{Pt}$	2.726	5.6	0.008	-9.3
	Re-M$_{Re}$	2.670	6.6	0.009	-4.5

The fit parameters derived from the FT EXAFS spectra recorded for some of the reduced catalysts are collected in Table 4.2. The coordination numbers (CN) for the Pt-Pt shell in Pt/CeO$_2$ and Pt/TiO$_2$ are different. The CN for Pt/TiO$_2$ is substantially higher than the value for Pt/CeO$_2$, consistent with the difference in dispersion. Besides, Pt/CeO$_2$ contains a Pt-O shell with a CN of 0.8, which agrees with the slightly oxidic character of a similar catalyst that we studied (Chapter 7). TEM analysis indicated that the dispersion of Pt is much higher for the ceria-supported catalyst. The strong Pt-support interaction is thought to be the cause of the high dispersion of Pt on the ceria surface [37]. Upon alloying with Re, the CN of the Pt-M and Re-M shells (M = Pt or Re) of Pt/TiO$_2$ decreased slightly in agreement with the presence of smaller nanoparticles in PtRe/TiO$_2$. It is also seen that PtRe/CeO$_2$ contains a Re-O shell with a CN of 0.8, indicative of incomplete Re reduction and in line with the other characterization data. The decrease in the CN of the Pt-O shell of Pt/CeO$_2$ from 0.8 to 0.1 upon Re addition shows that Re helps to reduce the Pt precursor in this catalyst. Most likely,

this is caused by a stronger interaction between the Pt and Re precursors than between Pt and the ceria support.

FTIR spectroscopy of adsorbed pyridine was performed for Pt/TiO_2 and $PtRe/TiO_2$ catalysts reduced at 300 °C. The measurements were carried out before and after exposure to steam at 225 °C (Fig. 4.5). The bands observed at 1638 and 1538 cm^{-1} are assigned to pyridine coordinating to Brønsted acid sites. The band at 1490 cm-1 is related to both Brønsted and Lewis acid sites [38,39]. The two spectra of $PtRe/TiO_2$ clearly evidence the formation of Brønsted acid sites upon steaming (Fig. 4.5b). Without steaming, $PtRe/TiO_2$ does not contain such sites. Based on extinction coefficients reported in literature [40], the concentration of Brønsted acid sites for steamed $PtRe(1:2)/TiO_2$ was 122 μmol/g. Steamed Pt/TiO_2 contains a small amount of Brønsted acid sites (27 μmol/g, Fig. 4.5c). The spectra recorded for reduced Pt/TiO_2 and the bare TiO_2 support show very similar features to that of steamed Pt/TiO_2. The bands at 1445, 1575 and 1604 cm^{-1} are related to Lewis acid sites due to the TiO_2 support [39,41]. The band observed for steamed $PtRe/TiO_2$ at 1456 cm^{-1} is ascribed to Lewis acid sites formed due to isolated Re species after steam treatment of the bimetallic catalyst [42]. The small bands associated with Brønsted acid sites on steamed Pt/TiO_2 at 1638 and 1538 cm^{-1} are observed for reduced Pt/TiO_2 and the bare TiO_2 support as well. These results indicate that the minor Brønsted acidity of Pt/TiO_2 mainly stems from the TiO_2 support itself, and it is not induced by the steaming procedure of Pt/TiO_2.
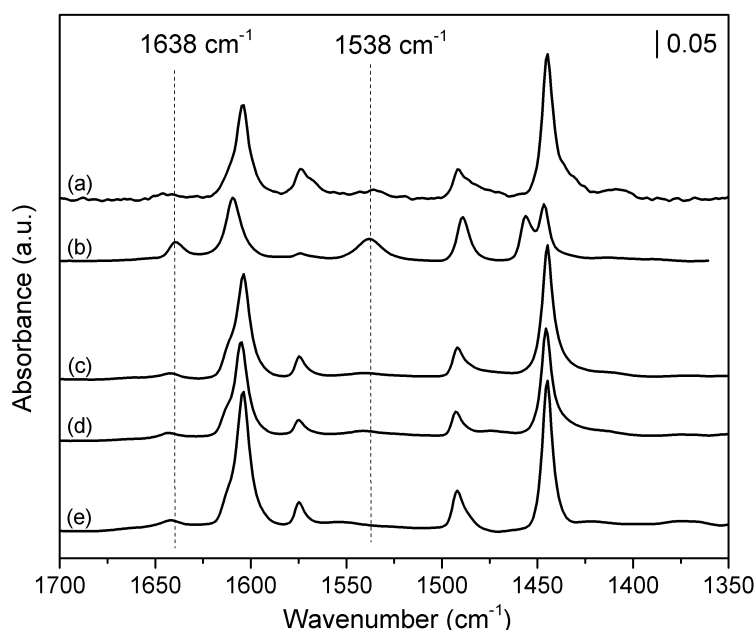

Figure 4.5: FTIR spectra of adsorbed pyridine on (a) $PtRe/TiO_2$, (b) steamed $PtRe/TiO_2$, (c) steamed Pt/TiO_2, (d) Pt/TiO_2 and (e) TiO_2 recorded after evacuation of the physisorbed pyridine at 150 °C.

4.3.2 Catalytic activity measurements

The catalytic performance in the APR of glycerol of Pt/CeO_2, $Pt/CeZrO_2$, Pt/ZrO_2 and Pt/TiO_2 and their Re-promoted counterparts was determined. Fig. 4.6 shows the glycerol conversion by batch time. For the Pt catalysts, the glycerol conversion decreased in the order

Pt/TiO$_2$ > Pt/ZrO$_2$ > Pt/CeZrO$_2$ > Pt/CeO$_2$. These results are in line with the work of Shabaker et al., who found that Pt supported on TiO$_2$ gave the highest activity in APR of ethylene glycol, whereas Pt/ZrO$_2$ showed moderate activity and Pt/CeO$_2$ was the least active [21]. For the PtRe catalysts, the activity order is PtRe/TiO$_2$ > PtRe/CeZrO$_2$ > PtRe/ZrO$_2$ > PtRe/CeO$_2$. Although this trend is almost similar to the one for the monometallic catalysts, the activity differences among the PtRe catalysts are smaller than for the Pt ones. The least active catalyst, Pt/CeO$_2$, becomes nearly an order of magnitude more active upon alloying with Re. In contrast, the most active one, PtRe/TiO$_2$, is only twice as active as Pt/TiO$_2$.
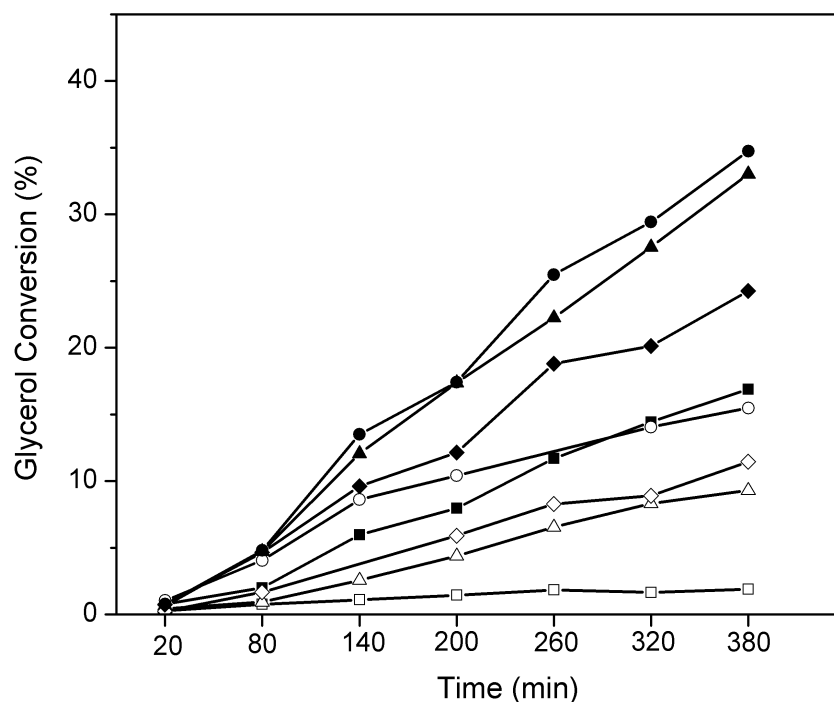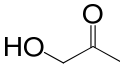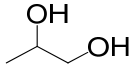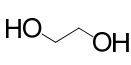

Figure 4.6: Glycerol conversion by time obtained over the CeO$_2$ (*square*), CeZrO$_2$ (*triangle*), ZrO$_2$ (*diamond*), TiO$_2$ (*circle*) supported Pt (open symbols) and PtRe (closed symbols) in APR of glycerol at 225 °C. (Feed: 60 g of 10 wt% aqueous glycerol solution, catalyst amount: 75 mg).

The yield of H$_2$ and CO$_2$, representative of complete reforming of glycerol, increases in the order Pt/CeZrO$_2$ > Pt/ZrO$_2$ > Pt/TiO$_2$ > Pt/CeO$_2$ (Table 4.3). Initially, the yield of reforming products is the highest for Pt/TiO$_2$, but after a reaction time of 4 h the Pt/CeZrO$_2$ is the most active. For the PtRe alloys the order is PtRe/TiO$_2$ > PtRe/CeZrO$_2$ > PtRe/ZrO$_2$ > Pt/CeO$_2$, consistent with the overall glycerol conversion rate trend for these catalysts. For almost all of these catalysts, the total H$_2$ yield is lower than what would be expected in terms of the stoichiometric ratio of H$_2$ to CO$_2$ in the overall reforming reaction (~2.3). This is because product H$_2$ is consumed in the hydrogenation of dehydrated reaction intermediates. The large H$_2$/CO$_2$ ratio of Pt/CeO$_2$ is an exception. Manfro et al. also reported very large H$_2$/CO$_2$ ratios during glycerol APR [43]. Based on the following discussion, it can be stated that the high H$_2$ yield is due to the low hydrogenation activity of Pt/CeO$_2$.

Table 4.3: Yields (Y) of H_2 and CO_2 (%) for aqueous phase reforming of glycerol over CeO_2, $CeZrO_2$, ZrO_2 and TiO_2 supported Pt and PtRe (Pt:Re=1:2) catalysts as a function of time. (Feed: 60 g of 10 wt% aqueous glycerol solution, catalyst amount: 75 mg).

Catalyst	Time (min)													
	20		80		140		200		260		320		380	
	$Y(H_2)$	$Y(CO_2)$	$Y(H_2)$	$Y(CO_2)$	$Y(H_2)$	$Y(CO_2)$	$Y(H_2)$	$Y(CO_2)$	$Y(H_2)$	$Y(CO_2)$	$Y(H_2)$	$Y(CO_2)$	$Y(H_2)$	$Y(CO_2)$
Pt/CeO$_2$	-	0.15	1.4	0.5	5.7	1.2	8.2	1.7	8.9	2.2	9.0	2.0	9.0	2.3
PtRe/CeO$_2$	0.7	0.4	0.8	0.4	8.6	3.9	14.1	7.3	11.6	7.6	15.1	10.1	15.5	12.4
Pt/CeZrO$_2$	-	0.5	1.0	0.5	8.0	3.2	15.5	6.2	20.8	9.5	24.9	11.7	26.5	13.3
PtRe/CeZrO$_2$	1.0	0.5	0.8	0.8	9.3	7.5	15.4	13.4	19.8	19.8	22.4	25.0	28.6	29.2
Pt/ZrO$_2$	-	0.1	3.1	1.4	n/d	n/d	14.3	1.9	19.1	5.6	20.8	8.9	21.2	11.5
PtRe/ZrO$_2$	-	0.4	3.0	2.4	9.6	8.1	14.2	13.2	16.7	18.4	19.7	23.8	20.3	26.7
Pt/TiO$_2$	1.6	1.1	6.1	2.3	13.7	6.5	13.9	8.2	n/d	n/d	12.1	9.3	12.7	10.4
PtRe/TiO$_2$	0.7	0.6	4.6	3.3	16.3	14.0	17.5	19.3	20.3	24.7	21.0	28.7	23.9	34.2

Table 4.4: Product selectivities (%), H_2/CO_2 and C-O/C-C cleavage products ratios in APR of glycerol for Pt(Re) supported on carbon or reducible oxide supports after 320 min of reaction at 225 °C. (Feed: 60 g of 10 wt% aqueous glycerol solution, catalyst amount: 75 mg).

Catalysts	TOF (mol/mol$_{Pt}$.h)	CO_2	CH_4	C_2H_6	C_3H_8	hydroxyacetone	1,2-propanediol	ethylene glycol	alcohols[1]	acids[2]	others[3]	C-O/C-C	H_2/CO_2
Pt/CeO$_2$	20	40.4	3.6	1.8	0.3	34.3	10.7	4.0	1.5	1.6	1.8	0.5	4.5
PtRe/CeO$_2$	167	23.3	1.4	1.8	1.3	15.3	43.7	7.2	1.5	4.0	0.5	1.1	1.5
Pt/CeZrO$_2$	95	46.9	6.0	2.2	0.3	16.1	22.9	2.8	1.6	0.9	0.3	0.5	2.1
PtRe/CeZrO$_2$	345	30.3	3.9	4.5	1.8	8.2	39.5	4.9	1.6	3.9	1.4	0.9	0.9
Pt/ZrO$_2$	99	43.1	6.0	3.4	0.8	18.9	22.0	1.6	2.5	1.3	0.4	0.6	1.8
PtRe/ZrO$_2$	248	39.3	7.2	9.7	4.3	8.6	22.9	1.8	1.4	4.2	0.6	0.8	0.8
Pt/TiO$_2$	150	24.8	2.3	2.2	0.8	18.2	46.4	0	1.2	0.9	3.2	1.1	1.2
PtRe/TiO$_2$	345	32.5	4.7	6.6	3.8	6.6	37.8	3.1	0.5	2.9	1.5	0.9	0.7
Pt/C	117	47.7	9.3	6.2	0.9	8.9	23.5	1.7	1.4	0	0.4	0.6	1.3
PtRe/C	546	34.4	5.0	17.7	13.0	2.1	16.2	2.2	3.2	5.1	1.1	1.3	0.5

[1]alcohols: methanol, ethanol, 1-propanol, 2-propanol
[2]acids: acetic acid, propanoic acid
[3]others: CO, propionaldehyde, 1,3-propanediol

The selectivities towards carbon-containing compounds after a reaction time of 320 min are collected in Table 4.4. Selectivities as a function of time are given in Tables 4.5-4.12). It is worthwhile to briefly discuss the mechanism of the APR reaction. The APR of glycerol proceeds through two main pathways. The first one involves dehydrogenation of glycerol to glyceraldehyde followed by decarbonylation (C-C bond cleavage) to form CO and ethylene glycol. CO is converted to CO_2 in the WGS reaction. The second pathway involves cleavage of C-O bonds glycerol and its intermediates by dehydration. These reaction intermediates are hydrogenated by the *in situ* produced hydrogen from the first reaction pathway. The main product obtained via this route is 1,2-propanediol. The other products of its further conversion are 1- and 2-propanol and propane. Combining these two pathways in the conversion of glycerol leads to a mixture of monofunctional alcohols, alkanes, CO_2 and H_2 next to 1,2-propanediol, hydroxyacetone and ethylene glycol. The main gas-phase products are CO_2, H_2 and a small amount of methane for the monometallic catalysts. In the liquid phase, hydroxyacetone and 1,2-PDO are the main products. The dehydration activity of the monometallic catalysts is increased by the presence of Re. For instance, the selectivity towards propane is much higher for PtRe as compared to Pt catalysts. Consecutive dehydration and hydrogenation reactions result in propane, which is relatively unreactive under the APR reaction conditions. Another consequence of the increased dehydration/hydrogenation rate is that the alkane product distribution shifts to higher hydrocarbons (less methane, more propane). Rhenium addition also enhances the rate of hydroxyacetone hydrogenation to 1,2-PDO. The H_2/CO_2 ratio and the ratio of products obtained from C-O *vs.* C-C bond cleavage reactions are compared in Fig. 4.7. The CeO_2, $CeZrO_2$ and ZrO_2 supported monometallic catalysts exhibit lower C-O/C-C bond cleavage ratios and, consequently, higher H_2/CO_2 values than the bimetallic catalysts. These differences show that the reaction proceeds more predominantly through the decarbonylation pathway for the monometallic than for the bimetallic catalysts. Alloying with Re results in a significant increase in the rate of dehydration relative to the increase in the rate of decarbonylation. Importantly, the C-O/C-C bond cleavage ratio of Pt/TiO_2 is much higher than that of the other monometallic catalysts. This is in line with the findings of Shabaker et al., who identified Pt/TiO_2 as the most selective catalyst towards formation of gaseous alkanes in APR of ethylene glycol [21]. A recent work by Murzin and co-workers also showed that addition of Re to Pt/TiO_2 for the APR of xylitol resulted in higher selectivity towards alkane products, whereas Pt/TiO_2 was more selective towards hydrogen formation [44]. Although we did not compare the Brønsted acidity of the Pt catalysts supported on different oxides, it was seen by pyridine IR that steamed Pt/TiO_2 also contains a small amount of Brønsted acid sites. The increased rate of dehydration for $PtRe/TiO_2$ is consistent with its much higher density of Brønsted acid sites. The influence of Re alloying on the C-O bond cleavage activity of Pt and other transition metals (Rh, Ru or Ir) catalysts has been described by many other research groups [12,44-48].
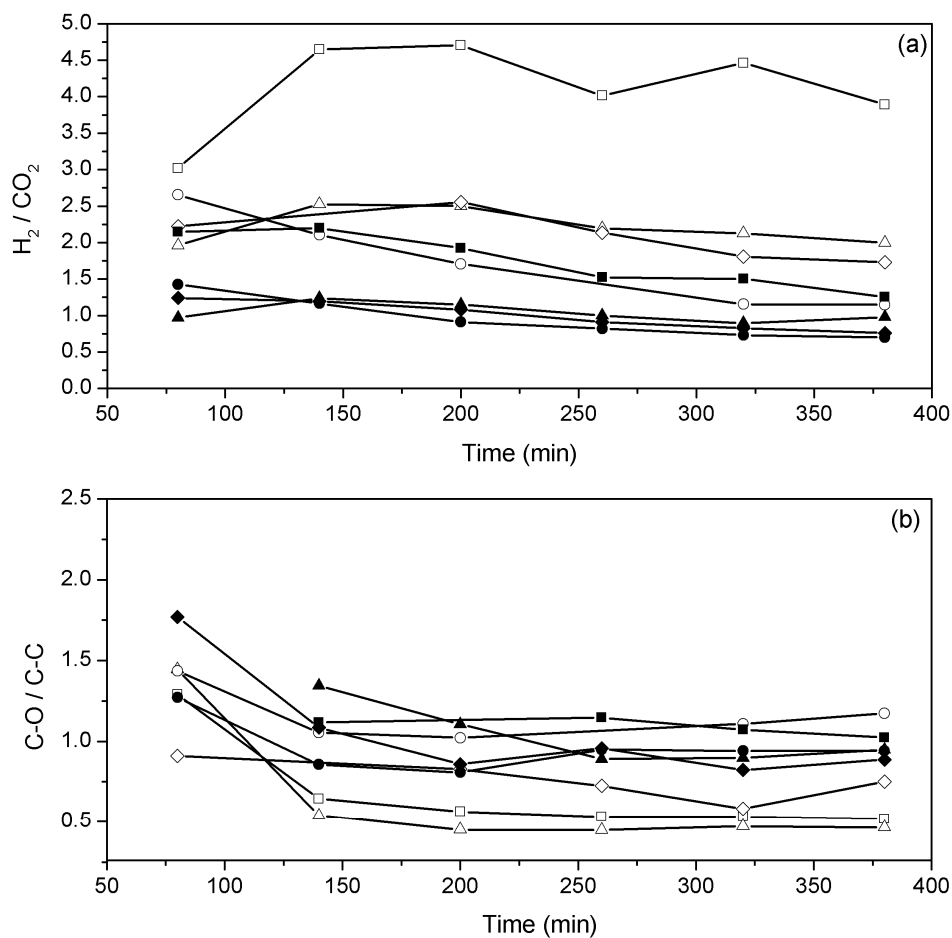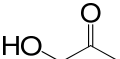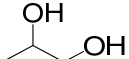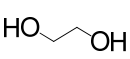
Figure 4.7: H_2/CO_2 ratios (top) and C-O/C-C ratios (bottom) in APR of glycerol for CeO_2 (*square*), $CeZrO_2$ (*triangle*), ZrO_2 (*diamond*), TiO_2 (*circle*) supported Pt (open symbols) and PtRe (closed symbols) catalysts at 225 °C. (Feed: 60 g of 10 wt% aqueous glycerol solution, catalyst amount: 75 mg).

Table 4.5: Conversion (X) of glycerol (%) and product selectivities (%) in APR of glycerol for Pt/CeO$_2$ as a function of time at 225 °C. (Feed: 60 g of 10 wt% aqueous glycerol solution, catalyst amount: 75 mg).
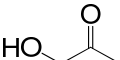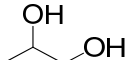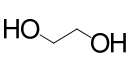
Time (min)	Xglycerol	CO$_2$	CH$_4$	C$_2$H$_6$	C$_3$H$_8$	hydroxyacetone	1,2-propanediol	ethylene glycol	alcohols[1]	acids[2]	others[3]
20	0.3	17.2	1.0	0.8	0	60.5	6.7	3.2	1.4	3.3	5.9
80	0.8	20.5	3.0	0.8	0	57.0	9.6	4.1	1.3	2.0	1.7
140	1.1	37.3	6.1	1.7	0	38.8	8.2	3.4	1.5	1.5	1.5
200	1.5	39.9	5.0	1.7	0.2	34.9	10.3	3.9	1.3	1.5	1.3
260	1.9	39.9	3.6	1.5	0.3	33.2	12.3	4.7	1.7	1.5	1.3
320	1.7	40.4	3.6	1.8	0.3	34.3	10.7	4.0	1.5	1.6	1.8
380	1.9	40.4	2.9	2.1	0.5	31.8	12.3	4.5	1.5	1.6	2.4

[1]alcohols: methanol, ethanol, 1-propanol, 2-propanol
[2]acids: acetic acid, propanoic acid
[3]others: CO, propionaldehyde, 1,3-propanediol

Table 4.6: Conversion (X) of glycerol (%) and product selectivities (%) in APR of glycerol for Pt/CeZrO$_2$ as a function of time at 225 °C. (Feed: 60 g of 10 wt% aqueous glycerol solution, catalyst amount: 75 mg).
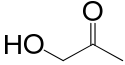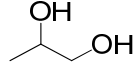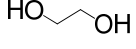
Time (min)	Xglycerol	CO$_2$	CH$_4$	C$_2$H$_6$	C$_3$H$_8$	hydroxyacetone	1,2-propanediol	ethylene glycol	alcohols[1]	acids[2]	others[3]
20	0.4	38.1	0.4	0.9	0	40.4	4.3	2.4	2.2	3.8	7.5
80	0.9	18.2	1.9	0.6	0	57.0	11.1	3.6	2.9	2.1	2.6
140	2.6	41.0	5.2	1.1	0.1	30.6	14.5	2.9	1.9	1.2	1.5
200	4.4	47.3	6.2	1.5	0.1	21.7	17.0	2.7	1.3	1.0	1.2
260	6.5	48.4	6.3	1.9	0.2	18.1	19.1	2.6	1.8	1.0	0.6
320	8.3	46.9	6.0	2.2	0.3	16.1	22.9	2.8	1.6	0.9	0.3
380	9.3	47.6	5.9	2.4	0.3	14.6	23.8	2.7	1.5	0.9	0.3

[1]alcohols: methanol, ethanol, 1-propanol, 2-propanol
[2]acids: acetic acid, propanoic acid
[3]others: CO, propionaldehyde, 1,3-propanediol

Table 4.7: Conversion (X) of glycerol (%) and product selectivities (%) in APR of glycerol for Pt/ZrO$_2$ as a function of time at 225 °C. (Feed: 60 g of 10 wt% aqueous glycerol solution, catalyst amount: 75 mg).
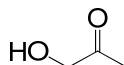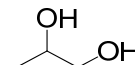
Time (min)	Xglycerol	CO$_2$	CH$_4$	C$_2$H$_6$	C$_3$H$_8$	hydroxyacetone	propylene glycol	ethylene glycol	alcohols[1]	acids[2]	others[3]
20	0.2	15.5	0.8	1.7	0	53.4	6.9	3.1	3.8	5.4	9.4
80	1.7	27.6	2.6	1.1	0.1	43.4	16.1	2.5	3.0	1.9	1.7
200	5.9	31.4	3.8	2.2	0	27.7	27.5	2.1	3.2	1.5	0.6
260	8.3	35.9	5.1	2.4	0.6	22.7	27.0	1.8	2.7	1.4	0.4
320	8.9	43.1	6.0	3.4	0.8	18.9	22.0	1.6	2.5	1.3	0.4
380	11.5	35.7	5.1	3.2	0.9	19.8	29.3	1.9	2.4	1.4	0.3

[1]alcohols: methanol, ethanol, 1-propanol, 2-propanol,
[2]acids: acetic acid, propanoic acid
[3]others: CO, propionaldehyde, 1,3-propanediol

Table 4.8: Conversion (X) of glycerol (%) and product selectivities (%) in APR of glycerol for Pt/TiO$_2$ as a function of time at 225 °C. (Feed: 60 g of 10 wt% aqueous glycerol solution, catalyst amount: 75 mg).
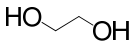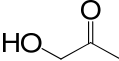
Time (min)	Xglycerol	CO$_2$	CH$_4$	C$_2$H$_6$	C$_3$H$_8$	hydroxyacetone	propylene glycol	ethylene glycol	alcohols[1]	acids[2]	others[3]
20	1.0	36.0	2.0	2.5	0.8	43.9	4.5	0.3	2.8	3.2	4.0
80	4.1	19.0	1.2	0.8	0.2	51.9	20.4	0.1	2.3	1.6	2.5
140	8.6	25.1	2.1	1.4	0.4	36.9	27.9	0	1.8	1.5	2.9
200	10.4	26.1	2.2	1.7	0.5	33.1	30.8	0	1.7	1.5	2.4
320	14.1	24.8	2.3	2.2	0.8	18.2	46.4	0	1.2	0.9	3.2
380	15.5	23.9	2.3	2.5	0.9	28.4	35.9	0.1	1.8	2.0	2.2

[1]alcohols: methanol, ethanol, 1-propanol, 2-propanol
[2]acids: acetic acid, propanoic acid
[3]others: CO, propionaldehyde, 1,3-propanediol

Table 4.9: Conversion (X) of glycerol (%) and product selectivities (%) in APR of glycerol for PtRe/CeO$_2$ as a function of time at 225 °C. (Feed: 60 g of 10 wt% aqueous glycerol solution, catalyst amount: 75 mg).
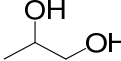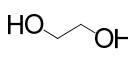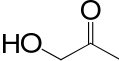
Time (min)	Xglycerol	CO$_2$	CH$_4$	C$_2$H$_6$	C$_3$H$_8$	HO—C(=O)— (hydroxyacetone)	OH / OH (1,2-propanediol)	HO—OH (ethylene glycol)	alcohols[1]	acids[2]	others[3]
20	0.8	14.9	0.5	0	0	56.0	16.5	3.6	1.1	2.8	4.6
80	2.0	5.9	0.4	0.3	0	42.8	34.0	7.9	2.3	4.3	2.1
140	6.0	21.8	1.5	1.0	0.7	26.5	35.1	6.9	1.7	4.1	0.7
200	8.0	30.6	1.8	1.6	1.2	19.3	33.6	5.4	1.2	4.5	0.8
260	11.7	21.7	1.4	1.9	0.8	17.9	42.2	7.2	1.8	4.7	0.4
320	14.4	23.3	1.4	1.8	1.3	15.3	43.7	7.2	1.5	4.0	0.5
380	16.9	24.4	1.5	2.2	1.5	13.5	43.2	7.1	1.9	4.4	0.3

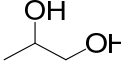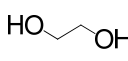[1]alcohols: methanol, ethanol, 1-propanol, 2-propanol
[2]acids: acetic acid, propanoic acid
[3]others: CO, propionaldehyde, 1,3-propanediol

Table 4.10: Conversion (X) of glycerol (%) and product selectivities (%) in APR of glycerol for PtRe/CeZrO$_2$ as a function of time at 225 °C. (Feed: 60 g of 10 wt% aqueous glycerol solution, catalyst amount: 75 mg).
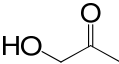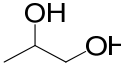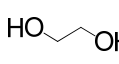
Time (min)	Xglycerol	CO$_2$	CH$_4$	C$_2$H$_6$	C$_3$H$_8$	HO—C(=O)— (hydroxyacetone)	OH / OH (1,2-propanediol)	HO—OH (ethylene glycol)	alcohols[1]	acids[2]	others[3]
20	0.7	25.2	3.0	1.5	0	40.7	17.3	3.3	2.8	2.7	3.5
80	4.7	5.6	0.4	0.3	0.1	37.5	41.6	6.7	3.9	2.5	1.4
140	12.1	20.9	2.6	2.1	1.0	20.9	39.5	5.0	4.9	2.5	0.6
200	17.4	25.7	3.4	3.2	1.3	13.0	36.9	4.9	7.4	3.5	0.7
260	22.3	29.7	3.4	3.8	1.4	10.2	39.8	4.8	1.6	3.9	1.4
320	27.6	30.3	3.9	4.5	1.8	8.2	39.5	4.9	1.6	3.9	1.4
380	33.0	29.5	4.0	5.0	2.0	7.3	39.6	4.9	1.7	4.3	1.7

[1]alcohols: methanol, ethanol, 1-propanol, 2-propanol
[2]acids: acetic acid, propanoic acid
[3]others: CO, propionaldehyde, 1,3-propanediol

Table 4.11: Conversion (X) of glycerol (%) and product selectivities (%) in APR of glycerol for PtRe/ZrO$_2$ as a function of time at 225 °C. (Feed: 60 g of 10 wt% aqueous glycerol solution, catalyst amount: 75 mg).
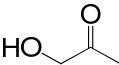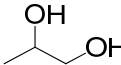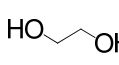
Time (min)	Xglycerol	CO$_2$	CH$_4$	C$_2$H$_6$	C$_3$H$_8$	HO–C(=O)–CH$_3$	CH$_3$CH(OH)CH$_2$OH	HOCH$_2$CH$_2$OH	alcohols[1]	acids[2]	others[3]
20	0.8	15.5	0.4	0.6	0.4	55.6	12.3	1.9	4.0	4.1	5.2
80	4.6	17.1	2.4	2.7	1.7	39.9	26.8	2.3	2.5	3.4	1.2
140	9.6	28.0	4.8	5.3	2.6	20.9	29.4	2.7	1.7	4.0	0.6
200	12.2	36.2	6.6	7.6	3.6	14.3	23.3	2.0	1.5	4.1	0.8
260	18.8	32.6	5.8	7.3	3.3	11.5	30.5	2.7	1.5	4.4	0.4
320	20.1	39.3	7.2	9.7	4.3	8.6	22.9	1.8	1.4	4.2	0.6
380	24.3	36.7	6.7	9.6	4.2	7.9	25.9	2.3	1.6	4.6	0.5

[1]alcohols: methanol, ethanol, 1-propanol, 2-propanol
[2]acids: acetic acid, propanoic acid
[3]others: CO, propionaldehyde, 1,3-propanediol

Table 4.12: Conversion (X) of glycerol (%) and product selectivities (%) in APR of glycerol for PtRe/TiO$_2$ as a function of time at 225 °C. (Feed: 60 g of 10 wt% aqueous glycerol solution, catalyst amount: 75 mg).

Time (min)	Xglycerol	CO$_2$	CH$_4$	C$_2$H$_6$	C$_3$H$_8$	HO–C(=O)–CH$_3$	CH$_3$CH(OH)CH$_2$OH	HOCH$_2$CH$_2$OH	alcohols[1]	acids[2]	others[3]
20	0.8	25.3	1.2	1.6	0.9	45.3	15.8	3.0	1.2	2.3	3.4
80	4.8	22.5	2.3	2.7	2.0	35.2	26.6	2.5	1.9	2.9	1.4
140	13.5	34.6	4.8	5.6	3.5	10.0	34.8	3.1	1.2	1.7	0.7
200	17.4	36.8	5.3	6.5	3.9	12.7	26.7	1.9	1.7	3.8	0.7
260	25.5	32.4	4.7	6.4	3.7	6.8	37.5	3.1	1.5	2.2	1.7
320	29.4	32.5	4.7	6.6	3.8	6.6	37.8	3.1	0.5	2.9	1.5
380	34.7	32.8	4.8	7.2	4.1	8.3	32.9	2.5	1.4	4.6	1.4

[1]alcohols: methanol, ethanol, 1-propanol, 2-propanol
[2]acids: acetic acid, propanoic acid
[3]others: CO, propionaldehyde, 1,3-propanediol

We investigated the effect of the Pt particle size on the overall catalytic performance of carbon-supported Pt catalysts in glycerol APR in Chapter 5. It was observed that the reforming rate increased with the Pt particle size. In the present work, we find that besides particle size also the support has a significant influence on the reaction rate. The catalyst with the largest Pt particles, Pt/TiO_2, exhibits the highest overall glycerol conversion rate. The much smaller particles on Pt/CeO_2 give rise to a much lower activity. The activities of Pt/CeO_2 and $Pt/CeZrO_2$, whose average Pt particle sizes are quite similar, differ substantially. The particularly low activity of Pt/CeO_2 may be due to the low reduction degree of Pt due to the relatively strong metal-support interactions.

The APR activity of Pt catalysts has been correlated to their WGS activity on the premise that efficient CO removal from the catalytic surface is important at the relatively low reaction temperatures [6,11,36]. We have recently shown that the substantial promoting effect of Re on carbon-supported Pt-based APR catalysts is at least in part related to the increased performance in the WGS reaction [6]. To better understand the support effect for the APR reaction, we also determined the catalytic performance of the present set of catalysts in the WGS reaction. Fig. 4.8 provides Arrhenius plots for mono- and bimetallic catalysts. For the monometallic Pt catalysts, the WGS rates increases in the order $Pt/ZrO_2 < Pt/CeO_2 < Pt/CeZrO_2 < Pt/TiO_2$. The superior activity of Pt/TiO_2 when compared to Pt catalysts supported on CeO_2 and ZrO_2 is in concord with literature [7,25,49]. The PtRe catalysts are more active in the WGS reaction than their monometallic counterparts. The activity trends in the same manner as for the monometallic catalysts. A comparison of the changes in the WGS activity upon alloying the reducible oxides supported Pt catalysts with Re shows the following trend $PtRe/ZrO_2 > PtRe/CeO_2 > PtRe/TiO_2 > PtRe/CeZrO_2$. An important corollary from these trends is that with increasing WGS activity of the monometallic Pt catalyst the promotion as a result of Re alloying becomes less substantial. XANES spectra recorded at the Re L_{III} edge during WGS (Fig. 4.9) do not provide indications for the oxidation of Re in the bimetallic catalysts. In WGS, we observe that most of the catalysts become more active when the temperature is decreased from 400 to 130 °C (Fig. 4.10). In order to investigate the structural changes in the catalysts we determined the fit parameters determined for the FT EXAFS spectra recorded during WGS (Table 4.13). For Pt/CeO_2 the CN of the Pt-O shell decreased from 0.8 to 0.4 accompanied by an increase in the Pt-Pt shell from 4.1 to 5.4. These results may be taken to indicate that the Pt phase in Pt/CeO_2 further reduces under WGS conditions. Accordingly, Pt/CeO_2 shows higher activity during the decreasing temperature branch of the WGS activity measurements. $PtRe/CeO_2$ also shows an increase in the CN of the Pt-M shell from 4.1 to 5.9. Similarly, the coordination numbers of the Pt-M and Re-M shells for $PtRe/TiO_2$ increase from 5.6 and 6.6 to 7.2. These results fortify our surmise that the activity increase in WGS by time should be related to minor structural changes in some of the catalysts. For Pt/TiO_2, the changes in the CN of the Pt-Pt shell are relatively minor. This is in line with the similar activity of this catalyst during the increasing and decreasing temperature branches in WGS.
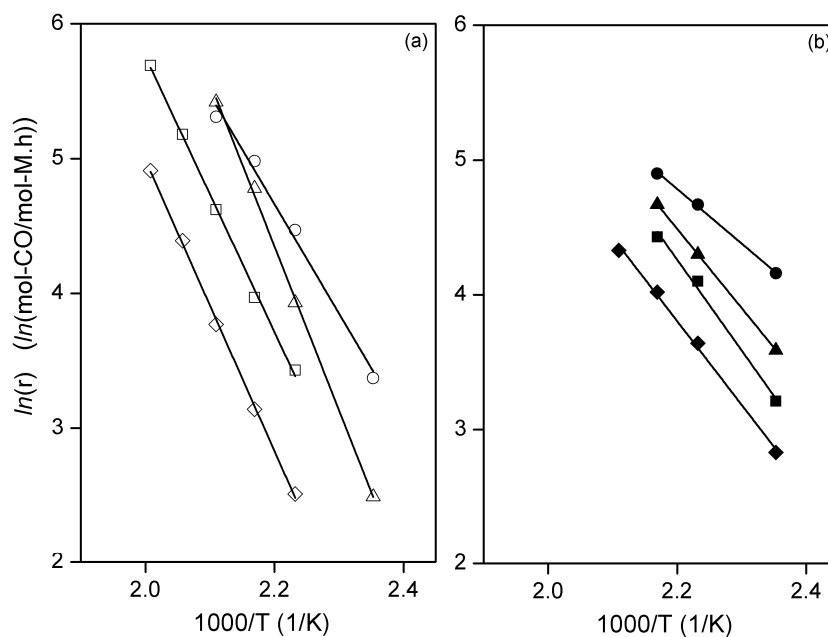
Figure 4.8: Arrhenius plots for WGS over CeO_2 (*square*), $CeZrO_2$ (*triangle*), ZrO_2 (*diamond*) and TiO_2 (*circle*) supported Pt (open symbols) and PtRe (Pt:Re=1:2) (closed symbols) catalysts. (2.5 vol% CO and 7.5 vol% H_2O balanced by He at a dry GHSV of ~1.3×10^5 h^{-1}).
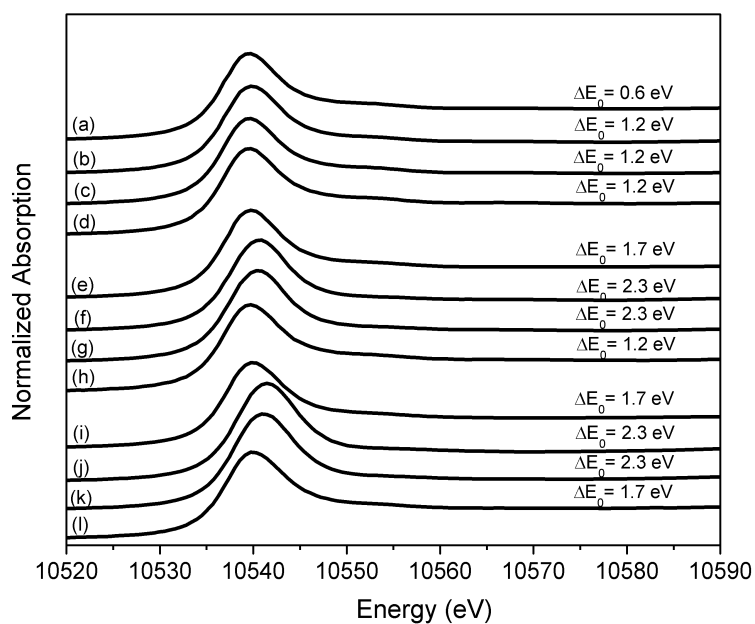

Figure 4.9: Re L_{III}-edge XANES spectra of PtRe/TiO_2 reduced at 300 °C (a) and the spectra recorded during WGS at 200 °C (b), 250 °C (c) and 300 °C (d); PtRe/$CeZrO_2$ reduced at 300 °C (e) and the spectra recorded during WGS at 200 °C (f), 250 °C (g) and 300 °C (h); PtRe/CeO_2 reduced at 300 °C (i) and the spectra recorded during WGS at 200 °C (j), 250 °C (k) and 300 °C (l). ΔE_0 is the shift in the edge energy when compared to metallic Re.
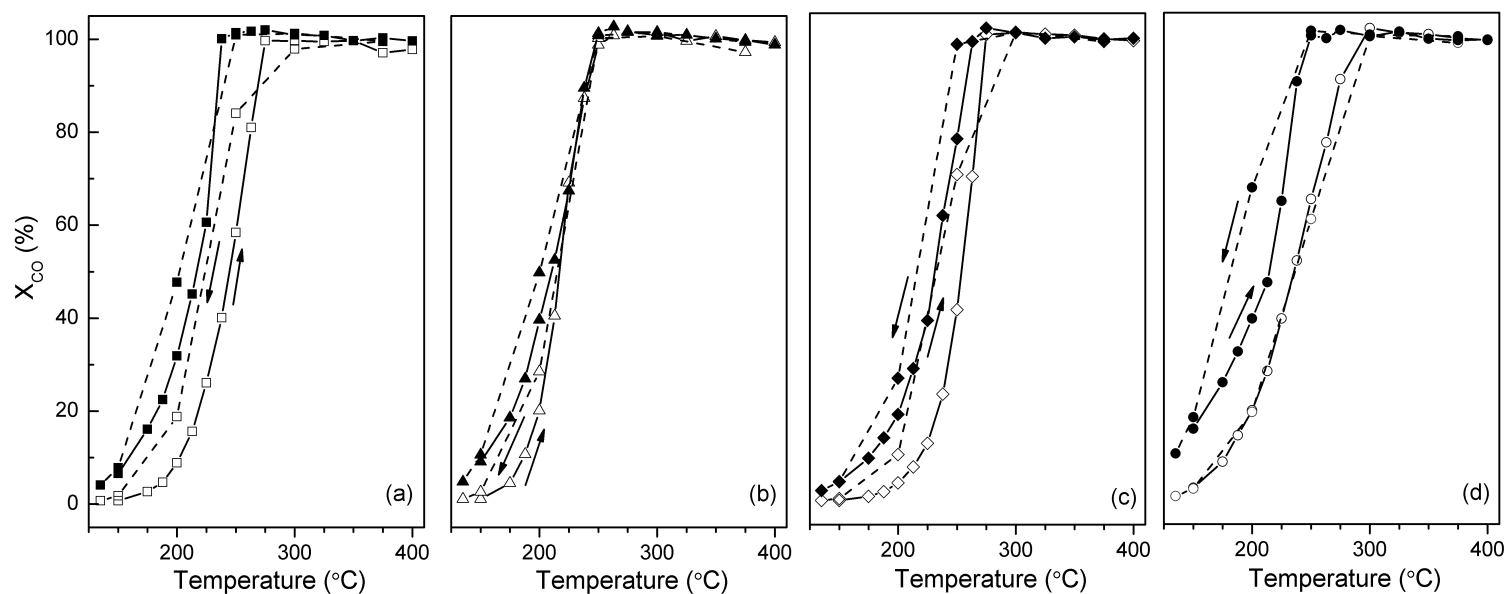
89

Figure 4.10: Conversion of CO in WGS over (a) CeO_2 (*square*), (b) $CeZrO_2$ (*triangle*), (c) ZrO_2 (*diamond*), (d) TiO_2 (*circle*) supported Pt (open symbols) and PtRe (closed symbols) catalysts. The arrows indicate the increasing (solid lines) and decreasing temperature (dashed lines) curves during the experiments performed in a cycle. 2.5 vol% CO and 7.5 vol% H_2O balanced by He at a dry GHSV of $\sim 1.3 \times 10^5$ h^{-1}).

Table 4.13: Fit parameters of k^3-weighted EXAFS spectra at the Pt L_{III}-edge and Re L_{III}-edge of reduced (300 °C) catalysts recorded during WGS reaction at 300 °C. M represents the backscatterer atom (Pt or Re).

Catalyst	EXAFS analysis				
	Shell	R (Å)	CN	$\Delta\sigma^2$ (Å^2)	E_0 (eV)
Pt/CeO$_2$	Pt-Pt	2.727	5.4	0.007	-8.5
	Pt-O	2.075	0.4	0.001	
PtRe/CeO$_2$	Pt-M$_{Pt}$	2.725	5.9	0.012	-8.0
	Re-M$_{Re}$	n/d	n/d	n/d	n/d
Pt/TiO$_2$	Pt-Pt	2.749	9.3	0.014	-9.3
PtRe/TiO$_2$	Pt-M$_{Pt}$	2.735	7.2	0.011	-8.5
	Re-M$_{Re}$	2.669	7.2	0.011	-4.5

For this set of catalysts, addition of Re increased the WGS activity ~2-6 fold at a temperature of 200 °C. This promoter effect is smaller than observed for Pt/C and PtRe/C catalysts investigated in Chapter 3 of this thesis. The increase in the APR activities upon Re addition is similar for Pt/TiO$_2$, Pt/ZrO$_2$ and Pt/CeZrO$_2$ (about 3-4 folds) and it is higher for Pt/CeO$_2$, which is related to the low reduction degree of Pt in Pt/CeO$_2$. The strong Pt-Re interaction in PtRe/CeO$_2$ facilitates reduction of Pt as evidenced by EXAFS analysis. Pt/TiO$_2$, the most active monometallic catalyst in APR, contains a small portion of Brønsted acid sites in the absence of Re as shown by FTIR of adsorbed pyridine. It is well-known that the high WGS activity of Pt/TiO$_2$ is related to the reducibility of the titania support [18,50]. This has a strongly positive effect on the APR activity. As follows from the pyridine IR measurements of the bare titania support (Fig. 4.5e), the hydroxyl groups of titania are directly involved in the catalytic reactions. Alternatively, the OH groups of the support spillover to the Pt. In any case, the involvement of these support OH groups is consistent with the relatively small promotional effect of Re on Pt/TiO$_2$ for the WGS and APR reactions as compared to other supports and especially so compared to carbon-supported Pt catalysts.

Finally, we compare in some detail the catalytic performance of titania- and carbon-supported Pt and PtRe catalysts. The data for the carbon-supported catalysts are taken from Chapter 3 of this thesis and included in Table 4.4. The activity order in overall glycerol conversion in APR is PtRe/C > PtRe/TiO$_2$ > Pt/TiO$_2$ > Pt/C. From Table 4.4, it is seen that the main difference in product composition between Pt/TiO$_2$ and PtRe/TiO$_2$ is the increase in CO$_2$ and methane formation upon alloying. Alloying also led to increased ethane and propane formation, whereas the selectivity towards hydroxyacetone and 1,2-PDO decreased. The decrease in the H$_2$/CO$_2$ ratio from 1.2 to 0.7 further points to an increase in the rate of hydrogenation of dehydrated reaction intermediates. As discussed, the presence of Re results in a higher rate of C-O bond cleavage, shifting the alkane product mixture to higher alkanes. However, among all catalysts shown in Table 4.4, PtRe/TiO$_2$ stands out as the only Re-promoted catalyst for which methane selectivity is higher than for Pt/TiO$_2$. This will be further explained below. Table 4.4 also shows that Re addition to Pt/C results in increased yield of ethane and propane and decreased yield of methane, consistent with the notion that

Re-induced acidity will increase the ratio of C-O over C-C bond cleavage rates. In order to determine possible differences in the rate of C-C bond cleavage reactions, acetaldehyde decomposition was used as a model reaction. The CO yield of titania and carbon supported Pt and PtRe catalysts having comparable Pt/Re ratios are given in Fig. 4.11 as a function of reaction time on stream. The initial activity of Pt/TiO_2 is slightly lower than that of Pt/C. In contrast to Pt/C, Pt/TiO_2 deactivates in time. The two bimetallic catalysts also show similar initial CO yields, which are significantly higher than their monometallic counterparts. The promoter effect of Re is similar for both catalysts. It is again observed that the titania supported PtRe catalyst deactivates in time. After a reaction time of 4 h, the activity appears to become stable. PtRe/C shows stable activity for at least 9 h. It is interesting to briefly discuss the selectivity differences during acetaldehyde conversion between carbon and titania supported catalysts. The selectivities as a function of time on stream are plotted in Fig. 4.12. For Pt/C and PtRe/C, CO and CH_4 are the predominant products with a small amount of ethanol being formed by PtRe/C, consistent with the known better hydrogenation properties of the bimetallic catalyst. The product composition of Pt/TiO_2 is very different. Ethanol yield is higher than observed for PtRe/C and Pt/C. It is also found that Pt/TiO_2 gives rise to formation of small amounts of ethylene and ethane, presumably due to dehydration of ethanol on acid sites of the support, and further hydrogenation of ethylene to ethane. Besides, the formation of propylene and some propane is also seen. From the relatively low CH_4/CO ratio, we infer that Pt/TiO_2 is active for the reaction between ethylene and CH_x surface species, the latter formed by C-C bond cleavage of acetaldehyde. Hydrogenation of the coupled product results in formation of propylene and propane. Another important product on Pt/TiO_2 is acetic acid. We believe that this intermediate stems from reaction of a CH_x-CO intermediate with OH groups of the titania support. The selectivity data show that with increasing time on stream the CH_4/CO ratio increases with a concomitant decrease of the yields of ethanol, ethylene, ethane, propylene, propane and acetic acid. Accordingly, we surmise that the high initial activity is due to the abundance of hydroxyl groups of the titania support. Part of these hydroxyl groups will be rapidly consumed. If regeneration of the support by hydroxylation with water produced by ethanol dehydration is not fast enough, the catalytic activity of this side-reactions to C_2 and C_3 products decreases and the selectivity to CH_4 and CO increases, consistent with experimental observation. The product composition for $PtRe/TiO_2$ catalyst is very similar, however the yield of ethylene and ethane is negligible. As propylene and propane are still formed and their selectivities are higher as compared with Pt/TiO_2, we infer that ethylene will react more rapidly with CH_x than on Pt/TiO_2. This is perhaps not surprising taking into account that Re is known to be a reasonable catalyst for the Fischer-Tropsch reaction [51], C-C coupling reactions evidently being important in its mechanism. The groups of Vlachos and Liu have shown that the intermediate undergoing C-C bond cleavage during ethanol reforming is CH-CO [52,53]. The CH surface intermediate has also been argued to be the most relevant species undergoing chain growth in the Fischer-Tropsch reaction. Although Pt is not the preferred metal for Fischer-Tropsch, mainly because CO dissociation is much slower than on metals such as Co and Ru, formation of CH by dissociation of acetaldehyde opens another route for reaction with a CH_x-CH_y intermediate from ethanol dehydration.

Finally, we note that the chemistry is different for carbon supported catalysts, because of the absence of acidic sites on the support. An acetaldehyde decomposition experiment for PtRe/C in which water was added to the acetaldehyde/H_2 feed did not lead to formation of products different from the experiment without water.
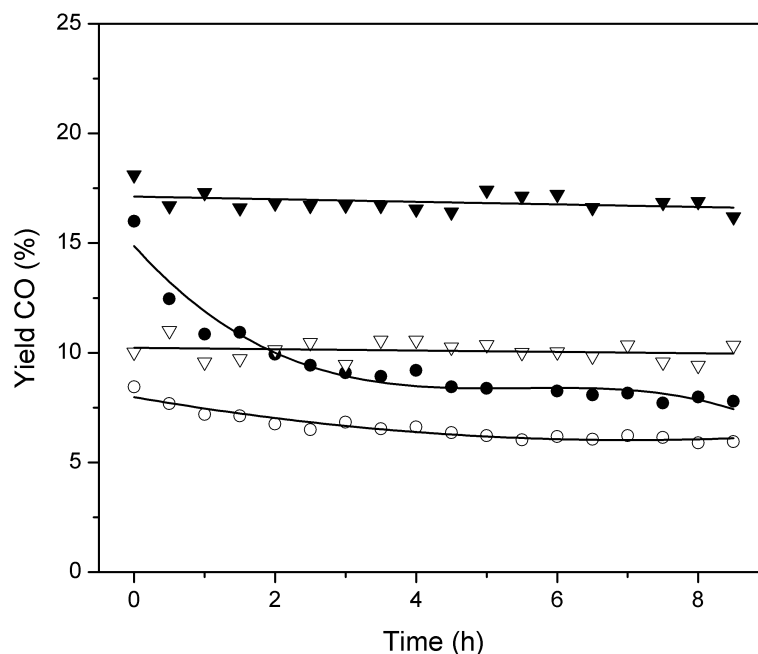

Figure 4.11: Yield of acetaldehyde decomposition product CO as a function of time on stream for TiO_2 (*circle*) and C (*down triangle*) supported Pt (open symbols) and PtRe (closed symbols). (T= 225 °C, GHSV= 7200 $ml_{acetaldehyde}/g_{cat}.h$; gas-phase composition H_2:C_2H_4O=1:1 by volume with balance He).

The trends observed in this model reaction are in line with the selectivity trends in APR as far as the formation of decarbonylation products is concerned. The increase in the ratio of C-O/C-C bond cleavage of 0.6 for Pt/C to 1.3 for PtRe/C points to a stronger increase of the dehydration activity (C-O bond cleavage) as compared to the decarbonylation activity (C-C bond cleavage). For the two titania support catalysts, a slight decrease of this ratio is observed. We speculate that the higher initial ratio of 1.1 for Pt/TiO_2 is due to the presence of Brønsted acid sites on the support or derived from the support. The reason for the lower ratio for PtRe/TiO_2 is the higher methane selectivity. Here we argue that the decomposition of intermediate ethanol via acetaldehyde will also produce CO and CH species. The surface overlayer composition is, however, different under APR and acetaldehyde conversion conditions, so that in APR the CH intermediate is preferably hydrogenated to CH_4 instead of being coupling to other intermediates. Titania supported Pt and PtRe catalysts are much more active in the WGS reaction than their carbon supported counterparts. Clearly, the use of a reducible oxide support to activate water for the WGS reaction is preferred over alloying Pt with Re. The promoting effect of Re on the WGS activity is much greater for Pt/C (10-fold) than for Pt/TiO_2 (~ 3-fold). This difference also emerges from the APR activity data, the promoter effect of Re being twice as high for Pt/C as for Pt/TiO_2. Overall, PtRe/C is the most active APR catalyst.
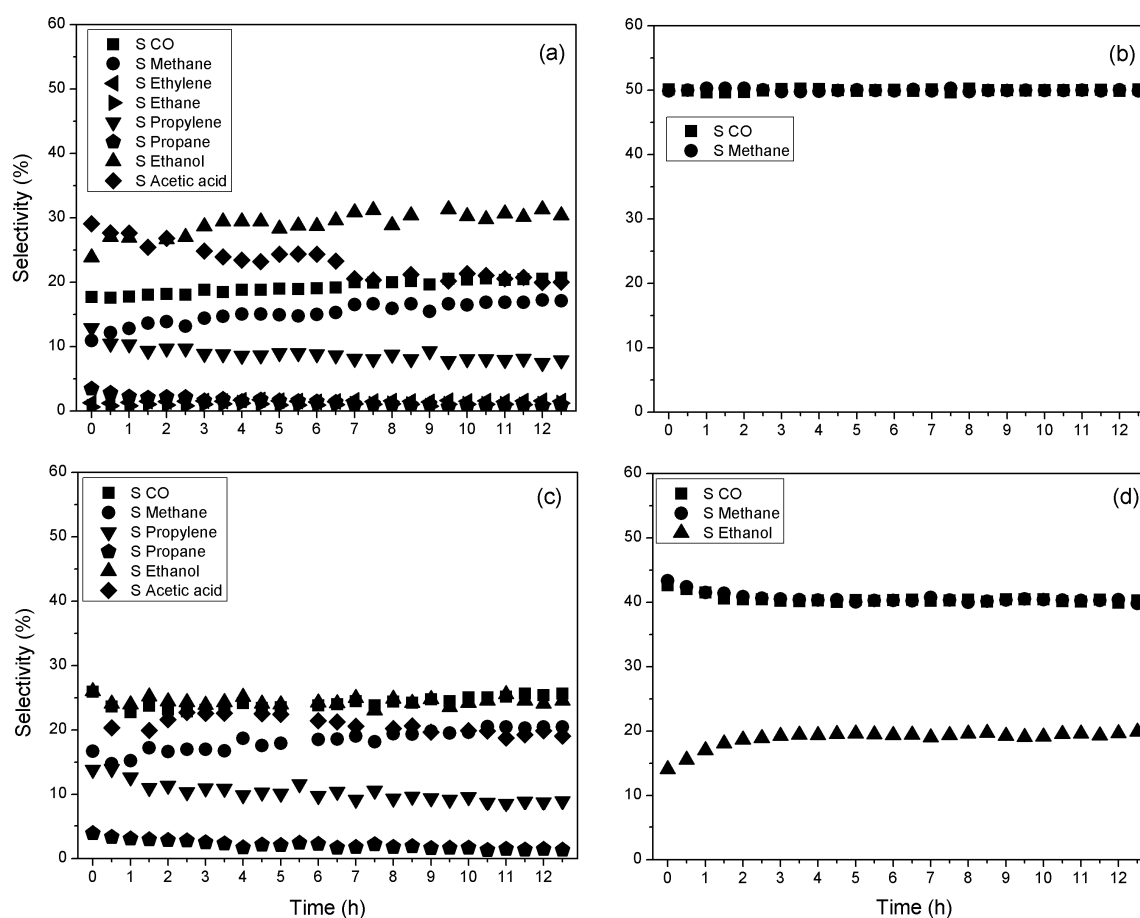
Figure 4.12: Selectivities obtained during acetaldehyde decomposition over (a) Pt/TiO$_2$, (b) Pt/C, (c) PtRe/TiO$_2$, (d) PtRe/C at 225 °C. (T= 225 °C, GHSV= 7200 ml$_{acetaldehyde}$/g$_{cat}$.h; gas-phase composition H$_2$:C$_2$H$_4$O=1:1 by volume with balance He).

4.4 Conclusions

The results of catalytic activity measurements of supported Pt and PtRe nanoparticles for aqueous phase reforming of glycerol, the water-gas shift reaction and acetaldehyde decomposition attest to a strong support (ceria, ceria-zirconia, zirconia, titania) effect. Among the monometallic catalysts, Pt/TiO$_2$ and Pt/CeO$_2$ were, respectively, the most and least active in glycerol APR. The promoting effect of Re is strongest for Pt/CeO$_2$ and weakest for Pt/TiO$_2$. Incomplete Pt reduction in Pt/CeO$_2$ due to the strong metal-support interaction is the cause of its low APR activity. The strong interaction between Pt and Re improves total metal reduction in PtRe/CeO$_2$, increasing overall APR activity. The much higher APR activity of Pt/TiO$_2$ stems from (i) the involvement of hydroxyl groups of titania, making it the most active WGS catalyst among monometallic materials and (ii) the Brønsted acidity of these hydroxyl groups, catalyzing dehydration/C-O bond cleavage reactions. The support effect is most evident by comparison of data for Pt and PtRe on titania (this study) with data for Pt and PtRe on carbon (previous data in Chapter 3). The most salient differences between Pt(Re)/TiO$_2$ and Pt(Re)/C are then as follows:

- Pt/C and Pt/TiO$_2$ display similar activity in the glycerol APR reaction with different selectivity patterns due to the presence of acidic OH surface groups in the titania supported catalyst (higher C-O vs. C-C bond cleavage ratio). Re promotion introduces (additional) acidic OH surface groups on the bimetallic surface, increasing (i) the ratio of C-O over C-C bond cleavage reactions and (ii) the WGS activity. These effects are most pronounced for Pt/C, as Pt/TiO$_2$ already contains such acidic OH groups.

- The use of a reducible oxide support such as TiO$_2$ for Pt nanoparticles to activate water for the WGS reaction is preferred over alloying Pt with Re (PtRe/TiO$_2$ > Pt/TiO$_2$ > PtRe/C > Pt/C).

- The rate of C-C bond cleavage as determined by acetaldehyde decomposition experiments is higher for the PtRe alloys than for Pt. Initially, there is no difference in conversion rate between the carbon and titania supported catalysts, but the titania supported catalysts deactivate with time on stream. This is related to a more complex reaction mechanism induced by the presence of acid sites. Pt and PtRe on titania produce, besides CO and CH$_4$, a range of products due to ethanol dehydration (ethylene and ethane), ethylene reaction with the CH$_x$ surface intermediate (propylene and propane) and acetic acid. The activity order in overall glycerol conversion in APR is PtRe/C > PtRe/TiO$_2$ > PtRe/CeZrO$_2$ > PtRe/ZrO$_2$ > PtRe/CeO$_2$ > Pt/TiO$_2$ > Pt/C > Pt/ZrO$_2$ > Pt/CeZrO$_2$ > Pt/CeO$_2$.

References

[1] R.R. Davda, J.W. Shabaker, G.W. Huber, R.D. Cortright, J.A. Dumesic, Appl. Catal. B 56 (2005) 171-186.
[2] A. Wawrzetz, B. Peng, A. Hrabar, A. Jentys, A.A. Lemonidou, J.A. Lercher, J. Catal. 269 (2010) 411-420.
[3] A. Behr, J. Eilting, K. Irawadi, J. Leschinski, F. Lindner, Green Chem. 10 (2008) 13-30.
[4] C.H.C. Zhou, J.N. Beltramini, Y.X. Fan, G.Q.M. Lu, Chem. Soc. Rev. 37 (2008) 527-549.
[5] R.R. Davda, J.W. Shabaker, G.W. Huber, R.D. Cortright, J.A. Dumesic, Appl. Catal. B 43 (2003) 13-26.
[6] Y. Guo, M.U. Azmat, X.H. Liu, Y.Q. Wang, G.Z. Lu, Appl. Energ. 92 (2012) 218-223.
[7] S.C. Ammal, A. Heyden, J. Catal. 306 (2013) 78-90.
[8] J.B. Park, J. Graciani, J. Evans, D. Stacchiola, S.D. Senanayake, L. Barrio, P. Liu, J.F. Sanz, J. Hrbek, J.A. Rodriguez, J. Am. Chem. Soc. 132 (2009) 356-363.
[9] P. Panagiotopoulou, D.I. Kondarides, Catal. Today 112 (2006) 49-52.
[10] D.L. King, L.A. Zhang, G. Xia, A.M. Karim, D.J. Heldebrant, X.Q. Wang, T. Peterson, Y. Wang, Appl. Catal. B 99 (2010) 206-213.
[11] E.L. Kunkes, D.A. Simonetti, J.A. Dumesic, W.D. Pyrz, L.E. Murillo, J.G.G. Chen, D.J. Buttrey, J. Catal. 260 (2008) 164-177.
[12] L. Zhang, A.M. Karim, M.H. Engelhard, Z.H. Wei, D.L. King, Y. Wang, J. Catal. 287 (2012) 37-43.
[13] T.W. Kim, H.D. Kim, K.E. Jeong, H.J. Chae, S.Y. Jeong, C.H. Lee, C.U. Kim, Green Chem. 13 (2011) 1718-1728.
[14] J.W. Shabaker, R.R. Davda, G.W. Huber, R.D. Cortright, J.A. Dumesic, J. Catal. 215 (2003) 344-352.
[15] G. Wen, Y. Xu, H. Ma, Z. Xu, Z. Tian, Int. J. Hydrogen Energ. 33 (2008) 6657-6666.
[16] Z.A. Qiao, Z. Wu, S. Dai, ChemSusChem 6 (2013) 1821-1833.
[17] K. Liu, A. Wang, T. Zhang, ACS Catal. 2 (2012) 1165-1178.
[18] C. Ratnasamy, J.P. Wagner, Catal. Rev. 51 (2009) 325-440.
[19] T. Bunluesin, R.J. Gorte, G.W. Graham, Appl. Catal. B 15 (1998) 107-114.
[20] D.S. Newsome, Catal. Rev. 21 (1980) 275-318.
[21] J.W. Shabaker, G.W. Huber, R.R. Davda, R.D. Cortright, J.A. Dumesic, Catal. Lett. 88 (2003) 1-8.
[22] B. Roy, H. Sullivan, C.A. Leclerc, J. Power Sources 196 (2011) 10652-10657.

[23]   A.O. Menezes, M.T. Rodrigues, A. Zimmaro, L.E.P. Borges, M.A. Fraga, Renew. Energ. 36 (2011) 595-599.
[24]   K.G. Azzam, I.V. Babich, K. Seshan, L. Lefferts, J. Catal. 251 (2007) 153-162.
[25]   K.G. Azzam, I.V. Babich, K. Seshan, L. Lefferts, J. Catal. 251 (2007) 163-171.
[26]   K.G. Azzam, I.V. Babich, K. Seshan, L. Lefferts, Appl. Catal. B 80 (2008) 129-140.
[27]   H. Iida, A. Igarashi, Appl. Catal. A 303 (2006) 48-55.
[28]   H. Iida, A. Igarashi, Appl. Catal. A 303 (2006) 192-198.
[29]   H. Iida, K. Yonezawa, M. Kosaka, A. Igarashi, Catal. Comm. 10 (2009) 627-630.
[30]   W. Ruettinger, X.S. Liu, X.M. Xu, R.J. Farrauto, Top. Catal. 51 (2008) 60-67.
[31]   Y. Sato, K. Terada, S. Hasegawa, T. Miyao, S. Naito, Appl. Catal. A 296 (2005) 80-89.
[32]   Y. Sato, K. Terada, Y. Soma, T. Miyao, S. Naito, Catal. Comm. 7 (2006) 91-95.
[33]   K.G. Azzam, I.V. Babich, K. Seshan, B.L. Mojet, L. Lefferts, ChemCatChem 5 (2013) 557-564.
[34]   D.A.J.M. Ligthart, R.A. van Santen, E.J.M. Hensen, J. Catal. 280 (2011) 206-220.
[35]   D.A.J.M. Ligthart, R.A. van Santen, E.J.M. Hensen, Angew. Chem. Int. Edit. 50 (2011) 5306-5310.
[36]   D.A. Simonetti, E.L. Kunkes, J.A. Dumesic, J. Catal. 247 (2007) 298-306.
[37]   P. Ciambelli, V. Palma, A. Ruggiero, Appl. Catal. B 96 (2010) 18-27.
[38]   O.M. Busch, W. Brijoux, S. Thomson, F. Schuth, J. Catal. 222 (2004) 174-179.
[39]   J. Ryczkowski, Catal. Today 68 (2001) 263-381.
[40]   J. Datka, A.M. Turek, J.M. Jehng, I.E. Wachs, J. Catal. 135 (1992) 186-199.
[41]   S. Chen, S.P. Wang, X.B. Ma, and J.L. Gong, Chem. Commun., 2011, 47, 9345-9347.
[42]   T. Kawai, K.M. Jiang, and T. Ishikawa, J. Catal., 1996, 159, 288-295.
[43]   R.L. Manfro, A.F. da Costa, N.F.P. Ribeiro, M.M.V.M. Souza, Fuel Process. Technol. 92 (2011) 330-335.
[44]   A.V. Kirilin, A.V. Tokarev, H. Manyar, C. Hardacre, T. Salmi, J.P. Mikkola, D.Y. Murzin, Catal. Today (in press) DOI: 10.1016/j.cattod.2013.09.020.
[45]   M. Chia, Y.J. Pagan-Torres, D. Hibbitts, Q.H. Tan, H.N. Pham, A.K. Datye, M. Neurock, R.J. Davis, J.A. Dumesic, J. Am. Chem. Soc. 133 (2011) 12675-12689.
[46]   S. Koso, Y. Nakagawa, K. Tomishige, J. Catal. 280 (2011) 221-229.
[47]   L. Ma, Y.M. Li, D.H. He, Chinese J. Catal. 32 (2011) 872-876.
[48]   Y. Nakagawa, K. Mori, K. Chen, Y. Amada, M. Tamura, and K. Tomishige, Appl. Catal. A 468 (2013) 418-425.
[49]   O. Thinon, K. Rachedi, F. Diehl, P. Avenier, Y. Schuurman, Top Catal 52 (2009) 1940-1945.
[50]   P. Panagiotopoulou, A. Christodoulakis, D.I. Kondarides, S. Boghosian, J. Catal. 240 (2006) 114-125.
[51]   T. Matsuzaki, K. Takeuchi, T.A. Hanaoka, H. Arawaka, Y. Sugi, Appl. Catal. A 105 (1993) 159-184.
[52]   H.F. Wang, Z.P. Liu, J. Am. Chem. Soc. 130 (2008) 10996-11004.
[53]   J.E. Sutton, P. Panagiotopoulou, X.E. Verykios, D.G. Vlachos, J. Phys. Chem. C 117 (2013) 4691-4706.

Chapter 5

Carbon-supported bimetallic PtRe catalysts for aqueous phase reforming of glycerol prepared by catalytic reduction of Re on Pt nanoparticles

Summary

This study investigates the structure sensitivity of aqueous phase reforming of glycerol on carbon-supported Pt and PtRe catalysts. Pt/C with average Pt nanoparticle sizes of 1.2, 1.6 and 2.0 nm were obtained by reduction of a parent Pt/C catalyst at 400, 600 and 800 °C. The glycerol conversion in APR increased with increasing Pt particle size. The increased APR activity goes together with increased WGS activity to be attributed to more facile activation of water on step-edge sites. Decarbonylation rates (acetaldehyde decomposition) also increase with increasing particle size. PtRe nanoparticles were prepared by in situ catalytic reduction of the Re precursor on reduced Pt/C catalysts. The APR activity of Re-promoted catalysts increased for the smallest Pt particle size Pt/C catalyst, yet decreased for the other Pt/C catalysts containing larger Pt particles. In contrast, bimetallic catalysts proved to be much more active in the WGS reaction than their Pt-only parents. An increase in the reduction temperature of the PtRe alloys from 300 to 600 °C resulted in a further increase of the WGS activities. The different ways Re addition affects APR and WGS activities of Pt/C catalysts relates to different site requirements for these reactions. On the one hand, for WGS, the presence of some isolated Pt atoms at the nanoparticle surface, whose fraction increases upon reduction of the alloys at higher temperatures, is sufficient for obtaining a synergetic effect between Pt and Re. For APR, on the other hand, the presence of surface ensembles of Pt atoms is essential for obtaining high rates of the elementary reaction steps resulting in reforming.
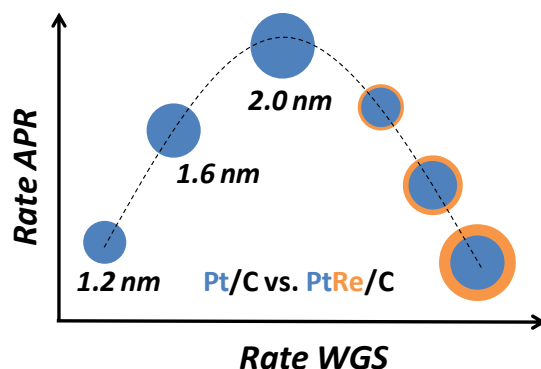
5.1 Introduction

Liquid phase processing of carbohydrate constituents of biomass is a promising method for generating clean energy and obtaining platform chemicals in a sustainable manner. Aqueous phase reforming (APR) of glycerol, an abundant feedstock formed as a by-product of biodiesel production, is an energy-efficient process for obtaining hydrogen, alkanes and alcohols. Besides, it serves as a model reaction to the aqueous phase reforming of more complex biomass constituents such as sugars. Important reaction steps in the APR reaction mechanism include dehydration, decarbonylation and the water-gas shift (WGS) reaction [1,2].

Because of its high activity, Pt is the most studied transition metal for liquid phase glycerol conversion reactions [1-7]. Although a significant number of studies have been devoted to the influence of the nature of the transition metal [3,8] and the support type [4,7,9,10], the effect of metal particle size (structure sensitivity) on the overall activity and selectivity in APR reactions has not been discussed in detail. For instance, Wawrzetz et al. [2] showed for Pt/Al_2O_3 that an increase of the Pt particle size from 1.1 to 2.6 nm resulted in a decrease in the H_2 and CO_2 formation rates, while the hydrodeoxygenation rate increased. However, Lehnert et al. [6] reported on a similar system that an increase in the Pt particle size from 1.6 to 3.2 nm resulted in an increase in the selectivity towards hydrogen in APR of glycerol, while the overall glycerol conversion did not change. As with increasing particle size the surface contains more face atoms at the expense of corner and edge atoms, it was argued that adsorption of oxygenated hydrocarbons for subsequent C-C cleavage would be easier on face atoms. Tomishige and co-workers also reported that small Ru particles were less selective towards 1,2-PDO formation than large ones [11].

Alloying precious metals with other transition metals (Re, W, Mo) increases the overall activity in liquid phase reforming and hydrogenolysis of biomass-derived polyols [12-16]. We have previously reported about the significant synergistic effect between Pt and Re in aqueous phase reforming of glycerol and its relation to the WGS reaction. A PtRe/C catalyst prepared by sequential impregnation with a Re:Pt ratio of 2 (first Pt then Re) was found to exhibit maximum activity as a function of the ratio between the two metals (Chapter 3 of this thesis). The average particle size of the PtRe alloy prepared by incipient wetness impregnation method decreased when compared to the monometallic Pt/C catalyst when the Re:Pt ratio was 0.5-1.

In this work, we employ the catalytic reduction method to deposit Re on pre-reduced Pt nanoparticles dispersed on a carbon support. The preparation of PtRe catalysts by catalytic reduction was first described by Pieck et al. [17-19]. It involves the surface redox reaction of a suitable Re precursor with H atoms adsorbed on a pre-reduced Pt nanoparticle catalyst. For catalytic reforming of naphtha feedstock it has been used to prepare PtRe/Al_2O_3 catalysts with a stronger Pt-Re interaction in comparison with bimetallic catalysts prepared by successive impregnation [17]. Here, we employ for the first time this method to prepare PtRe/C catalysts for use in the APR of glycerol. The bimetallic catalysts were reduced at 300

°C and 600 °C to investigate the effect of further mixing the alloyed metals in the particles on their catalytic performance. The catalysts were extensively characterized by TPR, TEM, XANES and EXAFS at the Pt and Re edges. Their activities were evaluated in model gas phase water-gas shift (WGS) and acetaldehyde decomposition reactions. Activitiy and selectivity trends in APR of glycerol are discussed.

5.2 Experimental

5.2.1 Preparation of catalysts

A set of Pt catalysts supported on activated carbon was prepared by incipient wetness impregnation method. After drying the activated carbon support (Norit RX3-extra) at 110 °C overnight, an appropriate amount of $H_2PtCl_6.6H_2O$ precursor was dissolved in deionized water. After impregnation of the Pt precursor, the sample was dried at 110 °C overnight. Pt/C with different average particle sizes were obtained by reducing portions of the parent catalyst at 400, 600, 800 and 1000 °C. The reduction was carried out under a flow of 30% H_2 in He (total flow 300 ml/min) at a rate of 2 °C/min and a dwell time of 4 h followed by passivation at room temperature under a ~1% O_2/He flow for 8 h. The bimetallic PtRe/C catalysts were prepared by the addition of Re on the Pt/C catalysts (molar Pt/Re ratio of 0.5) by the *in situ* catalytic reduction method based on published literature [17-20]. Reduced and passivated Pt/C catalysts were dispersed in a 0.05 M HCl solution (32 cm³/g catalyst) in a sealed glass reactor equipped with a magnetic stirrer. Air was removed by bubbling N_2 through the solution at room temperature for 1 h. In order to remove the N_2 and reduce the Pt, hydrogen was bubbled through the solution at 90 °C for 3 h. In a separate vessel, appropriate amount of Re precursor (NH_4ReO_4) was dissolved in 56 ml of 0.05 M HCl solution and stirred at room temperature by bubbling N_2 through the solution for 1 h in order to remove air. The Re precursor solution was added through a air-tight syringe to the Pt/C slurry under H_2 bubbling. The slurry was stirred at 90 °C for 1h under H_2. Then the reactor was cooled to room temperature and purged with N_2 before being exposed to air. The catalyst was filtered and washed with 2 L of deionized water. After drying at 110 °C overnight, the material was divided into two portions. One portion was reduced at 300 °C, while the other portion was reduced at 600 °C (ramp rate 5 °C/min) under a 20 % H_2/He flow for 2 h followed by passivation at room temperature under a ~1% O_2/He flow for 8 h. The passivated catalysts are denoted as Pt/C(r*X*)-Re(r*Y*), where *X* and *Y* represent the reduction temperature after Pt impregnation and Re addition, respectively.

5.2.2 Catalyst characterization

The metal loading of the materials was determined by inductively coupled plasma atomic emission spectrometry (ICP-AES) analysis performed on a Goffin Meyvis Spectro Cirus[ccd] apparatus. The samples were dissolved in a 3:1 HCl/HNO₃ solution.

Transmission electron micrographs (TEM) were acquired on a FEI Tecnai 20 transmission electron microscope at an acceleration voltage of 200 kV with a LaB₆ filament.

Typically, a small amount of sample was ground and suspended in pure ethanol, sonicated and dispersed over a Cu grid with a holey carbon film.

X-ray absorption spectroscopy was carried out at the Dutch-Belgian Beamline (Dubble) at the European Synchrotron Radiation Facility (ESRF), Grenoble, France (storage ring 6.0 GeV, ring current 200 mA). Data were collected at the Pt L_{III} and Re L_{III} edges in transmission mode. Energy selection was done by a double crystal Si(111) monochromator solid-state detector. Background removal was carried out by standard procedures. EXAFS analysis was then performed with EXCURVE931 on k^3-weighted unfiltered raw data using the curved wave theory. Phase shifts were derived from ab initio calculations using Hedin-Lundqvist exchange potentials and Von Barth ground states. Energy calibration was carried out with Pt foil. The amplitude reduction factor S_0^2 associated with central atom shake-up and shake-off effects was set at 0.99 by calibration of the first- and second shell Pt–Pt coordination numbers to 12 and 4, respectively, for the k^3-weighted EXAFS fits of the Pt foil. For the spectra recorded at the Re L_{III} edge, Re powder was fitted as the reference spectra and So^2 for the Re-Re shell was set as 0.75. Spectra were recorded in a stainless-steel controlled atmosphere cell. The cell was heated with two firerods controlled by a temperature controller. A thermocouple was placed close to the catalyst sample. Typically, a predetermined amount of finely grinded sample was pressed in a stainless steel holder and placed in the cell. Carbon foils were held between two carbon spacers. Gases (He and H_2) were delivered by thermal mass flow controllers (Bronkhorst). The catalyst sample was heated at a rate of 10 °C/min, whilst recording XANES spectra. After reduction at 300 °C for 15 min, the sample was cooled and two EXAFS spectra were recorded. Subsequently, the sample was heated in a He flow and at 150 °C a CO flow was introduced and redirected through a Controlled Evaporator Mixer (CEM) to obtain a feed mixture with a H_2O:CO ratio of 3. The sample was heated at a rate of 10 °C/min to 200, 250 and 300 °C. XANES and EXAFS spectra were recorded during WGS reaction.

Temperature programmed reduction (TPR) experiments were performed in a flow apparatus equipped with a fixed-bed reactor, a computer-controlled oven and a thermal conductivity detector. Typically, 25 mg catalyst was loaded in a tubular quartz reactor. The sample was reduced in 4 vol% H_2 in N_2 at a flow rate of 8 ml/min, whilst heating from room temperature up to 800 °C at a ramp rate of 10 °C/min. The H_2 signal was calibrated using a CuO/SiO_2 reference catalyst.

5.2.3 Catalytic activity measurements

5.2.3.1 Aqueous phase reforming of glycerol

APR reactions were carried out at 225 °C under 25 bar initial N_2 pressure using 60 g of 10 wt% aqueous glycerol solution in a 120 ml autoclave. An amount of 75 mg of reduced catalyst was loaded in the autoclave together with an appropriate amount of deaerated water in a N_2-flushed glovebag. The autoclave was purged five times with 10 bars of N_2 in order to remove air from the autoclave. A 50/50 w/w mixture of glycerol and water was charged into the reactor from an external holding vessel after the autoclave containing water and the

catalyst reached the desired reaction temperature. The stirring speed was 600 rpm. Liquid samples were withdrawn by a ROLSI injector and analyzed by a Trace GC equipped using a Stabilwax column and a FID detector. Gas samples were collected online and analyzed by a Focus GC equipped with a TCD detector and CP-Porabond Q and RT-MolSieve-5A columns. The carbon product selectivities were calculated by:

$$S_i(\%) = \frac{mol\ of\ product_i\ formed \times number\ of\ C\ atoms}{mol\ of\ glycerol\ in\ the\ feed \times conversion \times 3} \times 100$$

5.2.3.2 Acetaldehyde decomposition

Acetaldehyde decomposition experiments were performed in a continuous flow reactor setup. Hydrogen and acetaldehyde were fed as the feed components. Acetaldehyde was fed by bubbling helium through a saturator kept at such a temperature to obtain a gas-phase acetaldehyde concentration of 3 vol%. Samples were first reduced at 300 $^\circ$C. The reaction was carried out at 225 °C at a GHSV of 7200 $ml_{acetaldehyde}/g_{cat}$.h. The reactor effluent was analyzed by online gas chromatography (Interscience GC-8000 Top, permanent gases on Shincarbon ST80/100 packed column connected to a TCD and hydrocarbons on a RT-Q bond column connected to a FID).

5.2.3.3 Water-gas shift reaction (WGS)

WGS reaction experiments were performed in a parallel ten-flow microreactor system [21]. Steam was supplied by evaporation of deionized water in a Controlled Evaporator Mixer unit (Bronkhorst) in combination with a liquid flow controller. Gas flows were controlled by thermal mass flow controllers (Brooks and Bronkhorst). All tubings were kept above 100 °C after the point of steam introduction. The dry product gas mixture was analyzed by an online gas chromatograph (Interscience CompactGC) equipped with TCD columns (Porapak Q and Molecular sieve 5A). Experiments were carried out in a mixture of 2.5 vol% CO and 7.5 vol% H_2O balanced by He at a dry GHSV of $\sim 1 \times 10^5$ h^{-1} in the temperature range 150-400 °C. Typically, the catalyst was diluted with an appropriate amount of SiC of the same sieve fraction. The material was contained between two quartz wool plugs in a quartz reactor. Prior to catalytic activity measurements, the catalyst was reduced in a flow of 20 vol% H_2 in He at a ramp rate of 5 °C/min to 300 ^{o}C followed by an isothermal period of 0.5 h. The reactor was cooled in He to the reaction temperature. The catalyst was exposed to the reaction mixture for 10 min prior to the start of recording product gas mixture. At each reaction temperature, the CO conversion was followed for 1.5 h.

5.3 Results and discussion

5.3.1 Catalyst characterization

The metal loadings of the mono- and bimetallic catalysts as determined by ICP elemental analysis are shown in Table 5.1. The Pt content of the parent Pt/C catalyst was 2.3 wt%. The Pt-to-Re molar ratio of the bimetallic catalysts was found to be approximately 0.6, close to the targeted value. TEM analysis of the Pt/C catalysts shows that the Pt particles in

the monometallic catalysts become larger with increasing reduction temperature (Fig. 5.1 and Table 5.1). Pt/C(r400) contained the smallest Pt particles with an average size of 1.2 nm. Reduction at 600 and 800 °C led to modest increases of the average particle size to 1.6 and 2.0 nm, respectively, while the average particle size increased to 4.2 nm after reduction at 1000 °C. Especially, in the latter catalyst, the development of some well-facetted Pt nanoparticles is seen. TEM analysis of the bimetallic catalysts did not evidence significant changes of these average particle sizes upon Re addition (Table 5.1). It is also seen that there is not a significant difference in particle size between re-reduction of the freshly prepared PtRe/C catalysts at 300 *vs*. 600 °C.

Table 5.1: Metal loadings and average particle sizes for the carbon-supported catalysts.

Catalyst	Metal loading[1] (wt%)		Pt/Re ratio	Average particle size[2] (nm)
	Pt	Re		
Pt/C(r400)				1.2
Pt/C(r600)				1.6
Pt/C(r800)	2.27	-	-	2.0
Pt/C(r1000)				4.2
Pt/C(r400)-Re(r300)				1.3
Pt/C(r400)-Re(r600)	2.19	3.51	0.60	1.3
Pt/C(r600)-Re(r300)				1.5
Pt/C(r600)-Re(r600)	2.19	3.85	0.54	1.3
Pt/C(r800)-Re(r300)				2.6
Pt/C(r800)-Re(r600)	2.19	3.54	0.59	2.5

[1] determined by ICP analysis
[2] determined by TEM analysis of the reduced catalysts

H$_2$-TPR was used to follow the reduction of the Pt catalysts (Fig. 5.2). The metal precursor in all catalysts was reduced below 300 °C in agreement with our previous work presented in Chapter 3 and literature [22]. The weak broad features observed for all Pt/C catalysts starting above 400 °C and ending around 800 °C are related to the reduction of the oxygen functionalities on the activated carbon support. The reduction features in the TPR patterns of the bimetallic PtRe catalysts prepared by the catalytic reduction method are substantially lower than those seen in PtRe/C prepared by sequential impregnation (Chapter 3). The main cause of this difference is the pre-reduction of Pt/C prior to catalytic reduction deposition of Re. The presence of several peaks at lower temperatures for the bimetallic catalysts may be due to the presence of PtRe nanoparticles of different size.
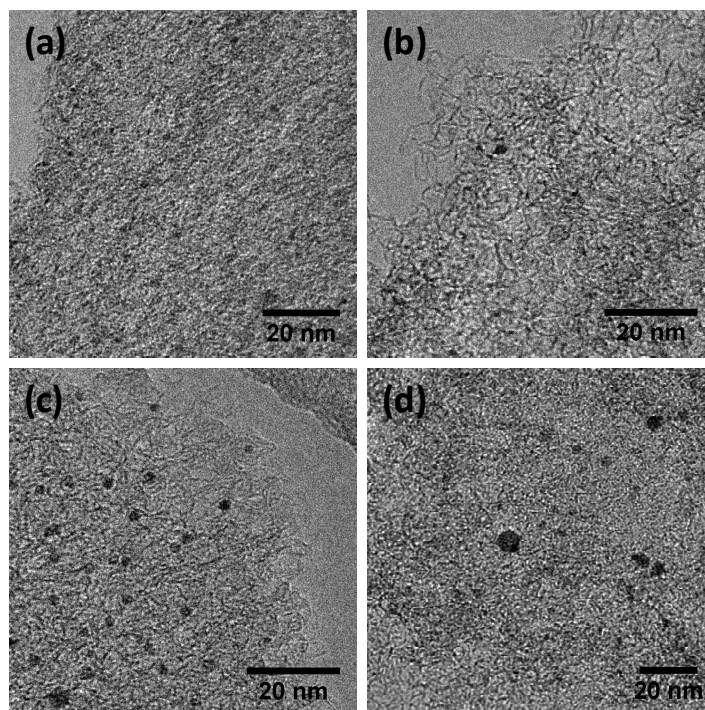
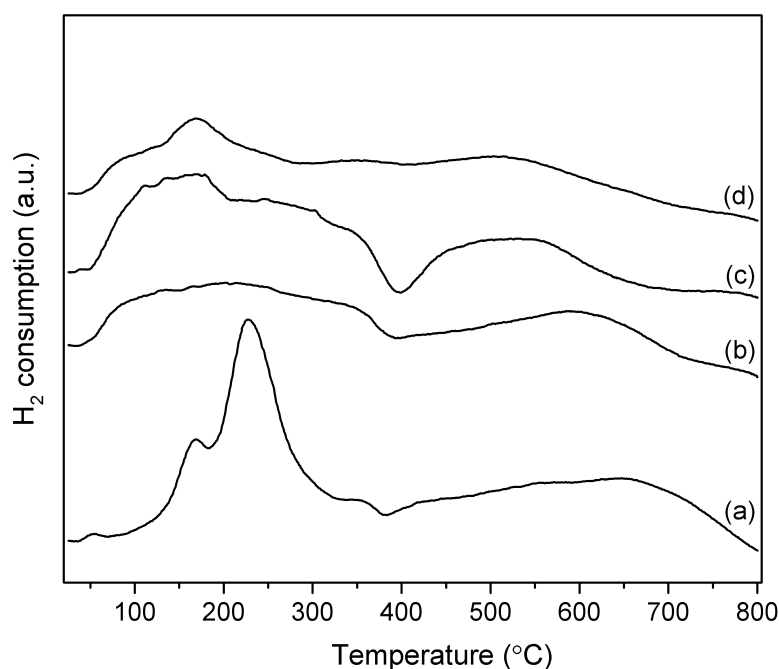**Figure 5.1:** TEM pictures of (a) Pt/C(r400), (b) Pt/C(r600) (c) Pt/C(r800) and (d) Pt/C(r1000).

Figure 5.2: TPR profiles of (a) Pt/C, (b) Pt/C(r400)-Re, (c) Pt/C(r600)-Re and (d) Pt/C(r800)-Re.

Near-edge spectra at the Pt L_{III} and Re L_{III} edges were recorded for catalysts reduced at 300 °C (Fig.s 5.3 and 5.4). The spectra of the Pt/C catalysts closely resemble that of the Pt foil. This also applies to the bimetallic catalysts. For the bimetallic catalysts the XANES spectra at the Re L_{III} edge show small shifts in the edge energy (1.2-1.7 eV) when compared to that of the reference Re powder. These values are similar to what we observed for a PtRe/C

catalyst prepared by successive impregnation in our previous study (Chapter 3). Such small shifts in the Re L_{III} edge XANES spectra are attributed to the presence of a small portion of Re in a partially oxidated state without any contact with Pt [23,24]. The Fourier Transforms of the EXAFS spectra at the Pt L_{III} edge show the presence of a single Pt-Pt shell for all four Pt catalysts (Table 5.2). The coordination number of the Pt-Pt shell increases with reduction temperature, e.g. the coordination numbers for Pt/C(r400) and Pt/C(r1000) are 6.3 and 10, respectively. This trend is consistent with the increasing Pt particle size apparent from TEM analysis. In line with the increasing coordination numbers, the bond distance of the Pt-Pt shell gradually increases with reduction temperature. We determined the average Pt particle size on the basis of the Pt-Pt shell coordination numbers by using the approach developed by Calvin et al. [25-28]. For Pt/C reduced at 400, 600, 800 and 1000 °C, average Pt particle sizes determined by this method amounted to 0.8, 1.0, 1.2 and 2.5 nm, respectively. We mention two limitations of this approach. Firstly, the thus determined particle size usually underestimates the real particle size as it is based on atom average coordination numbers and the accuracy becomes lower as the coordination number approaches that of bulk Pt [25]. Secondly, the TEM analysis shows that there is a broad distribution of Pt particle sizes, especially upon high-temperature reduction, making use of the EXAFS-derived Pt particle sizes at most qualitative. When Re is added to the reduced Pt/C catalysts, the coordination numbers of the Pt-M and Re-M shells increase with reduction temperature of the parent Pt/C catalyst. The CN of the Pt-M shells for the bimetallic particles are similar to what we observed for the monometallic Pt/C catalysts. The CN of the Re-M shells increase from 5.3 to 5.9 as with an increase in the reduction temperature of the parent Pt/C catalyst from 400 to 800 °C. This suggests that the thickness of the Re shell formed around Pt slightly increases as the core Pt nanoparticles become larger.
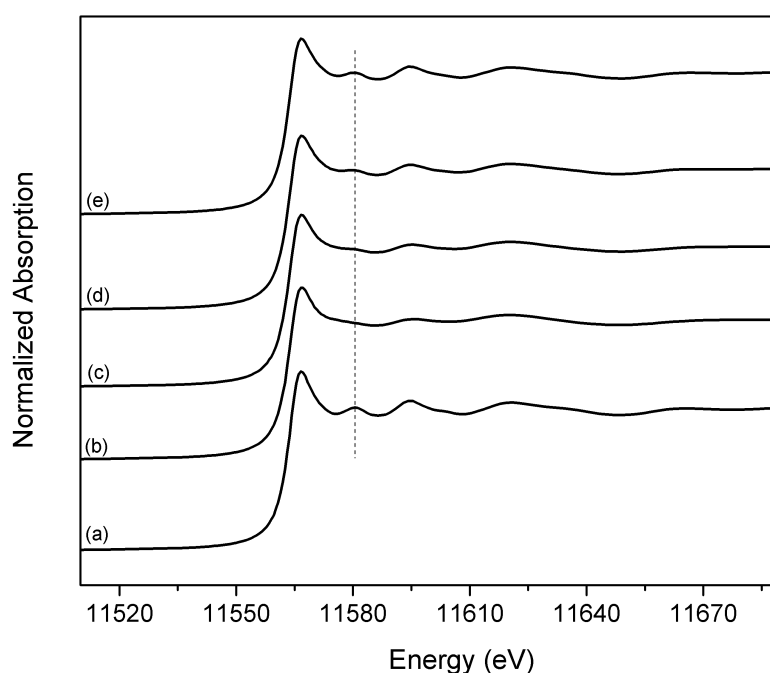

Figure 5.3: Pt L_{III}-edge XANES spectra of (a) Pt foil, (b) Pt/C(r400), (c) Pt/C(r600), (d) Pt/C(r800) and (e) Pt/C(r1000). All catalysts were reduced at 300 °C before recording the XANES spectra.
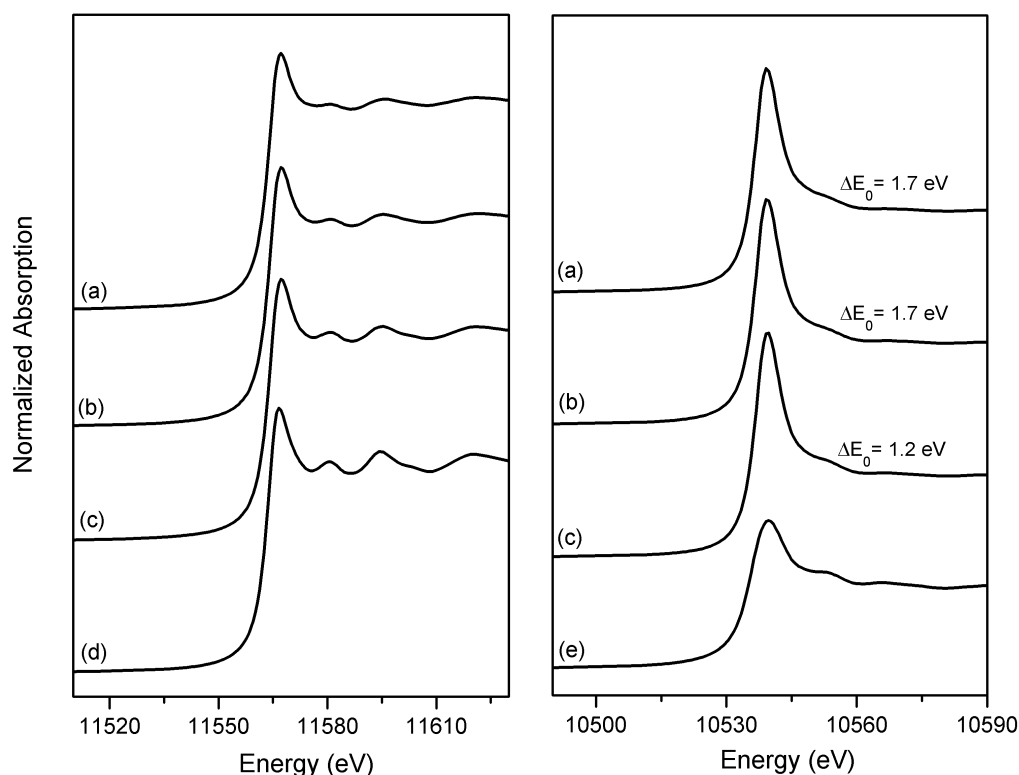
Figure 5.4: Pt L_{III}-edge (left) and Re L_{III}-edge (right) XANES spectra of Pt/C(r400)-Re(r300) (a), Pt/C(r600)-Re(r300) (b), Pt/C(r800)-Re(r300) (c) reduced at 300 °C. XANES spectra of Pt foil (d) and Re powder (e) are plotted as reference.

Table 5.2: Fit parameters of k^3-weighted EXAFS spectra at the Pt L_{III}-edge of supported Pt and PtRe catalysts reduced at 300 °C. M represents the backscatterer atom (Pt or Re).

Catalyst	EXAFS analysis				
	Shell	R (Å)	CN	$\Delta\sigma^2$ (Å^2)	E_0 (eV)
Pt/C(r400)	Pt-Pt	2.685	6.3	0.010	-3.3
Pt/C(r600)	Pt-Pt	2.719	7.2	0.011	-7.1
Pt/C(r800)	Pt-Pt	2.755	7.7	0.008	-10.0
Pt/C(r1000)	Pt-Pt	2.763	10	0.008	-10.5
Pt/C(r400)-Re(r300)	Pt-M$_{Pt}$	2.715	5.8	0.009	-8.8
	Re-M$_{Re}$	2.656	5.3	0.007	-3.2
Pt/C(r600)-Re(r300)	Pt-M$_{Pt}$	2.727	6.8	0.009	-9.5
	Re-M$_{Re}$	2.662	5.5	0.007	-4.1
Pt/C(r800)-Re(r300)	Pt-M$_{Pt}$	2.747	8.1	0.008	-10.5
	Re-M$_{Re}$	2.682	5.9	0.007	-6.8

5.3.2 Catalytic activity measurements

The carbon-supported Pt and PtRe catalysts were evaluated for their activity in APR of glycerol at 225 °C. Fig. 5.5 shows glycerol conversion as a function of the reaction time. The glycerol conversion of the Pt/C catalysts strongly increases with reduction temperature. Notably, glycerol conversion for Pt/C(r800) is about 3 times higher than that for Pt/C(r400).

The APR reaction mechanism proceeds via two main routes. The first path starts with the dehydration (C-O cleavage) of glycerol and subsequent hydrogenation leads to the production of diols, monofunctional alcohols and alkanes. Decarbonylation pathway mainly generates CO and ethylene glycol. Due to the low temperature and high water activity, nearly all CO is converted with water to CO_2 and H_2 with high selectivity by the WGS reaction [2]. The selectivity trends for all catalysts after 320 min of APR reaction are collected in Table 5.3. The detailed product distributions for all catalysts are given in Tables 5.4-5.12. From the trends in H_2 and CO_2 yields, it is evident that the rate of reforming increases with the Pt particle size. The selectivity towards alkanes and hydroxyacetone decreases with increasing particle size, opposite of the trend in 1,2-PDO selectivity. The increased selectivity of ethylene glycol implies an increase in decarbonylation rate with increasing Pt particle size. In line with this, the overall ratio of C-O/C-C cleavage products is found to be the highest for Pt/C(r400) (Table 5.3). An increase in activity with increasing Pt particle size was also noted by Lehnert et al. in APR of glycerol [6]. Recently, Kirilin et al. found similar results in APR of xylitol over Pt/C catalysts with particle sizes in the range 1.5-9 nm [29]. The reaction was found to be structure sensitive and the intrinsic activity of the Pt loaded catalysts were shown to increase linearly with increasing average Pt cluster size.
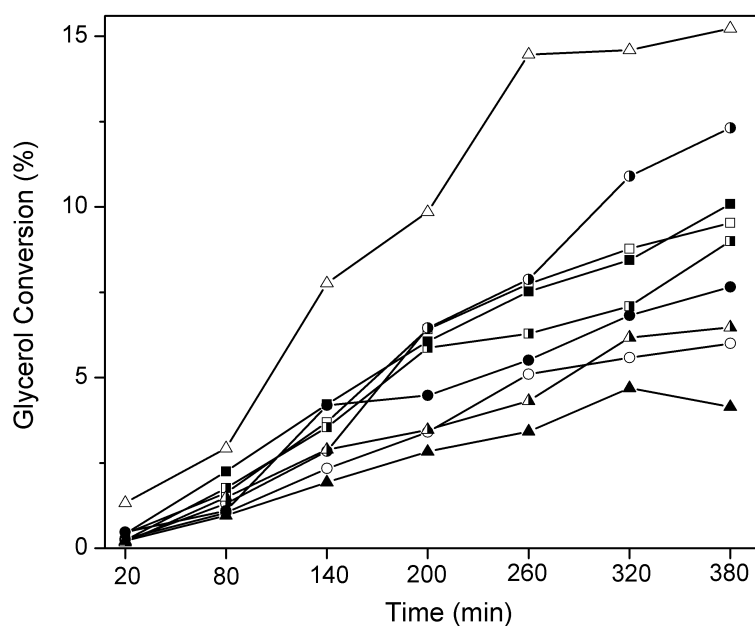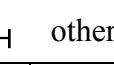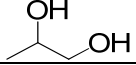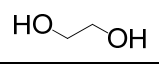

Figure 5.5: Glycerol conversion by time in APR of glycerol over the Pt/C(r400) (*circle*), Pt/C(r600) (*square*), Pt/C(r800) (*triangle*) catalysts before (open symbols) and after Re addition by catalytic reduction method followed by reduction at 300 °C (half closed symbols) and 600 °C (closed symbols). All catalysts reduced at 300 °C prior to reaction. (Feed: 60 g of 10 wt% aqueous glycerol solution, catalyst amount: 75 mg).
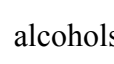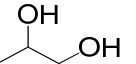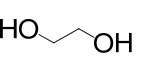
Table 5.3: Conversion (X) of glycerol (%), Yield (Y) of H_2 and CO_2, product selectivities (%) in APR of glycerol for the carbon supported Pt and PtRe catalysts after 320 min of reaction at 225 °C. (Feed: 60 g of 10 wt% aqueous glycerol solution, catalyst amount: 75 mg).

Catalyst	Xglycerol	CO_2	CH_4	C_2H_6	C_3H_8	HO-acetone	propanediol	ethylene glycol	others[1]	Y H_2	Y CO_2	C-O/C-C
Pt/C(r400)	5.6	35.6	6.1	7.5	2.1	28.0	17.4	1.0	2.3	9.6	7.0	0.9
Pt/C(r600)	8.8	43.8	6.6	5.9	1.2	13.1	25.8	1.6	2	17.2	13.0	0.6
Pt/C(r800)	14.6	39.7	2.9	3.0	1.2	10.6	36.7	3.3	2.6	20.5	18.8	0.6
Pt/C(r400)-Re(r300)	10.9	33.8	5.3	12.6	6.4	10.9	26.1	2.6	2.3	9.5	14.2	1.1
Pt/C(r400)-Re(r600)	6.8	33.5	5.7	11.4	4.6	23.0	16.8	1.4	3.6	7.8	7.5	1.1
Pt/C(r600)-Re(r300)	7.1	33.4	5.3	13.5	6.4	19.1	17.5	1.7	3.1	7.6	8.0	1.1
Pt/C(r600)-Re(r600)	8.5	29.9	4.8	11.4	5.8	24.9	17.2	1.5	4.5	7.3	9.0	1.2
Pt/C(r800)-Re(r300)	6.2	18.5	1.6	6.7	4.5	55.0	10.1	1.1	2.5	5.0	3.1	1.9
Pt/C(r800)-Re(r600)	4.7	15.2	1.4	6.1	4.4	54.2	13.8	1.4	3.5	2.3	2.3	2.3
Pt/C[2]	6.3	46.5	9.8	9.0	1.9	12.0	18.0	1.6	1.2	15	8.7	0.7
PtRe/C[2]	30.2	34.4	5.0	17.7	13.0	2.1	16.2	2.2	9.4	22	45	1.3

[1] other products include alcohols (methanol, ethanol, 1-propanol, 2-propanol), acids (acetic acid, propanoic acid) and CO, propionaldehyde, 1,3-propanediol.
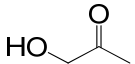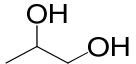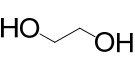[2] prepared by impregnation on activated carbon followed by reduction at 300 °C; for PtRe sequential impregnation was used .

Table 5.4: Conversion (X) of glycerol (%) and product selectivities (%) in APR of glycerol for Pt/C(r400) as a function of time at 225 °C. (Feed: 60 g of 10 wt% aqueous glycerol solution, catalyst amount: 75 mg).

Time (min)	Xglycerol	CO_2	CH_4	C_2H_6	C_3H_8	HO-acetone	propanediol	ethylene glycol	alcohols[1]	acids[2]	others[3]
20	0.3	18.7	0.8	2.7	0	59.6	5.2	1.2	3.0	3.2	5.6
80	1.0	25.2	1.7	3.3	0.7	58.4	5.5	1.1	1.0	1.2	1.9
140	2.3	29.4	2.8	4.4	1.1	48.9	9.3	1.0	1.3	0.9	0.9
200	3.4	37.6	5.5	6.6	1.9	34.2	11.1	0.9	0.9	0.7	0.6
260	5.1	36.5	6.1	7.3	2.1	30.5	14.5	0.9	1.0	0.7	0.4
320	5.6	35.6	6.1	7.5	2.1	28.0	17.4	1.0	1.1	0.8	0.4
380	6.0	38.8	6.2	7.8	2.2	24.9	16.9	1.0	1.1	0.8	0.3

[1] alcohols: methanol, ethanol, 1-propanol, 2-propanol, [2] acids: acetic acid, propanoic acid, [3] others: CO, propionaldehyde, 1,3-propanediol

Table 5.5: Conversion (X) of glycerol (%) and product selectivities (%) in APR of glycerol for Pt/C(r600) as a function of time at 225 °C. (Feed: 60 g of 10 wt% aqueous glycerol solution, catalyst amount: 75 mg).
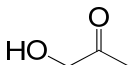
Time (min)	Xglycerol	CO_2	CH_4	C_2H_6	C_3H_8	hydroxyacetone	1,2-propanediol	ethylene glycol	alcohols[1]	acids[2]	others[3]
20	0.4	13.7	0.7	1.0	0	74.9	3.8	1.7	1.1	1.3	1.8
80	1.6	32.2	3.0	1.7	0.3	45.7	12.6	1.7	1.2	0.8	0.8
140	3.7	47.8	6.8	4.2	1.1	22.9	13.8	1.2	1.1	0.5	0.6
200	6.4	41.5	6.0	4.1	0.9	18.4	25.1	2.1	1.0	0.5	0.4
260	7.8	38.7	5.9	4.3	0.9	15.9	29.9	2.3	1.2	0.6	0.3
320	8.8	43.8	6.6	5.9	1.2	13.1	25.8	1.6	1.2	0.5	0.3
380	9.5	45.2	7.1	7.2	1.5	11.1	24.4	1.8	1.0	0.5	0.2

[1] alcohols: methanol, ethanol, 1-propanol, 2-propanol
[2] acids: acetic acid, propanoic acid
[3] others: CO, propionaldehyde, 1,3-propanediol

Table 5.6: Conversion (X) of glycerol (%) and product selectivities (%) in APR of glycerol for Pt/C(r800) as a function of time at 225 °C. (Feed: 60 g of 10 wt% aqueous glycerol solution, catalyst amount: 75 mg).
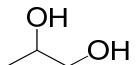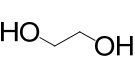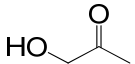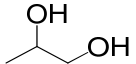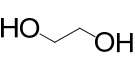
Time (min)	Xglycerol	CO_2	CH_4	C_2H_6	C_3H_8	hydroxyacetone	1,2-propanediol	ethylene glycol	alcohols[1]	acids[2]	others[3]
20	1.3	64.8	3.8	3.8	0.9	21.1	2.9	0.8	0.6	0.4	0.9
80	2.9	17.3	0.6	0.4	0.1	37.1	35.9	4.5	2.6	0.9	0.6
140	7.8	44.3	2.8	1.9	0.8	14.7	30.0	3.0	1.7	0.6	0.2
200	9.9	46.4	3.1	2.5	1.0	12.1	29.8	2.6	1.7	0.6	0.2
260	14.5	36.0	2.5	2.3	0.9	8.7	43.7	4.5	0.7	0.5	0.2
320	14.6	39.7	2.9	3.0	1.2	10.6	36.7	3.3	1.7	0.8	0.1
380	15.2	41.1	3.0	3.5	1.4	10.6	34.7	3.1	1.7	0.8	0.1

[1] alcohols: methanol, ethanol, 1-propanol, 2-propanol
[2] acids: acetic acid, propanoic acid
[3] others: CO, propionaldehyde, 1,3-propanediol

Table 5.7: Conversion (X) of glycerol (%) and product selectivities (%) in APR of glycerol for Pt/C(r400)-Re(r300) as a function of time at 225 °C. (Feed: 60 g of 10 wt% aqueous glycerol solution, catalyst amount: 75 mg).

Time (min)	Xglycerol	CO_2	CH_4	C_2H_6	C_3H_8	hydroxyacetone	1,2-propanediol	ethylene glycol	alcohols[1]	acids[2]	others[3]
20	0.2	9.4	0	0	0	69.2	6.2	2.8	2.6	4.6	5.2
80	1.3	10.7	0.6	1.2	0.7	60.8	16.1	3.1	2.7	2.2	1.9
140	2.8	23.7	2.3	4.7	2.7	37.4	21.2	2.8	2.1	1.9	1.2
200	6.5	36.4	4.9	10.5	5.7	19.7	17.4	1.8	1.4	1.4	0.8
260	7.9	36.1	5.6	12.7	6.7	15.9	17.7	1.7	1.2	1.7	0.7
320	10.9	33.8	5.3	12.6	6.4	10.9	26.1	2.6	0.5	1.3	0.5
380	12.3	38.4	5.0	12.9	6.8	12.4	19.0	1.6	1.3	1.9	0.7

[1] alcohols: methanol, ethanol, 1-propanol, 2-propanol
[2] acids: acetic acid, propanoic acid
[3] others: CO, propionaldehyde, 1,3-propanediol

Table 5.8: Conversion (X) of glycerol (%) and product selectivities (%) in APR of glycerol for Pt/C(r400)-Re(r600) as a function of time at 225 °C. (Feed: 60 g of 10 wt% aqueous glycerol solution, catalyst amount: 75 mg).
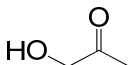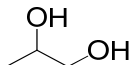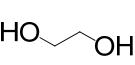
Time (min)	Xglycerol	CO_2	CH_4	C_2H_6	C_3H_8	hydroxyacetone	1,2-propanediol	ethylene glycol	alcohols[1]	acids[2]	others[3]
20	0.5	36.7	3.5	9.6	4.2	38.3	0	1.0	0.4	1.4	4.9
80	1.1	8.7	0.4	1.0	0.4	71.6	9.3	2.1	1.5	1.9	3.1
200	4.5	34.8	5.4	9.1	3.8	28.9	13.5	1.2	0.8	1.2	1.3
260	5.5	36.6	5.9	10.9	4.4	23.7	13.7	1.3	0.9	1.4	1.2
320	6.8	33.5	5.7	11.4	4.6	23.0	16.8	1.4	1.0	1.7	0.9
380	7.7	32.8	5.7	12.1	4.7	21.5	18.7	1.4	0.8	1.7	0.6

[1] alcohols: methanol, ethanol, 1-propanol, 2-propanol
[2] acids: acetic acid, propanoic acid
[3] others: CO, propionaldehyde, 1,3-propanediol

Table 5.9: Conversion (X) of glycerol (%) and product selectivities (%) in APR of glycerol for Pt/C(r600)-Re(r300) as a function of time at 225 °C. (Feed: 60 g of 10 wt% aqueous glycerol solution, catalyst amount: 75 mg).
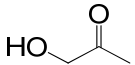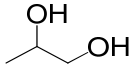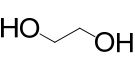
Time (min)	Xglycerol	CO_2	CH_4	C_2H_6	C_3H_8	hydroxyacetone	1,2-propanediol	ethylene glycol	alcohols[1]	acids[2]	others[3]
80	1.8	22.8	2.1	4.3	2.4	44.3	14.3	2.8	1.5	0.9	4.6
140	3.6	32.1	4.2	8.7	4.9	28.4	14.9	2.0	0.9	0.7	3.2
200	5.9	28.3	4.1	9.1	5.1	33.3	13.9	1.4	1.4	1.2	2.2
260	6.3	31.1	4.7	11.5	5.7	23.3	18.5	1.8	0.9	0.9	1.6
320	7.1	33.4	5.3	13.5	6.4	19.1	17.5	1.7	0.9	1.1	1.1
380	9.0	29.4	4.8	13.1	6.0	24.8	16.5	1.4	1.0	1.9	1.1

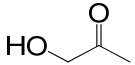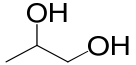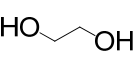[1]alcohols: methanol, ethanol, 1-propanol, 2-propanol
[2]acids: acetic acid, propanoic acid
[3]others: CO, propionaldehyde, 1,3-propanediol

Table 5.10: Conversion (X) of glycerol (%) and product selectivities (%) in APR of glycerol for Pt/C(r600)-Re(r600) as a function of time at 225 °C. (Feed: 60 g of 10 wt% aqueous glycerol solution, catalyst amount: 75 mg).

Time (min)	Xglycerol	CO_2	CH_4	C_2H_6	C_3H_8	hydroxyacetone	1,2-propanediol	ethylene glycol	alcohols[1]	acids[2]	others[3]
80	2.3	15.2	1.8	2.7	2.0	61.0	10.2	1.7	2.3	1.8	1.3
140	4.2	26.5	3.9	7.2	4.7	38.6	13.3	1.6	1.4	1.5	1.3
200	6.1	27.9	4.2	8.7	4.8	32.2	16.3	1.6	1.3	1.8	1.2
260	7.5	27.5	4.2	9.3	4.9	24.8	24.1	2.2	0.6	1.5	0.9
320	8.5	29.9	4.8	11.4	5.8	24.9	17.2	1.5	1.3	2.2	1.0
380	10.1	29.8	4.7	11.9	5.8	16.3	26.2	2.3	1.0	1.3	0.7

[1]alcohols: methanol, ethanol, 1-propanol, 2-propanol
[2]acids: acetic acid, propanoic acid
[3]others: CO, propionaldehyde, 1,3-propanediol

Table 5.11: Conversion (X) of glycerol (%) and product selectivities (%) in APR of glycerol for Pt/C(r800)-Re(r300) as a function of time at 225 °C. (Feed: 60 g of 10 wt% aqueous glycerol solution, catalyst amount: 75 mg).
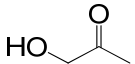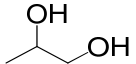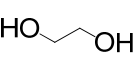
Time (min)	Xglycerol	CO_2	CH_4	C_2H_6	C_3H_8	hydroxyacetone	1,2-propanediol	ethylene glycol	alcohols[1]	acids[2]	others[3]
20	0.2	5.6	0	0	0	85.1	0	0	2.5	0.8	6.0
80	1.5	13.0	1.0	2.5	2.4	72.1	4.2	1.0	1.0	1.4	1.4
140	2.9	19.5	2.0	5.9	4.4	58.3	5.7	0.9	0.9	1.4	1.0
200	3.5	22.7	2.8	8.5	6.0	45.5	10.2	1.3	0.6	1.1	1.3
260	4.3	21.2	2.4	8.4	5.7	44.8	12.4	1.6	1.0	1.4	1.1
320	6.2	18.5	1.6	6.7	4.5	55.0	10.1	1.1	0.9	0.7	0.9
380	6.5	15.8	1.7	6.9	4.1	56.7	11.3	1.1	1.0	0.7	0.7

[1]alcohols: methanol, ethanol, 1-propanol, 2-propanol
[2]acids: acetic acid, propanoic acid
[3]others: CO, propionaldehyde, 1,3-propanediol

Table 5.12: Conversion (X) of glycerol (%) and product selectivities (%) in APR of glycerol for Pt/C(r800)-Re(r600) as a function of time at 225 °C. (Feed: 60 g of 10 wt% aqueous glycerol solution, catalyst amount: 75 mg).
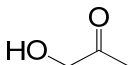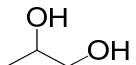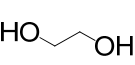
Time (min)	Xglycerol	CO_2	CH_4	C_2H_6	C_3H_8	hydroxyacetone	1,2-propanediol	ethylene glycol	alcohols[1]	acids[2]	others[3]
80	1.0	16.1	1.1	2.2	2.2	64.9	6.7	1.4	0.7	0.8	3.9
140	1.9	22.5	2.0	6.1	5.4	50.7	7.5	1.2	0.9	0.7	3.0
200	2.8	20.7	1.8	6.8	5.6	51.5	7.8	1.1	1.2	1.0	2.5
260	3.4	18.7	1.8	6.9	5.4	51.2	10.8	1.4	0.7	1.1	2.0
320	4.7	15.2	1.4	6.1	4.4	54.2	13.8	1.4	0.5	1.2	1.8
380	4.1	18.8	1.8	7.9	5.5	50.6	10.5	1.1	0.5	1.7	1.6

[1]alcohols: methanol, ethanol, 1-propanol, 2-propanol
[2]acids: acetic acid, propanoic acid
[3]others: CO, propionaldehyde, 1,3-propanediol

The addition of Re to the Pt/C catalysts reduced at different temperatures has significant effects on the catalytic performance. The glycerol conversion over Pt/C(400)-Re(300) is nearly two times higher than the parent Pt/C(400) catalyst. The increase in overall glycerol conversion for Pt/C(r400)-Re(r600) is much smaller than for Pt/C(r400)-Re(r300). For the Pt/C catalysts initially reduced above 400 °C, it is seen that Re addition leads to a decrease of the catalytic activity in all cases, whose extent becomes more significant for Pt/C catalysts reduced at higher temperature. The temperature of the second reduction step also has a small effect on the catalytic activity. Regarding the product selectivities, the ratio of products formed via C-O bond cleavage to those formed via C-C bond cleavage reactions is higher for the PtRe catalysts when compared to the Pt/C catalysts (Table 5.3). This points to the relatively higher rate of dehydration reactions over the bimetallic catalysts. The promotion of C-O bond cleavage reaction rates upon alloying Pt with Re has been reported in previous works in literature and it is related to the generation of Brønsted acid sites on PtRe catalysts under APR conditions [16] as discussed in Chapter 3 as well. Accordingly, the selectivities towards higher alkanes (ethane and propane) are seen to increase for the bimetallic catalysts when compared to their monometallic counterparts (Table 5.3). Note that the promotional effect of Re on the formation of alkanes decreases as Re is alloyed on larger Pt particles. The Pt/C(r800)-Re catalysts reduced at 300 and 600 °C, which are the least active catalysts among the PtRe alloys, show lower selectivities towards alkanes when compared to the other alloy catalysts. These materials show about 50 % selectivity towards hydroxyacetone. This relates to the very low rate of hydrogenation of hydroxyacetone to 1,2-PDO as well as its further dehydration to alkanes. Chia et al. recently reported similar observations for RhRe/C catalysts used for aqueous phase hydrogenolysis of 2-(hydroxymethyl)tetrahydropyran [30]. They observed the formation of RhRe nanoparticles with Rh-rich cores and a shell of metallic Re islands. An interesting finding of that study was that the increase in the coordination number of Re with increasing reduction temperature from 120 to 250 and 450 °C led to a decrease in the concentration of acid sites which resulted in a decrease in C-O hydrogenolysis activity of the RhRe/C catalysts. Similarly, in the current study, deposition of Re on larger Pt particles results in an increase in the coordination number of Re-M shells (as follows from EXAFS). This may relate to the decrease in the active sites for hydrogenolysis reactions. Furthermore, an increase in the reduction temperature of PtRe catalysts from 300 to 600 °C generally results in a decrease in the APR activity.

Fast removal of CO from the catalytic metal surface by the WGS reaction has been discussed to be important to maintain high rates of glycerol APR [9,15,22]. Fig. 5.6 shows Arrhenius plots for the WGS reaction of Pt and PtRe catalysts. It is seen that there is strong particle size dependence for the Pt/C catalysts. The WGS activity of Pt/C reduced at 400 °C is lowest and is followed by Pt/C(r1000), Pt//C(r600) and Pt/C(r800) for the monometallic Pt catalysts (Fig. 5.6a). Addition of Re to the reduced Pt/C catalysts results in significant increases of the WGS activity (Fig. 5.6b-d). For the PtRe catalysts reduced at 300 °C, the relative increase in WGS rate per mol of Pt is highest for Pt/C(r400) and decreases with increasing reduction temperature of the parent Pt/C catalyst (Table 5.13). These data indicate

that higher reduction temperature of the freshly prepared PtRe catalyst results in increased Pt-Re synergy in the WGS reaction.

Table 5.13: WGS activity results obtained over the carbon-supported Pt and PtRe catalysts at 225 °C.

Catalyst	Rate (mmol/g_{cat}·h)	Rate (mol/mol_{Pt}·h)	Rate[1] (mol/mol_M·h)
Pt/C(r400)	0.1	0.9	0.9
Pt/C(r600)	1.3	12	12
Pt/C(r800)	3.0	27	27
Pt/C(r1000)	1.2	11	11
Pt/C(r400)-Re(r300)	4.4	39	15
Pt/C(r400)-Re(r600)	12	107	40
Pt/C(r600)-Re(r300)	17	151	53
Pt/C(r600)-Re(r600)	23	205	72
Pt/C(r800)-Re(r300)	20	178	66
Pt/C(r800)-Re(r600)	27	241	89
Pt/C[2]	0.2	1.4	1.4
PtRe(1:2)/C[2]	6.2	50	15

[1] M=Pt+Re
[2] prepared by impregnation on activated carbon followed by reduction at 300 °C; for PtRe sequential impregnation was used.

It is well known that the strong adsorption of CO on Pt surfaces leads to their severe poisoning, for instance under APR conditions. A high rate of removal of adsorbed CO as CO_2 by reaction with O and OH surface intermediates, that is the WGS reaction, will increase the overall catalytic activity during APR. The microkinetic model of Mavrikakis' group based on DFT-computed kinetic parameters for the Pt(111) surface shows that the reaction proceeds through a COOH surface intermediate formed by reaction of adsorbed CO and OH. Water activation, i.e. $H_2O_{ads} \rightarrow OH_{ads} + H_{ads}$, was identified as the rate-controlling step for Pt(111) [31]. Linear free-energy relations, in catalysis usually termed as Brønsted-Evans-Polanyi (BEP) relations [32], predict that the activation barrier of water activation will depend significantly on the metal-OH bond strength [33]. An increase of the metal-OH bond strength lowers the reaction barrier. The metal-OH bond strength of 346 kJ/mol for Re(0001) is higher than the corresponding value of 282 kJ/mol for Pt(111). As a result, the formation of OH_{ads} is slightly endothermic for Pt(111) and exothermic for Re(0001) [34]. Accordingly, BEP predicts that the initial water activation step is kinetically favored for the close-packed Re surface. In line with this, we found that Re/C is a more active WGS catalyst than Pt/C (Chapter 3). From the data herein, a more complex picture emerges, in the sense that Re/C is more active than Pt/C when the latter catalyst is reduced at 400 C, while reduction of Pt/C at a temperature of 600 °C or higher leads to a significant increase of the WGS activity , such that Pt/C becomes active than Re/C. Kalamaras et al. also found that the WGS activity increased with Pt nanoparticle size [35]. Given Marvrikakis' conclusions, this particle size effect must be related to more facile water activation on larger particles. Quantum-chemical calculations of Zhu et al. predict that O and OH binds stronger on a stepped Pt(210) surface than on Pt(111) [34], so that, again according to BEP, the overall barrier for OH_{ads} formation
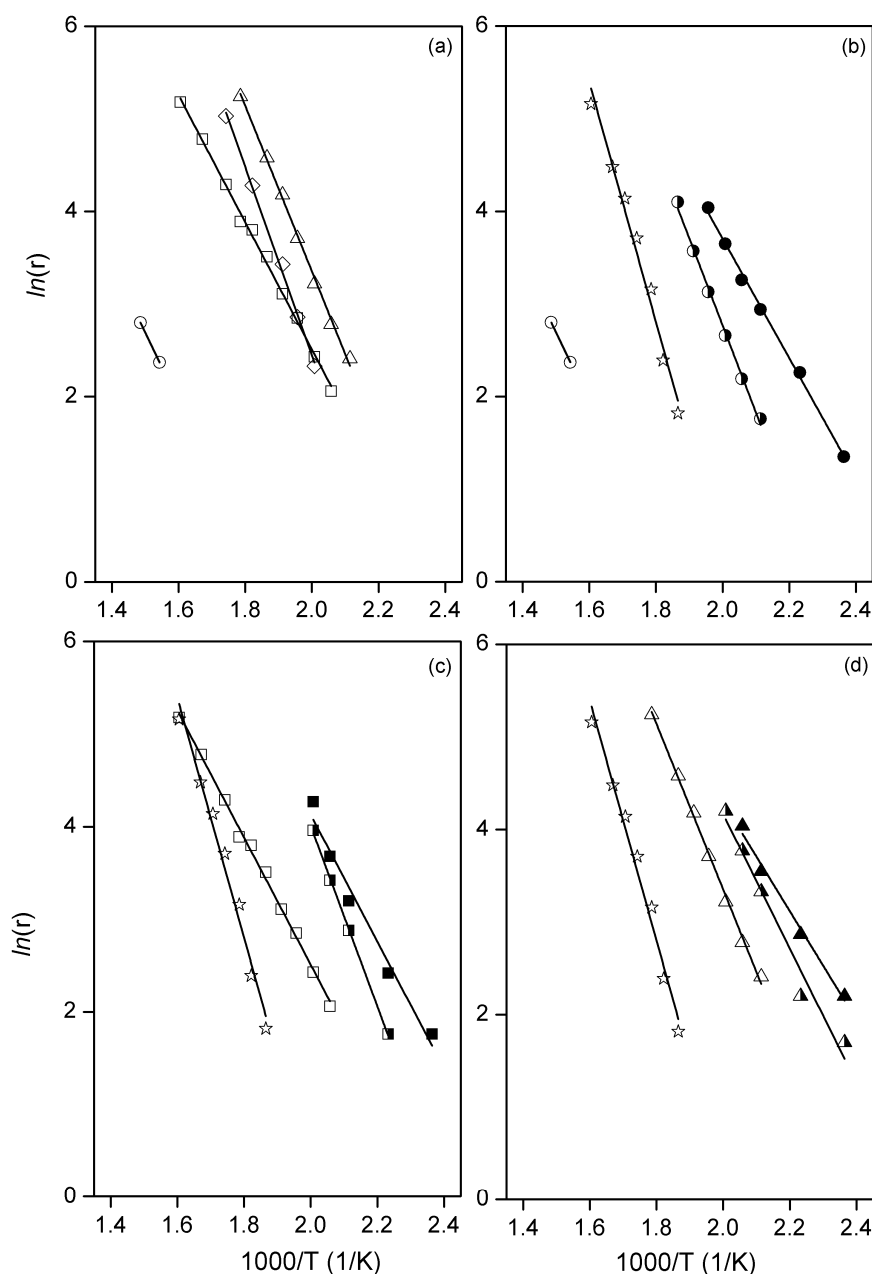
Figure 5.6: Arrhenius plots for WGS over the Pt/C(r400) (*circle*), Pt/C(r600) (*square*), Pt/C(r800) (*triangle*), Pt/C(r1000) (*diamond*) catalysts before (open symbols) and after Re addition by catalytic reduction method followed by reduction at 300 °C (half closed symbols) and 600 °C (closed symbols). Re/C reduced at 500 °C (*star*) is included for comparison. (2.5 vol% CO and 7.5 vol% H_2O balanced by He at a dry GHSV of ~1×10^5 h^{-1}).

should be more favorable for the corrugated surface than for Pt(111). This is consistent with values for the activation barrier for water activation of 53 and 87 kJ/mol for Pt(210) and Pt(111), respectively. This suspected particle size dependence is consistent with the literature discussing the decrease of the number of step-edge sites when the particle size becomes smaller than 2 nm [36]. A similar explanation can be put forward when considering other surface facets more reactive than the (111) surface of Pt, such as the (100) one. On the one hand, at least on the face of it, TEM imaging supports this assertion as reduction at increased

temperature is seen to induce the development of well-facetted Pt nanoparticles. On the other hand, the lower activity of Pt/C(r1000) would be in favour of the step-edge explanation.

Turning now back to the Re effect, it is seen from Table 5.13 that addition of Re to the Pt/C catalysts led to increased WGS activities. The activity differences between the PtRe/C catalysts tend to be smaller than those between the parent Pt/C catalysts. As Re is a more reactive metal than Pt, it is reasonable to assume that Re will facilitate the water activation step [32]. Despite the formation of a Re shell around the Pt nanoparticles, it is likely that the subsequent reduction step results in some rearrangement of the alloying metals. Indeed, a pure Re coating on a Pt nanoparticle would not be expected to give rise to the observed tremendous activity increase, unless perhaps one would attribute some new properties to a Re surface layer around Pt as for instance observed in PtM (M = Co, Ni, Cu) alloys used in the oxygen reduction reaction [37,38]. Obviously, the latter effect is especially pronounced once a significant part of the promoting base metal from the outer shells of the bimetallic particle has been leached into solution. These effects should not play a role, as (i) the Re will not leach in the gas-phase WGS reaction and (ii) the Re skin should be significantly thicker than a single Re layer, so that the Re atoms will not be affected by Pt neighbours. Such idealized bimetallic nanoparticles would be expected to exhibit similar WGS activity as Re/C. As the Re alloying strongly increases the WGS activity, a more likely explanation is that the final reduction step of the bimetallic catalyst leads to rearrangement of the nanoparticles such that Pt atoms appear at the surface. Microkinetic modeling of the WGS reaction on a bimetallic PtRe surface explained the increased WGS activity in terms of Re surface atoms being fully covered by O_{ads} and OH_{ads} with the Pt surface atoms providing centers for CO adsorption [39]. It might then be that the increased WGS activity of alloys reduced at 600 °C instead of 300 °C is due to the emergence of more Pt atoms at the surface. Consistent with this, Pt/C(r400)-Re(r600) is more active than a conventional PtRe/C catalyst (Table 5.13). The smaller variation in catalytic performance in the PtRe set as compared to the Pt set is in our simple picture due to water formation on Re becoming more predominant than on Pt sites, making the reaction less structure dependent.

To exclude that the above picture is not influenced by a change in oxidation state of the surface during the WGS reaction, we carried out *operando* XANES of several catalyst and found that there were not significant changes in the Pt L_{III} edge and Re L_{III} near-edge spectra (Fig.s 5.7-5.9). Fit parameters determined for corresponding in situ FT EXAFS data during the WGS reaction are collected in Table 5.14. The Pt-M (M = Pt, Re) coordination numbers of the Pt/C(r400), Pt/C(r600) and Pt/C(r800) increase only slightly, The coordination number for Pt/C(r1000) does not change. For the bimetallic catalysts, coordination numbers of the Pt-M shell remain almost unchanged as compared to values for the reduced catalysts. The Re-M shell coordination becomes slightly more prominent. Most importantly, the trends in Pt-M and Re-M coordination numbers for the reduced PtRe alloys and those measured under WGS reaction conditions remain almost the same.
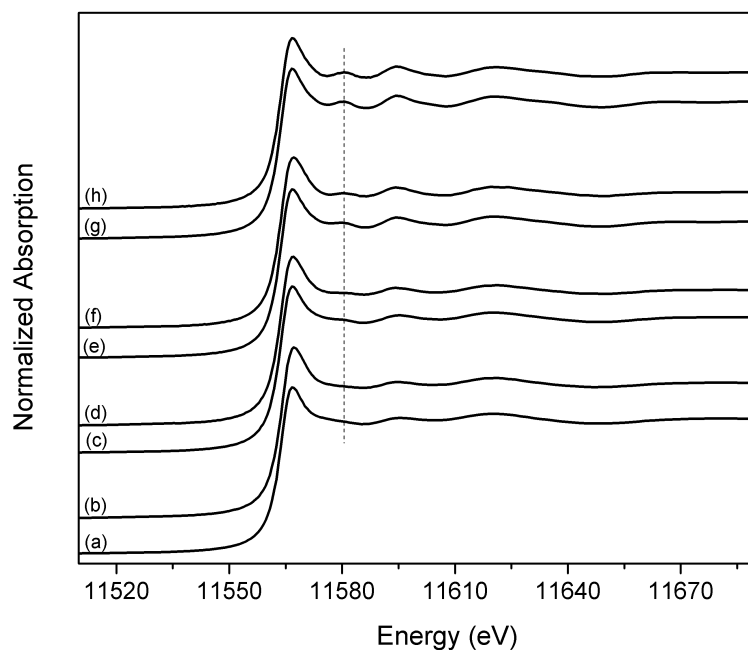
Figure 5.7: Pt L_{III}-edge XANES spectra of Pt/C(r400) reduced at 300 °C (a), during WGS at 300 °C (b); Pt/C(r600) reduced at 300 °C (c), during WGS at 300 °C (d); Pt/C(r800) reduced at 300 °C (e), during WGS at 300 °C (f); Pt/C(r1000) reduced at 300 °C (g), during WGS at 300 °C (h).
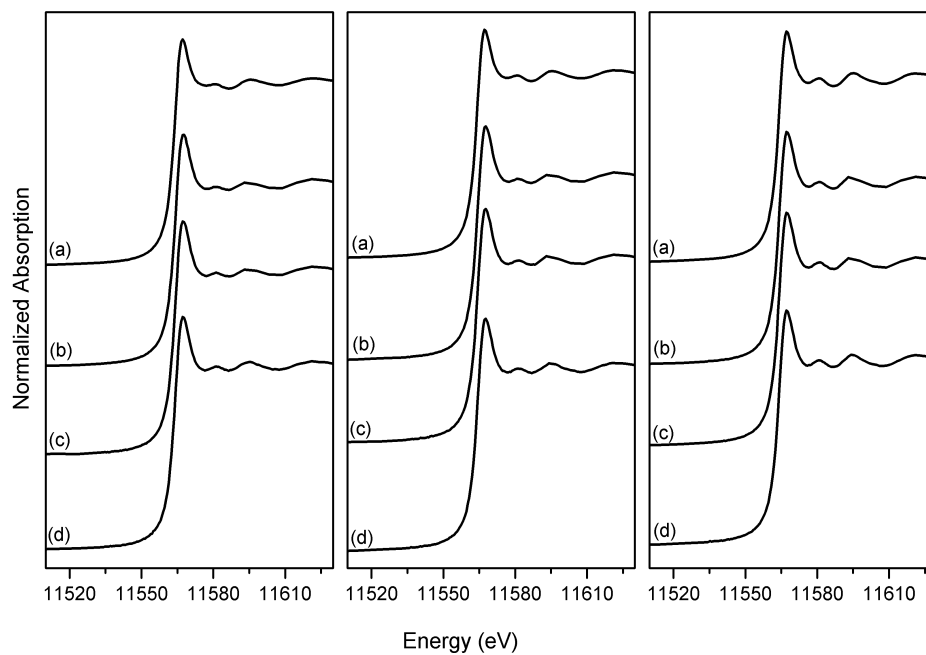

Figure 5.8: Pt L_{III}-edge XANES spectra of Pt/C(r400)-Re(r300) (left), Pt/C(r600)-Re(r300) (middle), Pt/C(r800)-Re(r300) (right) reduced at 300 °C (a) and the spectra recorded during WGS at 200 °C (b), 250 °C (c) and 300 °C (d).

Figure 5.9: Re L_{III}-edge XANES spectra of Pt/C(r400)-Re(r300) (left), Pt/C(r600)-Re(r300) (middle), Pt/C(r800)-Re(r300) (right) reduced at 300 °C (a) and the spectra recorded during WGS at 200 °C (b), 250 °C (c) and 300 °C (d). ΔE_0 is the shift in the edge energy when compared to metallic Re.
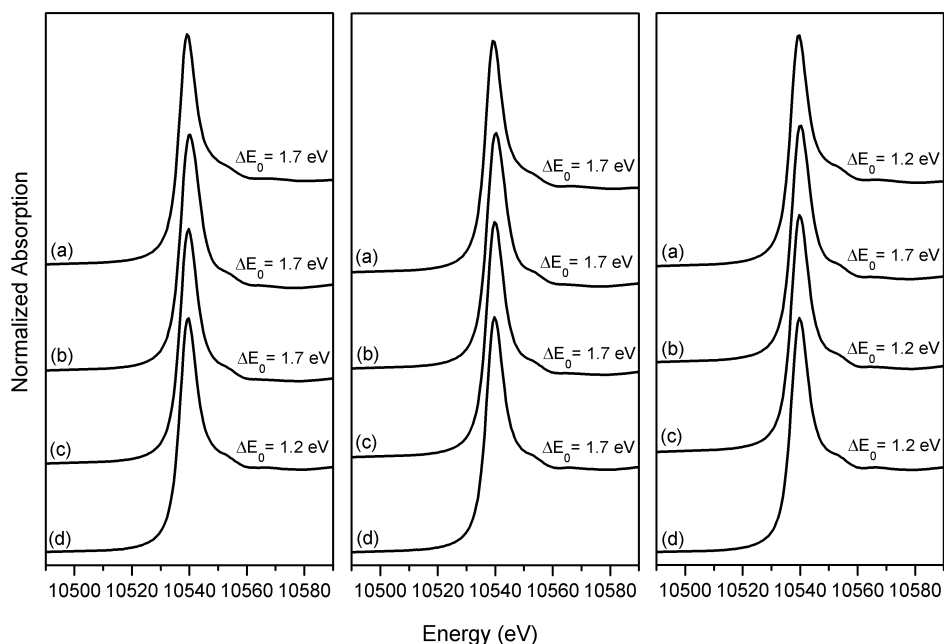
Table 5.14: Fit parameters of k^3-weighted EXAFS spectra at the Pt L_{III}-edge and Re L_{III}-edge of reduced (300 °C) catalysts recorded during WGS reaction at 300 °C. M represents the backscatterer atom (Pt or Re).

Catalyst	EXAFS analysis				
	Shell	R (Å)	CN	$\Delta\sigma^2$ (Å^2)	E_0 (eV)
Pt/C(r400)	Pt-Pt	2.692	8.3	0.014	-2.3
Pt/C(r600)	Pt-Pt	2.719	8.6	0.015	-6.5
Pt/C(r800)	Pt-Pt	2.756	9.1	0.013	-9.8
Pt/C(r1000)	Pt-Pt	2.759	9.3	0.011	-10.0
Pt/C(r400)-Re(r300)	Pt-M$_{Pt}$	2.724	6.5	0.012	-7.4
	Re-M$_{Re}$	2.646	6.8	0.009	-0.5
Pt/C(r600)-Re(r300)	Pt-M$_{Pt}$	2.724	7.3	0.012	-7.5
	Re-M$_{Re}$	2.654	7.2	0.009	-1.0
Pt/C(r800)-Re(r300)	Pt-M$_{Pt}$	2.746	8.4	0.011	-8.5
	Re-M$_{Re}$	2.675	7.5	0.009	-3.9

The rate of acetaldehyde decomposition of the Pt and their Re-alloyed counterparts was investigated to determine their reactivity in a model reaction in which only C-C bond cleavage is involved (no C-O bond cleavage). The reaction was carried out in the gas phase and hydrogen was added in order to avoid undesired deactivation by extensive carbon lay-down. The main reaction products were CO and CH_4 and a small amount of ethanol. Ethanol is the product of acetaldehyde hydrogenation. The activity results collected in Table 5.15 show that the CO yield for Pt/C catalysts does not vary significantly for reduction temperatures up to 800 °C. The nearly constant CO yield for the Pt/C catalysts implies an

117

increase of the intrinsic rate of acetaldehyde decomposition with increasing Pt particle size. The activity of Pt/C(r1000) was substantially lower. The particle size dependence of acetaldehyde trends well with the dependence of the WGS reaction. Candidate intermediates to undergo C-C bond cleavage are CH_x-CO, with CH-CO being proposed by Liu et al. for Pt(100) [40]. The dissociation of CH_x-CO proceeds through a late transition state and, hence, we predict that the barrier for C-C bond cleavage will decrease with increasing bond energy of the CH_x and CO fragments. This implies that open and corrugated surfaces should favor C-C bond cleavage. Consistent with this, Zhu found that the barrier for cleavage of the C-C bond in CH-CO is 57 kJ/mol on the (520) facet of Pt [39], whereas it is much higher for its (111) facet with values of 93 kJ/mol reported by Liu [40] and Vlachos [41]. Accordingly, we infer that the similar particle size dependence for WGS and C-C bond cleavage reactions relates to the preference for step-edge sites on the Pt surface.

Table 5.15: Acetaldehyde conversion, CO (CH_4) yields and selectivities for acetaldehyde decarbonylation experiments (T = 225 °C, GHSV = 7200 $ml_{acetaldehyde}/g_{cat}$.h; gas-phase composition H_2:C_2H_4O=1:1 by volume with balance He).

Catalyst	Conversion C_2H_4O (%)[1]	Yield CO (CH_4) (%)[1]	Selectivity CO (CH_4) (%)[1]
Pt/C(r400)	19.6	9.7	49.6
Pt/C(r600)	20.3	10.1	49.8
Pt/C(r800)	19.9	9.8	49.3
Pt/C(r1000)	9.7	4.4	45.8
Pt/C(r400)-Re(r300)	37.9	15.1	39.9
Pt/C(r600)-Re(r300)	39.1	14.4	36.7
Pt/C(r800)-Re(r300)	28.4	9.6	33.8

[1] Average of at least 4 h time on stream.

Upon addition of Re on Pt/C reduced at 400, 600 and 800 °C, the acetaldehyde conversion is seen to increase, albeit that the increase is less significant than for the WGS reaction. Comparing CO yields, it is noted that the PtRe catalyst prepared from Pt/C(400) and Pt/C(600) exhibit activities 1.5 times greater than the corresponding parent Pt/C catalysts. The activity of Pt/C(800)-Re(300) is similar to that of Pt/C(r800). We earlier found that Re/C is not active in this reaction, which is presumably due to its low hydrogenation activity resulting in excessive carbon deposit formation (Chapter 3). The higher activity of Re is consistent with the low barrier for CH-CO cleavage on Re(0001) of 64 kJ/mol. The much higher activity of the herein prepared PtRe catalysts by the catalytic reduction method further points to a surface composition different from a pure Re skin around the Pt nanoparticles. The presence of Pt at the surface is further confirmed by the much higher hydrogenation activity of acetaldehyde to ethanol as compared with the parent Pt/C catalysts, consistent with the notion that PtRe is a better hydrogenation catalyst than Pt. This better hydrogenation activity prevents carbon lay-down. The shift in acetaldehyde conversion towards hydrogenation for larger PtRe nanoparticles can also be traced in the glycerol APR data as Pt/C(r800)-Re(r300) exhibits low glycerol conversion rate and H_2 yield.

Finalizing, the increase in the APR activity of Pt/C with increasing particle size is consistent with the trends observed in separate model WGS and acetaldehyde decomposition measurements. The removal of CO by the WGS reaction results in increased overall glycerol conversion rates. The increased C-C bond cleavage activity favors complete reforming over dehydration-hydrogenation reactions to alcohol intermediates and alkane end-products. These trends are attributed to the higher density of step-edge sites on the surface of increasingly larger particles. The addition of Re has different effects on the APR activity. It strongly improves the activity of Pt/C(r400), whilst the Pt/C(r600) is unaffected and Pt/C(r800) becomes less active. Table 5.3 also contains data for Pt/C and PtRe/C catalysts prepared by conventional methods, that is impregnation and drying of the Pt precursor followed by NH_4ReO_4 loading for the bimetallic catalyst (Chapter 3). Reduction of these catalysts was done at 300 °C. The synergy between Pt and Re for the conventional catalysts is much greater than for the present set of catalysts. The difference may be traced back to the preparation procedure. The catalytic reduction method deposits a shell of Re around the reduced Pt nanoparticles, whereas reduction of the sequentially impregnated PtRe catalyst will result in better mixing of Pt and Re in the final nanoparticles. The elementary reaction steps giving rise to C-O and C-C bond cleavage are expected to require Pt ensembles, as Re ensembles are likely to be covered by oxygen or hydroxyl groups. The catalytic WGS and acetaldehyde decomposition data show that (i) some Pt atoms have appeared at the surface of the metal nanoparticles and (ii) the hydrogenation activity of the alloy is better than that of Pt and Re. Thus, we argue that the much lower activity of Pt/C(r400)-Re(r300) than the reference PtRe/C catalyst is due to lower Pt surface atom content. The less pronounced and even negative effect of Re addition for larger Pt nanoparticles, namely for Pt/C(r600) and Pt/C(r800), should be due to the formation of a thicker Re shell around larger nanoparticles (note that all Re was deposited during the catalytic reduction method). It should lead to a smaller amount of Pt atoms on the nanoparticle surface, decreasing the likelihood of having Pt ensembles large enough to catalyze the bond breaking reactions required in APR. For the bimetallic catalyst containing the largest particles, it is also seen that the C-O/C-C bond cleavage ratio is the highest, consistent with the predominance of Re on the catalytic surface. Another interesting observation to be made is that the hydrogenation of hydroxyacetone to 1,2-PDO during glycerol APR decreases with increasing PtRe particle size, whereas the hydrogenation of acetaldehyde to ethanol trends oppositely. Re sites will be covered by OH surface intermediates under APR conditions, while such intermediates are absent in the acetaldehyde model reaction experiments. Thus, the hydrogenation activity of PtRe appears to increase with increasing Re enrichment of the surface, but this effect is not seen in the APR data because of increasing OH surface coverage with particle size.

Summarizing, the APR reaction of glycerol is strongly structure sensitive for Pt nanoparticle catalysts due to the importance of step-edge sites to water activation and C-C bond cleavage steps. For bimetallic PtRe catalysts it can be inferred that the WGS reaction is preferred over Re-enriched surfaces, whereas the APR reaction requires Pt ensembles large enough to accommodate bond cleavage reactions.

5.4 Conclusions

The APR activities of a set of carbon supported Pt catalysts were found to be strongly dependent on the Pt particle size. Reduction at 400, 600 and 800 °C of a freshly prepared Pt/C catalyst resulted in average Pt particle sizes of 1.2, 1.6 and 2.0 nm as determined by the TEM analysis of the reduced catalysts. Yields of reforming products (H_2 and CO) as well as the C-C bond cleavage rates of the catalysts were found to increase with increasing particle size. These results were in line with the trends observed in model gas-phase water-gas shift and acetaldehyde decomposition reactions. This is explained by similar site requirements for these two reactions. Binding of O and OH species and the cleavage of C-C bonds of CH-CO intermediate occurs at higher rates on stepped Pt surfaces. In agreement with this, a Pt/C catalyst with an average particle size of 4.2 nm, obtained by reduction of Pt/C at 1000 °C, showed a decrease in activity in model C-C bond cleavage (acetaldehyde decomposition) and CO removal (WGS) experiments. This was explained by the decrease in step-edge sites with an increase in Pt particle size from 2 to 4.2 nm. Addition of Re on the reduced Pt/C catalysts following the catalytic reduction method resulted in an increase in the C-O bond cleavage products when compared to those obtained by C-C bond cleavage reactions. The glycerol conversion in APR increased for only the PtRe catalyst prepared on the Pt/C catalyst with the smallest particle size. For the rest of the alloys, APR activity was not affected or decreased. The larger particle size of the core Pt particles resulted in the formation of a thicker Re shell. The decrease in the APR activity with increasing particle size of the Pt core was related to the absence of Pt ensembles required for hydrogenolysis reactions. In acetaldehyde decomposition, the addition Re on large Pt particles resulted in increased C-C bond cleavage rates as well as increased hydrogenation rates to ethanol. The WGS activity of PtRe catalysts increased substantially when compared to the monometallic Pt/C catalysts. The promotional effect of Re increased with increased Pt particle size and increasing reduction temperature of the PtRe alloys in WGS. This was related to the rearrangement of the particles and appearance of Pt atoms on the surface. A conventional PtRe/C catalyst prepared by sequential impregnation followed by reduction at 300 °C showed a more pronounced increase in APR activity when compared to its parent Pt/C catalyst. This is in line with our assertion that, for glycerol APR, well-mixed PtRe alloys are preferred over a Pt (core)-Re (shell) structure obtained by the catalytic reduction method.

References

[1] R.R. Davda, J.W. Shabaker, G.W. Huber, R.D. Cortright, J.A. Dumesic, Appl. Catal. B 56 (2005) 171-186.
[2] A. Wawrzetz, B. Peng, A. Hrabar, A. Jentys, A.A. Lemonidou, J.A. Lercher, J. Catal. 269 (2010) 411-420.
[3] R.R. Davda, J.W. Shabaker, G.W. Huber, R.D. Cortright, J.A. Dumesic, Appl. Catal. B 43 (2003) 13-26.
[4] J.W. Shabaker, G.W. Huber, R.R. Davda, R.D. Cortright, J.A. Dumesic, Catal. Lett. 88 (2003) 1-8.
[5] G.W. Huber, J.W. Shabaker, S.T. Evans, J.A. Dumesic, Appl. Catal. B 62 (2006) 226-235.
[6] K. Lehnert, P. Claus, Catal. Comm. 9 (2008) 2543-2546.
[7] S.N. Delgado, D. Yap, L. Vivier, C. Especel, J. Mol. Catal. A 367 (2013) 89-98.
[8] B. Meryemoglu, A. Hesenov, S. Irmak, O.M. Atanur, O. Erbatur, Int. J. Hydrogen Energ. 35 (2010) 12580-12587.

[9]   Y. Guo, M.U. Azmat, X.H. Liu, Y.Q. Wang, G.Z. Lu, Appl. Energ. 92 (2012) 218-223.
[10]   G. Wen, Y. Xu, H. Ma, Z. Xu, Z. Tian, Int. J. Hydrogen Energ. 33 (2008) 6657-6666.
[11]   T. Miyazawa, S. Koso, K. Kunimori, K. Tomishige, Appl. Catal. A 318 (2007) 244-251.
[12]   D.M. Alonso, S.G. Wettstein, J.A. Dumesic, Chem. Soc. Rev. 41 (2012).
[13]   D.L. King, L.A. Zhang, G. Xia, A.M. Karim, D.J. Heldebrant, X.Q. Wang, T. Peterson, Y. Wang, Appl. Catal. B 99 (2010) 206-213.
[14]   S. Koso, H. Watanabe, K. Okumura, Y. Nakagawa, K. Tomishige, Appl. Catal. B 111 (2012) 27-37.
[15]   E.L. Kunkes, D.A. Simonetti, J.A. Dumesic, W.D. Pyrz, L.E. Murillo, J.G.G. Chen, D.J. Buttrey, J. Catal. 260 (2008) 164-177.
[16]   L. Zhang, A.M. Karim, M.H. Engelhard, Z.H. Wei, D.L. King, Y. Wang, J. Catal. 287 (2012) 37-43.
[17]   C.L. Pieck, P. Marecot, C.A. Querini, J.M. Parera, J. Barbier, Appl. Catal. A 133 (1995) 281-292.
[18]   C.L. Pieck, P. Marecot, J. Barbier, Appl. Catal. A 134 (1996) 319-329.
[19]   C.L. Pieck, P. Marecot, J. Barbier, Appl. Catal. A 143 (1996) 283-298.
[20]   E.P. Maris, W.C. Ketchie, M. Murayama, R.J. Davis, J. Catal. 251 (2007) 281-294.
[21]   D.A.J.M. Ligthart, R.A. van Santen, E.J.M. Hensen, Angew. Chem. Int. Edit. 50 (2011) 5306-5310.
[22]   D.A. Simonetti, E.L. Kunkes, J.A. Dumesic, J. Catal. 247 (2007) 298-306.
[23]   J. Sa, C. Kartusch, M. Makosch, C. Paun, J.A. van Bokhoven, E. Kleymenov, J. Szlachetko, M. Nachtegaal, H.G. Manyar, C. Hardacre, Chem. Commun. 47 (2011) 6590-6592.
[24]   J.L. Xiao, R.J. Puddephatt, Coord. Chem. Rev. 143 (1995) 457-500.
[25]   X.M. Wang, N. Li, Z.T. Zhang, C. Wang, L.D. Pfefferle, G.L. Haller, ACS Catal. 2 (2012) 1480-1486.
[26]   S. Calvin, M.M. Miller, R. Goswami, S.F. Cheng, S.P. Mulvaney, L.J. Whitman, V.G. Harris, J. Appl. Phys. 94 (2003) 778-783.
[27]   S. Calvin, S.X. Luo, C. Caragianis-Broadbridge, J.K. McGuinness, E. Anderson, A. Lehman, K.H. Wee, S.A. Morrison, L.K. Kurihara, Appl. Phys. Lett. 87 (2005) 233102-233103.
[28]   S. Calvin, C.J. Riedel, E.E. Carpenter, S.A. Morrison, R.M. Stroud, V.G. Harris, Phys. Scripta 2005 (2005) 744.
[29]   A.V. Kirilin, B. Hasse, A.V. Tokarev, L.M. Kustov, G.N. Baeva, G.O. Bragina, A.Y. Stakheev, A.R. Rautio, T. Salmi, B.J.M. Etzold, J.P. Mikkola, D.Y. Murzin, Catal. Sci. Technol. 4 (2014) 387-401.
[30]   M. Chia, B.J. O'Neill, R. Alamillo, P.J. Dietrich, F.H. Ribeiro, J.T. Miller, J.A. Dumesic, J. Catal. 308 (2013) 226-236.
[31]   L.C. Grabow, A.A. Gokhale, S.T. Evans, J.A. Dumesic, M. Mavrikakis, J. Phys. Chem. C 112 (2008) 4608-4617.
[32]   R.A.van Santen and M.Neurock, Molecular Heterogeneous Catalysis: A Conceptual and Computational Approach, Wiley-VCH, Weinheim, 2007.
[33]   P.W. van Grootel, E.J.M. Hensen, R.A. van Santen, Surf. Sci. 603 (2009) 3275-3281.
[34]   T. Zhu, P.W. van Grootel, I.A.W. Filot, S.G. Sun, R.A. van Santen, E.J.M. Hensen, J. Catal. 297 (2013) 227-235.
[35]   C.M. Kalamaras, S. Americanou, A.M. Efstathiou, J. Catal. 279 (2011) 287-300.
[36]   R.A. van Santen, Accounts of Chem. Res. 42 (2009) 57-66.
[37]   R. Srivastava, P. Mani, N. Hahn, P. Strasser, Angew. Chem. Int. Edit. 46 (2007) 8988-8991.
[38]   K. Jayasayee, J.A.R. Van Veen, E.J.M. Hensen, F.A. de Bruijn, Electrochim. Acta 56 (2011) 7235-7242.
[39]   T. Zhu, PhD Thesis, ISBN 978-90-386-3505-7, Technische Universiteit Eindhoven, 2013.
[40]   H.F. Wang, Z.P. Liu, J. Am. Chem. Soc. 130 (2008) 10996-11004.
[41]   J.E. Sutton, P. Panagiotopoulou, X.E. Verykios, D.G. Vlachos, J. Phys. Chem. C 117 (2013) 4691-4706.

Chapter 6

Aqueous phase reforming of glycerol over Re-promoted Pt and Rh catalysts

Summary

The potential of Re-promotion for carbon-supported Pt and Rh nanoparticles was investigated for aqueous phase reforming (APR) of biobased feedstock. Upon alloying with Re, overall conversion rate of glycerol was substantially increased for both metals. Whereas Pt/C is more active than Rh/C in glycerol APR, the RhRe/C catalyst outperforms PtRe/C. The overall catalytic performance correlates with the activity trend observed in the gas-phase water-gas shift (WGS) reaction. RhRe/C exhibited the highest activity in APR and WGS reactions. A very strong synergy between Rh and Re and Pt and Re is observed in the model WGS reaction. The role of Re in the bimetallic catalysts is to facilitate water dissociation, effectively increasing the WGS activity. During APR, this results in lower steady-state CO coverage and increased glycerol conversion. The addition of Re also resulted in significant changes in the product selectivities during glycerol APR. Whereas Rh/C is more selective for C-C bond cleavage than Pt/C as evidenced by gas-phase acetaldehyde decomposition measurements, the product mixtures of their alloys with Re reflect a high ratio of C-O vs. C-C bond cleavage reaction rates.
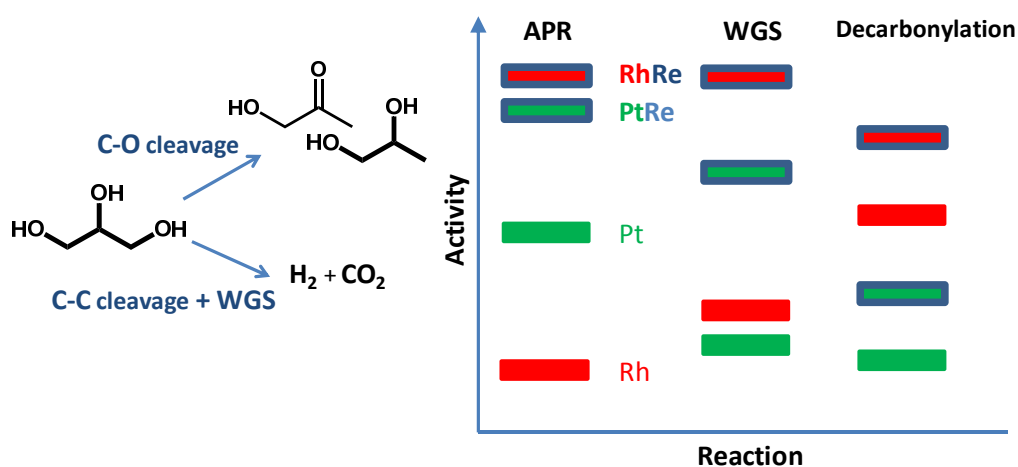
6.1 Introduction

The depletion of fossil fuel reserves and the increasing rate of greenhouse gas emissions as a result of the current coal and oil-based chemical processes motivate the search for green and sustainable chemical technologies. The use of biomass, the only source of renewable carbon at this moment, opens up new opportunities for sustainable production of fuels and chemicals. Carbohydrates, the constituent monomers of the most abundant (hemi)cellulose biopolymers, contain much more oxygen than fossil feedstock. A major challenge involved in catalytic upgrading of biomass is, therefore, the cleavage of C-O bonds originating from hydroxide and ether bonds in the lignocellulosic feedstock [1-3].

Liquid phase reforming of water-soluble organic compounds obtained from woody biomass feedstock is an attractive process for obtaining a gas mixture of hydrogen and carbon dioxide as well as alkanes and monofunctional alcohols [4]. Hydrogen is a key reactant in many refinery processes for producing liquid fuels and biofuels and may also become an important energy vector in the future [5]. Glycerol serves as a model compound for the aqueous phase reforming (APR) process, as it contains C-O, C-C, C-H and O-H bonds in its structure, similar to complex biomass-derived carbohydrates [6,7]. Glycerol can be obtained via hydrogenolysis of cellulose or C_6 sugars. At the moment the dominant source of glycerol is as a by-product of biodiesel production. Utilization of this over-produced glycerol as a novel feedstock for green chemicals production is essential for the applicability of the biodiesel production process [8,9].

Generally, Pt group metals are preferred as catalysts for APR [7,10,11]. Recently, experiments in reforming and hydrogenolysis of polyols show that the overall conversion and selectivity towards deoxygenated products increases when a highly reducible metal catalyst (such as Pt, Rh, Ru or Ir) is combined with Re [12-21]. So far, significant efforts have been devoted to explain the nature of the active sites of PtRe system. Due to their enhanced activity in C-O cleavage, RhRe catalysts have also been explored in recent studies for selective hydrogenolysis of polyols [12]. For instance, Koso et al. [22] found Rh-ReO$_x$/SiO$_2$ to be much more active and selective in the hydrogenolysis of the C-O bond of tetrahydrofurfuryl alcohol to form 1,5-pentanediol when compared to conventional Pt hydrogenolysis catalysts. In another study, a similar catalyst with a Re/Rh molar ratio of 0.5 was found to give the highest activity in the hydrogenolysis of glycerol to 1,3-propanediol in comparison with Mo and W modified Rh/SiO$_2$ [16]. The C-C bond cleavage activity of Rh/SiO$_2$ was significantly suppressed upon addition of Re resulting in an increase of the yield of propanediols. Recently, Chia et al. studied the hydrogenolysis of polyols and cyclic ethers over a bifunctional Rh-Re catalyst [13]. The hydrogenolysis activity of RhRe was explained by a bifunctional mechanism in which acid-catalyzed ring-opening at the more substituted carbon center followed by metal-catalyzed hydrogenation. Heeres and his co-workers [23] reported the transformation of 5-hydroxymethylfurfural to caprolactone in a process which involves the conversion of 2,5-THF-dimethanol (THFDM) to 1,6-hexanediol over a RhRe/SiO$_2$ catalyst in the presence of various solid acid catalysts [23]. The main advantage of Re-modified catalysts over the conventional ones was reported to be the cleavage of C-O bond neighboring a –CH$_2$OH group.

Unlike H_2-assisted polyol hydrogenolysis reactions, hydrogen and carbon dioxide are among the major products in APR of glycerol. Hydrogen can be used directly to produce work, for instance in hydrogen fuel cells, or as an external source of hydrogen required in biomass upgrading processes [24]. During APR of glycerol, the in situ produced hydrogen is consumed to hydrogenate the dehydrated reaction intermediates which are produced via C-O bond cleavage. Hydrogen formation derives from the dehydrogenation of terminal alcohols (e.g., glycerol) to aldehydes (e.g., glyceraldehyde), followed by decarbonylation to CO and subsequent water-gas shift (WGS) to CO_2 [7,25-27]. The WGS activity of APR catalysts has been found to be important to their overall activity. Dumesic and his co-workers have attributed the promotional effect of Re on Pt/C in aqueous phase glycerol conversion to increased WGS activity [19]. In a recent study by Guo et al. [28], the basic properties of a set of catalysts were correlated to their WGS and APR activities.

In this work, we aimed at comparing the promotional effect of Re on the catalytic performance of Rh and Pt catalysts in the water-gas shift reaction and aqueous phase reforming of glycerol. Activated carbon is chosen as a hydrophobic high surface area support for dispersing the metal oxide precursors. Bimetallic RhRe and PtRe catalysts and their monometallic counterparts were prepared at similar Rh(Pt)/Re molar ratios. These catalytic materials were evaluated in the WGS reaction, acetaldehyde decomposition and APR of glycerol and characterized using X-ray absorption spectroscopy and temperature programmed reduction.

6.2 Experimental methods

6.2.1 Catalyst synthesis

Rh, Pt and Re-containing catalysts were prepared by incipient wetness impregnation using appropriate solutions of $H_2PtCl_6.6H_2O$, $RhCl_3 \cdot (H_2O)_x$ and $HReO_4$. As support, activated carbon (Norit RX3-EXTRA) was used. Prior to preparation, the carbon support was dried overnight at 110 °C. Bimetallic RhRe/C and PtRe/C samples were prepared by sequential impregnation of dried Rh/C and Pt/C catalysts with a perrhenic acid solution of appropriate concentration followed by drying at 110 °C overnight. The molar Rh/Re and Pt/Re ratios were targeted at 2.

6.2.2 Catalyst characterization

The metal content of the catalysts was determined by inductively coupled plasma atomic emission spectrometry (ICP-AES) analysis performed on a Goffin Meyvis Spectro Cirus^{ccd} apparatus. The samples were dissolved in a 3:1 HCl/HNO_3 solution.

Temperature programmed reduction (TPR) was carried out in a flow apparatus equipped with a fixed-bed reactor, a computer-controlled oven and a thermal conductivity detector. Typically, 25 mg catalyst was loaded in a tubular quartz reactor. The sample was reduced in 4 vol% H_2 in N_2 at a flow rate of 8 ml/min, whilst heating from room temperature up to 800 °C at a ramp rate of 10 °C/min. The H_2 signal was calibrated using a CuO/SiO_2 reference catalyst.

Transmission electron micrographs were acquired on a FEI Tecnai 20 transmission electron microscope at an acceleration voltage of 200 kV with a LaB_6 filament. Typically, an amount of sample was ground and suspended in pure ethanol, sonicated and dispersed over a Cu grid with a holey carbon film. All samples were reduced in 10 vol% H_2 in He (total flow 100 ml/min) at 300 °C for 2 hours, followed by passivation in 1 vol% O_2 in He for 2 hours.

X-ray absorption spectroscopy (XAS) measurements were carried out at the Dutch-Belgian Beamline (Dubble) at the European Synchrotron Radiation Facility (ESRF), Grenoble, France (storage ring 6.0 GeV, ring current 200 mA). Data were collected at the Rh K, Pt L_{III} and Re L_{III} edges in transmission mode. Energy selection was done by a double crystal Si(111) monochromator solid-state detector. Background removal was carried out by standard procedures. EXAFS analysis was then performed with EXCURVE931 on k^3-weighted unfiltered raw data using the curved wave theory. Phase shifts were derived from ab initio calculations using Hedin-Lundqvist exchange potentials and Von Barth ground states. Energy calibration was carried out using Rh and Pt foils and Re powder. The amplitude reduction factors S_0^2 associated with central atom shake-up and shake-off effects were set at 0.90, 0.75 and 0.99 by calibration of the first shell Rh-Rh, Re-Re and Pt–Pt coordination numbers to 12, respectively, for the k^3-weighted EXAFS fits of the Pt foil, Rh foil and Re powder. Spectra were recorded in a stainless-steel controlled atmosphere cell. The cell was heated with two firerods controlled by a temperature controller. A thermocouple was placed close to the catalyst sample. Typically, a predetermined amount of finely grinded sample was pressed in a stainless steel holder and placed in the cell. Carbon foils were held between two high-purity carbon spacers. Gases (He and H_2) were delivered by thermal mass flow controllers (Bronkhorst). The catalyst sample was heated at a rate of 10 °C/min up to a final temperature of 550 °C, whilst recording XANES spectra. EXAFS spectra were recorded at room temperature after reduction of the sample at the desired temperature for 1 hour. A second set of XAS measurements were performed under in situ WGS reaction conditions. After recording the room temperature EXAFS of the catalysts reduced at 300 °C, the sample was heated to 150 °C under Helium flow. At 150 °C, CO was mixed with He and fed through a Controlled Evaporator Mixer unit where steam was generated to obtain a $H_2O:CO$ ratio of 3. The sample was heated at a ramp rate of 10 °C/min and EXAFS spectra for each sample were recorded during WGS reaction at 300 °C.

6.2.3 Catalytic activity measurements

6.2.3.1 Water-gas shift reaction

The water-gas shift (WGS) reaction was performed in a parallel ten-flow microreactor system [29]. Steam was supplied by evaporation of deionized water in a Controlled Evaporator Mixer unit (Bronkhorst) in combination with a liquid-flow controller and gas flows were controlled by mass flow controllers (Brooks and Bronkhorst). All tubings were kept above 100 °C after the point of steam introduction to avoid condensation. The dry product gas mixture was analyzed by an online gas chromatograph (Interscience CompactGC) equipped with Porapak Q (TCD) and Molecular sieve 5A (TCD) columns.

Experiments were carried out in a mixture of 2.5 vol% CO and 7.5 vol% H_2O balanced by He at a dry GHSV of ~1.5×10^5 h^{-1} in the temperature range 130-400 °C. Typically, the catalyst was diluted with SiC of the same sieve fraction. The material was contained between two quartz wool plugs in a quartz reactor. Prior to catalytic activity measurements, the catalyst was reduced in a flow of 20 vol% H_2 in He at a ramp rate of 5 °C/min to 300 or 500 °C followed by an isothermal period of 0.5 h. The reactor was cooled in He to the reaction temperature. The catalyst was exposed to the reaction mixture for 10 min prior to the start of recording product gas mixture. At each reaction temperature, the product gas mixture was recorded for 1.5 h.

6.2.3.2 Acetaldehyde decomposition

Acetaldehyde decomposition experiments were performed in a continuous flow reactor setup. Hydrogen and acetaldehyde were fed in equimolar amounts as the feed components. Acetaldehyde was fed by bubbling helium through a saturator kept at such a temperature to obtain an acetaldehyde concentration of 3 vol%. Catalyst samples were first reduced at 300 °C. The reaction was carried out at 225 °C at a GHSV of 7200 ml$_{acetaldehyde}$/g$_{cat}$.h. The reactor effluent was analyzed by online gas chromatography (Interscience GC-8000 Top). CO, CH_4 and H_2 were analyzed on a Shincarbon ST80/100 packed column connected to a TCD. Acetaldehyde and ethanol were analyzed on a RT-Q bond column connected to a FID.

6.2.3.3 APR of glycerol

APR reactions were carried out at 225 °C under 25 bar initial N_2 pressure using 60 g of 10 wt% aqueous glycerol solution in a 120 ml autoclave. An amount of 75 mg of reduced catalyst was loaded in the autoclave together with an appropriate amount of deaerated water in a N_2-flushed glovebag. The autoclave was purged five times with 10 bars of N_2 in order to remove residual air from the autoclave. A 50/50 w/w mixture of glycerol and water was charged into the reactor from an external holding vessel after the autoclave containing water and the catalyst reached the desired reaction temperature. The stirring speed was 600 rpm. Liquid samples were withdrawn by a ROLSI injector and analyzed by a Trace GC equipped using a Stabilwax column and a FID detector. Gas samples were collected online and analyzed by a Focus GC equipped with a TCD detector and CP-Porabond Q and RT-MolSieve-5A columns. The carbon product selectivities were calculated by:

$$S_i(\%) = \frac{mol \ of \ product_i \ formed \times number \ of \ C \ atoms}{mol \ of \ glycerol \ in \ the \ feed \times conversion \times 3} \times 100$$

6.3. Results and discussion

6.3.1 Catalyst characterization

The metal contents of the catalysts are collected in Table 6.1. The Rh loading in Rh/C and RhRe/C is ~2 wt% and the Pt loading in Pt/C and PtRe/C is ~2.5 wt%. The molar ratios of Rh and Pt to Re in the bimetallic catalysts were determined to be ~1.5.

The TPR traces of the catalysts are plotted in Fig. 6.1. The trace of Re/C shows a hydrogen consumption peak at 378 °C and the reduction is complete at 410 °C. Reduction of Rh/C and Pt/C takes place at much lower temperature. The trace of Rh/C shows two maxima at 157 and 206 °C. H_2 consumption below 250 °C is typically attributed to the reduction of rhodium oxide [30,31]. The reduction of Rh/C in two steps is in line with literature [13]. Similar to Rh/C, the TPR profile of the Re-promoted Rh catalyst (Fig. 6.1f) shows a low temperature peak at 162 °C accompanied by a broad peak centered at around 200 °C. The intensity of this second broad peak is higher than that observed for Rh/C, which suggests that the reduction of Re oxide precursor (Re_2O_7) takes place in this temperature regime. The easier reduction of Re in the presence of an easily reducible metal is attributed to hydrogen spillover from metallic Rh or Pt to neighboring Re-oxides [32-35]. Reduction of RhRe/C commences around 75 °C, whereas reduction of PtRe/C starts at around 155 °C. Easier reduction of Rh than Pt is in agreement with results reported by Samoila et al. [36]. The broad features observed at temperatures higher than 400 °C are attributed to reduction of oxygen-functionalized groups on the surface of the activated carbon support.

Representative TEM images of the reduced samples are shown in Fig. 6.2. The average particle size of all catalysts is close to 1 nm. Due to the smallness of the particles, it is not straightforward to accurately determine the particle size of the catalysts. The contrast is better for the Pt catalysts. The Rh-based catalysts appear to be somewhat smaller than the Pt-ones. The average size of the nanoparticles in Rh/C and RhRe/C are around 1.0 and 0.8 nm, respectively. The Pt-based catalysts contain slightly larger nanoparticles, *i.e.* 1.2 nm for Pt/C and 1.0 nm for PtRe/C.

Table 6.1: Metal loading as determined by ICP analysis.

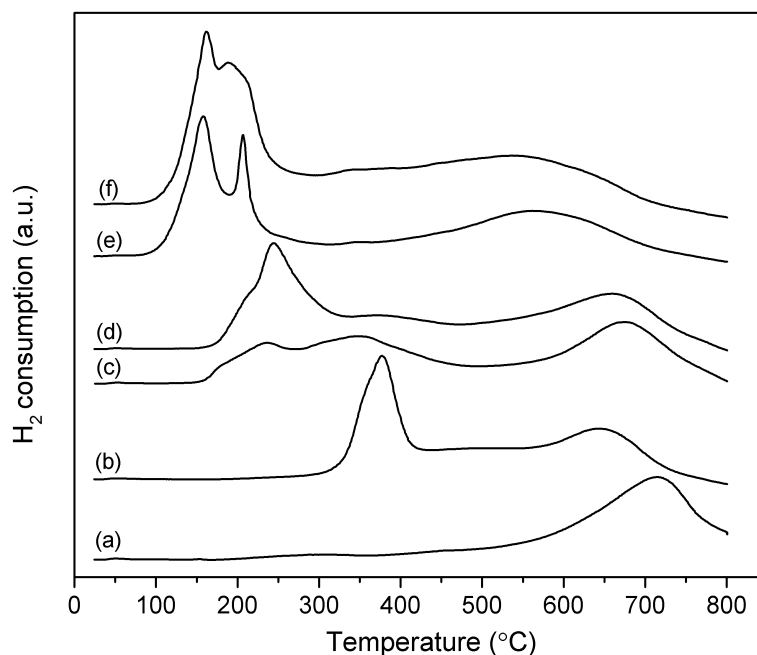| Catalyst	Metal Loading (wt%)		Rh(Pt)/Re atomic ratio
	Rh (Pt)	Re	
Rh/C	2.08	-	-
RhRe/C	2.04	2.41	1.54
Pt/C	2.44	-	-
PtRe/C	2.48	1.53	1.54
Re/C	-	2.78	-

Figure 6.1: TPR traces of (a) the bare carbon support, (b) Re/C, (c) Pt/C, (d) PtRe/C, (e) Rh/C and (f) RhRe/C.

XANES spectra at the Rh-K and Re L_{III}-edge of RhRe/C as a function of temperature during reduction under H_2 flow are shown in Fig. 6.3. There is a clear shift to lower values of the Rh K and Re L_{III}- edge energies with increasing reduction temperature. In line with this, the intensities of the whiteline features, which originate from the density of the unoccupied d-states, decrease with increasing reduction temperature. Whereas at 100 °C the Rh XANES spectrum resembles that of the Rh_2O_3 reference (Fig. 6.3a), it is very similar to that of the Rh foil after reduction at 200 °C (Fig. 6.3i). This shows that reduction takes place between 100 and 200 °C. The most significant changes in the XANES spectra of RhRe/C at the Re L_{III} edge also occur in the same temperature regime. These findings are in line with the TPR results.
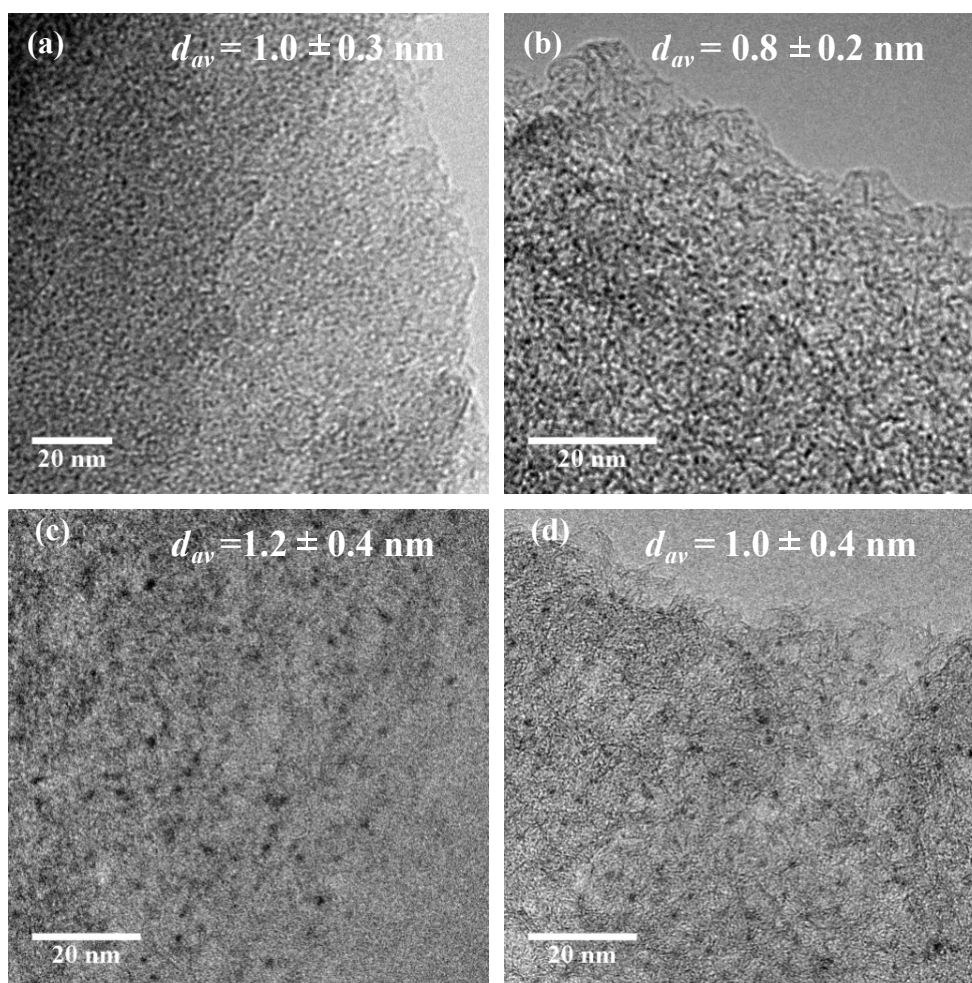
Figure 6.2: TEM images and average particle sizes determined for (a) Rh/C, (b) RhRe/C, (c) Pt/C and (d) PtRe/C.

Figs. 6.4 shows the experimentally obtained FT EXAFS spectra and their fits at the Rh K, Re L_{III} and Pt L_{III} edges of the reduced catalysts. The fit parameters are collected in Table 6.2. Rh/C reduced at 300 °C contains a Rh-Rh shell with a coordination number (CN) of 6.9 and a bond distance (R) of 2.681 Å (Table 6.2). The CN of the Pt-Pt shell in reduced Pt/C is 8.3. The difference points to higher dispersion of Rh/C, although also smaller ordering of the atoms in nanoparticles can also cause lower coordination numbers. For the bimetallic RhRe catalyst Rh-Re and Rh-Rh interactions can be distinguished. The bond distance of the Re-Rh shell in the bimetallic catalyst is 2.656 Å (Table 6.2). In view of the metal bonding radii of 0.134 and 0.137 nm for Rh and Re, respectively [34], this bond distance represents a direct Rh-Re interaction. A Re-O shell with a CN of 0.5 was also included during fitting, which indicates that a fraction of the Re species remains in (partially) oxidic state in line with XANES results. At the Rh K edge, no Rh-O shell was observed, which points to the presence of well-reduced Rh metal particles. The smaller CN of the Rh-Re shell (0.4) compared to the Re-Rh shell (CN = 2.5) points to the isolated nature of the Re atoms in the bimetallic nanoparticles [34]. The CN of the Rh-Rh shell for the Re-modified bimetallic catalyst is lower (2.5), even if the Rh-Re coordination is taken into account (total 2.9), than the Rh-Rh

CN of the monometallic Rh/C catalyst (6.9). This points to higher dispersion of the bimetallic catalyst. The EXAFS results for the PtRe/C catalysts are less informative, as the Pt-Re and Pt-Pt as well as Re-Pt and Re-Re interactions cannot be separated due to the similarity of the backscattering properties of Pt and Re. The effect of setting the backscatterer to Pt or Re was found to be negligible for the EXAFS analysis of the Pt and Re L_{III}-edge data. The backscattering atom used in fitting was denoted as M with a subscript to indicate the atom type. The PtRe/C catalyst contains a Pt-M_{Pt} shell with a CN of 7.5. The CN of the Re-M_{Re} shell is 7.2. No Pt-O or Re-O coordination was found. In summary, X-ray absorption spectroscopy points to higher dispersion of RhRe/C compared to PtRe/C. The decrease in the CN of the metal-metal shell for Pt upon alloying with Re is much lower than for Rh. All catalysts are well reduced, although a small Re-O contribution is seen in the data for reduced RhRe/C.
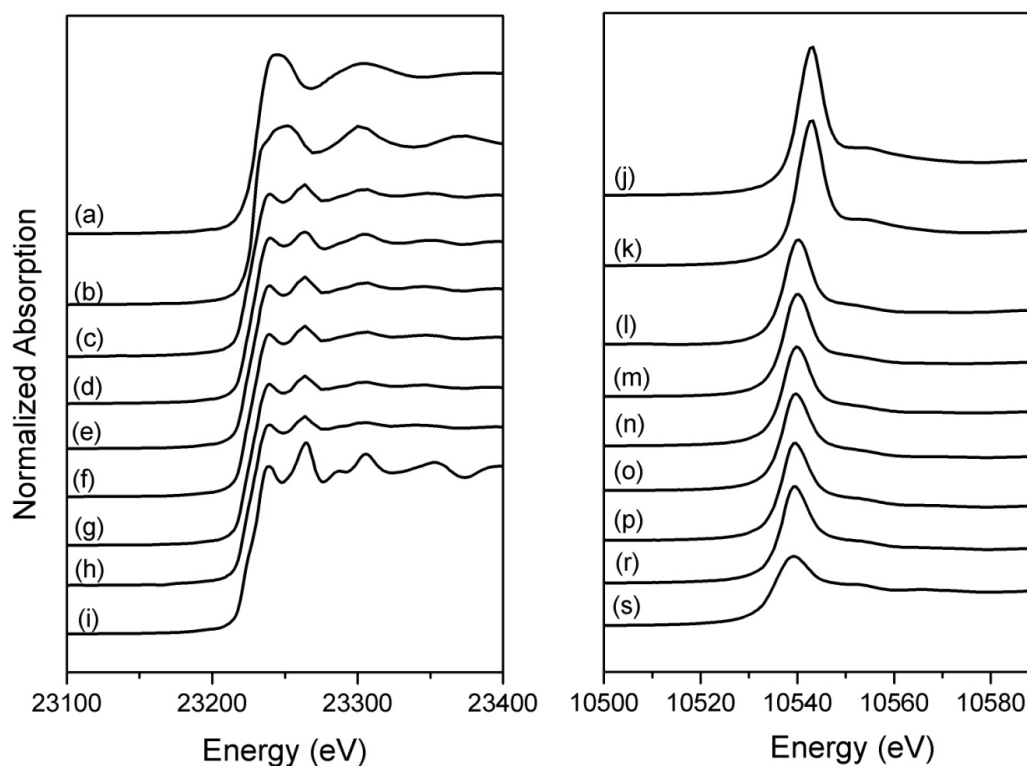

Figure 6.3: Rh K-edge (left) and Re L_{III}-edge (right) XANES spectra of RhRe/C during in situ reduction (b, k) at 100 °C, (c, l) 200 °C, (d, m) 250 °C, (e, n) 300 °C, (f, o) 400 °C, (g, p) 500 °C and (h, r) 550 °C. Re L_{III}-edge XANES spectrum of the as-prepared sample at room temperature is shown as trace j. XANES spectra of Rh_2O_3 (a), Rh foil (i) and Re powder (s) are also included for comparison.

Table 6.2: Fit parameters of k^3-weighted EXAFS spectra at the Rh K, Re L_{III} and Pt L_{III}-edges of supported catalysts recorded at room temperature (catalyst reduced at 300 °C).

Catalyst	EXAFS analysis				
	Shell	R (Å)	CN	$\Delta\sigma^2$ (Å^2)	E_0 (eV)
Rh/C	Rh-Rh	2.681	6.9	0.007	-2.5
Pt/C	Pt-Pt	2.745	8.3	0.009	-9.8
RhRe/C	Rh-Rh	2.678	2.5	0.006	-1.6
	Rh-Re	2.657	0.4	0.002	
	Re-O	2.060	0.5	0.007	-11.3
	Re-Re	2.840	1.2	0.012	
	Re-Rh	2.656	2.5	0.005	
PtRe/C	Pt- M_{Pt}	2.728	7.5	0.010	-8.9
	Re-M_{Re}	2.658	7.2	0.007	-3.6
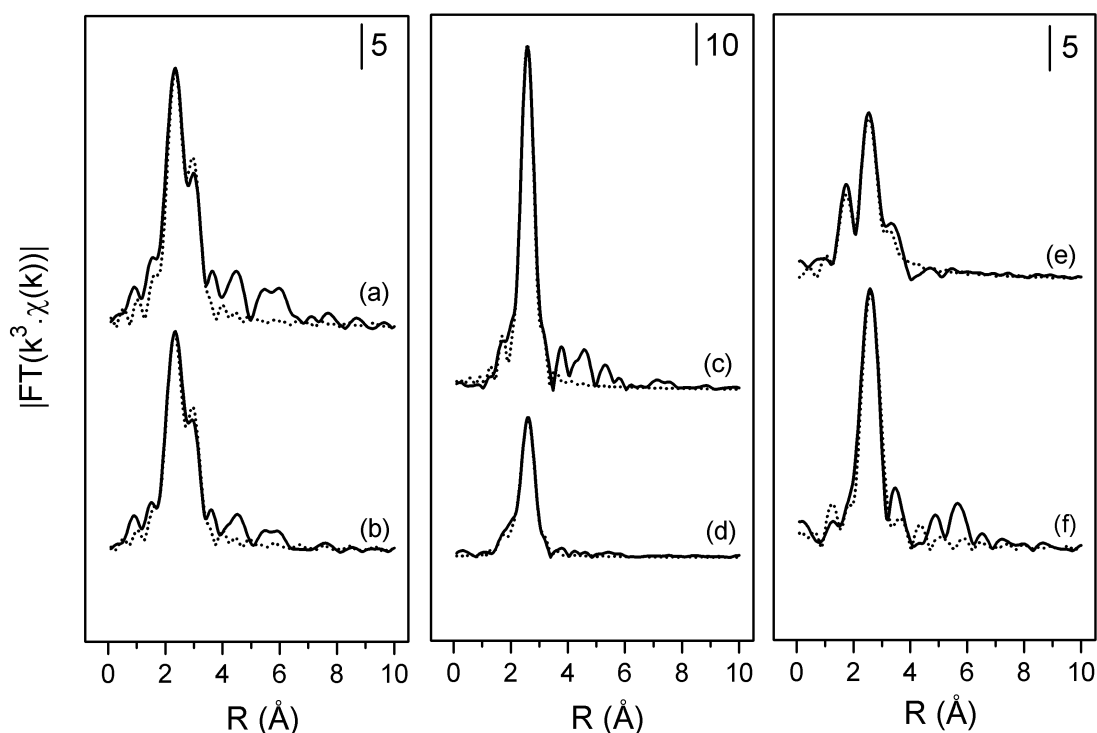
Figure 6.4: FT EXAFS functions obtained from the k^3-weighted Pt L_{III} edge EXAFS oscillations (left) of Pt/C (a), and PtRe/C (b) reduced at 300 °C; FT EXAFS functions obtained from the k^3–weighted Rh K edge EXAFS oscillations (middle) of Rh/C (c), and RhRe/C (d) reduced at 300 °C; FT EXAFS functions obtained from the k^3-weighted Re L_{III} edge EXAFS oscillations (right) of RhRe/C (e), and PtRe/C (f) reduced at 300 °C. Dotted lines represent the fitted spectra.

6.3.2 Catalytic activity measurements

The WGS reaction is a key step in the APR reaction mechanism, because it removes adsorbed CO product from the catalyst surface and generates additional H_2 by reaction with water [4]. Separate gas-phase WGS activity measurements were carried out to establish possible differences in the WGS rate for the carbon-supported catalysts. Fig. 6.5 shows Arrhenius plots for all of the catalysts. Among the monometallic catalysts, Re/C is more

active than Pt/C and Rh/C, especially at higher temperatures. Rh/C and Pt/C have nearly similar catalytic activities. The bimetallic catalysts are significantly more active in WGS than the monometallic ones. The apparent activation energies are 70, 85, 106, 102 and 126 kJ/mol for Pt/C, Rh/C, Re/C, PtRe/C and RhRe/C, respectively. The promotional effect of Re is substantially higher for Rh than for Pt. EXAFS recorded during the WGS reaction at 300 °C shows that the Rh and Pt nanoparticles in the monometallic catalysts remain metallic (Fig. 6.6, Table 6.3). The metal-metal coordination numbers in Rh/C and Pt/C increase only slightly. For RhRe/C, the coordination numbers of the metal-metal shells increase significantly. These data suggest the growth of the initially small bimetallic RhRe nanoparticles during WGS operation. However, this is at odds with the finding that the WGS activity of RhRe/C was very similar during cooling from 400 °C as it was during the initial forward heating trend. An alternative interpretation of the EXAFS data is that the RhRe particles become better ordered during the WGS reaction. This is then also in line with the nearly similar total Rh-(Rh+Re) coordination shells (~6.8) as compared to that of Rh/C during WGS (7.1). EXAFS data analysis does not show significant changes in the structure around Pt and Re for the PtRe catalyst during the WGS.
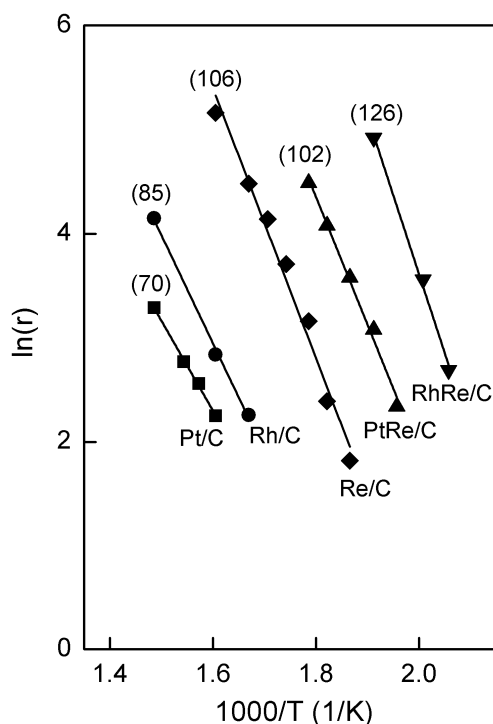

Figure 6.5: Arrhenius plot for WGS reaction over Pt/C (*square*), Rh/C (*circle*), PtRe/C (*up triangle*), RhRe/C (*down triangle*) and Re/C (*diamond*). All catalysts reduced at 300 °C, except for Re/C which was reduced at 500 °C (2.5 vol% CO and 7.5 vol% H_2O balanced by He at a dry GHSV of ~1.5×10^5 h^{-1}).
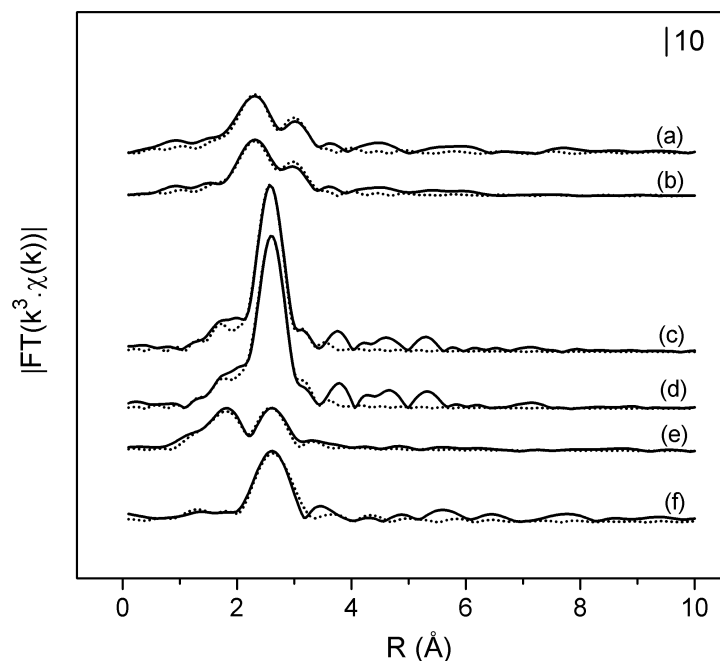
Figure 6.6: FT EXAFS functions obtained from the k^3-weighted Pt L_{III} edge EXAFS oscillations of Pt/C (a), and PtRe/C (b) during WGS at 300 °C; FT EXAFS functions obtained from the k^3-weighted Rh K edge EXAFS oscillations of Rh/C (c), and RhRe/C (d) during WGS at 300 °C; FT EXAFS functions obtained from the k^3-weighted Re L_{III} edge EXAFS oscillations of RhRe/C (e), and PtRe/C (f) during WGS at 300 °C. Dotted lines represent the fitted spectra.

Table 6.3: Fit parameters of k^3-weighted EXAFS spectra at the Rh K, Re L_{III} and Pt L_{III}-edges of supported catalysts recorded during the WGS reaction at 300 °C.

Catalyst	EXAFS analysis				
	Shell	R (Å)	CN	$\Delta\sigma^2$ (Å^2)	E_0 (eV)
Rh/C	Rh-Rh	2.675	7.1	0.010	-0.3
Pt/C	Pt-Pt	2.744	9.8	0.014	-9.5
RhRe/C	Rh-Rh	2.679	6.2	0.008	-1.6
	Rh-Re	2.645	0.6	0.002	
	Re-O	2.001	0.5	0.003	-8.0
	Re-Re	2.729	4.8	0.016	
	Re-Rh	2.670	3.5	0.009	
PtRe/C	Pt-M_{Pt}	2.734	7.8	0.013	-9.6
	Re-M_{Re}	2.675	8.3	0.010	-4.6

Acetaldehyde decomposition was used as a model reaction to probe catalytic activity in C-C bond cleavage. The feed mixture contained hydrogen to avoid excessive carbon lay-down on the metal nanoparticles. The decomposition products CO and CH_4 were found in equimolar ratios. For PtRe/C, a small amount of ethanol was found due to acetaldehyde hydrogenation (selectivity ~10 %). Fig. 6.7 shows the yield of CO as a function of time on stream for the various catalysts. Re/C was inactive under the reaction conditions, which is likely due to its high metal-carbon energy resulting in blocking of the active sites by

carbonaceous deposits. The acetaldehyde decomposition activity of Rh/C is three times higher than that of Pt/C. This difference is consistent with the higher activity of Rh compared to Pt in ethane hydrogenolysis as reported by Sinfelt [37]. Whereas the rate determining step in ethane hydrogenolysis is the C-H bond cleavage step, the higher rate of Rh in ethane and acetaldehyde hydrogenolysis compared to Pt should be related to the higher metal-carbon bond energy for the former metal [38]. Addition of Re to the monometallic catalysts strongly increases the reaction rate. Although there might be an effect of the smaller particle size upon alloying with Re, the higher metal-carbon bond energy of Re is expected to be the dominant factor for the higher activity in decarbonylation. The presence of Pt or Rh in the alloy with Re ensures the removal of the CH_3 surface intermediates following acetaldehyde decarbonylation, these metals being better hydrogenation catalysts than Re. Based on pseudo-first order kinetics with respect to acetaldehyde, the activity increased by a factor ~2.2 for Pt/C and ~1.8 for Rh/C upon alloying with Re. In contrast to the other catalysts, RhRe/C deactivates slowly. The reason for this deactivation is not clear but might be related to the high rate of acetaldehyde decomposition and the low rate of hydrogenation resulting in carbon deposition on the catalytic surface.
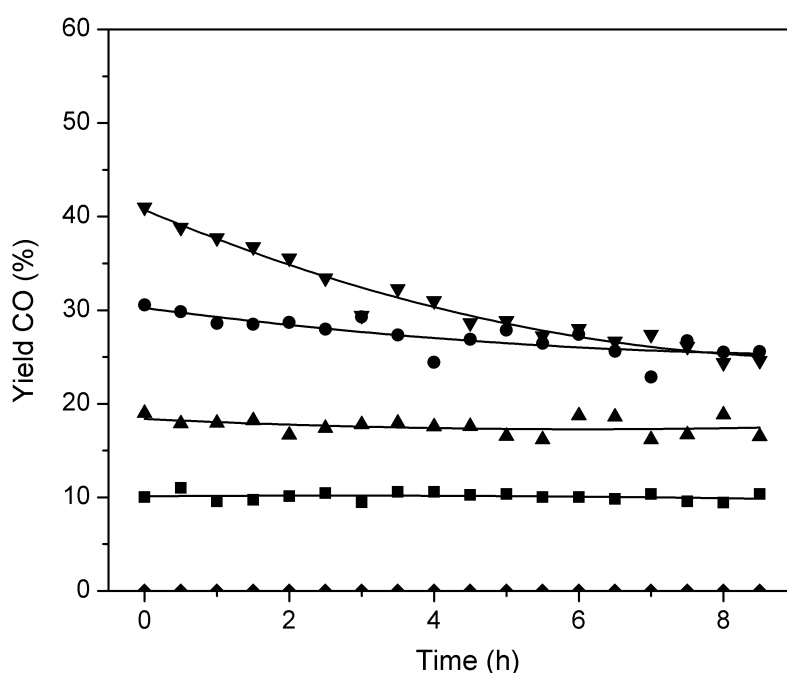

Figure 6.7: Yield of acetaldehyde decomposition product CO as a function of time on stream for Rh/C (*circle*), Pt/C (*square*), RhRe/C (*down triangle*), PtRe/C (*up triangle*) and Re/C (*diamond*).(T= 225 °C, GHSV= 7200 $ml_{acetaldehyde}/g_{cat}$.h; gas-phase composition H_2:C_2H_4O=1:1 by volume with balance He).

The glycerol conversion in APR as a function of batch time for the various catalysts is shown in Fig. 6.8. All catalysts were reduced at 300 °C, except for Re/C which was reduced at 500 °C to ensure complete reduction. The activity increases in the order Re/C < Rh/C < Pt/C < PtRe/C < RhRe/C. The low activity of Re/C is consistent with literature on the reforming and hydrogenolysis of polyols [13,18,22,39]. Pt/C exhibits higher APR activity than Rh/C, in line with the results reported by Dumesic et al. for APR of ethylene glycol [10].

As the atomic Pt(Rh)/Re ratios of the two bimetallic catalysts are very similar, the promoting effect of Re is higher for Rh/C than for Pt/C in glycerol APR.
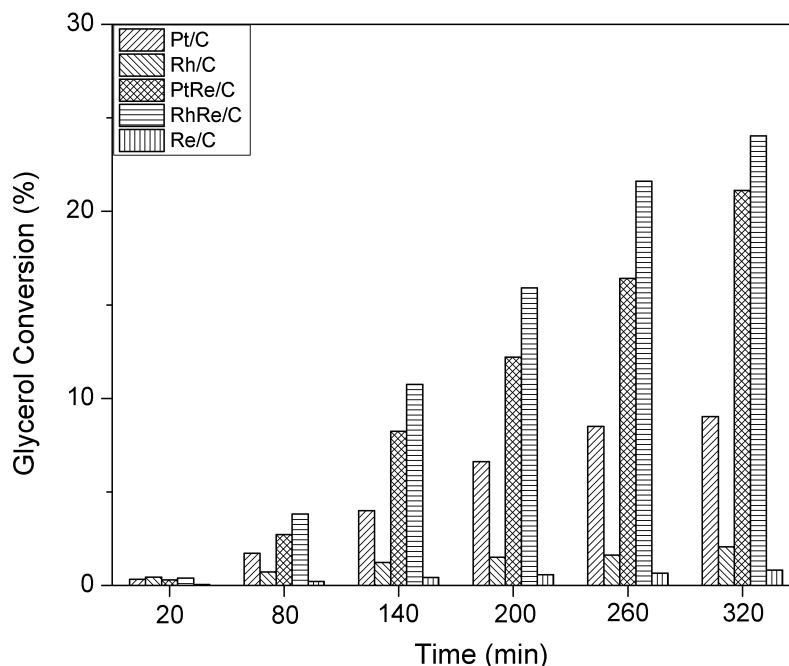

Figure 6.8: Glycerol conversion by time obtained over the Rh/C, Pt/C and RhRe/C, PtRe/C and Re/C in APR of glycerol at 225 °C. (Feed: 60 g of 10 wt% aqueous glycerol solution, catalyst amount: 75 mg).

The reaction mechanism in APR involves two competing reaction pathways differing in the way oxygen is removed [17]. In the first one, oxygen is removed by dehydration of an alcohol group followed by hydrogenation of the resulting olefinic bond (C-O bond cleavage) and, in the second one by decarbonylation of aldehyde intermediates obtained after initial dehydrogenation (C-C bond cleavage). Dehydrogenation of glycerol to glyceraldehyde is the first step for the latter reaction pathway. Decarbonylation of glyceraldehyde via C-C cleavage leads to the formation of CO and ethylene glycol. Product CO is converted to CO_2 via the water-gas shift reaction. Because of the low temperature and excess water, the gas phase will mainly contain CO_2 with only minor amounts of CO [4]. Dehydration and subsequent hydrogenation removes oxygen via water. The intermediate product observed following glycerol dehydration is hydroxyacetone. Upon hydrogenation, 1,2-propanediol and a small amount of 1,3-propanediol are formed and they are converted to propanols and finally to propane by similar reactions [7]. The hydrogenation reaction in the C-O bond cleavage pathway consumes the hydrogen produced in the dehydrogenation and C-C bond cleavage pathway. Thus, while formation of propane requires exclusively dehydration and hydrogenation reactions (C-O bond cleavage), formation of ethane involves one decarbonylation step and two dehydration steps. Ethanol is formed via hydrogenolysis of ethylene glycol [13,40]. Methane is the product of decarbonylation of acetaldehyde obtained from ethanol. Note that blank reactions in APR and also in the WGS reaction did not show any formation of methane, so that we can exclude undesired reforming of the carbon support.
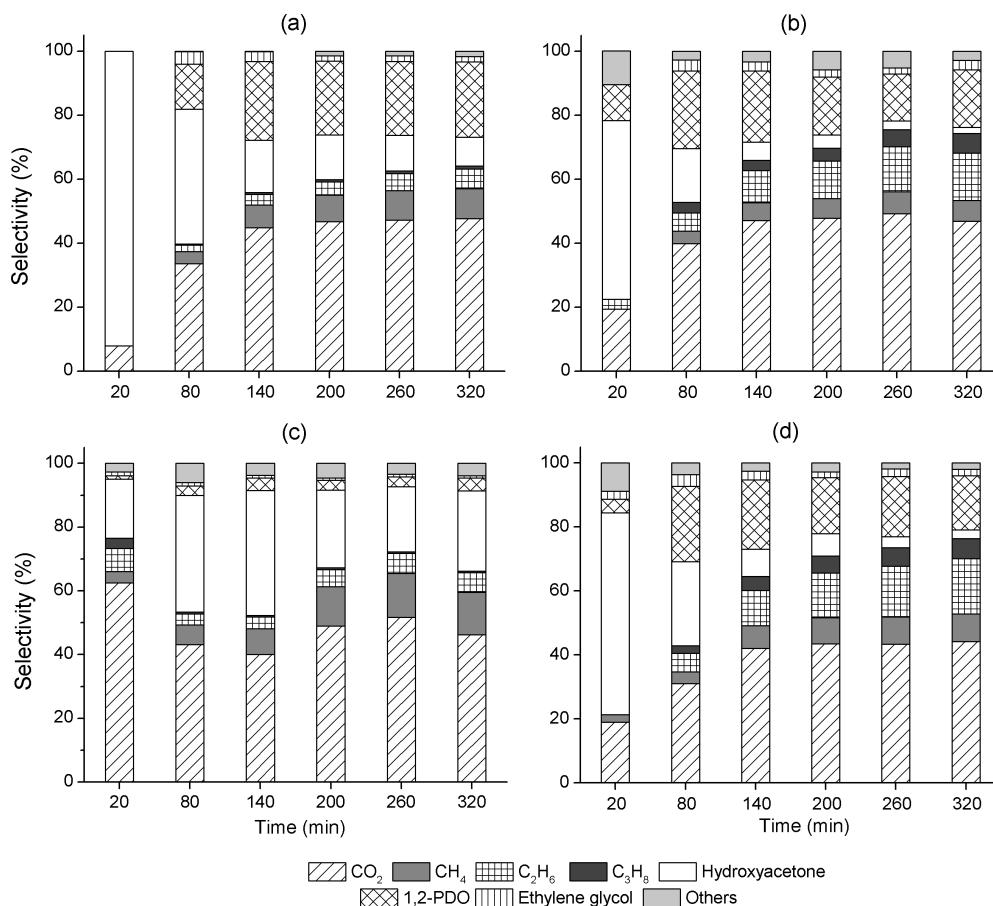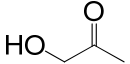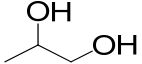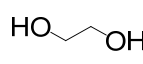
Figure 6.9: Selectivities as a function of time during APR of glycerol over (a) Pt/C, (b) PtRe/C, (c) Rh/C and (d) RhRe/C at 225 °C. (Feed: 60 g of 10 wt% aqueous glycerol solution, catalyst amount: 75 mg).

Product selectivites as a function of time for Pt/C, Rh/C, PtRe/C and RhRe/C are shown in Fig. 6.9 (detailed product distribution in Tables 6.4-6.9). The main products for Re/C are hydroxyacetone and 1,2-propanediol with minor amounts of CO_2 produced. This product distribution is consistent with the low acetaldehyde decarbonylation activity for Re/C. Note that, initially no 1,2-propanediol is formed over Re/C (Table 6.4). With increasing batch time, only a minor part of hydroxyacetone is hydrogenated to 1,2-propanediol, as Re/C alone is a poor hydrogenation catalyst [18]. The product selectivities of Pt/C and Rh/C with increasing batch time are significantly different. At low conversion, hydroxyacetone is the dominant product for Pt/C (C-O bond cleavage), whereas Rh/C produces mainly CO_2 and alkanes next to a much smaller amount of hydroxyacetone. The difference with Pt/C is due to the much higher decarbonylation activity of Rh/C consistent with the much higher rate of acetaldehyde decarbonylation. The ratio of 1,2-propanediol over hydroxyacetone is also much lower for Rh/C than for Pt/C, which points to a lower rate of hydrogenation. The most likely reason for the higher rate of decarbonylation of Rh/C is the higher metal-carbon bond energy for Rh compared to Pt. The overall differences in the product selectivities are also reflected in the data shown in Fig. 6.10. Fig. 6.10a shows the ratio of C-O and C-C bond cleavage reaction rates. The value determined for Pt/C (around
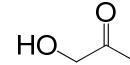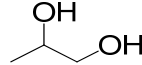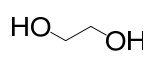
0.6) is in agreement with the results obtained by Zhang et al. in APR of glycerol over Pt/C in a fixed bed continuous flow reactor system [17]. This ratio is initially lowest for Rh/C. Fig. 6.10b shows the H_2/CO_2 ratio, which is close to the theoretical value of 2.3 for complete reforming of glycerol to CO_2 and H_2. The reason is the low rate of hydrogenation over Rh/C throughout the experiment. Thus, it is concluded that the main reaction pathway for Rh/C involves dehydrogenation and decarbonylation of glycerol to alkanes and CO which is rapidly converted to CO_2. With increasing batch time more hydroxyacetone is formed. As the APR reaction proceeds, the dominance of C-C bond cleavage over Rh/C becomes less pronounced as intermediate products will also undergo C-O bond cleavage reactions. For Pt/C we observe a decreasing selectivity of hydroxyacetone with time, which is related to its hydrogenation to 1,2-propanediol. Although Rh/C is slightly more active than Pt/C in the WGS reaction, Pt/C shows a higher glycerol conversion rate. The higher H_2 and CO_2 yields obtained for Pt/C when compared to Rh/C (Table 6.10) is also related to the higher overall conversion obtained using Pt/C.

Table 6.4: Conversion (X) of glycerol (%) and product selectivities (%) in APR of glycerol for Pt/C, PtRe/C, Rh/C, RhRe/C and Re/C catalysts after 20 min of reaction. (Feed: 60 g of 10 wt% aqueous glycerol solution, catalyst amount: 75 mg).

	Xglycerol	CO_2	CH_4	C_2H_6	C_3H_8	hydroxyacetone	1,2-propanediol	ethylene glycol	alcohols[1]	acids[2]	others[3]
Pt/C	0.3	7.9	-	-	-	92.1	-	-	-	-	-
PtRe/C	0.3	19.4	-	3.1	-	55.8	11.3	-	5.9	4.6	-
Rh/C	0.4	62.5	3.6	7.2	3.3	18.5	1.1	1.1	0.9	-	1.9
RhRe/C	0.4	19.0	2.4	-	-	63.0	4.3	2.5	0.9	2.4	5.5
Re/C	0.1	13.2	-	-	-	86.7	-	-	-	-	0.1

[1] alcohols: methanol, ethanol, 1-propanol, 2-propanol. [2] acids: acetic acid, propanoic acid. [3] others: CO, propionaldehyde, 1,3-propanediol

Table 6.5: Conversion (X) of glycerol (%) and product selectivities (%) in APR of glycerol for Pt/C, PtRe/C, Rh/C, RhRe/C and Re/C catalysts after 80 min of reaction. (Feed: 60 g of 10 wt% aqueous glycerol solution, catalyst amount: 75 mg).

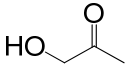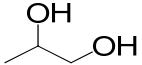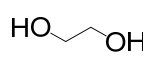|	Xglycerol	CO_2	CH_4	C_2H_6	C_3H_8	hydroxyacetone	1,2-propanediol	ethylene glycol	alcohols[1]	acids[2]	others[3]
Pt/C	1.7	33.6	3.8	2.0	0.4	42.1	14.1	3.9	-	-	0.1
PtRe/C	2.7	39.9	3.9	5.7	3.3	16.8	24.2	3.5	1.9	0.8	-
Rh/C	0.7	43.2	6.2	3.4	0.7	36.5	3.0	1.0	-	0.8	5.2
RhRe/C	3.8	31.0	3.8	5.8	2.3	26.3	23.6	3.6	0.9	0.7	2.0
Re/C	0.2	11.6	-	-	-	88.2	-	-	-	-	0.2

[1] alcohols: methanol, ethanol, 1-propanol, 2-propanol. [2] acids: acetic acid, propanoic acid. [3] others: CO, propionaldehyde, 1,3-propanediol

Table 6.6: Conversion (X) of glycerol (%) and product selectivities (%) in APR of glycerol for Pt/C, PtRe/C, Rh/C, RhRe/C and Re/C catalysts after 140 min of reaction. (Feed: 60 g of 10 wt% aqueous glycerol solution, catalyst amount: 75 mg).

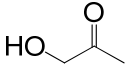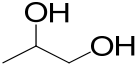|	Xglycerol	CO_2	CH_4	C_2H_6	C_3H_8	hydroxyacetone	1,2-propanediol	ethylene glycol	alcohols[1]	acids[2]	others[3]
Pt/C	4.0	44.8	7.1	3.4	0.5	16.4	24.6	3.0	-	-	0.2
PtRe/C	8.3	47.1	5.5	10.1	3.2	5.7	22.1	2.8	2.3	0.7	0.5
Rh/C	1.2	40.0	8.2	3.7	0.4	39.2	3.9	0.9	0.3	0.4	3.0
RhRe/C	10.8	42.1	7.1	11.0	4.4	8.6	21.6	2.7	0.9	0.4	1.2
Re/C	0.4	11.1	-	-	-	79.6	9.3	-	-	-	-

[1] alcohols: methanol, ethanol, 1-propanol, 2-propanol. [2] acids: acetic acid, propanoic acid. [3] others: CO, propionaldehyde, 1,3-propanediol

Table 6.7: Conversion (X) of glycerol (%) and product selectivities (%) in APR of glycerol for Pt/C, PtRe/C, Rh/C, RhRe/C and Re/C catalysts after 200 min of reaction. (Feed: 60 g of 10 wt% aqueous glycerol solution, catalyst amount: 75 mg).

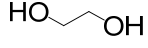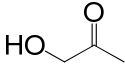|	Xglycerol	CO_2	CH_4	C_2H_6	C_3H_8	hydroxyacetone	1,2-propanediol	ethylene glycol	alcohols[1]	acids[2]	others[3]
Pt/C	6.6	46.7	8.3	4.2	0.7	14.0	23.1	1.7	1.4	-	-
PtRe/C	12.2	47.8	6.1	11.8	4.1	4.1	18.1	2.3	4.3	0.9	0.5
Rh/C	1.5	49.0	12.4	5.3	0.5	24.4	3.2	0.7	0.5	0.4	3.6
RhRe/C	15.9	43.5	8.2	14.0	5.3	7.0	17.5	1.9	1.2	0.7	0.7
Re/C	0.6	10.2	-	-	-	78.3	11.5	-	-	-	-

[1]alcohols: methanol, ethanol, 1-propanol, 2-propanol. [2]acids: acetic acid, propanoic acid. [3]others: CO, propionaldehyde, 1,3-propanediol

Table 6.8: Conversion (X) of glycerol (%) and product selectivities (%) in APR of glycerol for Pt/C, PtRe/C, Rh/C, RhRe/C and Re/C catalysts after 260 min of reaction. (Feed: 60 g of 10 wt% aqueous glycerol solution, catalyst amount: 75 mg).

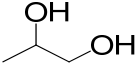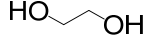|	Xglycerol	CO_2	CH_4	C_2H_6	C_3H_8	hydroxyacetone	1,2-propanediol	ethylene glycol	alcohols[1]	acids[2]	others[3]
Pt/C	8.5	47.2	9.2	5.4	0.8	11.1	23.1	1.8	1.4	-	-
PtRe/C	16.4	49.3	6.8	14.1	5.3	2.7	14.7	1.9	4.0	0.8	0.4
Rh/C	1.6	51.8	13.7	6.3	0.5	20.5	3.1	0.8	0.2	0.3	2.8
RhRe/C	21.6	43.4	8.5	15.8	5.9	3.4	18.9	2.3	0.6	0.4	0.8
Re/C	0.7	11.2	-	-	-	71.5	17.4	-	-	-	-

[1]alcohols: methanol, ethanol, 1-propanol, 2-propanol. [2]acids: acetic acid, propanoic acid. [3]others: CO, propionaldehyde, 1,3-propanediol.

Table 6.9: Conversion (X) of glycerol (%) and product selectivities (%) in APR of glycerol for Pt/C, PtRe/C, Rh/C, RhRe/C and Re/C catalysts after 320 min of reaction. (Feed: 60 g of 10 wt% aqueous glycerol solution, catalyst amount: 75 mg).

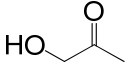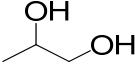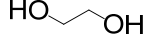|	Xglycerol	CO_2	CH_4	C_2H_6	C_3H_8	hydroxyacetone	1,2-propanediol	ethylene glycol	alcohols[1]	acids[2]	others[3]
Pt/C	9.0	47.7	9.3	6.2	0.9	8.9	23.5	1.7	1.4	0	0.4
PtRe/C	21.1	46.8	6.5	14.9	6.1	1.9	18.0	2.9	1.4	0.5	0.2
Rh/C	2.1	46.3	13.3	6.2	0.4	25.2	4.0	0.7	0.5	0.4	3.0
RhRe/C	24.0	44.2	8.6	17.3	6.3	2.7	17.0	2.0	0.7	0.4	0.8
Re/C	0.8	10.7	-	-	-	75.3	14.0	-	-	-	-

[1]alcohols: methanol, ethanol, 1-propanol, 2-propanol. [2]acids: acetic acid, propanoic acid. [3]others: CO, propionaldehyde, 1,3-propanediol

Table 6.10: Yields (Y) of H_2 and CO_2 (%) for aqueous phase reforming of glycerol over Pt/C, PtRe/C, Rh/C and RhRe/C as a function of time. (Feed: 60 g of 10 wt% aqueous glycerol solution, catalyst amount: 75 mg).

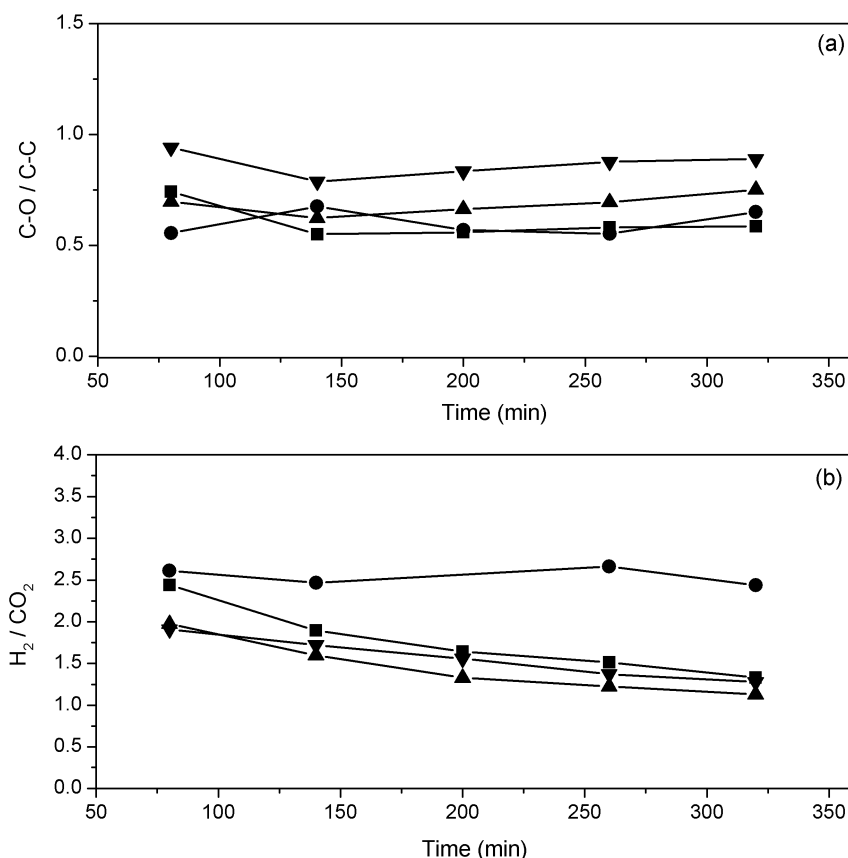| Catalyst	Time (min)											
	20		80		140		200		260		320	
	$Y(H_2)$	$Y(CO_2)$	$Y(H_2)$	$Y(CO_2)$	$Y(H_2)$	$Y(CO_2)$	$Y(H_2)$	$Y(CO_2)$	$Y(H_2)$	$Y(CO_2)$	$Y(H_2)$	$Y(CO_2)$
Pt/C	-	0.1	4.2	1.7	10.2	5.4	15.3	9.3	18.2	12.0	17.2	12.9
PtRe/C	-	0.2	6.4	3.3	18.6	11.7	23.3	17.5	29.7	24.3	33.5	29.7
Rh/C	0.3	0.8	2.5	1.0	3.7	1.5	7.0	2.2	6.7	2.5	7.0	2.9
RhRe/C	-	0.2	6.8	3.6	23.3	13.6	32.3	20.7	38.6	28.1	40.7	31.8

Figure 6.10: C-O/C-C bond cleavage ratios (a) and H_2/CO_2 ratios (b) for Rh/C (*circle*), Pt/C (*square*), RhRe/C (*down triangle*) and PtRe/C (*up triangle*) during glycerol APR at 225 °C. (Feed: 60 g of 10 wt% aqueous glycerol solution, catalyst amount: 75 mg).

Alloying with Re leads to much higher overall reaction rates and significant changes in the product composition in the APR of glycerol. The ratio of C-O over C-C bond cleavage reactions is significantly increased (Fig. 6.10a). The acetaldehyde decomposition activity data show that addition of Re increases the decarbonylation activities of Pt/C and Rh/C. This is explained by the formation of an alloy of Pt and Rh with the more reactive Re metal. It is consistent with the findings for PtRe alloys in naphtha reforming [41]. In classical reforming, Re sites are poisoned by H_2S to decrease the rate of undesired C-C bond cleavage reactions. In glycerol APR, the dominant effect of Re is to bring about a much higher rate of dehydration as is evident from the very different product distributions obtained upon alloying and the finding that the product distributions for PtRe/C and RhRe/C are similar. Fig. 6.10b shows that alloying results in lower H_2/CO_2 ratios because of the use of product H_2 for hydrogenation of the intermediates obtained by dehydration. The initial values for Pt/C and PtRe/C of around 2.3 and 2.0 are in agreement with the results reported by Zhang et al. for similar catalysts in APR of glycerol [17]. The shift to higher selectivity of ethane and propane at the expense of methane selectivity upon Re addition is also a consequence of the higher C-O over C-C bond cleavage reaction rates. In addition, the overall yields of H_2 and CO_2 are substantially increased upon alloying Rh and Pt with Re (Table 6.10). The increase in the H_2 (CO_2) yield is the highest for the RhRe/C catalyst.

The influence of Re as a metal to bring about Brønsted acidity during aqueous phase reactions has been well established by now [13]. For instance, the formation of such acid sites upon steaming of PtRe/C at 225 °C has been followed by NH_3-TPD [17]. The increased surface acidity of Rh/C upon addition of Re was also noted for non-steamed samples [13]. Similar acidic properties were identified for Re-modified Ru/SiO$_2$ catalysts [42]. The work of Dumesic, Neurock and their co-workers has shown that Re-OH surface species can catalyze dehydration reactions of alcohol groups [13]. The stronger metal-oxygen bond energy results in more facile dissociation of water. Note that Re/C is apparently not very active for dehydration. This is most likely due to the propensity of Re to become oxidized when no other more noble metal is present. The stability of the PtRe alloy appears to be in accord with the extensive alkane reforming literature for PtRe catalysts [43,44]. DFT calculations suggest higher stability for RhRe alloys [45]. While we cannot draw firm conclusions on the stability of the RhRe bimetallic particles during APR of glycerol, the in situ EXAFS data show that RhRe is stable under gaseous WGS conditions.

The overall conversion of glycerol in APR for Rh/C increased more than an order of magnitude upon alloying with Re, whereas the PtRe catalyst was only twice as active as Pt/C. Although glycerol conversion obtained at a reaction time of 320 min for Pt/C (9 %) is similar to the value (7.4) reported for a Pt/C catalyst with similar Re content in a recent study [17], glycerol conversion for PtRe/C (21.1 %) is substantially lower than the one reported in the published work (68.2 %). This difference most probably relates to the higher Re content (almost twice as much) used during the synthesis of PtRe/C in that study. A general feature of the APR reaction at relatively low temperatures is the poisoning of the metal surface by product CO [19]. A high rate of the WGS reaction will lower the steady-state CO coverage and, accordingly, increase the overall conversion during APR. The addition of Re has a very positive effect on the WGS activity of the monometallic catalysts (Fig. 6.5). For instance, alloying with Re increases the WGS activity of Rh/C by almost 40 times at 225 °C. For Pt/C, on the other hand, the promotional effect of Re is less pronounced. At 225 °C, PtRe/C is nearly 3 times more active than Pt/C. These differences between the effect of Re on Pt/C and Rh/C in the WGS reaction are consistent with the trends for the overall conversion and yield of H$_2$ obtained in APR of glycerol. The main reason for the improved WGS performance of the bimetallic catalysts is argued to be the higher activity of metallic Re in the activation of water. Quantum-chemical calculations have shown that the main reaction path for the WGS reaction on Pt(111) involves COOH by reaction of CO with OH [46]. As outlined before, the relatively weak metal-oxygen bond energy for Pt makes water dissociation to OH and O surface intermediates endothermic [47]. Comparatively, the stronger Rh-O bond energy makes O and OH surface intermediate formation nearly thermoneutral and slight exothermic, respectively. This trend is in line with the slightly higher WGS reaction rate for Rh. Accordingly, the strong Re-O bond energy can be argued to be at the origin of the higher WGS activity of Re/C. The nature of the strong synergy between Pt and Rh on the one hand and Re on the other in the WGS reaction is the subject of our further studies. Summarizing, the high activity of carbon-supported PtRe and RhRe for glycerol APR can be related to the

high WGS reaction rate for these bimetallic catalysts. Upon alloying Rh and Pt with Re, the product distributions for glycerol APR are very similar because of the dominance of C-O bond cleavage reactions on Re-OH sites. The role of Pt and Rh, besides bringing about strong synergy in the WGS reaction, is to retain the Re in bimetallic nanoparticles in its metallic state.

6.4 Conclusions

Carbon-supported Pt and Rh nanoparticles are active catalysts for wet reforming of glycerol for generating CO-free hydrogen and useful chemicals. Addition of Re to Pt and Rh increases the overall conversion rate of glycerol. Model reaction studies show how the promoter affects the elementary reaction steps. Addition of Re significantly enhances the gas-phase water-gas shift activity of Pt and Rh. The APR conversion rates trend well with these water-gas shift activities. The increased water-gas shift activity is argued to fastly remove product CO from the bimetallic nanoparticle surface as CO_2, which would otherwise block the active sites. As a consequence, the yield of H_2 in APR of glycerol increases upon addition of Re to Rh and Pt catalysts. The increased water-gas shift activity is argued to be related to the stronger binding of OH on Re. The dominant effect of alloying Pt and Rh with Re on the product selectivities is increased formation of products derived from dehydration reactions involving Re-OH species. Besides, acetaldehyde decarbonylation activity measurements show that the alloys with Re are substantially more active in C-C bond cleavage reactions. The effect of acidity induced by the presence of Re on dehydration (C-O bond cleavage) reactions dominates over the increased C-C bond cleavage rate. As a consequence, the overall effect of alloying with Re is increased formation of products involving selective deoxygenation as well as an increase of the overall reforming to CO_2 and H_2.

References

[1] G. Centi and R.A.van Santen, Catalysis for Renewables: From Feedstock to Energy Production, Wiley-VCH, Weinheim, 2007.
[2] J.N. Chheda, G.W. Huber, J.A. Dumesic, Angew. Chem. Int. Edit. 46 (2007) 7164-7183.
[3] G.W. Huber, S. Iborra, A. Corma, Chem. Rev. 106 (2006) 4044-4098.
[4] R.R. Davda, J.W. Shabaker, G.W. Huber, R.D. Cortright, J.A. Dumesic, Appl. Catal. B 56 (2005) 171-186.
[5] T.A. Milne, C.C. Elam, R.J. Evans, International Energy Agency Report (2002) IEA/H2/TR-02/001.
[6] S. Adhikari, S.D. Fernando, A. Haryanto, Energ. Convers. Manage. 50 (2009) 2600-2604.
[7] A. Wawrzetz, B. Peng, A. Hrabar, A. Jentys, A.A. Lemonidou, J.A. Lercher, J. Catal. 269 (2010) 411-420.
[8] E. Santacesaria, G.M. Vicente, M. Di Serio, R. Tesser, Catal. Today 195 (2012) 2-13.
[9] C.H.C. Zhou, J.N. Beltramini, Y.X. Fan, G.Q.M. Lu, Chem. Soc. Rev. 37 (2008) 527-549.
[10] R.R. Davda, J.W. Shabaker, G.W. Huber, R.D. Cortright, J.A. Dumesic, Appl. Catal. B 43 (2003) 13-26.
[11] J.W. Shabaker, G.W. Huber, R.R. Davda, R.D. Cortright, J.A. Dumesic, Catal. Lett. 88 (2003) 1-8.
[12] D.M. Alonso, S.G. Wettstein, J.A. Dumesic, Chem. Soc. Rev. 41 (2012).
[13] M. Chia, Y.J. Pagan-Torres, D. Hibbitts, Q.H. Tan, H.N. Pham, A.K. Datye, M. Neurock, R.J. Davis, J.A. Dumesic, J. Am. Chem. Soc. 133 (2011) 12675-12689.
[14] S. Koso, Y. Nakagawa, K. Tomishige, J. Catal. 280 (2011) 221-229.
[15] S. Koso, H. Watanabe, K. Okumura, Y. Nakagawa, K. Tomishige, Appl. Catal. B 111 (2012) 27-37.
[16] Y. Shinmi, S. Koso, T. Kubota, Y. Nakagawa, K. Tomishige, Appl. Catal. B 94 (2010) 318-326.
[17] L. Zhang, A.M. Karim, M.H. Engelhard, Z.H. Wei, D.L. King, Y. Wang, J. Catal. 287 (2012) 37-43.

[18] D.L. King, L.A. Zhang, G. Xia, A.M. Karim, D.J. Heldebrant, X.Q. Wang, T. Peterson, Y. Wang, Appl. Catal. B 99 (2010) 206-213.
[19] E.L. Kunkes, D.A. Simonetti, J.A. Dumesic, W.D. Pyrz, L.E. Murillo, J.G.G. Chen, D.J. Buttrey, J. Catal. 260 (2008) 164-177.
[20] Y. Amada, Y. Shinmi, S. Koso, T. Kubota, Y. Nakagawa, K. Tomishige, Appl. Catal. B 105 (2011) 117-127.
[21] Y. Nakagawa, Y. Shinmi, S. Koso, K. Tomishige, J. Catal. 272 (2010) 191-194.
[22] S. Koso, I. Furikado, A. Shimao, T. Miyazawa, K. Kunimori, K. Tomishige, Chem. Commun. (2009) 2035-2037.
[23] T. Buntara, S. Noel, P.H. Phua, I. Melian-Cabrera, J.G. de Vries, H.J. Heeres, Angew. Chem. Int. Edit. 50 (2011) 7083-7087.
[24] D.M. Alonso, J.Q. Bond, J.A. Dumesic, Green Chem. 12 (2010) 1493-1513.
[25] R.D. Cortright, R.R. Davda, J.A. Dumesic, Nature 418 (2002) 964-967.
[26] G.W. Huber, J.W. Shabaker, J.A. Dumesic, Science 300 (2003) 2075-2077.
[27] G.W. Huber, J.W. Shabaker, S.T. Evans, J.A. Dumesic, Appl. Catal. B 62 (2006) 226-235.
[28] Y. Guo, M.U. Azmat, X.H. Liu, Y.Q. Wang, G.Z. Lu, Appl. Energ. 92 (2012) 218-223.
[29] D.A.J.M. Ligthart, R.A. van Santen, E.J.M. Hensen, Angew. Chem. Int. Edit. 50 (2011) 5306-5310.
[30] P. Fornasiero, R. Dimonte, G.R. Rao, J. Kaspar, S. Meriani, A. Trovarelli, M. Graziani, J. Catal. 151 (1995) 168-177.
[31] D.A.J.M. Ligthart, R.A. van Santen, E.J.M. Hensen, J. Catal. 280 (2011) 206-220.
[32] O.M. Daniel, A. DeLaRiva, E.L. Kunkes, A.K. Datye, J.A. Dumesic, R.J. Davis, ChemCatChem 2 (2010) 1107-1114.
[33] T. Ebashi, Y. Ishida, Y. Nakagawa, S. Ito, T. Kubota, K. Tomishige, J. Phys. Chem. C 114 (2010) 6518-6526.
[34] S. Koso, H. Watanabe, K. Okumura, Y. Nakagawa, K. Tomishige, J. Phys. Chem. C 116 (2012) 3079-3090.
[35] D.A. Simonetti, E.L. Kunkes, J.A. Dumesic, J. Catal. 247 (2007) 298-306.
[36] P. Samoila, M. Boutzeloit, C. Especel, F. Epron, P. Marecot, J. Catal. 276 (2010) 237-248.
[37] J.H.Sinfelt, Adv. Catal. (1973) 91-119.
[38] R.A.van Santen and M.Neurock, Molecular Heterogeneous Catalysis: A Conceptual and Computational Approach, Wiley-VCH, Weinheim, 2007.
[39] K.Y. Chen, S. Koso, T. Kubota, Y. Nakagawa, K. Tomishige, ChemCatChem 2 (2010) 547-555.
[40] M. El Doukkali, A. Iriondo, P.L. Arias, J. Requies, I. Gandarias, L. Jalowiecki-Duhamel, F. Dumeignil, Appl. Catal. B 125 (2012) 516-529.
[41] G.M. Bickle, J.N. Beltramini, D.D. Do, Ind. Eng. Chem. Res. 29 (1990) 1801-1807.
[42] L. Ma, Y.M. Li, D.H. He, Chinese J. Catal. 32 (2011) 872-876.
[43] J.L. Xiao, R.J. Puddephatt, Coord. Chem. Rev. 143 (1995) 457-500.
[44] J.M. Parera, J.N. Beltramini, J. Catal. 112 (1988) 357-365.
[45] G.H. Johannesson, T. Bligaard, A.V. Ruban, H.L. Skriver, K.W. Jacobsen, J.K. Norskov, Phys. Rev. Lett. 88 (2002).
[46] L.C. Grabow, A.A. Gokhale, S.T. Evans, J.A. Dumesic, M. Mavrikakis, J. Phys. Chem. C 112 (2008) 4608-4617.
[47] T. Zhu, P.W. van Grootel, I.A.W. Filot, S.G. Sun, R.A. van Santen, E.J.M. Hensen, J. Catal. 297 (2013) 227-235.

Nanostructured ceria supported Pt and Au catalysts for the reactions of ethanol and formic acid

Summary

Decomposition reactions of ethanol and formic acid were studied over a series of Au and Pt nanoparticle catalysts. CeO_2 nanorods and nanocubes served as model supports representing the (110) and (100) surfaces of CeO_2 nanocrystals. Pt was more active than Au in low temperature (< 400 °C) steam reforming, oxidation and decomposition (without an oxygen source) of ethanol. Similar trends were observed in the WGS reaction. Different from Au, for Pt the initial step of ethanol dehydrogenation to acetaldehyde is followed by the cleavage of the C-C bonds of acetaldehyde to CH_4 and CO due to the higher Pt-C bond strength when compared to that of Au-C. The catalysts supported on nanorod-shaped ceria were more active than those derived from nanocube-shaped ones in ethanol steam reforming and WGS reactions due to the abundance of OH species formed by activation of water on the oxygen vacancies in the $CeO_2(110)$ surfaces. These catalysts were active for decomposition of formic acid starting from near-ambient temperatures up to 200 °C. Au was more active and it selectively dehydrogenated formic acid into CO_2 and H_2. The intrinsic activity of the CN-leached $Au/CeO_2(rod)$ catalyst containing highly dispersed sub-nanometer Au clusters was higher than the parent catalyst. Pt, on the other hand, showed lower selectivity towards the dehydrogenation pathway due to its higher activity in WGS reaction and enhanced Pt-O bond strength resulting in decarbonylation of formic acid.
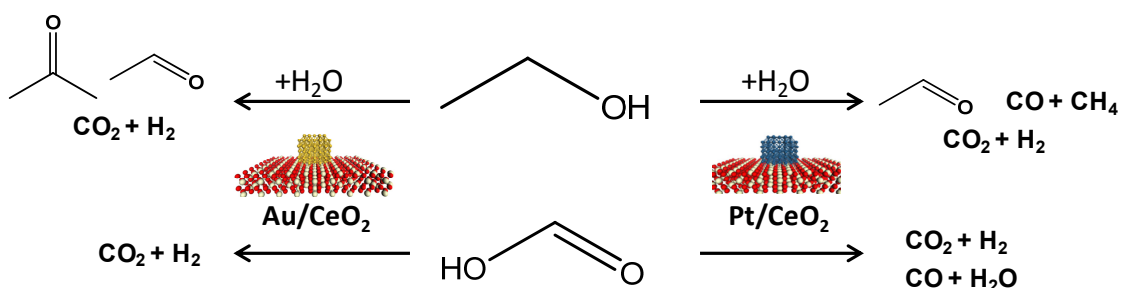
7.1 Introduction

Depletion of fossil fuels and the associated higher costs of these feedstocks in the future as well as environmental concerns related to their combustion have resulted in profound interest in alternative more sustainable energy resources. Therefore, the primary feedstock of the chemical industry is likely to shift from petroleum resources to renewable biomass [1-3]. Ethanol is a renewable feedstock which can be produced from carbohydrate biomass by fermentation. Through catalytic processes ethanol can be transformed into useful chemicals such as acetaldehyde, acetic acid, ethyl acetate, diethyl ether, ethylene oxide, ethylene and through aromatization of ethylene to aromatics like benzene and toluene [1,4,5]. Besides, ethanol is a suitable feedstock for the production of renewable hydrogen, which may become a clean energy carrier in the future. Hydrogen production from bio-ethanol may also become an integral part of future biorefineries because it can be used to upgrade certain biomass fractions [1,2]. Steam reforming of bio-ethanol to produce hydrogen is considered as a more sustainable alternative compared to steam reforming of non-renewable methane [6]. Bio-ethanol is obtained as an aqueous solution of ethanol, which can be almost directly used for steam reforming. The overall reaction of ethanol steam reforming is $C_2H_5OH + 3 H_2O \rightarrow 2 CO_2 + 6 H_2$ [7,8]. Associated with steam reforming is the water-gas shift (WGS) reaction, which plays a key role in the generation of (additional) H_2 from CO [2,9,10]. Due to its easy handling and storage, ethanol is also considered as a promising green fuel for generation of hydrogen for use in H_2-fueled PEM fuel cells. Alternatively, it can be used as a reactant in direct ethanol fuel cells as a non-toxic, renewable alternative to direct methanol fuel cells [11,12].

Similar to ethanol, formic acid is also considered as an attractive liquid fuel for use in PEM fuel cells or in direct formic acid fuel cells (DFAFCs) [13]. Formic acid is generated as a by-product of levulinic acid production during the acid-catalyzed conversion of carbohydrates [14]. It has also been coined as an environmentally benign hydrogen storage material [13,15-17]. Formic acid can also be used as a hydrogen donor in transfer hydrogenation reactions [18,19]. As it is the simplest carboxylic acid, decomposition of formic acid is an interesting model reaction to understand better the more complex chemistry of carboxylic acid conversion reactions. Biomass-derived carboxylic acids are potential feedstocks for obtaining clean hydrogen, fuel-grade alkanes and useful chemicals [1-3]. The decomposition of formic acid may proceed via decarboxylation (dehydrogenation), $HCOOH \rightarrow CO_2 + H_2$ with $\Delta G = -28.5$ kJ/mol or decarbonylation (dehydration), $HCOOH \rightarrow CO + H_2O$ with $\Delta G = -48.4$ kJ/mol. Decarbonylation is the dominant route in the gas phase in the absence of a catalyst. Studies on formic acid decomposition have been mostly concentrated on the use of homogeneous catalysis [15,16,20]. For the gas-phase decomposition of formic acid by heterogeneous catalysts, Rh supported on TiO_2, Al_2O_3, MgO and SiO_2 [21], Pt group metals supported on carbon [22], Au and Pt on Al_2O_3 [23], Pd and Au on carbon and TiO_2 [24], Au supported on SiO_2, carbon, CeO_2, Al_2O_3 and ZSM-5 [25] and supported Mo_2C catalysts [26] have been reported to be effective. Since CO-free H_2 is desired for fuel cell applications, the key point in formic acid decomposition would be to avoid formation of CO

[13]. Accordingly, WGS activity of the formic acid decomposition catalysts is typically undesired.

CeO$_2$ is known to be a promising support for metal nanoparticles used to catalyze steam reforming of organic substances, reportedly because of ceria's involvement in the activation of water [27,28]. Recent works have emphasized that the surface plane of the ceria support on which the active metal phase is supported greatly influences its catalytic activity [29-32]. For instance, the group of Flytzani-Stephanopoulos showed that {110} surface planes of ceria support, the predominant surface on ceria with the nanorod morphology, are able to stabilize highly active Au nanoparticles for the WGS reaction, whereas {100} surface planes yield much less active catalysts [32]. Besides, Yi et al. showed that gold dispersed on CeO$_2$ nanorods showed excellent catalytic activity in low-temperature steam reforming of methanol, whereas Au deposited on CeO$_2$ nanocubes were inactive [29]. Besides, Au also Pt is very active in the WGS reaction [33-37]. As far as ethanol steam reforming is concerned, it is expected that Pt will outperform Au because the former is more active in C-C bond breaking reactions [38]. Although Au and Pt nanoparticle catalysts has received considerable attention in the conversion of ethanol [39-45] and formic acid [22-25] to useful chemicals and hydrogen, a comparison of the catalytic performances of Pt and Au supported on ceria and the effect of different crystal planes of the ceria support on the activity and selectivity of ethanol and formic acid conversion has not been reported yet. Therefore, we investigate the reaction pathways over Au and Pt catalysts supported on nanorod- and nanocube-shaped CeO$_2$ in ethanol (in the presence of O$_2$/H$_2$O and in the absence of an oxygen source) and formic acid decomposition reactions as well as in WGS reaction.

7.2 Experimental

7.2.1 Catalyst synthesis

CeO$_2$ nanorods and -cubes were synthesized according to literature procedures [46]. Typically, 40 mL of 0.5 M Ce(NO$_3$)$_3$ aqueous solution and 60 mL of 10 M NaOH solution were added to a 125 mL Teflon-lined stainless steel autoclave. After stirring for 30 min, the autoclave was transferred to an oven and kept at 100 °C or 180 °C for 24 hours to obtain CeO$_2$ nanorods or nanocubes, respectively. Thereafter, the precipitate was filtered and washed with deionized water until the pH of the filtrate was 7. Finally, the filtrate was dried at 110 °C overnight and calcined at 500 °C in static air for 4 h. The rod- and cube-shaped crystals are denoted by CeO$_2$(rod) and CeO$_2$(cube), respectively.

Platinum was loaded onto the ceria supports by pore volume impregnation using an aqueous Pt(NH$_3$)$_4$(NO$_3$)$_2$ solution. The CeO$_2$ support material was first sieved into a fraction of 125-250 μm and dried overnight at 110 °C. After impregnation, the materials were calcined in air at 450 °C for 2 h. Gold was introduced on the CeO$_2$ supports by homogeneous deposition-precipitation. To this end, a known amount of HAuCl$_4$ and urea were dissolved in 50 mL of water. 1 g of CeO$_2$ was added to this solution and mixed at 90 °C for 1 h. After filtration, washing and drying overnight at 110 °C, the catalyst was calcined at 400 °C for 2 h. A portion of the catalysts was treated with a cyanide-containing solution as outlined by Fu

et al. [33]. An amount of catalyst was suspended in an aqueous solution of 2 wt% NaCN solution. NaOH was added to keep the pH at 12. The mixture was stirred at room temperature for 2 h by bubbling O_2 through the solution. Subsequently, the resulting suspension was filtered, dried at 110 °C overnight and calcined at 400 °C for 4 h. The CN leached samples are denoted as $Au/CeO_2(rod)$-CN and $Au/CeO_2(cube)$-CN.

7.2.2 Catalyst characterization

The metal loading was determined by inductively coupled plasma atomic emission spectrometry (ICP-OES) analysis performed on a Goffin Meyvis Spectro Cirus[ccd] apparatus. The samples were dissolved in a 3:1 HCl/HNO_3 solution by the addition of a few droplets of diluted H_2O_2.

Temperature programmed reduction (TPR) experiments were performed in a flow apparatus equipped with a fixed-bed reactor, a computer-controlled oven and a thermal conductivity detector. Typically, 30 mg catalyst was loaded in a tubular quartz reactor. Prior to TPR, the catalyst was oxidized by exposing to a flowing mixture of 4 vol% O_2 in He by heating to the calcination temperature of the catalyst. After cooling down to room temperature in flowing N_2, the sample was reduced in 4 vol% H_2 in N_2 at a flow rate of 8 ml/min, whilst heating from room temperature up to 800 °C at a ramp rate of 10 °C/min. The H_2 signal was calibrated using a CuO/SiO_2 reference catalyst.

Transmission electron micrographs were acquired on a FEI Tecnai 20 transmission electron microscope at an acceleration voltage of 200 kV with a LaB_6 filament. Typically, a small amount of sample was ground and suspended in pure ethanol, sonicated and dispersed over a Cu grid with a holey carbon film.

H_2-chemisorption was carried out at -80 °C using a Micromeritics ASAP 2020C setup [47]. Before analysis, an amount of sample was reduced from room temperature to 300 °C with a ramp rate of 2 °C/min for 2 h and evacuated at 435 °C. The double isotherm method was employed to determine the irreversibly bound chemisorbed hydrogen. To calculate the metal dispersion, an adsorption stoichiometry of one hydrogen atom per surface platinum atom was assumed. The accuracy of the analysis equipment was regularly verified by measuring a standard Pt/SiO_2 catalyst. The BET surface area was measured by nitrogen adsorption at -196 °C on a Micromeritics Tristar 3000 analyzer after drying the materials at 150 °C.

X-ray photoelectron spectroscopy (XPS) measurements were performed using a Kratos AXIS Ultra spectrometer, equipped with a monochromatic X-ray source and a delay-line detector (DLD). Spectra is obtained by using the aluminium anode (Al Kα = 1486.6 eV) operating at 150 W. Survey scans are measured at constant pass energy of 160 eV and region scans at 40 eV. The background pressure is kept at $2x10^{-9}$ mbar. Quasi-in situ XPS measurements were performed after reduction of the samples in a tubular quartz reactor with 10 °C/min heating rate from room temperature to 400 °C in a flow of 10 vol% H_2 in He (total flow 100 ml/min). After cooling to room temperature, the lids at the inlet and outlet of the

reactor were closed to prevent any interaction with air and the samples were prepared for XPS measurement in an Ar-flushed glove box.

7.2.3 Catalytic activity measurements

Ethanol decomposition experiments were carried out in a fixed bed plug flow reactor system. Typically, 50 mg of catalyst (sieve fraction 125-250 μm) diluted with 300 mg of α-Al_2O_3 was loaded into a stainless steel reactor with an internal diameter of 6 mm. Prior to reaction, the catalyst was reduced in a mixture 20 vol% H_2 in N_2 at 400 °C for 2 hours. Three types of feed compositions were used. The volumetric composition of these feed mixtures were C_2H_5OH:H_2O:He = 1:3:8. C_2H_5OH:O_2:He = 1:3:8 and C_2H_5OH:He=1:11. In the case of ethanol steam reforming experiments the reactant feed mixture was obtained by evaporating ethanol and water in a He stream in two controlled evaporator mixers (Bronkhorst). All tubings were kept above 120 °C to avoid condensation of the reactants and products. The total gas flow rate was 150 ml/min and the GHSV was 15000 ml_{EtOH}/g-cat h for all experiments. The reactor effluent was analyzed by online gas chromatography (Interscience GC-8000 Top, permanent gases on Shincarbon ST80/100 packed column connected to a TCD and hydrocarbons on a RT-Q bond column connected to a FID). The conversion (X) and carbon product selectivities (S_i) were calculated by:

$$X(\%) = \frac{Total\ C\ mol\% - 2 \times C_2H_5OH\ mol\%}{Total\ C\ mol\%} \times 100$$

$$S_i(\%) = \frac{mol\%\ product_i \times number\ of\ C\ atoms}{Total\ C\ mol\% - 2 \times C_2H_5OH\ mol\%} \times 100$$

The H_2 selectivity and yield were calculated by:

$$S_{H_2}(\%) = \frac{mol\%\ H_2}{6 \times \left(Total\ C\ mol\% - 2 \times C_2H_5OH\ mol\%\right)/2} \times 100$$

$$Y_{H_2}(\%) = \frac{mol\%\ H_2}{6 \times \left(Total\ C\ mol\%\right)/2} \times 100$$

The catalytic activity in the WGS reaction was evaluated in a parallel ten-flow microreactor system [48]. Steam was supplied by evaporation of deionized water in a controlled evaporator mixer unit in combination with a liquid-flow controller and gas flows were controlled by mass flow controllers (Brooks and Bronkhorst). All tubings were kept above 100 °C after the point of steam introduction to avoid condensation. The dry product gas mixture was analyzed by an online gas chromatograph (Interscience CompactGC) equipped with Porapak Q (TCD) and Molecular sieve 5A (TCD) columns. Experiments were carried out in a mixture of 2.5 vol% CO and 7.5 vol% H_2O balanced by He at a dry GHSV of 9×10^4 h^{-1} (4×10^4 h^{-1} for the Au/CeO_2(rod)-CN sample) in the temperature range 135-400 °C. Typically, the catalyst was diluted with appropriate amount of SiC of the same sieve fraction. Prior to catalytic activity measurements, the catalyst was reduced in a flow of 20 vol% H_2 in He at 300 °C followed by an isothermal period of 0.5 h. The reactor was cooled in He to the

reaction temperature. The conversion of CO was calculated by dividing the mol% CO converted by the initial concentration of CO in the feed.

The catalytic decomposition of formic acid was investigated in a fixed bed plug flow reactor system. Typically, 50 mg of catalyst (sieve fraction 125-250 μm) diluted with 250 mg of SiC was loaded into a tubular quartz reactor. Prior to the reaction, the catalyst was reduced in a mixture of 20 vol% H_2 in He for 2 hours. The reactant feed mixture was obtained by leading 50 ml/min He through liquid formic acid kept at such temperature that a gas phase concentration of 5 vol% was obtained. The composition of the effluent gas was analyzed by a Compact GC (Interscience) equipped with three channels. Formic acid was analyzed on a Stabilwax-DA column connected to a FID, CO_2 on a RT-Q-bond column connected to a TCD and CO and H_2 by a Molesieve-5A column connected to a TCD. The selectivity to CO_2 (H_2) was calculated by dividing the CO_2 concentration in the products to the sum of CO and CO_2 concentrations.

7.3 Results and discussion

7.3.1 Characterization of the catalysts

The XRD patterns in Fig. 7.1 evidence the crystalline nature of the CeO_2 supports. By use of Scherrer's equation, the particle size of the nanorods and −cubes was determined to be 10 and 75 nm, respectively. Representative transmission electron micrographs of these CeO_2 supports are shown in Fig. 7.2a-d. The *d*-spacing as determined from the electron micrographs is 0.30 nm. The nanorods have an average width of 8.5 nm and lengths between 30 and 150 nm. The nanocubes also exhibit a broad size distribution between 20 and 120 nm. The surface areas of the CeO_2(rod) and CeO_2(cube) samples were measured to be 130 and 14 m^2/g, respectively. The morphology of these nanostructured ceria supports is very similar to what has been reported in recent literature [29,30].

Table 7.1 lists the metal loading of the ceria-supported catalysts. In all cases, the metal content of the prepared catalysts is close to the targetted 2 wt%. Cyanide leaching led to the nearly complete removal of Au from Au/CeO_2(cube). The gold content of Au/CeO_2(cube)-CN is below 0.01 wt%. The gold content of Au/CeO_2(rod)-CN is substantially higher (0.09 wt%) and corresponds quantitatively to an earlier report [30]. The different effect of cyanide leaching for nanorods and −cubes has been related to the stronger interaction of gold cations with the ceria {110} planes, which dominate the surface of the ceria nanorods, than with the {100} planes of the ceria nanocubes. Cyanide leaching was not effective for removing a substantial fraction of Pt, despite the harsher leaching conditions (80 °C) employed for Pt/CeO_2 (results not shown). Transmission electron micrographs of the Au/CeO_2 catalysts are shown in Fig. 7.2e-g. The average sizes of the gold particles in Au/CeO_2(rod) and Au/CeO_2(cube) were 4.7 and 4.8 nm, respectively. Representative for Au/CeO_2(cube)-CN, Fig. 7.2g does not show gold nanoparticles in accordance with the negligible gold loading.
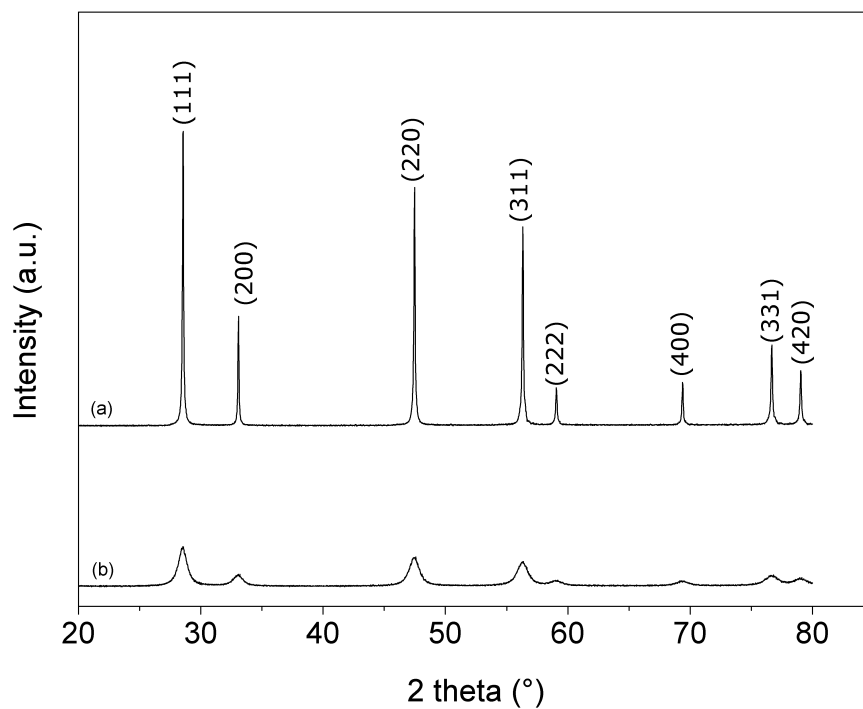
Figure 7.1: X-ray diffraction patterns of (a) CeO_2 cubes and (b) CeO_2 rods.

Table 7.1: Metal loading as determined by ICP analysis and the total hydrogen consumption during the H_2-TPR of ceria-supported catalysts.

Catalyst	Metal loading (wt%)	n_{H2} (μmol/g)	(H_2/M)[1]
Pt/CeO$_2$(rod)	2.05	565	5.4
Pt/CeO$_2$(cube)	1.79	43	0.5
Au/CeO$_2$(rod)	2.14	416	3.8
Au/CeO$_2$(rod)-CN	0.09	514	n.d.[2]
Au/CeO$_2$(cube)	2.13	32	0.3
Au/CeO$_2$(cube)-CN	<0.01	60	n.d.
CeO$_2$(cube)	-	50	-
CeO$_2$(rod)	-	368	-

[1] H_2/Metal (Au/Pt) ratio; [2] not determined.
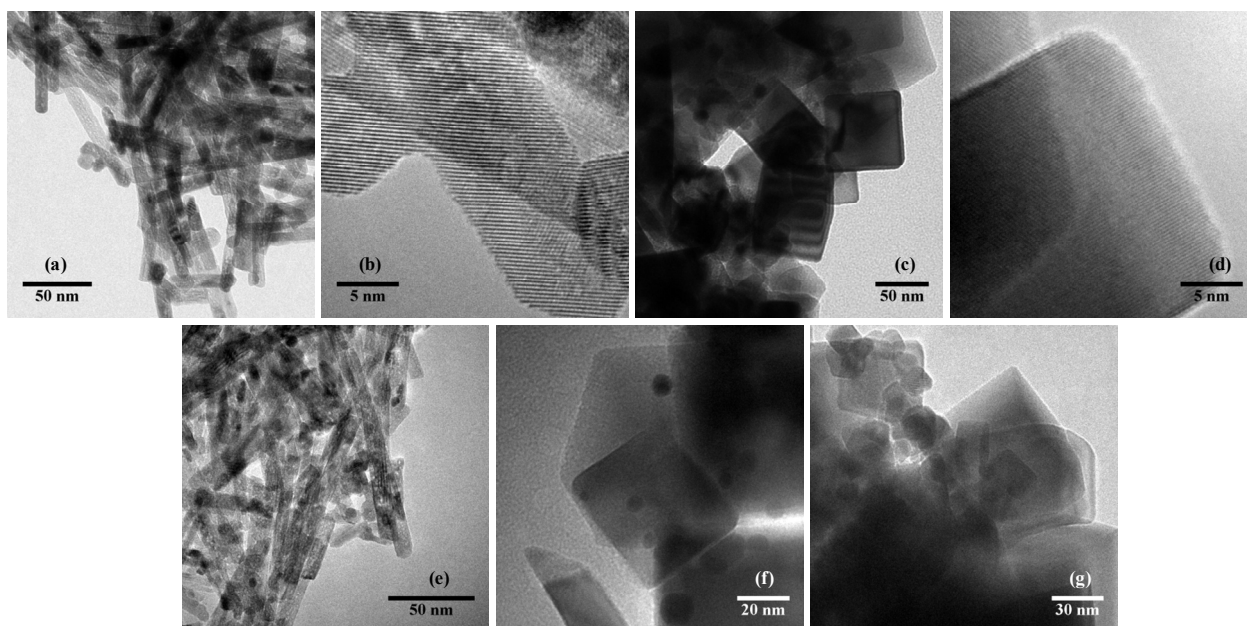
Figure 7.2: TEM images of (a, b) CeO$_2$ rods, (c, d) CeO$_2$ cubes, (e) Au/CeO$_2$(rod), (f) Au/CeO$_2$(cube) and (g) Au/CeO$_2$(cube)-CN.
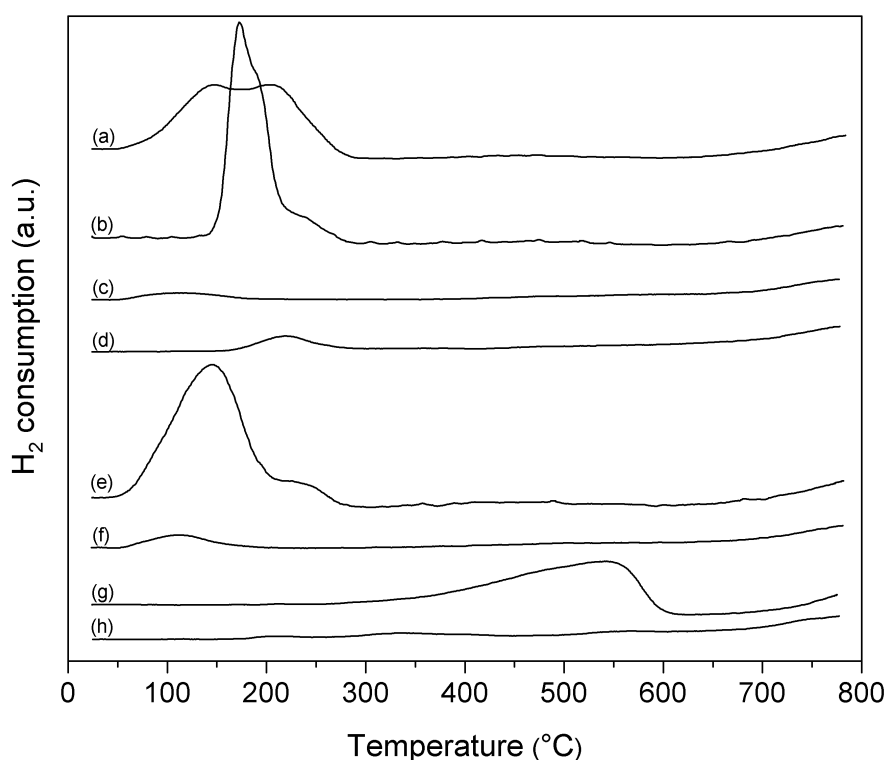
Figure 7.3: TPR profiles of (a) Au/CeO$_2$(rod), (b) Au/CeO$_2$(rod)-CN, (c) Au/CeO$_2$(cube), (d) Au/CeO$_2$(cube)-CN, (e) Pt/CeO$_2$(rod), (f) Pt/CeO$_2$(cube), (g) CeO$_2$(rod) and (h) CeO$_2$(cube).

The reducibility of the various catalysts was evaluated by temperature programmed reduction (TPR). TPR profiles of Au/CeO$_2$, Pt/CeO$_2$ and the bare ceria supports are given in Fig. 7.3 and the amounts of consumed H$_2$ are collected in Table 7.1. In all cases, the H$_2$

consumption was higher for the catalysts based on nanorods than for those based on nanocubes. The difference is due to the lower reducibility of the ceria nanocube surface [30-32]. The TPR profile of the bare CeO_2 nanorod support shows the commonly observed surface reduction feature around 550 °C followed by a H_2 evolution peak and, from 800 °C onwards, a peak due to bulk reduction [41,49-52]. This latter peak is also evident for CeO_2(cube), but its profile does not contain a clear separate peak for the reduction of the ceria surface. The TPR traces of the metal-containing samples look very different. They contain a strong feature at low temperature, which is due to reduction of the metal precursor and surface ceria reduction facilitated by spillover hydrogen from the metal [30,32,42,49]. The latter is evident from the high H_2/metal ratio (Table 7.1). The total amount of H_2 consumed is quite similar for Pt/CeO_2(rod), Au/CeO_2(rod) and Au/CeO_2(rod)-CN in line with the dominant part of H_2 consumption being the result of surface ceria reduction. Qualitatively, these trends are similar for the ceria nanocube catalysts with a lower total H_2 consumption. Note that the low temperature reduction peak for Au/CeO_2(cube)-CN indicates that this sample contains some residual gold which facilitate the reduction of the ceria surface at low temperature.

XP spectra of Au and Pt 4f regions of the fresh and reduced catalysts are shown in Fig. 7.4. The binding energy scales of all XP spectra were calibrated to the Ce 3d peak at 881.8 eV and the areas of all components were normalized against the area of Ce 3d envelope. The Au 4f spectra of Au/CeO_2(rod) and Au/CeO_2(cube) show that gold is predominantly present in the metallic state after calcination (BE = 83.4 eV). In the XP spectrum of Au/CeO_2(rod)-CN, this peak has shifted to higher binding energy (84.0 eV), which evidences that the small amount of Au left on the surface is cationic. After reduction at 400 °C, the binding energy shifts to 83.4 eV, indicating complete reduction of these gold cations. A previous investigation of leached Au/CeO_2 by means of X-ray Absorption Spectroscopy (XAS) [30] showed that fresh Au/CeO_2(rod) contains Au nanoparticles and a small amount of Au cations on the surface, whereas Au/CeO_2(rod)-CN only contains Au cations in close interaction with CeO_2, which are converted to very small Au clusters upon reduction at 250 °C.

Table 7.2: Distribution of Pt oxidation states as determined from XPS measurements.

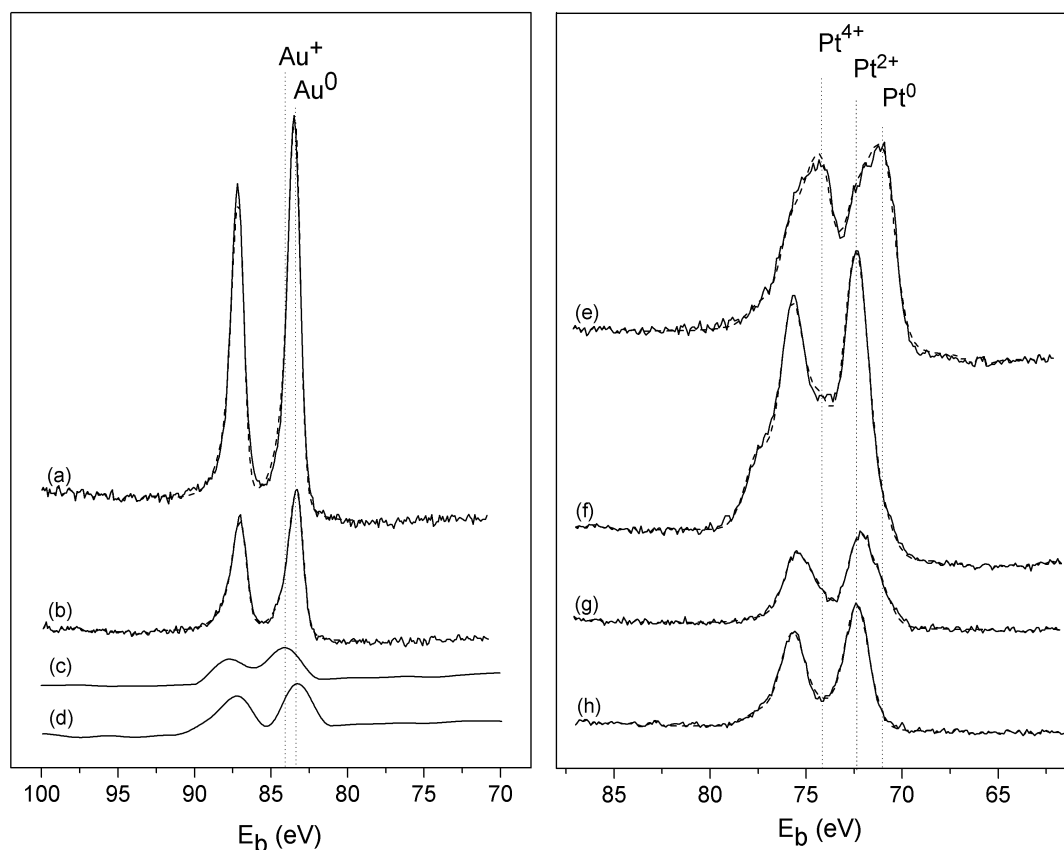| Catalyst	Pretreatment	Pt^0 (71.0 eV)	Pt^{2+} (72.4 eV)	Pt^{4+} (74.2 eV)
Pt/CeO_2(rod)	Fresh	1	87	12
	Reduced 400 °C	56	43	1
Pt/CeO_2(cube)	Fresh	12	66	22
	Reduced 400 °C	77	19	4

Figure 7.4: XP spectra of Au 4f region of (a) calcined Au/CeO$_2$(cube), (b) calcined Au/CeO$_2$(rod) (c) calcined Au/CeO$_2$(rod)-CN (magnified 10 times), (d) calcined Au/CeO$_2$(rod)-CN after reduction at 400°C (magnified 10 times), the positions of Au^0 and Au$^+$ 4f$_{7/2}$ are indicated; Pt 4f region of (e) calcined Pt/CeO$_2$(cube) after reduction at 400 °C (f) calcined Pt/CeO$_2$(cube), (g) calcined Pt/CeO$_2$(rod) after reduction at 400 °C and (h) calcined Pt/CeO$_2$(rod), the positions of Pt^0, Pt^{2+} and Pt^{4+} 4f$_{7/2}$ are indicated. Full line represents the original spectra, dashed line represents the fitting.

A similar set of XP spectra of Pt/CeO$_2$(rod) and Pt/CeO$_2$(cube) and the corresponding fits are shown in Fig. 7.4e-h. The results of fitting these spectra with three different oxidation states for Pt, namely Pt^0, Pt^{2+} and Pt^{4+}, are collected in Table 7.2. The two fresh Pt/CeO$_2$(rod) catalysts mainly contain Pt-oxide. The Pt^0 content for Pt/CeO$_2$(cube) was higher. After reduction at 400 °C, the fraction of metallic Pt is 56 % and 77 %, respectively for Pt/CeO$_2$(rod) and Pt/CeO$_2$(cube). For the Pt/CeO$_2$(rod) sample a considerable amount of Pt with a 4f$_{7/2}$ binding energy of 72.4 eV was observed, which has been assigned to surface Pt associated with Ce^{3+} in a Pt-CeO$_x$ surface complex [53]. This shift to higher binding energies for Pt in Pt/CeO$_2$ catalysts has been reported previously in literature [53,54] and it is mainly attributed to strong Pt-CeO$_2$ interactions [42,44,54-56], as is also evident from the difference in reducibility between Au/CeO$_2$ and Pt/CeO$_2$. These Pt^{2+} species are thought to be responsible for the high Pt dispersion on the ceria support. The Pt particle size in Pt/CeO$_2$(rod) and Pt/CeO$_2$(cube) were found to be 0.8 and 5.5 nm, respectively, by use of H$_2$ chemisorption taking into account the fraction of metallic Pt in these cases. The O 1s region of the metal-loaded CeO$_2$ nanorod and -cube catalysts (not shown here) evidence the presence of two oxidation states: one at 529.2 eV representing the oxygen anions of the ceria

and one at 531.7 eV, appearing in some cases as a broad shoulder, attributed to hydroxyl groups on the surface. It has been reported that the peaks at 529.6, 530.3 and 532.7 eV are due to CeO_2, Ce_2O_3 and $OH(a)$ (or some hydroxyl-containing oxide), respectively [57,58]. For all of the catalysts, reduction led to an increase of the hydroxyl species and a comparison of the spectra of nanorod and nanocube catalysts shows that the latter typically contains more of these hydroxyl groups than the former.

7.3.2 Catalytic activity measurements

7.3.2.1 Reactions of ethanol

With the purpose to obtain insight into the reaction mechanism, ethanol steam reforming was carried out at relatively low temperature (T < 400 °C) as compared to typical temperatures (600-800 °C) required to obtain complete conversion and high H_2 yields [7,8]. The results of ethanol steam reforming for the ceria-supported Pt and Au catalysts are collected in Table 7.3. It can be concluded that (i) the Pt catalysts are more active than the corresponding Au catalysts and (ii) catalysts derived from CeO_2(rod) are more active than those prepared using CeO_2(cube). The conversion of ethanol is almost complete for Pt/CeO_2(rod) at 400 °C. Under these conditions, the conversion is much lower for Pt/CeO_2(cube). At this temperature, the Au catalysts perform better than Pt/CeO_2(cube). The dominant product at 200 °C is acetaldehyde for both Pt and Au catalysts. With increasing temperature, the selectivity to CH_4, CO and CO_2 strongly increases for the Pt catalysts at the expense of the amount of acetaldehyde. At the highest temperature, the formation of acetone is also observed. Unlike these trends for Pt, the Au catalysts do not yield significant amounts of CH_4 or CO and acetaldehyde remains the main product at the highest temperature. Under these conditions, the selectivity to acetone is higher for Au than for Pt. From Table 7.3 it is seen that the CH_4 yield is almost equal to the sum of CO and CO_2 yields for the Pt catalysts, the difference being due to the additional CO_2 formed together with acetone (*vide infra*). The trend of increasing (decreasing) methane (acetaldehyde) selectivity with temperature is consistent with a mechanism involving dehydrogenation of ethanol to acetaldehyde followed by its decomposition to CH_4 and CO through C-C bond cleavage [28,43,44,52,59-62]. Note that at these relatively low temperatures the reforming of CH_4 is very limited. CO_2 is produced from CO by the WGS reaction. Clearly, Au does not catalyze these C-C bond cleavage reactions, which is due to the much lower metal-carbon bond energy as compared to Pt [63]. Consequently, Au metal surfaces are only active in the dehydrogenation of ethanol to acetaldehyde. A major byproduct of the reaction is acetone, whose selectivity strongly increases with the reaction temperature. For the Au/CeO_2 catalysts, we observed that the formation of acetone was accompanied by a decrease in acetaldehyde selectivity and at the same time the evolution of CO_2 and H_2. This is in agreement with the mechanism suggested by Nishiguchi et al. [64], that acetone formation proceeds through the transformation of acetaldehyde via aldol condensation, followed by the reaction of the aldol with lattice oxygen on CeO_2 to form the surface intermediate and its dehydrogenation and decarboxylation (overall reaction: 2 C_2H_5OH + H_2O → CH_3COCH_3 + CO_2 + 4 H_2). The involvement of water

in these reactions towards acetone has also been reported [64]. Our results show that the rate of acetone formation is higher for the CeO_2(rod)-supported catalysts than for the CeO_2(cube)-supported ones (Table 7.3). The bare ceria supports exhibit a very low activity (conversion < 1 %) in ethanol steam reforming at 400 °C. The product mixture in this case consists of acetone, acetaldehyde, carbon dioxide and ethylene. For the CeO_2(rod) support, the major product is acetone, whereas the major product over the CeO_2(cube) is acetaldehyde. The Lewis acid sites formed by oxygen vacancies are likely the active sites for the condensation reactions towards acetone. The very low activities of the bare CeO_2 supports confirm the importance of the metal for the initial dehydrogenation of ethanol to acetaldehyde in the formation of acetone. Gazsi et al. in their work on ethanol decomposition on Au/CeO_2 also reported that lower amount of products were desorbed from pure CeO_2 [45]. They concluded that the Au/CeO_2 interface plays an important role in the high activity of Au/CeO_2.

Table 7.3: Catalytic activity (conversion, selectivities and H_2 yield)[1] for ethanol steam reforming by Pt and Au catalysts supported on CeO_2 nanorods and nanocubes (H_2O:C_2H_5OH=3:1, 50 mg catalyst, GHSV=15000 ml_{EtOH}/g_{cat}.h).

		Pt/CeO_2(rod)	Pt/CeO_2(cube)	Au/CeO_2(rod)	Au/CeO_2(cube)
200 °C	X (ethanol)	4.3	2.0	1.3	0.2
	S (acetaldehyde)	83	80	100	100
	S (methane)	8.7	11	-	-
	S (CO)	5.1	7.0	-	-
	S (CO_2)	3.3	1.7	-	-
	S (H_2)	23	20	-	-
	Y (H_2)	1	0.4	-	-
300 °C	X (ethanol)	30	9.0	4.8	3.3
	S (acetaldehyde)	34	32	97	100
	S (methane)	29	34	-	-
	S (CO)	22	23	-	-
	S (CO_2)	12	10	0.6	-
	S (acetone)	0.8	-	2.6	-
	S (ethyl acetate)	2.0	-	-	-
	S (H_2)	21	23	20	15
	Y (H_2)	6.5	2.0	1.0	0.5
400 °C	X (ethanol)	99	14	31	16
	S (acetaldehyde)	0.6	27	66	93
	S (methane)	43	35	0.1	-
	S (CO)	9.0	25	-	-
	S (CO_2)	42	13	10	1.2
	S (acetone)	3.4	-	24	4.0
	S (ethyl acetate)	-	-	-	2.2
	S (C_xH_y)[2]	1.6	0.2	0.1	-
	S (H_2)	15	22	22	16
	Y (H_2)	15	3.0	6.7	2.7

[1] X: conversion of ethanol (%); S: selectivities in C mol %; S (H_2): selectivity to hydrogen; Y (H_2): yield of hydrogen.
[2] Selectivity to C_2-C_3 alkanes and alkenes.

All of the catalysts showed stable activity at 200 and 300 °C, but tended to deactivate quite strongly at 400 °C. Especially, the activity of Pt/CeO$_2$(rod) decreased strongly from near complete ethanol conversion to a conversion of 15 % after 6 h time on stream (Table 7.4). The deactivation led to a strong decrease of the amounts of CH$_4$ and CO concomitant with an increase of the amount of the acetaldehyde intermediate. Deactivation is most likely due to the rapid buildup of carbonaceous deposits on the Pt metal surface. It is observed that acetone formation is less hindered by deactivation of the Pt catalysts. This is likely because it takes place by reaction of acetaldehyde on the ceria surface. Besides, one should take into account that a smaller number of Pt surface atoms are expected to be involved in the dehydrogenation of ethanol to acetaldehyde than in the decomposition of acetaldehyde (the ensemble effect). It has also been suggested that accumulation of acetate species on the surface causes catalyst deactivation [42,65]. Although smaller, the deactivation of the Au nanoparticles is evident from the decreasing acetaldehyde and increasing acetone selectivity.

Table 7.4: Catalytic activity (conversion, selectivities and H$_2$ yield)[1] for ethanol steam reforming by Pt and Au catalysts supported on CeO$_2$ nanorods as a function of time on stream at 400 °C. (H$_2$O:C$_2$H$_5$OH=3:1, 50 mg catalyst, GHSV=15000 ml$_{EtOH}$/g$_{cat}$.h).

	Pt/CeO$_2$(rod)			Au/CeO$_2$(rod)		
	initial	after 3h	after 6h	initial	after 3h	after 6h
X (ethanol)	99	20	15	31	19	15
S (acetaldehyde)	0.6	29	31	66	37	30
S (methane)	43	3.3	2.5	0.1	0.2	0.3
S (CO)	9.0	4.5	3.5	-	-	-
S (CO$_2$)	42	20	20	9.8	16	17
S (acetone)	3.4	40	39	24	45	50
S (C$_x$H$_y$)[2]	1.6	3.2	3.7	0.1	1.6	2.7
S (H$_2$)	15	29	32	22	27	28
Y (H$_2$)	15	5.9	4.7	6.7	5.1	4.3

[1] X: conversion of ethanol (%), S: selectivities in C mol %, S (H$_2$): selectivity to hydrogen, Y (H$_2$): yield of hydrogen. [2]Selectivity to C$_2$-C$_3$ alkanes and alkenes (mainly ethylene)
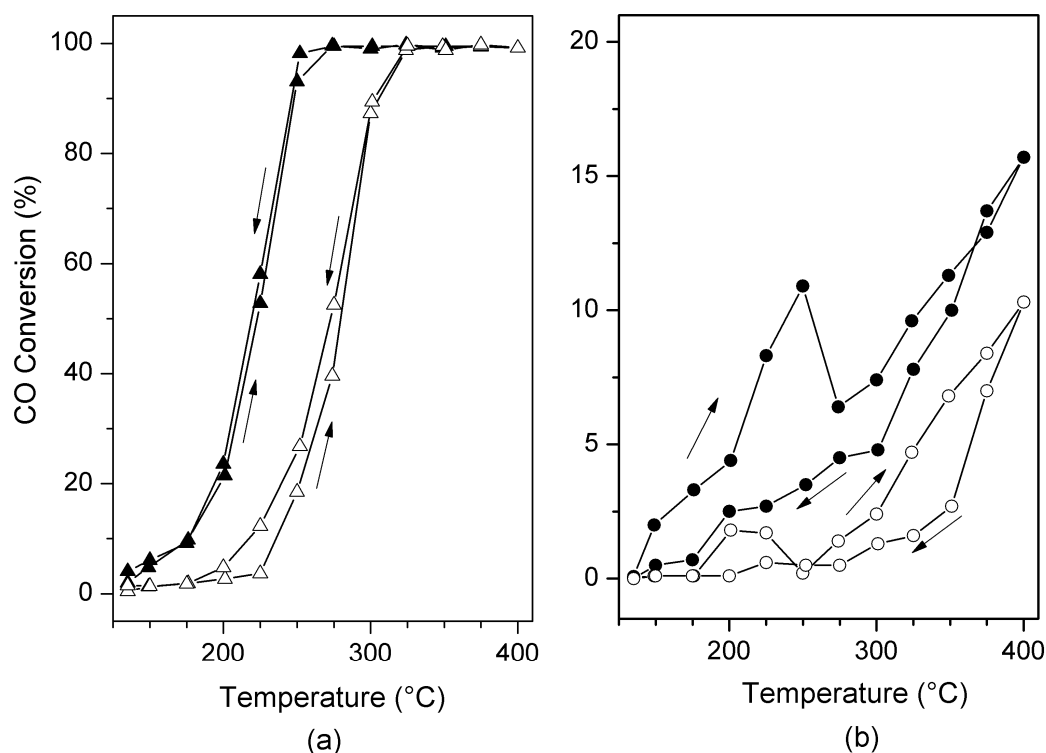
Figure 7.5: WGS conversion for (a) Pt/CeO$_2$(rod) (▲) and Pt/CeO$_2$(cube) (△); and (b) Au/CeO$_2$(rod) (●) and Au/CeO$_2$(rod)-CN (○) catalysts. The arrows indicate the increasing and decreasing temperatures during the experiments performed in a cycle.

The catalytic performance of Pt/CeO$_2$(rod) and Pt/CeO$_2$(cube) in the WGS reaction are compared in Fig. 7.5a. Pt/CeO$_2$(rod) is significantly more active than Pt/CeO$_2$(cube). This result explains the higher CO$_2$ selectivity for Pt/CeO$_2$(rod) during ethanol steam reforming. For completeness, we also show the WGS performance of Au/CeO$_2$(rod) and Au/CeO$_2$(rod)-CN catalysts (Fig. 7.5b). Their performance is very similar to reported data [30]. Au/CeO$_2$(cube) has a very low activity in the WGS reaction. In the present work we establish that Au/CeO$_2$(rod) is already active in the WGS reaction below 200 °C. These Au data stress (i) the role of reduced gold particles, the finer dispersed the better, in the WGS reaction and (ii) the role of the ceria support in the activation of water. Comparison of the results of Au and Pt catalysts demonstrates that Pt/CeO$_2$(rod) is significantly more active than Au/CeO$_2$(rod). Pierre et al. have stressed the role of oxidized Pt species strongly bound to ceria in catalyzing the WGS [56]. The metal-support interface is suggested to provide an increased amount of surface oxygen species for the WGS reaction. On the other hand, one should also acknowledge that CO binds much more strongly to Pt than to Au [66].

The present data show that the CeO$_2$(rod)-supported samples are significantly more active in ethanol steam reforming and the WGS reaction than the CeO$_2$(cube)-supported ones. These differences are related to the better reducibility of the ceria nanorod support. It has been reported that the activation of water to adsorbed O and OH species is thermodynamically unfavorable on Pt surfaces [67]. The minimum bond energy of atomic O on a metal should be larger than 480 kJ/mol for H$_2$O dissociation to occur spontaneously

$(H_2O_{(g)} \rightarrow OH_{ads} + \frac{1}{2} H_2$ and $H_2O_{(g)} \rightarrow O_{ads} + H_2)$. Estimates for the binding energies of atomic O based on DFT calculations on Pt (354 kJ/mol) and Au (270 kJ/mol) are much lower than this minimum energy for spontaneous water dissociation [63]. Accordingly, the reaction rate for Pt surfaces may be limited by the low coverage of OH surface intermediates when oxygen-containing species are formed from steam. The activation of water on the vacancies in the ceria surface can also provide the hydroxyl species. The catalytic reactions may take place at the interface of the metal nanoparticles and the ceria surface or the OH species may migrate to the metal nanoparticles. Note, that the latter is more likely for Pt than for Au because of the higher metal-oxygen bond energy for the former. The TPR results show that Pt and Au facilitate the reduction of the ceria surface at relatively low temperature. This leads to the formation of O vacancies and Ce^{3+} surface sites, which are centers for water adsorption and activation [32,33,68-71]. Therefore, we can relate the higher activity of the CeO_2(rod) derived catalysts to the higher H_2 consumption observed during TPR. This is in line with several reports evidencing the higher concentration of vacancies on CeO_2(rod) compared to CeO_2(cube) [29,32,72].
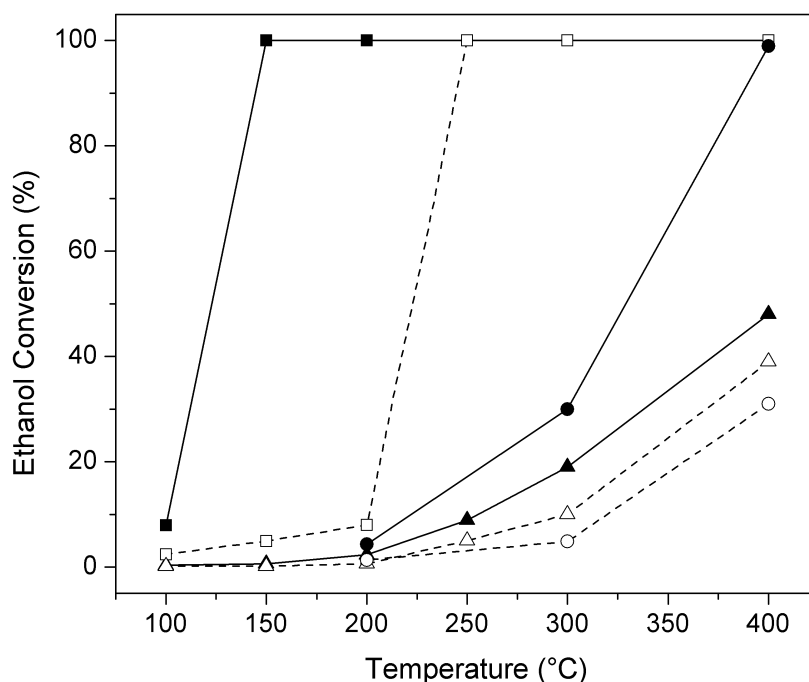
Figure 7.6: Ethanol conversion with respect to temperature over Pt/CeO_2(rod) (—) for a feed of C_2H_5OH:O_2:He=1:3:8(■),C_2H_5OH:H_2O:He=1:3:8 (●) and C_2H_5OH:He=1:11 (▲); and Au/CeO_2(rod) (----) for a feed of C_2H_5OH:O_2:He=1:3:8 (□),C_2H_5OH:H_2O:He=1:3:8 (○) and C_2H_5OH:He=1:11 (△).

As they were the most active catalysts, Pt/CeO_2(rod) and Au/CeO_2(rod) were additionally tested for their activity in the oxidative and non-oxidative conversion of ethanol (Fig. 7.6). In the presence of O_2, Pt/CeO_2(rod) completely oxidizes the ethanol feed starting from temperatures as low as 150 °C. In contrast, ethanol conversion for Au/CeO_2(rod) was complete only above 250 °C. Complete oxidation of ethanol over the Au/CeO_2 catalysts was previously reported by Haruta and co-workers [39]. CeO_2 is a good catalyst in oxidation reactions because of the formation of superoxide species on the defective ceria surface

[39,73]. Petkovic et al. [74] suggested that O_2 is adsorbed at perimeter of the ceria surface and Pt nanoparticles, where ethanol is decomposed to carbon dioxide and water. In this case, it was argued that the support plays a role in the mobility of ethanol and its decomposed fragments on the support. The difference between Pt and Au in this particular case may also be partly due to the higher O surface coverage on Pt. The high activity in complete oxidation of ethanol at relatively low temperatures shows that Pt/CeO_2(rod) and Au/CeO_2(rod) are potent catalysts for the removal of volatile organic compounds (VOC) emitted from ethanol-fueled vehicles or other industries as well as in ethanol fuel cell applications [39,74]. The activity of Pt/CeO_2(rod) increases in the order non-oxidative dehydrogenation < steam reforming < oxidative conversion. The main product of ethanol decomposition (in the absence of an oxygen source) is acetaldehyde (Tables 7.5 and 7.6). The activity in the presence is significantly higher, mainly because acetaldehyde is decomposed to CH_4 and CO. This points to a significant role of OH species generated on ceria in the decomposition of the acetaldehyde intermediate. The highest activity is obtained in the presence of O_2. Ethanol is totally combusted because of the high activity of O_2 on the ceria surface. Note, that the amount of acetone was also significantly lower during ethanol decomposition than during ethanol steam reforming. These results confirm the proposed role of water in the formation of acetone. For Au/CeO_2(rod) the activities in ethanol steam reforming and its non-oxidative dehydrogenation were similar. In both cases, the dominant product is acetaldehyde. These results are in keeping with results for reactions of ethanol on Au/CeO_2 reported by Gazsi et al. [45]. In that study it was also reported that the main process for the decomposition of ethanol was the dehydrogenation of ethanol and the addition of water did not improve the activity. This shows that, at least for Au, the dehydrogenation of ethanol is not catalyzed by OH groups on the ceria support. The much higher activity in the presence of O_2 is due to the activation of molecular oxygen on the ceria surface. Scheme 7.1 illustrates the mechanism of ethanol conversion over Pt and Au based CeO_2 catalysts.

Table 7.5: Comparison of product selectivities[1] and H_2 yield[2] for ethanol oxidation, ethanol steam reforming and ethanol decomposition experiments over Pt and Au catalysts supported on CeO_2 nanorods. (50 mg catalyst, GHSV=15000 $ml_{EtOH}/g_{cat}.h$).

		Pt/CeO$_2$(rod)			Au/CeO$_2$(rod)		
		$C_2H_5OH{:}H_2O$	$C_2H_5OH{:}O_2$	C_2H_5OH	$C_2H_5OH{:}H_2O$	$C_2H_5OH{:}O_2$	C_2H_5OH
300 °C	S (acetaldehyde)	34	-	60	97	-	90
	S (methane)	29	0.9	17	-	0.5	0.3
	S (CO)	22	-	17	-	-	0.3
	S (CO$_2$)	12	99	-	0.6	99	-
	S (acetone)	0.8	-	0.7	2.6	-	-
	S (ethyl acetate)	2.0	-	3.8	-	-	7.4
	S(C$_x$H$_y$)[3]	-	-	1.5	-	0.8	1.9
	S (H$_2$)	21	-	15	20	-	15
	Y (H$_2$)	6.5	-	2.9	1.0	-	1.6
400 °C	S (acetaldehyde)	0.6	-	75	66	-	72
	S (methane)	43	0.2	0.9	0.1	1.0	0.6
	S (CO)	9.0	-	1.5	-	-	1.0
	S (CO$_2$)	42	99.8	1.7	10	98	2.7
	S (acetone)	3.4	-	2.2	24	-	3.6
	S (ethyl acetate)	-	-	2.1	-	-	3.1
	S(acetic acid)	-	-	3.2	-	-	4.4
	S(C$_x$H$_y$)[3]	1.6	-	9.0	0.1	0.5	12.4
	S(others)[4]	-	-	4.4	-	-	0.5
	S (H$_2$)	15	-	15	22	-	16
	Y (H$_2$)	15	-	7.1	6.7	-	6.0

[1] S: selectivities in C mol%; S (H$_2$): selectivity to hydrogen,

[2] Y (H$_2$): yield of hydrogen,

[3] Selectivity to C$_2$-C$_3$ alkanes and alkenes,

[4] Selectivity to other products, mainly to diethyl ether.

Table 7.6: Comparison of product selectivities[1] and H_2 yield[2] for ethanol oxidation, ethanol steam reforming and ethanol decomposition experiments over Pt and Au catalysts supported on CeO_2 nanorods at 200 ºC. (50 mg catalyst, GHSV=15000 ml_{EtOH}/g_{cat}.h).

		Pt/CeO$_2$(rod)			Au/CeO$_2$(rod)		
		$C_2H_5OH:H_2O$	$C_2H_5OH:O_2$	C_2H_5OH	$C_2H_5OH:H_2O$	$C_2H_5OH:O_2$	C_2H_5OH
	S (acetaldehyde)	83	-	92	100	88	100
	S (methane)	8.7	0.7	4.5	-	-	-
	S (CO)	5.1	-	3.9	-	-	-
	S (CO$_2$)	3.3	99.3	-	-	4.7	-
200 °C	S (acetone)	-	-	-	-	1.3	-
	S (acetic acid)	-	-	-	-	1.8	-
	S (ethyl acetate)	-	-	-	-	3.9	-
	S (H$_2$)	23	-	15	-	-	-
	Y (H$_2$)	1.0	-	0.3	-	-	-

[1] S: selectivities in C mol%; S (H$_2$): selectivity to hydrogen.
[2] Y (H$_2$): yield of hydrogen.
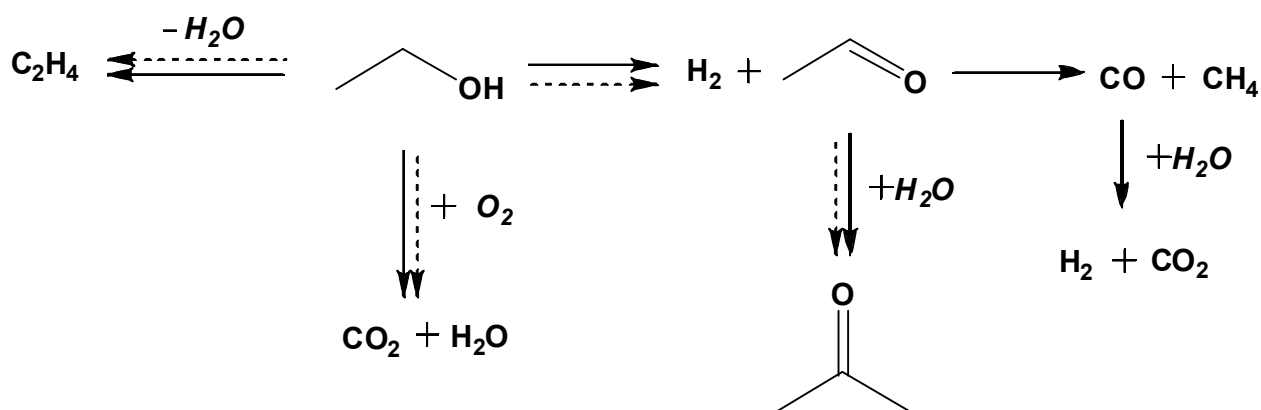
Scheme 7.1: The main reaction routes for ethanol conversion over the CeO_2 supported Pt ($\rightarrow$) and Au ($\dashrightarrow$) catalysts.

7.3.2.2 Reactions of formic acid

The Pt and Au catalysts were also tested for their activity in the decomposition of formic acid in the temperature range 50-200 °C. Fig. 7.7a compares the conversion of the various catalysts as a function of the temperature., Au/CeO_2(rod) is the most active one in the temperature range 50-150 °C. The Au catalysts performed better than Pt catalysts in accordance with the results of Iglesia and Ojeda [23], who compared the activities of Au and Pt supported on Al_2O_3. At a temperature of 200 °C formic acid was completely converted by all of the catalysts. The selectivities in the decomposition of formic acid as a function of temperature are given in Fig. 7.7b. For Pt and Au catalysts the selectivity to CO_2 (H_2) is very high at temperatures below 75 °C. Below 75 ^{0}C, formic acid conversion is below 1% with a CO_2 (H_2) selectivity of 100%. However, above this temperature also CO was observed and in much greater amounts for Pt than Au. Solymosi et al. also reported in their study of formic acid decomposition on Pt group metals supported on carbon that CO-free H_2 generation could not be achieved. However, carbon (Norit)-supported Pt in that work (98 % at 150°C and 99.1 % at 200 °C) gave a higher H_2 selectivity than our Pt/CeO_2 catalysts [22]. In the present study, the selectivity to CO was very low for Au. At 150 $^\circ$C, CO_2 selectivities of Au/CeO_2(rod) and Au/CeO_2(cube) were 99.4 % and 99.7 %, respectively. The CO_2 selectivities of the Au/CeO_2 catalysts are higher than the equilibrium CO_2 selectivities in the WGS reaction. These results show that the predominant pathway for formic acid decomposition over the Au/CeO_2 catalysts is decarboxylation and the WGS reaction is not involved in the reaction mechanism. As Au/CeO_2(rod) is already active in the WGS reaction below 200 °C (vide supra), one expects CO formation during formic acid decomposition. In contrast, at temperatures above 75 °C the CO_2 selectivities for the Pt/CeO_2 catalysts are below the equilibrium values for the WGS reaction, which evidences that the low CO_2 selectivity is not (only) due to the WGS reaction of CO_2 and H_2 but also due to decarbonylation of formic acid. In line with its higher WGS activity, Pt/CeO_2(rod) shows a lower selectivity to CO_2 than the Pt/CeO_2(cube) catalyst. The finding that decarbonylation

occurs for Pt and not for Au relates to the stronger metal-oxygen bond energies for Pt, resulting in a higher activity in elementary reaction steps leading to an adsorbed OH surface intermediate (e.g. $HCOOH_{ads} \rightarrow HCO_{ads} + OH_{ads}$). The work of Solymosi et al. suggested that the support choice may also influence the selectivity of Pt nanoparticles [22]. In-situ infrared spectroscopy studies of Beden et al. [75] showed that a substantial part of the Pt surface is covered by CO due to dissociative chemisorption of formic acid. Electrochemical studies show that Pt catalyzes formic acid oxidation by two pathways, namely via dehydrogenation and via dehydration. CO, the product of the dehydration pathway, will decrease the catalytic activity [76,77]. In contrast, Beltramo et al. [78] did not find any evidence for CO formation during the oxidation of formic acid on gold. The importance of surface formate as an intermediate ($HCOO_{ads}$) has been suggested in many previous studies. Typically, the stability of formate species is higher on Au than on Rh and Pt [21,22,25]. The catalytic activity of formic acid decomposition has also been related to the adsorption energy of CO. The adsorption energy of CO on Au particles is much weaker than on other transition metals. For instance, it has been argued that product CO strongly binds to Rh reducing the number of free Rh sites available for the dissociative adsorption of formic acid [25]. Accordingly, the higher activity of Au than Pt may be argued to be the result of the stronger adsorption of product CO to the Pt surface.
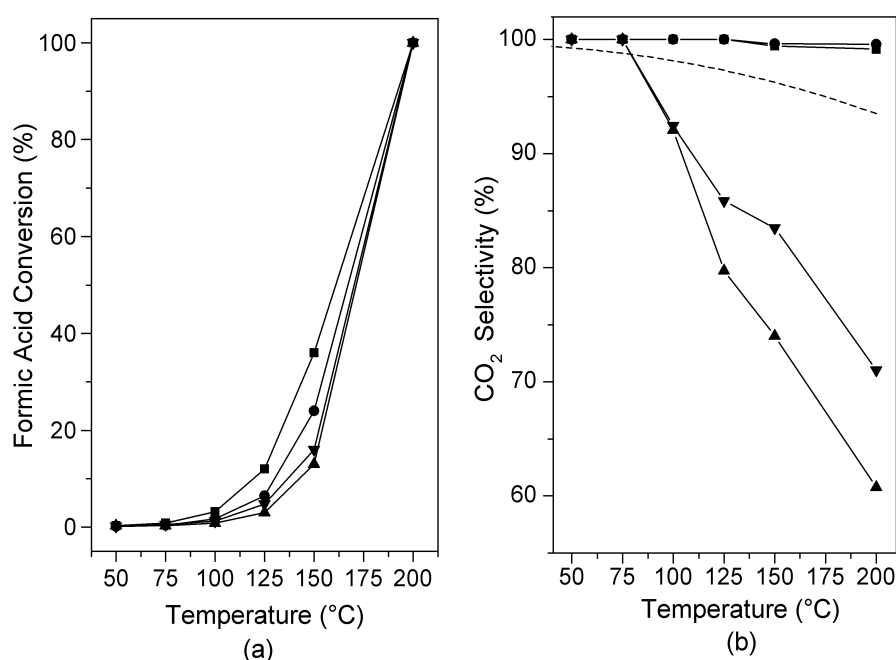
Figure 7.7: Formic acid conversion (a) and CO_2 selectivity (b) obtained over Au/CeO_2(rod) (■), Au/CeO_2(cube) (●), Pt/CeO_2(rod) (▲) and Pt/CeO_2(cube) (▼) at a GHSV of 3000 $ml_{formic\ acid}/g_{cat}$·h. All catalysts reduced in H_2 at 250 °C. Dotted line represents the CO_2 selectivity values at the WGS equilibrium.
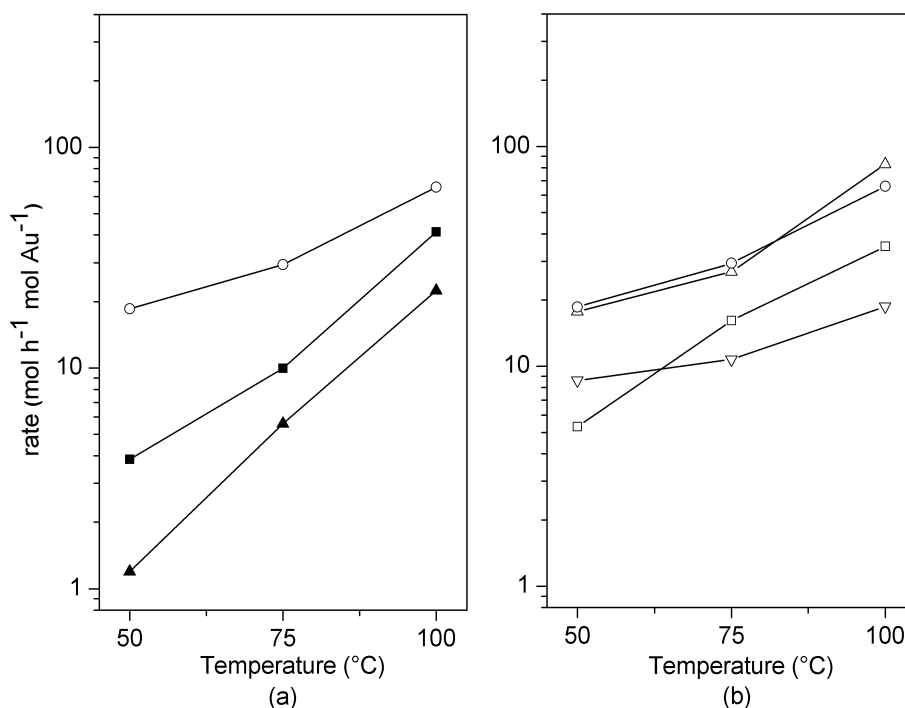
Figure 7.8: Rates of formic acid decomposition over (a) Au/CeO$_2$(rod)-CN (○), Au/CeO$_2$(rod) (■) and Au/CeO$_2$(cube) (▲) after reduction in H$_2$ at 250 °C; (b) Au/CeO$_2$(rod)-CN dried at 120 °C (□), reduced at 150 °C (△), reduced at 250 °C (○) and reduced at 500 °C (▽).

Fig. 7.8a compares the rates of formic acid decomposition over Au/CeO$_2$(rod), Au/CeO$_2$(rod)-CN and Au/CeO$_2$(cube). The rate of formic acid dehydrogenation per mol of gold was the highest for the CN-leached catalyst, which contains sub-nanometer Au clusters. A similar observation was made for Au/Al$_2$O$_3$ by Iglesia and Ojeda [23]. These authors proposed that very small (TEM–invisible) Au clusters are the active sites in formic acid dehydrogenation at near-ambient temperatures. The gold phase in Au/CeO$_2$(cube) mainly consists of reduced Au nanoparticles as evidenced by their complete removal upon cyanide treatment. By a similar argument as used by Iglesia and Ojeda, we suspect that the highly dispersed Au clusters in Au/CeO$_2$(rod), which are present next to the Au nanoparticles, dominate the catalytic activity in formic acid decomposition. Accordingly, the activity of this catalyst is higher than that of Au/CeO$_2$(cube). As a consequence of the removal of the low-activity gold nanoparticles, the intrinsic activity of the final Au/CeO$_2$(rod)-CN catalyst is much higher. Fig. 7.8b shows the influence of the pretreatment procedure of Au/CeO$_2$(rod)-CN on the rate of formic acid decomposition. After reduction in H$_2$ at 150 °C and 250 °C the activity of Au/CeO$_2$(rod)-CN is higher than the same catalyst dried in He at 120 °C. Clearly, reduced gold is required for formic acid decomposition. The activity of the catalyst reduced at 500 °C is much lower. These trends in activities are completely consistent with those reported for butadiene hydrogenation using a similar catalyst [30] and reinforce our conclusion that highly dispersed and metallic Au clusters are the active sites in formic acid decomposition. Au/CeO$_2$(rod)-CN reduced at 150°C and 250°C contains reduced subnanometer-sized Au clusters, whereas the sample dried in He at 120°C mostly contains

167

cationic Au species. The sample reduced at 500 °C contains somewhat larger Au nanoparticles as evidenced by EXAFS spectroscopy [30].

7.4 Conclusions

A set of Au and Pt supported CeO_2 nanorod and nanocube shaped catalysts were tested for their activity in the decomposition of ethanol and formic acid. Pt showed higher activity than Au in steam reforming of ethanol as well as its decomposition and oxidation. Besides, Pt was also found to be more active in the WGS reaction. In general, the nanorod-shaped CeO_2-supported catalysts are more active than nanocube-shaped ones. This difference relates to the higher activity of the former in the activation of water on oxygen vacancies in the $CeO_2(110)$ surface, forming OH intermediates. For Pt and Au, the first step in ethanol conversion is its dehydrogenation to acetaldehyde. The higher ethanol steam reforming reaction rates on Pt are due to its ability to decompose acetaldehyde into CH_4 and CO. The higher C-C bond breaking activity of Pt stems from the higher Pt-C than Au-C bond strength. Accordingly, the main product on Au is acetaldehyde. Comparison to activity measurements without H_2O (ethanol decomposition) shows that water mainly facilitates the decomposition of acetaldehyde and not so much ethanol dehydrogenation. These catalysts are also very active for ethanol oxidation with Pt being preferred over Au. In formic acid decomposition Au is more active and selective towards H_2 than Pt catalysts. The selectivity of the Pt catalysts is lower because of their higher WGS activity compared to gold and decarbonylation as a primary reaction pathway. The latter is likely due to the higher Pt-O bond strength leading to an increased rate of dissociation of surface formate to CO. The results show that the high activity in the Au catalysts stems from highly dispersed sub-nanometer Au clusters.

References

[1]   G.Centi, R.A. van Santen, Catalysis for Renewables: From Feedstock to Energy Production, Wiley-VCH, Weinheim, 2007.
[2]   G.W. Huber, S. Iborra, A. Corma, Chem. Rev. 106 (2006) 4044–4098.
[3]   A. Corma, S. Iborra, A. Velty, Chem. Rev. 107 (2007) 2411–2502.
[4]   T. Takei, N. Iguchi, M. Haruta, Catal. Surv. Asia 15 (2011) 80–88.
[5]   R. Barthos, A. Szechenyi, and F. Solymosi, J. Phys. Chem. B 110 (2006) 21816-21825.
[6]   N. Bion, F. Epron, D. Duprez, Catalysis 22 (2010) 1–55.
[7]   A. Haryanto, S. Fernando, N. Murali, S. Adhikari, Energ. Fuel 19 (2005) 2098–2106.
[8]   M. Ni, D.Y.C. Leung, M.K.H. Leung, Int. J. Hydrogen Energ. 32 (2007) 3238–3247.
[9]   J.D. Holladay, J. Hu, D.L. King, Y. Wang, Catal. Today 139 (2009) 244–260.
[10] C. Song, Catal. Today 77 (2002) 17–49.
[11] W. Zhou, Z. Zhou, S. Song, W. Li, G. Sun, P. Tsiakaras, Q. Xin, Appl. Catal. B 46 (2003) 273–285.
[12] E. Antolini, J. Power Sources 170 (2007) 1–12.
[13] B. Loges, A. Boddien, F. Gartner, H. Junge, M. Beller, Top Catal. 53 (2010) 902–914.
[14] D.J. Hayes, S. Fitzpatrick, M.H.B. Hayes, J.R.H. Ross, in: B. Kamm, P.R. Gruber, M. Kamm (Eds.), Biorefineries-Industrial Processes and Products, vol. 1, Wiley-VCH, Weinheim, 2006, p. 139.
[15] A. Boddien, B. Loges, H. Junge, M. Beller, ChemSusChem 1 (2008) 751–758.
[16] B. Loges, A. Boddien, H. Junge, M. Beller, Angew. Chem. Int. Ed. 47 (2008) 3962–3965.
[17] F. Joo, ChemSusChem 1 (2008)805–808.
[18] R.A.W. Johnstone, A.H. Wilby, Chem. Rev. 85 (1985) 129–170.
[19] D.A. Bulushev, J.R.H. Ross, Catal. Today 163 (2011) 42–46.
[20] C. Fellay, N. Yan, P.J. Dyson, G. Laurenczy, Chem. Eur. J. 15 (2009)3752–3760.

[21] F. Solymosi, A. Erdohelyi, J. Catal. 91 (1985) 327–337.
[22] F. Solymosi, A. Koos, N. Liliom, I. Ugrai, J. Catal. 279 (2011) 213–219.
[23] M. Ojeda, E. Iglesia, Angew. Chem. Int. Ed. 48 (2009) 4800–4803.
[24] D.A. Bulushev, S. Beloshapkin, J.R.H. Ross, Catal. Today 154 (2010) 7–12.
[25] A. Gazsi, T. Bansagi, F. Solymosi, J. Phys. Chem. C 115 (2011) 15459–15466.
[26] A. Koos, F. Solymosi, Catal. Lett. 138 (2010) 23–27.
[27] Y. Li, X. Wang, C. Xie, C. Song, Appl. Catal. A 357 (2009) 213–222.
[28] L.V. Mattos, G. Jacobs, B.H. Davis, F.B. Noronha, Chem. Rev. 112 (2012) 4094–4123.
[29] N. Yi, R. Si, H. Saltsburg, M. Flytzani-Stephanopoulos, Appl. Catal. B 95 (2010) 87–92.
[30] Y. Guan, D.A.J.M. Ligthart, O. Pirgon-Galin, J.A.Z. Pieterse, R.A. van Santen, E.J.M. Hensen, Top Catal. 54 (2011) 424–438.
[31] J. Han, H.J. Kim, S. Yoon, H. Lee, J. Mol. Catal. A 335 (2011) 82–88.
[32] R. Si, M. Flytzani-Stephanopoulos, Angew. Chem. Int. Ed. 47 (2008) 2884–2887.
[33] Q. Fu, H. Saltsburg, M. Flytzani-Stephanopoulos, Science 301 (2003) 5635, 935–938.
[34] R. Burch, Phys. Chem. Chem. Phys. 8 (2006) 5483–5500.
[35] D.C. Grenoble, M. Estat, D.F. Ollis, J. Catal. 67 (1981) 90–102.
[36] R. Radhakrishnan, R.R.Willigan, Z. Dardas, T.H. Vanderspurt, AIChE J. 52 (2006) 1888– 1894.
[37] P. Panagiotopoulou, D.I. Kondarides, Catal. Today 112 (2006) 49–52.
[38] A.V. Zeigarnik, R.E. Valdes-Perez, O.N. Myatkovskaya, J. Phys. Chem. B 104 (2000) 10578-10587.
[39] T. Takei, N. Iguchi, M. Haruta, New J. Chem. 35 (2011) 2227–2233.
[40] Y. Guan, E.J.M. Hensen, Appl. Catal. A 361 (2009) 49–56.
[41] G. Jacobs, R.A. Keogh, B.H. Davis, J. Catal. 245 (2007) 326–337.
[42] P. Ciambelli, V. Palma, A. Ruggiero, Appl. Catal. B 96 (2010) 18–27.
[43] P. Ciambelli, V. Palma, A. Ruggiero, Appl. Catal. B 96 (2010) 190–197.
[44] R.M. Navarro, M.C. Alvarez-Galvan, M. Cruz Sanchez-Sanchez, F. Rosa, J.L.G. Fierro, Appl. Catal. B 55 (2005) 229–241.
[45] A. Gazsi, A. Koos, T. Bansagi, F. Solymosi, Catal. Today 160 (2011) 70–78.
[46] H.X. Mai, L.D. Sun, Y.W. Zhang, R. Si, H.P. Zhang, H.C. Liu, C.H. Yan, J. Phys. Chem. B 109 (2005) 24380–24385.
[47] D.A.J.M. Ligthart, R.A. van Santen, E.J.M. Hensen, J. Catal. 280 (2011) 206–220.
[48] D.A.J.M. Ligthart, R.A. van Santen, E.J.M. Hensen, Angew. Chem. Int. Ed. 50 (2011) 5306–5310.
[49] H.C. Yao, Y.F.Y. Yao, J. Catal. 86 (1984) 254–265.
[50] B.B. Harrison, A.F. Diwell, C. Hallett, Platinum Metals Rev. 32 (1988) 73–83.
[51] L.A. Bruce, M. Hoang, A.E. Hughes, T.W. Turney, Appl. Catal. A 134 (1996) 351–362.
[52] J.Y. Siang, C.C. Lee, C.H. Wang, W.T. Wang, C.Y. Deng, C.T. Yeh, C.B. Wang, Int. J. Hydrogen Energ. 35 (2010) 3456–3462.
[53] J.Z. Shyu, K. Otto, J. Catal. 115 (1989) 16–23.
[54] A. Yee, S.J. Morrison, H. Idriss, J. Catal. 191 (2000) 30–45.
[55] W. Lin, A.A. Herzing, C.J. Kiely, I.E. Wachs, J. Phys. Chem. C 112 (2008) 5942–5951.
[56] D. Pierre, W. Deng, M. Flytzani-Stephanopoulos, Top Catal. 46 (2007) 363–373.
[57] E. Abi-aad, R. Bechara, J. Grimblot, A. Aboukais, Chem. Mater. 5 (1993) 793–797.
[58] G. Praline, B.E. Koel, R.L. Hance, H.I. Lee, J.M. White, J. Electron Spectrosc. 21 (1980) 17–30.
[59] H. Idriss, Platinum Metal Rev. 48 (2004) 105–115.
[60] D.A. Morgenstern, J.P. Fornango, Energ. Fuel 19 (2005) 1708–1716.
[61] B. Zhang, W. Cai, Y. Li, Y. Xu, W. Shen, Int. J. Hydrogen Energ. 33 (2008) 4377–4386.
[62] S. Ito, K. Tomishige, Catal. Commun. 12 (2010) 157–160.
[63] R.A. van Santen, M. Neurock, Molecular Heterogeneous Catalysis: A Conceptual and Computational Approach, Wiley-VCH, Weinheim, 2007.
[64] T. Nishiguchi, T. Matsumoto, H. Kanai, K. Utani, Y. Matsumura, W.J. Shen, S. Imamura, Appl. Catal. A 279 (2005) 273–277.
[65] A. Erdohelyi, J. Rasko, T. Kecskes, M. Toth, M. Domok, K. Baan, Catal. Today 116 (2006) 367–376.
[66] C.D. Zeinalipour-Yazdi, A.L. Cooksy, A.M. Efstathiou, Surf. Sci. 602 (2008) 1858–1862.
[67] M.A. Henderson, Surf. Sci. Rep. 46 (2002) 1–8.
[68] G. Jacobs, U.M. Graham, E. Chenu, P.M. Patterson, A. Dozier, B.H. Davis, J. Catal. 229 (2005) 499–512.
[69] Q. Fu, S. Kudriavtseva, H. Saltsburg, M. Flytzani-Stephanopoulos, Chem. Eng. J. 93 (2003) 41–53.
[70] R.J. Gorte, S. Zhao, Catal. Today 104 (2005) 18–24.
[71] G. Jacobs, B. H. Davis, Catalysis, 20 (2007)122–285.
[72] M. Nolan, S.C. Parker, G.W. Watson, Phys. Chem. Chem. Phys. 8 (2006) 216–218.
[73] T.X.T. Sayle, S.C. Parker, D.C. Sayle, Phys . Chem. Chem. Phys., 7 (2005) 2936–2941.
[74] L.M. Petkovic, S.N. Rashkeev, D.M. Ginosar, Catal. Today 147 (2009) 107–114.

[75] B. Beden, A. Bewick, C. Lamy, J. Electroanal. Chem. 148 (1983) 147–160.

[76] J.D. Lovic, A.V. Tripkovic, S.L.J. Gojkovic, K.D. Popovic, D.V. Tripkovic, P. Olszewski, A. Kowal, J. Electroanal. Chem. 581 (2005) 294–302.

[77] N. Kristian, Y. Yan, X. Wang, Chem. Commun. 3 (2008) 353–355.

[78] G.L. Beltramo,T.E. Shubina, M.T.M. Koper, ChemPhysChem 6 (2005) 2597–2606.

Summary

Reactivity of (bi)metallic catalysts for reforming of biomass derived alcohols

To meet the rapidly growing demand of energy in a sustainable manner, we need to explore the use of alternative resources. Depletion of finite resources such as coal, oil and natural gas as well as environmental impact of their excessive use are main drivers for research into novel technologies for production of energy, fuels and chemicals based on renewable feedstock. Energy needs such as heat and electricity can be met by using sustainable energy technologies such as wind, solar and hydroelectric power. For replacing petroleum derived transportation fuels and commodity chemicals, lignocellulosic biomass is a viable feedstock with no net CO_2 emissions to the atmosphere. Carbohydrate constituents of lignocellulosic biomass can be transformed into platform chemicals and hydrogen. In addition to its potential as an energy carrier, for instance, in fuel cell application, hydrogen is considered as an important reactant in future biorefineries essential for saturating the deoxygenated hydrocarbon molecules. Heterogeneous catalysis is the complex toolbox which enables the transition from a petroleum into a biomass based chemical industry. Metal nanoparticles dispersed on high surface area support materials provide the active surfaces for catalytic conversion of sugar molecules derived from lignocellulosic biomass.

Polyols obtained from bio-based sugars can be converted to alkanes, alcohols and hydrogen via aqueous phase reforming (APR). In this work we investigated the effect of the support material, structure of the Pt- and Rh-based metal catalysts and most importantly, the synergetic effect of Re as a promoter to conventional aqueous phase reforming catalysts. Chapter 2 deals with the influence of the support on the APR activity of Pt catalysts. As supports, alumina, silica and amorphous silica alumina supports with varying Al contents were compared. The influence of the Pt-Re synergy was investigated in Chapters 3, 4 and 5. Carbon was used as the support material because of its better hydrothermal stability and inert nature compared to oxide supports. In Chapter 3 we focused on the effect of varying Re content on Pt/C catalysts prepared by sequential impregnation. The use of different reducible oxide supports (ceria, ceria-zirconia, zirconia and titania) for dispersing PtRe alloys with an optimized Re to Pt ratio of 2 was studied in Chapter 4. In Chapter 5, we discussed the influence of Pt particle size on carbon-supported catalysts and their Re promoted counterparts prepared by the catalytic reduction method. The reaction mechanism of APR includes key steps such as decarbonylation, dehydration and water-gas shift (WGS). Gas-phase WGS and acetaldehyde decomposition experiments were employed for investigating the activities of the catalysts in CO removal and C-C bond cleavage reactions. In Chapter 6, the promotional

effect of Re on carbon-supported Pt and Rh catalysts was studied by using a Re to Pt(Rh) ratio of 0.5. Chapter 7 explores the reactivity of ethanol, a likely future key intermediate in the biobased industry, and of formic acid, a possible liquid platform for hydrogen storage. Pt and Au supported on ceria nanocrystals with different geometries were employed as catalysts for this purpose. Catalysts employed in the current work were extensively characterized in order to determine their chemical composition, reducibility, particle size, acidity and oxidation state using temperature programmed techniques, X-ray diffraction, nuclear magnetic resonance, electron microscopy, in situ X-ray absorption spectroscopy and infrared spectroscopy.

Chapter 2 examines the effect of the support in aqueous phase reforming of glycerol for a series of γ-Al_2O_3, SiO_2 and amorphous silica-alumina (ASA) supported Pt catalysts. The main products in the gas phase were H_2, CO_2 and C_1-C_3 alkanes and 1,2-propanediol, hydroxyacetone, ethylene glycol and C_1-C_3 monoalcohols were the products in the liquid phase. Significant changes in conversion and selectivity trends were observed with time on stream. These changes were found to be related to changes in the catalyst under the hydrothermal reaction conditions. For γ-Al_2O_3 and ASA supported catalysts formation of boehmite was observed. Characterization of fresh and spent catalysts by XRD and ^{27}Al NMR showed that for ASA catalysts with higher Al content, formation of boehmite was more pronounced. For ASA supports with low Al content (below monolayer coverage of parent silica), boehmite formation was limited and, instead, leaching of silica from the support was observed. The reaction data indicate that Pt in interaction with boehmite is more active in hydroxyacetone hydrogenation and glycerol dehydrogenation reactions than Pt in interaction with γ-Al_2O_3 and silica. Boehmite formation was observed to be beneficial for obtaining high yields in hydrodeoxygenation and reforming reactions when compared to Pt supported on γ-Al_2O_3 and SiO_2.

In Chapter 3 focus was on the synergy in Pt-Re catalyst systems for APR of glycerol. Activated carbon was used as the support because its inertness allows the investigation of the intrinsic properties of the Pt-Re synergy and also because the support is inherently stable under the hydrothermal APR conditions. Pt and PtRe catalysts were found to be reduced in hydrogen at 300 °C, whereas Re by itself needed reduction at 500 °C. The presence of isolated Re species in a slightly oxidized state was observed for catalysts with higher Re content. Increasing Re/Pt ratio led to increased glycerol conversion rates in the bimetallic catalysts. The higher C-O bond cleavage rates were correlated to the formation of Brønsted acid sites. This was evident from pyridine IR measuremens on a set of silica-supported Pt(Re) catalysts. Model experiments in gas phase acetaldehyde decomposition showed that the bimetallic catalysts were more active than Pt/C in C-C bond cleavage. These decarbonylation activities do not depend strongly on the Re content of the bimetallic PtRe catalysts. Enhanced APR activity of PtRe catalysts appears to correlate strongly with the water-gas shift (WGS) activities. The strong Pt-Re synergy for CO removal by the WGS reaction was also evident from liquid phase CO stripping voltammetry studies, evidencing lower onset for CO oxidation for PtRe/C compared to Pt/C. More facile CO removal from the catalyst surface

effectively increases the APR activity of PtRe/C, with a Re/Pt molar ratio of 2 identified as the optimum for the WGS reaction.

Chapter 4 deals with the effect of using reducible oxide supports for Pt and PtRe catalysts in APR of glycerol. Among a set of Pt loaded ceria, ceria-zirconia, zirconia and titania supported catalysts, ceria supported Pt was found to give the lowest activity. Pt/TiO_2 was the most active among the monometallic catalysts. The poor reducibility of Pt in Pt/CeO_2 catalyst due to strong metal-support interactions was the reason for its lowest activity. Upon addition of Re, glycerol conversion of all of the catalysts increased. The promotional effect of Re on Pt/CeO_2 was the most pronounced due to better reduction of the metal phase as a result of strong Pt-Re interactions. A comparison to data from carbon supported catalysts (Chapter 3) showed that the influence of the OH groups on the titania support resulted in higher C-O bond cleavage rates on Pt/TiO_2 when compared to Pt/C. WGS activities of the reducible oxide supported catalysts were much higher than those of the carbon-supported ones. The influence of Re addition on their WGS activity was much less pronounced when compared to the carbon-supported catalysts. Acetaldehyde decomposition on Re-promoted Pt/TiO_2 showed enhanced C-C cleavage rates in line with our observations for the carbon-supported catalysts. However, the influence of the titania support, presumably by acidic hydroxyl groups, on formation of C_2 and C_3 products via side-reactions led to deactivation of the $Pt(Re)/TiO_2$ catalysts. It is shown that PtRe/C is more active in glycerol APR than $PtRe/TiO_2$.

In Chapter 5 we investigated the effect of varying particle size of activated carbon supported Pt catalysts in APR of glycerol. Secondly, the activities of PtRe catalysts prepared by catalytic reduction method were investigated. An increase in APR activity was observed with increasing Pt particle size. The WGS activities of the catalysts followed a similar trend. Easier water activation on step-edge sites are thought to be at the origin of enhanced WGS and APR rates on larger Pt particles. In line with the APR results, larger Pt particles showed higher activity in model acetaldehyde decomposition experiments. Addition of Re to pre-reduced Pt/C by the catalytic reduction method resulted in an increase in APR activity of the Pt/C catalyst with the smallest particle size. Formation of a thicker Re shell around the Pt particles resulted in a decrease in the Pt ensembles on the catalyst surface. In light of the activity results, we conclude that the presence of Pt ensembles next to Re species is essential for obtaining high rates of C-O and C-C bond hydrogenolysis reactions in APR. This site requirement is less stringent for the WGS reaction, where an increase in activity with Re addition to Pt/C was observed. Reduction of PtRe alloys at higher reduction temperature resulted in enhanced WGS activity. A reasonable explanation is that appearance of single Pt atoms on the surface of bimetallic PtRe nanoparticles is sufficient for obtaining a synergetic effect between Pt and Re in the WGS reaction.

Chapter 6 compares the promotional effect of Re on Pt vs. Rh supported on activated carbon in APR of glycerol. Bimetallic catalysts were prepared with a Re/Pt(or Rh) ratio of 0.5. Monometallic Pt/C was found to be more active than Rh/C. However, RhRe was more active than PtRe in line with its highest activity in WGS. Although Rh/C was more selective for C-C bond cleavage than Pt/C as followed from the gas-phase acetaldehyde decomposition

measurements, their alloys with Re gave higher selectivities toward products obtained via C-O bond cleavage than those formed by C-C bond cleavage reactions.

Chapter 7 explores the decomposition of ethanol and formic acid on Au and Pt catalysts supported on ceria nanorods and nanocubes. Pt was found to be more active than Au in steam reforming of ethanol as well as its oxidation and decomposition (in the absence of steam or oxygen). These activity trends were correlated to the WGS activities of the catalysts. Nanorod supported Pt and Au was more active due to enhanced water activation on the oxygen vacancies in the Ce(110) planes. On both Pt and Au catalysts, the first step in ethanol decomposition was dehydrogenation to acetaldehyde. For Au, acetaldehyde remained the major product. Pt, on the other hand, due to its higher metal-carbon bond energy was much more active in cleavage of C-C bonds in acetaldehyde to form CH_4 and CO. The presence of water in the feed mainly facilitates the decomposition of acetaldehyde. These catalysts were also active in decomposition of formic acid starting from 50 °C. Conversion of formic acid was complete for all catalysts at 200 °C. Gold catalysts selectively decompose formic acid into hydrogen and carbon dioxide. Due to its higher WGS activity and higher Pt-O bond energy, Pt was less selective towards hydrogen and also catalyzed direct decarbonylation of formic acid.

Research with the aim to understand the origins of activity and selectivity in heterogeneous catalysis is crucial for developing novel catalytic processes when the feedstock for the chemical industry needs to maintain its diversity. Our efforts into understanding the synergetic effects in bimetallic systems as well as the interaction of the metal phase with the support are important for tailoring the properties of catalytic nanoparticles for efficient valorization of biomass. So far, most of the studies in the field of aqueous phase reforming have predominantly focused on the use of relatively simple model compounds. The number of scientific publications devoted to the use of biomass-derived polyols such as sorbitol, glucose or xylitol is limited. Application of the PtRe/C catalysts, which have been extensively studied in the present work, to water solutions of sugar alcohols originating from biomass processing has high scientific and industrial importance. Expanding the application of the APR process by coupling APR catalysts and reactor systems similar to those utilized in conventional petroleum oil refineries will enable the production of sustainable bio-based chemicals identical to their petroleum-derived counterparts. The model reactions explored in this study, namely gas phase water-gas shift and acetaldehyde decomposition reactions, were used to examine the removal of CO from the catalytic surface and C-C bond cleavage activities of the catalysts, respectively, in reaction media with reduced complexity when compared to the phenomena occurring during APR. However, further studies should take into account the influence of the products appearing in the real reaction mixture and, most importantly, these reactions should be carried out in the liquid phase. For instance, determining the activities of the present sets of catalyst in liquid phase CO removal would give more direct indications of the influence of the water-gas shift reaction on the overall performance in the APR reaction. Another important aspect of future studies could be the replacement of relatively expensive metals as Pt and Re by cheaper

alternatives. The first row transition metals should be reasonable first candidates as they are cheaper and more abundant when compared to Pt, Rh and Re. Copper, nickel and cobalt may be used to develop novel reforming catalysts for aqueous phase processing of biomass constituents. As discussed in detail in the present work, water activation is an important issue in APR catalysis. Therefore, alloying these metals with more reactive metals or the use of a reducible oxide support such as titania may be required. A problem with these first row metals may be catalyst stability problems due to leaching of the active metal components under hydrothermal conditions. Finally, developing more efficient methods for operando characterization of the catalysts is of great importance for fully resolving the nature of the active sites in biomass catalysis. In situ spectroscopy is one of the most effective tools to characterize heterogeneous catalysis. In the current study we used in situ X-ray absorption spectroscopy during aqueous phase reforming of ethylene glycol and gas-phase water-gas shift reaction to monitor the structural changes on our catalysts. Further characterization of the current catalytic systems in aqueous phase in the presence of more complex oxygenated carbohydrates derived from cellulosic biomass is evidently very important.

List of Publications

Journal Publications

- A. Ciftci, D.A.J.M. Ligthart, E.J.M. Hensen, Aqueous phase reforming of glycerol over Re-promoted Pt and Rh catalysts, *Green Chemistry*, DOI: 10.1039/c3gc42046a.
- A. Ciftci, D.A.J.M. Ligthart, A.O. Sen, A.J.F. van Hoof, H. Friedrich, E.J.M. Hensen, Pt-Re synergy in aqueous phase reforming of glycerol and the water-gas shift reaction, *Journal of Catalysis* 311 (2014) 88-101.
- A. Ciftci, D.A.J.M. Ligthart, P. Pastorino, E.J.M. Hensen, Nanostructured ceria supported Pt and Au catalysts for the reactions of ethanol and formic acid, *Applied Catalysis B: Environmental* 130-131 (2013) 325-335.
- A. Ciftci, B. Peng, A. Jentys, J.A. Lercher, E.J.M. Hensen, Support effects in the aqueous phase reforming of glycerol over supported platinum catalysts, *Applied Catalysis A: General* 431-432 (2012) 113-119.
- A. Ciftci, S. Eren, D.A.J.M. Ligthart, E.J.M. Hensen, Pt-Re synergy on reducible oxide supports in aqueous phase reforming of glycerol (submitted).
- A. Ciftci, T. Zhu, D.A.J.M. Ligthart, E.J.M. Hensen, Carbon-supported bimetallic PtRe catalysts for aqueous phase reforming of glycerol prepared by catalytic reduction of Re on Pt nanoparticles (submitted).
- E.J.M. Hensen, A. Ciftci, T. Zhu, I. Filot, D.A.J.M. Ligthart, Pt-Re synergy in water-gas shift reaction: a combined experimental and theoretical study (in preparation).

The author also contributed to the following publications outside the scope of this thesis:

- A.Ciftci, D. Varisli, K.C. Tokay, N.A. Sezgi, T. Dogu, Dimethyl ether, diethyl ether & ethylene from alcohols over tungstophosphoric acid based mesoporous catalysts, *Chemical Engineering Journal* 207 (2012) 85-93.
- A. Ciftci, N.A. Sezgi, T. Dogu, Nafion-incorporated silicate structured nanocomposite mesoporous catalysts for dimethyl ether synthesis, *Industrial & Engineering Chemistry Research* 49 (2010) 6753-6762.
- A. Ciftci, D. Varisli, T. Dogu, Dimethyl ether synthesis over novel silicotungstic acid incorporated nanostructured catalysts, *International Journal of Chemical Reactor Engineering* 8 (2010) A45.
- D. Varisli, K.C. Tokay, A. Ciftci, T. Dogu, G. Dogu, Methanol dehydration reaction to produce clean diesel alternative dimethylether over mesoporous aluminosilicate-based catalysts, *Turkish Journal of Chemistry* 33 (2009) 355-366.

Conference presentations

- A. Ciftci, T. Zhu, D.A.J.M. Ligthart, E.J.M. Hensen, Promotional effect of Re on catalytic performance of Pt/C in water-gas shift and aqueous phase reforming of glycerol, *EUROPACAT XI 20 years of European Catalysis... and beyond,* 1-6 September 2013, Lyon, France. [Oral]

- A. Ciftci, S. Eren, T. Zhu, D.A.J.M. Ligthart, E.J.M. Hensen, Enhanced activity of platinum-based bimetallic catalysts in aqueous phase reforming of glycerol, *Catalysis for Renewable Sources: Fuel, Energy, Chemicals*, 22-28 July 2013, Lund, Sweden. [Oral]

- A. Ciftci. T. Zhu, D.A.J.M. Ligthart, E.J.M. Hensen, Pt-Re synergy in aqueous phase reforming of glycerol and water-gas shift reaction, *2nd Summer School on Catalysis for Sustainability*, 23-26 June 2013, Rolduc Abbey, The Netherlands. [Oral]

- A. Ciftci, T. Zhu, D.A.J.M. Ligthart, E.J.M. Hensen, Pt-Re Synergy in water-gas shift and aqueous phase reforming of glycerol: a combined experimental and theoretical study, *23rd North American Catalysis Society Meeting*, 2-7 June 2013, Louisville, Kentucky, USA. [Poster]

- A. Ciftci, D.A.J.M. Ligthart, E.J.M. Hensen, Aqueous phase reforming of glycerol over PtRe/C catalysts, *14th Netherlands' Catalysis and Chemistry Conference (NCCC XIV)*, 11-13 March 2013, Noordwijkerhout, The Netherlands. [Oral]

- A. Ciftci., P. Pastorino, E.J.M. Hensen, Nanostructured ceria supported Pt and Au catalysts for the decomposition of ethanol and formic acid, *13th Netherlands' Catalysis and Chemistry Conference (NCCC XIII)*, 5-7 March 2012, Noordwijkerhout, The Netherlands. [Oral]

- A. Ciftci., P. Pastorino, E.J.M. Hensen, Nanostructured ceria supported Pt and Au catalysts for the decomposition of ethanol and formic acid, *Summer School Energy and Materials from the Sun*, 20-23 June 2011, Rolduc Abbey, The Netherlands. [Oral]

Acknowledgements

The long journey has now ended. I have had the most incredible experience of my life which helped me to grow not only scientifically but also personally. Undoubtedly, this work is a combined effort put together by me and a great number of people. My interactions with several individuals over the past four years have influenced me beyond the scientific findings presented here. It is a pleasure to take this opportunity and thank those wonderful people who inspired me and contributed in this thesis.

First and foremost, I would like to express my sincere gratitude to my supervisor prof. Emiel Hensen. Emiel, you have helped and taught me immensely throughout the years. I have always been impressed and inspired by your enthusiasm, devotion and passion about science. It has been a privilege to experience your in depth knowledge, unique perspective and insight. Your friendly attitude, suggestions and constructive comments helped me to tune myself to reach my goals as a researcher whenever I failed to see the big picture. You have given me unique opportunities and the freedom to explore my abilities. Thank you for always encouraging me to take a step out of my comfort zone and pushing me beyond. Your invaluable support and guidance made these four years very memorable for me.

I would like to offer my special thanks to my 2nd promoter prof. Rutger van Santen and other committee members: prof. Seshan, prof. Dmitry Murzin, prof. Hans Niemantsverdriet, dr. Xander Nijhuis and prof. Jaap Schouten for taking the time for evaluating my thesis and their valuable comments.

It was a pleasure to work in the group of prof. Johannes Lercher at the Technical University of Munich. I appreciate the opportunity and the help provided by Baoxiang Peng and Dr. Andreas Jentys during the month I spent in Munich.

Evgeny, our discussions and your constructive comments about my work have been very helpful. Thanks for always being open to share your ideas as well as your esthetical view. The latter is particularly acknowledged due to your great contribution in the cover design of my thesis, TOC for some of my papers and conference presentations. Michel, thanks for all your support. You have been a great example for me as a researcher, an excellent colleague in the lab, a kind and enjoyable instructor in Grenoble, a collaborator, an advisor and a friend. Your contribution to this work is immense. I am so happy that you will be one of my paranymphs.

Emma, a big thanks for your administrative and organizational assistance at all levels of my work. Beyond a management assistant, you are the backbone of SMK with all the "action" you initiate in the group. I will always remember our small chats and how much fun we had. I am looking forward to the day we will go skating at Kinderdijk and see the spectacular War Horse afterwards.

Thanks to Johan for helping me with all kinds of technical problems. My special thanks to you for always being so patient and positive no matter how frustrating things get.

for taking the picture on the last page of my thesis. Ceylan, you are a perfect friend the times spent with whom are always fun. You have been very supportive and caring especially during the most boring times while I was writing my thesis. Thanks for checking on me if I was still alive and encouraging me to join you in *çop-çop*. My thanks are extended to Berna and Irmak, the other members of *güncüler*, for the enjoyable cooking workshops, brunches and dinners. Special thanks to my friends with whom we shared many nice memories especially during the time when we first moved to the Netherlands: Fırat & Beril, Uğur, İlhan and Hilal.

I would like to express my sincere gratitude to Prof. Timur Doğu, my supervisor during my Master studies at METU. His help and encouragement paved the way for me to start this PhD work in the Netherlands. My dearest friends from Turkey whose support I have felt during the last four years are very valuable to me. Zeynep, Seda and Öznur, girls our friendship has no boundaries. Despite the distances between Eindhoven, Boston, Rotterdam and Ankara we always managed to stay up-to-date on every little issue. You are part of me which I carry along wherever I go. Ayça, my lifelong friend, thank you for supporting me at various stages of my life and despite the distances taking every little chance to keep up our friendship.

Finally, I would like to express my gratitude to my wonderful parents and my sister. Mom and dad, without your support I do not think I could have achieved any of these. No matter how difficult it was for you to let me go far away from home for such a long period, you pushed your limits to support me as you had always done at all stages of my life. I can never thank you enough for your efforts for creating this beautiful life for me. *Anne & baba, sizin desteğiniz olmadan bunların hiçbirini başaramazdım. Bu kadar uzun bir süre için bu kadar uzağa gitmem sizin için ne kadar zor olsa da hayatımın her aşamasında yaptığınız gibi yanımda olmak için elinizden gelenin fazlasını yaptınız. Benim için yarattığınız bu güzel hayat ve verdiğiniz emekler için size ne kadar teşekkür etsem az...* Emel, my sister and my best friend, I am very lucky to have someone like you who doesn't necessarily need the exact words to understand me. We have been living in different countries for the past eight years, but I feel you beside me at all times. Thanks a lot for keeping me motivated and cheerful. I would also like to express my appreciation to my extended family in Turkey: my parents-in-law, my aunts and cousins, my brother-in-law Mert and my little love Arda (who has been a source of enthusiasm for me throughout the past half year).

These past four years have been a whole new chapter in my life. But this story could never be the same as it has been without the presence of a special man. Selçuk, when we decided to take a step forward to this new experience, we had no idea how it would turn out to be. Now, when I look back I see that we have grown up together throughout the years and I feel proud of us. Surviving here together and most importantly creating a life which we would love and be happy with took some courage and commitment. Your unconditional support, patience and understanding made everything seem possible to me. As *Ece Temelkuran* says, *stories lived together make people each other's home.* Selçuk, in a place far away from home, thanks for being my peaceful home and taking care of me. Mom, dad, Emel and Selçuk, this booklet is for you.

About the author

Ayşegül Çiftçi (Sandıkcı) was born on December 16, 1984 in Ankara, Turkey. After graduating from Ankara Atatürk High School in 2002, she started her study at the department of Chemical Engineering at Middle East Technical University in Ankara. In 2007, she received her Bachelor of Science degree. Afterwards, she continued with the Master programme in the group of Catalysis and Reaction Engineering in the same department with a full scholarship from the TÜBİTAK Scientist Support Program. She carried out her research on the topic of "Nanocomposite nafion and heteropolyacid incorporated mesoporous catalysts for dimethyl ether synthesis from methanol" under the supervision of Prof. Dr. Timur Doğu. In 2008, she received the Middle East Technical University Prof. Dr. Hasan Orbey Memorial Award for Research in Graduate Work. In November 2009 she started her PhD project at the Inorganic Materials Chemistry group of Eindhoven University of Technology in the Netherlands under the supervision of prof. dr. ir. Emiel J.M. Hensen. Her PhD study focused on the conversion of biomass-derived alcohols to useful chemicals and hydrogen using heterogeneous catalysts. The most important results of this research are described in this thesis. In June 2010, she worked in the Catalysis Research Center at the Technical University of Munich, Germany as a visiting researcher in the framework of European Graduate School on Sustainable Energy. She presented her research work at several international conferences and received the EFCATS PhD student award by the Europacat XI-2013 Scientific Committee.